Technische Universität München
TUM School of Engineering and Design

Numerical Investigation of Secondary Currents in Partially Filled Pipe Flow

Julian Frederic Brosda

Vollständiger Abdruck der von der TUM School of Engineering and Design der Technischen Universität München zur Erlangung des akademischen Grades eines

Doktors der Ingenieurwissenschaften (Dr.-Ing.)

genehmigten Dissertation.

Vorsitzender:	Prof. Dr. phil. N. Rüther
Prüfer der Dissertation:	
	1. Prof. Dr.-Ing. habil. M. Manhart
	2. Prof. Dr. M. Uhlmann
	3. Prof. V. Nikora, Ph.D.

Die Dissertation wurde am 23.06.2022 bei der Technischen Universität München eingereicht und durch die TUM School of Engineering and Design am 4.10.2022 angenommen.

To Katharina

Abstract

This thesis investigates turbulence-driven secondary flow in a partially filled pipe. The aim of this thesis was to provide a detailed description of the flow and to analyse the secondary flow mechanism with a special focus on the role of the so-called mixed-corner (the corner between the pipe wall and the free surface) by means of a highly resolved data set. Therefore, direct numerical simulations were performed for the pipe flow with filling ratios (FR) of 25%, 50% and 75% and Reynolds numbers between $Re_\tau = 115$ and 460; the observed flow regimes cover marginally turbulent to moderately turbulent flow.

Over the considered parameter range, the friction coefficient was found to agree well with Prandtl's relation for smooth full pipe flow. The well-known *velocity-dip* phenomenon could be observed for $Re_\tau \geq 140$. In combination with all data available in literature on the position of the maximum streamwise velocity Δz, the present results indicate a linear relation between Δz and the FR. The secondary flow pattern is organised in four vortices which are arranged symmetrically to the centre plane in two counter-rotating pairs. In semifilled pipe flow the position and size of the inner secondary cell, which occurs in the mixed-corner, scale with wall units. A larger inner secondary cell could be detected for 25% FR, whereas it almost vanishes for 75% FR. Correspondingly, the outer secondary vortex, scaling in outer units, gets more dominant with increasing FR. The wall shear stress distribution is strongly influenced by the comparably weak secondary flow. In the mixed-corner a global wall shear stress maximum occurs, because the inner vortex transports high-momentum fluid from the free surface towards the wall. In the centre of the perimeter the wall shear stress is constant and similar to full pipe flow. The Reynolds stresses also behave similarly to full pipe flow, apart from near the free surface. In the mixed-corner a Reynolds stress anisotropy can be observed, which is linked to the generation of mean streamwise vorticity.

For the first time, the complete path of kinetic energy from its input until dissipation is quantified, focusing on how the secondary flow obtains its energy. The key term is the secondary production $P_{2,3}$, which generates mean secondary kinetic energy at the free surface around the stagnation point between the inner and outer vortices. In addition, three different techniques were employed to analyse the connection between instantaneous coherent structures and the mean secondary flow: proper orthogonal decomposition, Gaussian filtering and conditional averaging. It can be concluded that the generation of secondary flow via $P_{2,3}$ is a multi-scale and multi-mode process. Moreover, it is indicated that the mean secondary flow is not formed by a stable, instantaneous vortex pattern which only deviates from its mean. Instead, it is formed by averaging over a large number of individual large and small scale structures. Finally, conditional averaging of extreme $P_{2,3}$-events revealed an interaction between two counter-rotating vortices that generates mean secondary kinetic energy at the free surface. One vortex seems to be stable over a longer distance and resembles the inner secondary cell, whereas the other vortex occurs locally, reaches from the side wall towards the free surface and resembles the mean vorticity distribution.

Kurzfassung

Das Thema der vorliegenden Arbeit sind turbulenz-induzierte Sekundärströmungen in teilgefüllten Rohrströmungen. Das Ziel der Arbeit ist zum einen, die hochaufgelöste Strömung detailliert zu beschreiben, und zum anderen, den Mechanismus der Sekundärströmung unter besonderer Beachtung der gemischten Ecke (der Ecke zwischen Rohrwand und freier Oberfläche) zu untersuchen. Dazu wurden direkte numerische Simulationen einer Rohrströmung mit den Füllgraden 25%, 50% und 75% und Reynoldszahlen zwischen $Re_\tau = 115$ und 460 durchgeführt; die beobachteten Strömungsregime umfassen marginal turbulente bis moderat turbulente Strömungen.

Für den gesamten betrachteten Parameterbereich liegt der Reibungskoeffizient sehr nah an der Prandtlschen Beziehung für glatte voll-gefüllte Rohre. Das bekannte *velocity-dip* Phänomen konnte für Strömungen mit $Re_\tau \geq 140$ beobachtet werden. In Kombination mit allen in der Literatur verfügbaren Daten zur Position der maximalen Hauptströmungsgeschwindigkeit Δz legen die vorliegenden Ergebnisse eine lineare Beziehung zwischen Δz und dem Füllgrad nahe. Die Sekundärströmung besteht aus vier Wirbeln, die sich in zwei gegenläufig drehende Wirbelpaare gliedern, die symmetrisch zur zentralen Ebene angeordnet sind. In der halb-gefüllten Rohrströmung skalieren die Position und die Größe des inneren Sekundärströmungswirbel, der sich in der gemischten Ecke befindet, mit Wandeinheiten. Ein größerer innerer Sekundärströmungswirbel konnte für den Füllgrad 25% beobachtet werden, wohingegen der Wirbel für den Füllgrad 75% fast verschwindet. Ent-sprechend wird der äußere Sekundärströmungswirbel, der in äußeren Einheiten skaliert, mit steigendem Füllgrad dominanter. Die Wandschubspannungsverteilung ist stark von der relativ schwachen Sekundärströmung beeinflußt. Ein globales Wandschubspannungsmaximum tritt in der gemischten Ecke auf, wo der innere Wirbel Fluid mit starkem Impuls von der freien Oberfläche Richtung Wand transportiert. In der Mitte des Umfangs ist die Wandschubspannung konstant und ähnlich zur vollen Rohrströmung. Abgesehen von einem Bereich nahe der freien Oberfläche verhalten sich auch die Reynoldsspannungen ähnlich zur vollen Rohrströmung. In der gemischten Ecke kann eine Anisotropie der Reynoldsspannungen beobachtet werden, die mit der Erzeugung von gemittelter Wirbelsträrke in Hauptströmungsrichtung zusammenhängt.

In dieser Arbeit wurde zum ersten Mal der komplette Weg der kinetischen Energie von der Zufuhr bis zur Dissipation quantifiziert, und dargelegt, wie die Sekundärströmung ihre Energie erhält. Der wichtigste Term ist die Sekundärproduktion $P_{2,3}$, der an der freien Oberfläche zwischen dem inneren und äußeren Wirbel sekundäre kinetische Energie erzeugt. Darüber hinaus wurden drei verschiedene Methoden angewendet, um die Verbindung zwischen instantanen kohärenten Strukturen und der gemittelten Sekundärströmung zu untersuchen: die Hauptkomponentenanalyse, die Gaußfilterung und die Ereignisbedingte Mittelung. Diese Analysen deuten darauf hin, dass die mittlere Sekundärströmung nicht aus instantanen, annähernd konstanten Wirbeln besteht, die nur wenig vom mittleren Wirbel

abweichen, sondern durch die Mittelung vieler einzelner groß- und kleinskaliger Wirbel entsteht. Zudem kann der Schluss gezogen werden, dass für die Beschreibung der Erzeugung von Sekundärströmung durch $P_{2,3}$ viele unterschiedliche Skalen bzw. Moden nötig sind. Die bedingte Mittelung der extremen $P_{2,3}$-Ereignisse zeigte auf, dass das Zusammenspiel zwischen zwei gegenläufig drehenden Wirbeln gemittelte sekundäre kinetische Energie an der freien Oberfläche erzeugt. Ein Wirbel scheint über eine längere Strecke stabil zu sein und ähnelt dem inneren Sekundärströmungswirbel, wohingegen der andere Wirbel nur lokal auftritt. Dieser erstreckt sich von der Seitenwand bis an die Mitte der freien Oberfläche und ähnelt der Verteilung der mittleren Wirbelstärke in Hauptströmungsrichtung.

Preface

I am very grateful that I got the opportunity to do this PhD, especially, because I could bring in my own ideas into this project. Many years ago I popped up in Prof. Manhart's office with a vague idea of studying secondary flows in rivers. But instead of convincing me for a different, already established topic at the chair, he offered to supervise me for a Master's thesis on secondary flows. Based on the Master's thesis the idea of a PhD-project evolved and Prof. Manhart offered me a research and teaching assistant position. Throughout the last years, I was given a large freedom to choose what kind of investigations to do, and at the same time, Prof. Manhart was always guiding me patiently, was open for all upcoming questions and gave me lots of valuable advice. Therefore, I would like to thank you, Michael, very much!

I would like to sincerely thank Prof. Markus Uhlmann for taking on the role of mentor and being part of my PhD committee as second referee. I would like to express my gratitude to Prof. Vladimir Nikora, whose research had a large impact on this thesis, for being the third referee, and to Prof. Nils Rüther for taking over the chairmanship of the PhD committee.

The simulations for this dissertation were performed at the Leibniz Computing Centre (LRZ) of the Bavarian Academy of Sciences. The provided computation time, which was granted under project no. pn56ci, is gratefully acknowledged by the author.

Fortunately, Prof. Manhart did not only supervise myself, but also he forms a team of highly motivated and skilled, but most important, very nice colleagues. Thank you all for countless discussions, all your advice, the shared suffering, your friendship and the great time together. In particular: Claudia, Florian, Daniel, Sheema, Tianshi, Hao, Wolfgang, Alex (Bye, bye, birdie), Uli, Lukas, Simon, Ash and Yoshi.

To all my dear friends: I am deeply grateful to have you and that you have accompanied me on this journey.

Last but not least, I would like to thank my family for their support and love, especially my parents who always gave me the freedom and encouraged me to pursue my interests.

Julian Brosda
Munich, June 2022

Contents

List of Tables

List of Figures

Nomenclature

Abbreviations

2C-POD	Two Component POD
3C-POD	Three Component POD
DNS	Direct Numerical Simulation
FR	Filling Ratio
Fr	Froude Number
GF	Gaussian Filtering
IBM	Immersed Boundary Method
LES	Large Eddy Simulation
MKE	Mean Kinetic Energy
PDF	Probability Density Function
PIV	Particle Image Velocimetry
POD	Proper Orthogonal Decomposition
RANS	Reynolds-Averaged Navier-Stokes
Re	Reynolds Number
SSP	Self-Sustaining Process
TKE	Turbulent Kinetic Energy
VLSM	Very Large Scale Motion

Greek Letters

$\boldsymbol{\omega}$	Vorticity vector
δ	Boundary layer thickness
δ_ν	Viscous length scale
Δ_{cc}	Horizontal distance of the core of the structure to the symmetry plane
Δ_{fs}	Vertical distance of structure to free surface
δ_{ij}	Kronecker delta
ϵ	Dissipation
η	Kolmogorov length scale
Γ	Circulation

κ	von Kármán constant: 0.41
κ_{ij}	Standard two-point correlation of component i and j
λ	Friction factor
λ^k	Energy fraction of kth mode
λ_i	Eigenvalues of the Reynolds stress tensor
$\mathbf{\Lambda}$	Matrix of eigenvalues of POD
$\mathbf{\Phi}$	Matrix of spatial modes of POD
μ	Dynamic viscosity of fluid
ν	Kinematic viscosity of fluid
Ω	Cross-sectional domain
ω_i	Vorticity in i-direction
Ω_T	Vorticity tensor
Φ	Spatial mode of POD
$\phi(x_2, x_{2,b})$	Spanwise velocity distribution
ψ	Stream function
ρ	Density of fluid
σ	Standard deviation
τ_0	Globally averaged wall shear stress
τ_w	Wall shear stress
θ	Azimuthal component of Polar coordinate system
ξ	Invariant of the Reynolds stress tensor
ζ	Invariant of the Reynolds stress tensor

Mathematical Operators

$\cdot$	Scalar multiplication
Δ	Difference
$\frac{\partial \varphi}{\partial x_i}$	Partial derivative in i-direction
$\frac{d \varphi}{d x_i}$	Derivative in i-direction
$\int$	Integration operator
$\| \varphi \|^2$	L^2-norm
$\| \varphi \|_2$	Euclidean norm
∇	Nabla Operator in $x_1,\ x_2$ and x_3-direction
∇^2	Laplace Operator in $x_1,\ x_2$ and x_3-direction

$\overline{\varphi}$ Averaging operator in time and in homogeneous direction

$\sum$ Summation operator

$\tilde{\varphi}$ Filtering operator

$\times$ Cross product

φ' Fluctuation of a quantity φ around its mean $\overline{\varphi}$

φ^+ Quantity φ in wall units

φ_{rms} Root mean square of a quantity φ

$exp(\varphi) \equiv e^{\varphi}$ Exponential function

$ext(\varphi)$ Extreme value of quantity φ

Roman Letters

x_1, x_2, x_3 Components of Cartesian coordinate system

$\boldsymbol{u}$ Velocity vector

$\boldsymbol{x}$ Vector of Cartesian coordinates

Δt^+ Averaging time in viscous time units

Δt_b Averaging time in bulk time units

Δz Distance to free surface

ℓ Characterisitc length scale

$\mathbf{A}$ Matrix of the temporal coefficients of POD

$\mathbf{C}$ Temporal correlation matrix of POD

$\mathbf{U}$ Velocity matrix of POD

$\mathrm{N_{total}}$ Total number of grid points

A Cross section of pipe section

a^k Temporal coefficient of POD

A_S Area of a vortical structure

B Law of the wall constant: 5.1

C Convection of kinetic energy

$C(\boldsymbol{x})$ Coefficient to weigh Gaussian filter kernel

$C(t, t')$ Temporal correlation matrix of POD

C_C Empirical friction coefficient

C_f Friction coefficient

D Diameter of the pipe

D_m Ratio between A and W

$D_{2,3}$ Discriminant of the two-dimensional cross-stream velocity gradient tensor

D_H Hydraulic diameter: $D_H = 4 \cdot R_H$

$E(\boldsymbol{x}, t)$ Kinetic energy of the flow

E_{in} Energy income of kinetic energy budget equation

F Fourth central moment: Kurtosis

Fr Froude number

g Gravitational acceleration

G_1 Constant volume force

H Flow depth

H_{eq} Equivalent length scale

I_1 Geometry-dependent constant

I_2 Geometry-dependent constant

I_s Bed slope

J Velocity gradient tensor

K Mean kinetic energy

k Turbulent kinetic energy

k_s Relative wall roughness

L Length of the pipe/computational domain

L_{11} Integral length scale

L_{cs} Streamwise length of complete structure

L_{fs} Streamwise length of upper part of structure

N_T Number of instantaneous cross-sectional slices

N_X Number of points per cross-section

P Production of MKE or TKE

p Pressure

p_w Pressure at the wall

Q Second invariant of J

R Radius of the pipe

r Radial component of Polar coordinate system

R_H Hydraulic radius: $R_H = \frac{A}{U_w}$

Re Reynolds number

Re_b Bulk Reynolds number, based on u_b and D_H: $Re_b = \frac{u_b \cdot D_H}{\nu}$

Re_τ Friction Reynolds number, based on u_τ and R_H: $Re_\tau = \frac{u_\tau \cdot 2R_H}{\nu}$

RES Residuum of kinetic energy budget equations

S	Third central moment: Skewness
s	Coordinate along a path
S_T	Rate-of-strain tensor
T	Number of time steps
T	Transport/diffusion of kinetic energy
t	Time
T_{press}	Pressure transport of kinetic energy
T_{turb}	Turbulent transport of kinetic energy
T_{visc}	Viscous transport of kinetic energy
U	Characteristic velocity
u_1, u_2, u_3	Velocity components in x_1-, x_2- and x_3-direction
u_b	Bulk velocity
U_w	Wetted perimeter
u_η	Kolmogorov velocity scale
u_τ	Friction velocity
$u_{i,max}$	Maximum velocity of component i
W	Free surface width of an open-channel flow
W_{cs}	Transverse width of complete structure
W_{fs}	Transverse width of upper part of structure
x_n	Coordinate in wall-normal direction

1. Introduction

In this first chapter I would like to introduce the phenomenon of my study, a topic of fundamental research: Secondary currents in straight, turbulent, partially filled pipe flow. In contrast to the primary flow, which describes the flow in the main direction, secondary currents deal with the flow perpendicular to the main flow. In the investigated flow case, the secondary flow is turbulence-induced and rather weak, nevertheless, it strongly influences the primary flow and, therefore, the flow's impact on the surrounding structures and on the processes of sedimentation and resuspension of sedimented material. Secondary flows appear in almost every practical flow application, but how they are generated and their effects are hard to grasp in a complex surrounding. Hence, the flow setup has to be abstracted in order to limit the overwhelming complexity and limit other influences.
Fundamental research is often not directly linked to practical applications and its importance and purpose are not always obvious. Therefore, this first chapter explains the background and the motivation of the study. Next, the basic knowledge and concepts of turbulent flows, which are important for the present study, are introduced. Subsequently, an overview of the field of research and how the present study fits into it is given, followed by the current state of the art. The chapter finishes with the main objectives and the structure of this thesis.

1.1. Motivation

Turbulent flow in partially filled pipes are ubiquitous in the sewage system. All authorities that deal with waste water have to face the challenge of accurately measuring the discharge in partially filled pipe flow (DWA, 2011). So far a number of measurement techniques using different principles have been developed to determine the discharge, some of them relying on relations between flow velocities at some points and flow rate at various filling grades (DWA, 2011). However, an uncertainty of $5-10\%$ remains, hence, detailed knowledge of the flow and its velocity distributions might help to reduce this uncertainty.
Another important challenge in waste water channels is sedimentation and resuspension of sedimented material. Resuspension of toxic substances or heavy metals can lead to substantial pollution in rivers when waste water treatment plants are bypassed in stormwater conditions (Passerat *et al.*, 2011; Weyrauch *et al.*, 2010). Modeling sediment dynamics in waste water channels intrinsically suffers from an incomplete knowledge of the detailed turbulence structure and the distribution of wall shear stress and its fluctuations. Thus, so far integral estimations of the so-called *sediment transport capacity* (Macke, 1982; DWA, 2012) are used in the design process of waste water channels.
Partially filled pipe flow does not only represent a waste water channel, but can also be considered as a model flow for rivers and as a fundamental flow phenomenon that received little attention so far. Hence, it can be regarded as a model flow with special properties. One

of the properties is the generation of secondary flows in the intersections between the free surface and the pipe's wall, a so-called *mixed-corner*, that leads to a non-circular distribution of flow variables in the partially filled pipe, see figure 1.1. While, for example, in rectangular open-duct flow the secondary flow is generated by the mixed- and solid-corners (solid means with no-slip walls on both sides), in partially filled pipe flow secondary flow is generated by the mixed-corner only. Therefore, in partially filled pipes the generation of secondary flow at a mixed-corner can be studied without the influence of other inhomogeneities. Moreover, the corner can be acute or obtuse angled, thus having a variable effect on the flow dependent on filling grade.

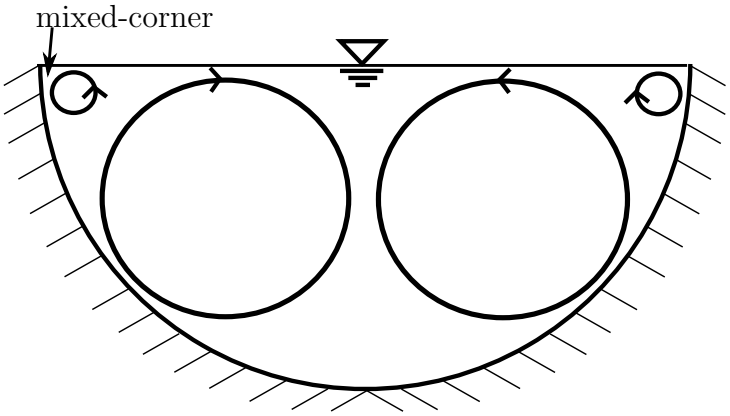

Figure 1.1: Sketch of secondary flow pattern in a semi filled pipe flow. The sense of rotation of the vortical structures is indicated by small arrows.

The first investigations of partially filled pipe flows at this institute, the Professorship of Hydromechanics, were conducted by Strauß (1978), who took measurements of the velocity distribution in the vertical symmetry line using a hydraulic impeller. Later on, Kölling (1994) validated his finite element simulation against the measurements of Strauß. Interestingly, his simulations were able to generate secondary flows by applying an anisotropic turbulence model based on algebraic stress equations. This thesis now adds the next element using the means of high performance computing.

The simulations performed for this thesis generated the first numerical, highly-resolved and three-dimensional data set for partially filled pipe flow. The close connection to full pipe flow might imply that the mean flow is homogeneously distributed in azimuthal direction, and the maximum mean velocity is, because of the wall friction, located furthest away from the wall: either at the centre of the free surface or in the pipe centre. But by looking at the flow in detail, it reveals that the dominant primary flow is influenced by a subtle secondary flow, which does not average over time to zero, because the free surface breaks the azimuthal symmetry. Hence, the primary flow shows various differences compared to full pipe flow and also generates an inhomogeneous wall shear stress distribution. In figure 1.1 the secondary flow that occurs in semi filled pipe flow is presented schematically, consisting of small vortices in each mixed-corner and two larger, counter-rotating vortices in the centre.

Hence, there are many open tasks and questions to be answered. First of all, a detailed description of the mean and turbulent flow is necessary in order to compare and validate

the few existing publications and to create a solid data basis for partially filled pipe flow. In a next step, the mean secondary flow, whose presence seems to be a key feature for the occurring flow pattern, needs to be further investigated. By understanding how secondary flow is generated, and how strong and weak flow components interact with and influence each other, one might be able to further understand what kind of flow is created by the mixed-corner and how the wall shear stress distribution is generated.
To address the tasks and answer the questions, the following sections introduce the necessary basic and more specific concepts for the present flow case before presenting the state of the art of turbulent partially filled pipe flow itself.

1.2. Turbulent Flows

Turbulent flows are considered to be chaotic, three-dimensional, unsteady, non-linear and consist of a wide range of different vortical motions. In many cases the variables of a turbulent flow are characterised as random (Pope, 2000), however, this does not mean that turbulent flows are generally random. Additionally, Jiménez (2018) states, that imagining turbulent flows generally as random, can hinder the viewer from seeing local connections and linking causal relationships that enables us to create a differentiated picture of turbulent flows. As turbulent flows are solutions of the Navier-Stokes equations they are mathematically determined. However, looking at the same flow case but introducing small changes to the initial conditions can lead to large instantaneous deviations between the two solutions, because of the non-linear character of the Navier-Stokes equations. Nevertheless, turbulent flows are statistically determined, thus, the flow statistics of the two solutions should hardly differ.
Within the approximately 150 years of scientific research in the field of turbulence, many achievements were made to unveil some of the secrets of turbulent flows. In the last decades, new developments of measurement techniques and increasing computational power made it possible to investigate turbulent flows by the most accurate model, the so-called Navier-Stokes equations. As the Navier-Stokes equations contain such a large number of degrees of freedom, only relatively simple flow cases became accessible at the end of the last century. Nowadays, more and more complicated flows can be investigated in detail by means of experimental measurements and numerical simulations. In this thesis, turbulent flows are numerically simulated on the basis of the Navier-Stokes equations and the results are studied via statistical methods and investigations of temporal and spatial developments of the flow.
In the following, the governing equations that are used to investigate the present turbulent flow case are introduced. Moreover, main achievements in the research of turbulent flows related to the present study are briefly introduced to set a common base for the following discussions. In order to study the particular flow phenomenon of this thesis, one needs to understand how turbulent flows interact with no-slip walls and free surfaces and what kind of structures evolve in such situations. This is addressed in the latter part of this section.

Conservation Laws

Most of the flows in our environment can be assumed to be incompressible. In order to describe the fluid motion in an incompressible flow, the two fundamental principles, the conservation of mass and the conservation of momentum, have to be considered. On the continuum scale, a flow of a *Newtonian* fluid that follows the above mentioned principles, can be mathematically described by the incompressible *Navier-Stokes equations*. The continuity equation expresses the conservation of mass by

$$\frac{\partial u_i}{\partial x_i} = \frac{\partial u_1}{\partial x_1} + \frac{\partial u_2}{\partial x_2} + \frac{\partial u_3}{\partial x_3} = 0. \tag{1.1a}$$

It describes the change of volume for a fluid element, which has to be zero for incompressible flows. The conservation of momentum is formulated by the momentum equations

$$\frac{\partial u_i}{\partial t} + u_j \frac{\partial u_i}{\partial x_j} = -\frac{1}{\rho}\frac{\partial p}{\partial x_i} + g_i + \nu \frac{\partial^2 u_i}{\partial x_j^2}, \qquad \text{with } i, j = 1, 2, 3. \tag{1.1b}$$

The conservation of momentum relates the acceleration of a fluid element with surface (friction) and body forces (pressure p and gravity g_i) acting on the fluid. The velocity is denoted as u_i with $i = 1, 2, 3$ or as vector with synonymous components $\boldsymbol{u} = (u_1, u_2, u_3)^T$ in Cartesian coordinates $x_1, x_2, x_3 = x, y, z$. The streamwise direction is conventionally defined in x_1 or x direction, x_2 or y is the spanwise component and normal to the free surface is the x_3- or z-component. Note that applying the index notation incorporates the use of *Einstein's sum convention*. Furthermore, the density ρ and the kinematic viscosity ν appear in the momentum equations (1.1b). Other influences on the flow, e.g. temperature gradients, are neglected in the present thesis.
Please note that the Navier-Stokes equations can describe both laminar and turbulent flows, which will be introduced in the next subsection.

Fundamentals of Turbulent Flows

Flows can be distinguished into laminar and turbulent. If a flow is laminar, the fluid flows in layers and no mixture between theses layers takes place. This behaviour occurs, because the friction forces are more dominant compared to the inertial forces and damp any perturbations. In contrast, in turbulent flows, small disturbances are amplified by nonlinear, inertial effects. Thus, vortical structures are created, which generate a mixing of the fluid, and, in contrast to laminar flow, turbulent flow is dominated by inertial forces. A distinction between the two flow states can be expressed by the dimensionless Reynolds number Re, which formulates a ratio between inertial and friction forces:

$$Re = \frac{\text{inertial forces}}{\text{friction forces}} = \frac{U\ell}{\nu} \tag{1.2}$$

with U being a characteristic velocity, ℓ being a characteristic length scale and ν the kinematic viscosity (Schlichting & Gersten, 2017). Re is named after Osborne Reynolds, who

published the results of an outstanding pipe flow experiment in 1883. He was able to change the flow state from laminar to turbulent and *vice versa* by adapting the flow velocity, hence, adapting Re. The transition between laminar and turbulent full pipe flow occurs at approximately $Re = 2300$. Please note that in a full pipe flow, which will be used as example in the following subsection, the bulk velocity and diameter are used to describe the flow, hence, are the characteristic velocity and length scale, respectively. The parameters of Re can be used to characterise the size, and therefore a length scale, of vortical structures that occur in a flow. This length scale of the occurring vortical structures is commonly called *scale*. The large scales in a flow obtain the kinetic energy from the force that drives the flow, e.g. gravity. For a fully developed pipe flow, a global balance between the incoming energy and the friction is established. The steady energy supply is balanced by the dissipation of energy to heat. Responsible for the dissipation are viscous processes, which are dominated by the small scales. Therefore, the energy needs to be transferred from the large to the small scales, which is commonly known as *Richardson cascade* (Pope, 2000). With increasing Reynolds number the range of scales increases, hence, the vortical structures are split up into smaller and smaller scales. For sufficiently high Reynolds numbers, the smallest scales in a flow are only governed by the energy they receive from the larger scales and the viscous effects, which makes them independent of the geometry and the largest scales. Hence, the smallest scales behave universally similar in any flow, which is known as *Kolmogorov's first similarity hypothesis* (Kolmogorov *et al.*, 1991; Pope, 2000). The smallest scales of turbulent motions are characterized by the so-called Kolmogorov scales which are defined by the rate of dissipation ε and the viscosity ν as:

$$\eta = (\nu^3/\varepsilon)^{1/4} \tag{1.3}$$

$$u_\eta = (\varepsilon\nu)^{1/4} \tag{1.4}$$

For motions of the Kolmogorov scale the Reynolds number is defined as $Re = \eta u_\eta/\nu = 1$, pointing out the dominant role of viscosity at the dissipative Kolmogorov's scale. Furthermore, the dissipation can be expressed as $\varepsilon = \nu(u_\eta/\eta)^2$, i.e. the dissipation is equal to viscosity-affected velocity gradients (Pope, 2000).
Because of the zero velocity condition at the wall, the strongest viscosity-affected velocity gradients occur at the wall, and they can also be interpreted as wall shear stress. As the viscous forces are strongly dominating the near-wall flow, convection and turbulent shear stresses can be neglected. Hence, the wall shear stress τ_w can be defined as

$$\tau_w = \mu \frac{\partial u_1}{\partial x_n}|_{x_n=0}, \tag{1.5}$$

with μ the dynamic viscosity, which is defined as $\mu = \rho\nu$ and x_n as wall normal component. The wall shear stress is a very important parameter in engineering, because it has a major influence on sedimentation and resuspension, as mentioned in section 1.1.
As last point in this subsection, another basic concept, the so-called *Reynolds decomposition*, is introduced. In contrast to laminar flow, turbulent flows have a significant and irregular fluctuating motion in space and time, which can be described as deviation from a base flow.

Thus, the variables velocity and pressure of a turbulent flow can be temporally decomposed into a mean $\overline{\varphi}$ and a fluctuating part φ'

$$\varphi(\boldsymbol{x}, t) = \overline{\varphi}(\boldsymbol{x}) + \varphi'(\boldsymbol{x}, t), \tag{1.6}$$

the so-called *Reynolds decomposition* (Pope, 2000). For flows that are statistically stationary, like the one considered in this thesis, ensemble averaging and time averaging give identical results. Hence, the mean flow can be gathered by time averaging of the quantities (eq. (1.7)):

$$\overline{\varphi}(\boldsymbol{x}) = \frac{1}{T} \sum_{t=1}^{T} \varphi(\boldsymbol{x}, t). \tag{1.7}$$

Because of the turbulent character of the flow, many samples are needed until the mean value converges. The fluctuations from the mean velocity can be interpreted as turbulent part of the flow. Moreover, if a flow case has a homogeneous direction, like the pipe axis in a partially filled pipe flow, a quantity can be further averaged in this homogeneous direction. Hence, the mean of a quantity $\overline{\varphi}(x_2, x_3)$ becomes a function of the non-homogeneous directions only.

Budget of Mean and Turbulent Kinetic Energy

The kinetic energy of the flow $E(\boldsymbol{x}, t) = \frac{1}{2}\rho(\boldsymbol{u}(\boldsymbol{x}, t) \cdot \boldsymbol{u}(\boldsymbol{x}, t))$ per volume can be ensemble-averaged $\overline{E}(\boldsymbol{x})$ over time. Applying *Reynolds decomposition* to $\overline{E}(\boldsymbol{x})$, splits it into the sum of mean kinetic energy (MKE) K and turbulent kinetic energy (TKE) k:

$$\overline{E}(\boldsymbol{x}) = \rho(K(\boldsymbol{x}) + k(\boldsymbol{x})) \tag{1.8a}$$

$$K = \frac{1}{2}(\overline{\boldsymbol{u}} \cdot \overline{\boldsymbol{u}}) \quad = \frac{1}{2}(\overline{u}_i\, \overline{u}_i) \quad = \frac{1}{2}(\overline{u}_1^2 + \overline{u}_2^2 + \overline{u}_3^2) \tag{1.8b}$$

$$k = \frac{1}{2}(\overline{\boldsymbol{u}' \cdot \boldsymbol{u}'}) \quad = \frac{1}{2}(\overline{u_i' u_i'}) \quad = \frac{1}{2}(\overline{u_1' u_1'} + \overline{u_2' u_2'} + \overline{u_3' u_3'}) \tag{1.8c}$$

Multiplied by the density, the single terms within the turbulent kinetic energy $\rho\,\overline{u_i' u_i'}$ denote the so-called *Reynolds normal stresses*, which are basically the same as the variance of a random variable. In order to obtain the budget equation of the mean kinetic energy $K(\boldsymbol{x})$, the Reynolds decomposition is applied on the momentum transport equation (eq. (1.1b)). Then the equation of the mean momentum transport is multiplied by the mean velocity $\overline{\boldsymbol{u}}$.

Symbolically it can be written as

$$\underbrace{\frac{\partial K(\boldsymbol{x})}{\partial t}}_{\text{local derivative}} = -\underbrace{C}_{\text{convection}} + \underbrace{\nabla T}_{\text{transport/diffusion}} + \underbrace{E_{in}}_{\text{energy income}} + \underbrace{P}_{\text{productionMKE/TKE}} + \underbrace{\varepsilon.}_{\text{dissipation}} \tag{1.9}$$

and in index-notation it reads (Kundu & Cohen, 2008):

$$\begin{aligned}\underbrace{\frac{\partial}{\partial t}\left(\frac{\overline{u}_i^2}{2}\right)}_{\text{local derivative}} = &-\underbrace{\overline{u}_j \frac{\partial}{\partial x_j}\left(\frac{\overline{u}_i^2}{2}\right)}_{\text{convection}} - \frac{\partial}{\partial x_j}\Bigg[\underbrace{\frac{1}{\varrho}\overline{u}_j\overline{p}}_{\text{pressure transport}} + \underbrace{\overline{u_i}\,\overline{u_i' u_j'}}_{\text{turbulent transport}} - \underbrace{\nu \frac{\partial}{\partial x_j}\left(\frac{\overline{u}_i^2}{2}\right)}_{\text{viscous transport}}\Bigg] \\ &+ \underbrace{g_i \overline{u}_i}_{\text{energy income}} \underbrace{+ \overline{u_i' u_j'}\frac{\partial \overline{u}_i}{\partial x_j}}_{\text{MKE-production}} \underbrace{- \nu\left(\frac{\partial \overline{u}_i}{\partial x_j}\right)^2}_{\text{dissipation}}, \qquad \text{with } i,j = 1,2,3,\end{aligned} \tag{1.10}$$

The mean equation, obtained from the Reynolds decomposition, can be subtracted from the original momentum equation in order to get the fluctuating momentum equation. By multiplying $\boldsymbol{u}'$ the turbulent kinetic energy budget can be obtained as follows (Kundu & Cohen, 2008):

$$\begin{aligned}\underbrace{\frac{\partial}{\partial t}\frac{\overline{u_i' u_i'}}{2}}_{\text{local derivative}} = &-\underbrace{\overline{u}_j \frac{\partial}{\partial x_j}\frac{\overline{u_i' u_i'}}{2}}_{\text{convection}} - \frac{\partial}{\partial x_j}\Bigg[\underbrace{\frac{1}{\varrho}\overline{p' u_j'}}_{\text{pressure transport}} + \underbrace{\frac{\overline{u_i' u_i' u_j'}}{2}}_{\text{turbulent transport}} - \underbrace{\overline{\nu u_i'\left(\frac{\partial u_i'}{\partial x_j} + \frac{\partial u_j'}{\partial x_i}\right)}}_{\text{viscous transport}}\Bigg] \\ &\underbrace{- \overline{u_i' u_j'}\frac{\partial \overline{u}_i}{\partial x_j}}_{\text{TKE-production}} \underbrace{- \frac{\nu}{2}\sum_{i,j}\overline{\left(\frac{\partial u_i'}{\partial x_j} + \frac{\partial u_j'}{\partial x_i}\right)^2}}_{\text{dissipation}}, \qquad \text{with } i,j = 1,2,3.\end{aligned} \tag{1.11}$$

The evaluation of both equations are powerful tools in order to understand the physical processes of the mean flow and its fluctuations. Please note that the external energy income $g_i\overline{u}_i$ is only present in the budget equation of MKE (eq. (1.10)). The energy income is due to gravity, which is consistent for the present study as it focuses on open-duct flow. However, in general other volume forces like a pressure gradient can also be assumed to drive the flow.

The flow cases of the present study are statistically steady, i.e. the local derivative $\partial/\partial t$ is zero, hence, all other terms have to balance themselves. Furthermore all derivatives in streamwise direction are zero, because of the homogeneous direction in the flow problem of straight, partially filled pipe flow. In these equations not only *Reynolds normal stresses* $\overline{u_i' u_i'}$, but also *Reynolds shear stresses* $\overline{u_i' u_j'}$ with $i \neq j$ appear, which can be, in a statistical sense, considered as covariance of two random variables. The production term P, linking the Reynolds stresses and the gradient of the mean velocity, is present in both budget equations.

Thus, P links both budget equations in terms of energy and denotes the transfer of kinetic energy from MKE, which obtains the energy from the driving force, to TKE. In a pipe flow the TKE-production term is generally positive, hence, energy is transferred from MKE to TKE, however, energy can be transferred in both directions, from MKE to TKE and from TKE to MKE.
The dissipation ε is the energy sink in both equations. By definition it is always negative and it converts the energy irreversibly to heat via the mean and fluctuating rates of strain. C represents the spatial rate of change of kinetic energy by convection. The spatial diffusion of kinetic energy T occurs via turbulent transport and pressure transport, as well as via viscous diffusion. E_{in} stands for the energy income (Nikora & Roy, 2012) or energy input and represents the driving force of the flow.

Transport Equation of Vortical Motion

For the introduction of the last basic equations, let us recall one of the characteristics of turbulent flow mentioned in the beginning of this section. Turbulent flows consist of vortical motions making the flow rotational. The rate of rotation $\boldsymbol{\omega}$, also called vorticity, is the curl of the velocity and is non-zero in turbulent flows (Pope, 2000).

$$\boldsymbol{\omega} = \nabla \times \boldsymbol{u} \tag{1.12}$$

By taking the curl of equation (1.1b) the vorticity equation can be derived to

$$\frac{D\boldsymbol{\omega}}{Dt} = \nu \nabla^2 \boldsymbol{\omega} + \boldsymbol{\omega} \cdot \nabla \boldsymbol{u}, \tag{1.13}$$

which also describes the flow as exact as the original Navier-Stokes equations, but from the perspective of vortical motion (Pope, 2000). Einstein & Li (1958) further transformed this equation by taking the mean and focusing on the streamwise component of the vorticity ω_1 only, to:

$$\underbrace{\frac{\partial \bar{\omega}_1}{\partial t}}_{\text{rate of change}} + \underbrace{\bar{u}_j \frac{\partial \bar{\omega}_1}{\partial x_j}}_{\text{convection by the mean flow}} = \underbrace{\bar{\omega}_j \frac{\partial \bar{u}_1}{\partial x_j}}_{\text{vortex stretching and tilting}} + \underbrace{\frac{\partial^2}{\partial x_2 \partial x_3}\left(\overline{u_3'^2} - \overline{u_2'^2}\right)}_{\substack{\text{vorticity generation} \\ \text{by Reynolds normal stresses}}} + \underbrace{\left(\frac{\partial^2}{\partial x_3^2} - \frac{\partial^2}{\partial x_2^2}\right)\left(-\overline{u_3' u_2'}\right)}_{\substack{\text{vorticity generation} \\ \text{by Reynolds shear stresses}}} + \underbrace{\frac{\partial}{\partial x_j}\left(\nu \frac{\partial \bar{\omega}_1}{\partial x_j}\right)}_{\text{viscous "dissipation" of mean vorticity}}, \quad \text{with } j = 2, 3. \tag{1.14}$$

The streamwise component of the vorticity equation is a widely used tool to analyse the mean secondary flow (e.g. Einstein & Li (1958); Nezu & Nakagawa (1993)). Let us consider the temporally averaged flow in a straight, partially filled pipe or in an open-duct. First of all, the temporal derivative is zero, $\partial/\partial t = 0$. Moreover, the derivatives in streamwise direction are zero, hence, $\partial \overline{u}_i / \partial x_1 = 0$. It follows that the term $\overline{\omega}_j \frac{\partial \overline{u}_1}{\partial x_j}$ is

zero, because $\overline{\omega}_2 \frac{\partial \overline{u}_1}{\partial x_2} = -\overline{\omega}_3 \frac{\partial \overline{u}_1}{\partial x_3}$. Hence, secondary flow can only be generated by the terms $\frac{\partial^2}{\partial x_2 \partial x_3}\left(\overline{u_3'^2} - \overline{u_2'^2}\right)$ and $\left(\frac{\partial^2}{\partial x_3^2} - \frac{\partial^2}{\partial x_2^2}\right)\left(-\overline{u_3' u_2'}\right)$, as the second term on the left hand side of equation (1.14) only convects vorticity and the last term on the right hand side is responsible for the dissipation of vorticity. This means streamwise vorticity and therefore secondary flow is generated only by turbulence inhomogeneities and turbulence anisotropy, which is also referred to as turbulence-induced secondary flow. Secondary flow that is only turbulence-induced is classified as secondary flow of Prandtl's second kind, whereas flows for which $\overline{\omega}_j \frac{\partial \overline{u}_1}{\partial x_j} \neq 0$ secondary flow of Prandtl's first kind are generated. Secondary flow of the first kind also include turbulence-induced secondary flow, however, it is dominated by the secondary flow generated by the centrifugal forces, which is equivalent to the first term on the right hand side.

Turbulent Boundary Layers

Let us assume a viscous flow parallel over a non-moving solid wall. The wall is impermeable and has a no-slip condition, hence, the velocity at the wall is $\boldsymbol{u} = 0$. Due to the viscosity of the fluid a layer establishes from zero velocity at the wall to the free-stream velocity far off the wall. This layer is called boundary layer, first introduced by Ludwig Prandtl (Schlichting & Gersten, 2017). The theory of turbulent boundary layers was found to be universally applicable for flows over a flat plate and its characteristics will be introduced in the following.
Directly at the wall the flow generates a shear stress, the so-called wall shear stress τ_w, which is defined in equation (1.5). In the near-wall region, the flow can be described by the *friction velocity*

$$u_\tau = \sqrt{\frac{\tau_w}{\rho}} \tag{1.15}$$

and the *viscous length scale*

$$\delta_\nu = \frac{\nu}{u_\tau}. \tag{1.16}$$

The wall distance and velocity can be normalised by the viscous length scale and the friction velocity, respectively, leading to the so-called *wall* or *inner units* denoted with a φ^+, e.g. $u^+ = u/u_\tau$. Moreover, the friction velocity is used to define the *friction Reynolds number*:

$$Re_\tau = \frac{u_\tau \delta}{\nu} \tag{1.17}$$

with δ being the boundary layer thickness.
A fully developed boundary layer can be described by three different wall-parallel layers. Directly at the wall the viscous sublayer evolves, where viscosity is highly dominating. From

zero velocity at the wall, the inner streamwise velocity $u_1^+ = u_1/u_\tau$ increases linearly with wall distance, representing a manifestation of the so-called *Law of the Wall* (Pope, 2000). The linear relation only is a good approximation as long as the pressure gradient term, which enters the near-wall velocity distribution multiplied with the squared wall distance, can be neglected. This is the case for $x_3^+ = x_3/\delta_\nu < 5$, which is the wall-normal extent of the viscous sublayer.
Coming from the free-stream flow towards the wall, a region establishes where the inner velocity u_1^+ follows a logarithmic scaling

$$u_1^+ = \frac{1}{\kappa}\, ln(x_3^+) + B. \tag{1.18}$$

κ is the von Kármán constant being approximately 0.41 and B is a second constant approximately 5.2 in channel flow Pope (2000). This scaling is valid from $x_3^+ > 30$ to $x_3/\delta < 0.3$ and gives the layer its name - the so-called *log-law region*. In between the viscous sublayer and the log-law region there is a transition from the linear to the logarithmic regime called *buffer layer*.
Another description of the turbulent boundary layer divides it into an inner and an outer layer (Pope, 2000). In the inner layer, which spans from the wall up to $0.1\, x_3/\delta$, the flow and its structures scale with wall units. Overlapping the inner layer, the outer layer begins at approximately $x_3^+ \approx 50 - 80$, where viscous effects are negligible. Moreover, the flow in the inner layer is exposed to strong shear forces. In the outer layer the flow is rather independent of the near-wall turbulence, however, this is not a strict interface and interaction between both regions takes place (Jiménez, 2018).

Coherent Structures in a Wall-Bounded Flow

The field of coherent structures in turbulent flows is a vast research field, which is still evolving dynamically. This brief summary on coherent structures in wall-bounded flows is mainly based on the reviews of Robinson (1991) and Jiménez (2018). Coherent structures can be defined as structures showing significant correlation of a flow parameter with itself or with another parameter over a certain flow area and keeping its correlation pattern over a dynamically significant time interval. One of the main coherent structures are vortices. They have an approximately circular or spiral pattern of streamlines around a pressure minimum. Another approach to describe coherent structures was introduced by Lumley (1967) and is based on the proper orthogonal decomposition (POD). It defines coherent structures with an objective, but rather abstract outcome, which is difficult to interpret. The POD will be introduced in more detail in chapter 4.2.1. In contrast to coherent structures in the instantaneous velocity field, there are rotational patterns in time averaged velocity field known as helical secondary currents.
Looking in more detail at the flow very close to the wall, a typical flow pattern with regions of fast and slow velocity fluctuations, the so-called high and low velocity streaks, respectively, appear in turn. The low and high velocity streaks can have a length up to 1000 wall units. The width of velocity streaks is approximately 50 wall units, which leads to approximately 100 wall units as distance between two high or low velocity streaks (Robinson, 1991). In connection to the velocity streaks quasi-streamwise vortices appear either as single vortex or

as a counter-rotating pair next to each other. They usually are slightly tilted by 3-7 degrees from streamwise direction and reach a length of up to $200\delta_\nu$ with a diameter of $15 - 50\delta_\nu$ and a core wall distance of $20 - 70\delta_\nu$ (Robinson, 1990). Hence, quasi-streamwise vortices are generated and occur in the buffer layer.
If there is a low velocity streak, with faster fluid further away from the wall, the faster flow starts to roll up above the slow velocity and creates a vortex. This vortex usually builds up and creates either one or more vortical legs, so-called arches or horseshoes, which keep contact with the wall in the initial phase. If two vortical legs are created, the two legs are counter-rotating and they transport fluid from the wall in between the two vortices towards the bulk-flow region. This generates again slow velocity in between the two legs, as a possible new low velocity streak. Due to the mutual induction of the two vortex legs they create an upward movement. This is the so-called hairpin vortex system (Robinson, 1991). These vortex systems grow, interact with smaller ones and often appear in groups. At some point the vortex system ejects from the wall into the bulk-flow region and gets detached from the wall. Such an *ejection* from the wall is also called *burst* and is often connected to an event of negative streamwise fluctuation and positive wall-normal fluctuation, also called *Q4*-event. Moreover, an event of ejection produces turbulence in the buffer layer. In contrast, another event that is observed in near-wall turbulence is the so-called *sweep* event. High velocity streaks with a high kinetic energy move towards the wall and if a high velocity streak flows over a low velocity streak, the present near-wall structure gets pushed away. This can be related to a positive u_1' and a negative u_3' occurrence, a *Q2*-event. The sweep- and ejection-events get their energy from areas where both u_1' and u_3' are positive or both are negative. Ejections are detected more often with wall distances $x_3^+ \geq 12$, whereas sweeps are predominantly found closer to the wall (Robinson, 1991). In streamwise direction often the same event, either sweep or ejection, can be observed behind each other, but in spanwise direction sweeps and ejections rather occur next to each other and form pairs.
As mentioned above, structures can be either wall-attached or detached from the wall. If the structure's lowest parts are over 20 wall units away from the wall they are classified as detached from the wall (Jiménez, 2018). Structures can evolve from being attached and then detach like ejections, whereas sweeps behave the other way around. Sorting the structures shows that attached structures are responsible for approximately 60% of the total Reynolds shear stress $\overline{u_1' u_3'}$ and account for approximately 70% of the volume of high kinetic energy structures (Jiménez, 2018). They are spatially and temporally self-similar as they grow and eventually detach from the wall. Streamwise vortices in the buffer layer often appear as counter-rotating pairs and move farther away from the wall into the log-layer. However, they also appear as single vortices with smaller, not dominating secondary vortices around them. The lifetime of these structures can be estimated by their wall-distance (Lozano-Durán & Jiménez, 2014), thus, the lifetime of vortices in the outer region compared to the quasi-streamwise near-wall vortices is relatively long.
The outer flow is directly influenced by the inner flow through near-wall ejections, which reach to the outer flow and transfer mass, and indirectly by growth of vortical structures. The outer flow interacts with the inner flow by entrainment of large structures and creates a foot-print of themselves in the inner flow. However, it is still debated how the near-wall region is exactly influenced by the outer flow structures (Jiménez, 2018). Lastly, the funda-

mental question of how structures of different scales interact with each other arises and is part of ongoing research, e.g. Motoori & Goto (2019).

From the description of the different structures in the different layers it can be concluded, that turbulence is produced at the wall and in the buffer layer, and from there it is transported to other places. Hence, the wall is a necessary part to generate structures close to the wall and these are responsible for the structures in the buffer layer. However, there have been simulations, e.g. Lozano-Durán & Jiménez (2014) and Mizuno & Jiménez (2011), indicating that the structures in the viscous sublayer are not really needed to generate the turbulence in the buffer layer. More important seems to be the presence of a strong shear layer that is generated by the wall in wall-bounded flows. This perspective is further supported by the observation that there are more structures moving towards the wall than away from it (Jiménez, 2018).
Another interesting perspective on turbulence was introduced by Waleffe (1997). He presented a self-sustaining process (SSP) of turbulence: an instability of high and low velocity streaks generates streamwise vortices, which feed back energy to the streaks again. With the knowledge of the above mentioned simulations one can argue, that for the SSP to work the flow might only need to have a strong shear flow, which was generated in this study by a wall. Jiménez (2018) argues that it is also possible, that it is not the streaks initializing new instabilities, but they enhance and give direction to the new vortices and instead the shear itself creates the instability. However, simulations of Jiménez & Pinelli (1999) showed that removing any component of the SSP changes the created turbulence strongly, underlining the importance of all components of the SSP interacting with each other.

Full pipe flows are described in literature as wall-bounded flows and they are characterised by the influence of the wall. Hence, partially filled pipe flows also can be regarded as wall-bounded flows, will show similar features, and generate a boundary layer. Moreover, an interaction with a free surface takes place, which will be introduced in the next section.

Free Surface Flows

Free surface flow means, that there are two continua flowing next to each other separated by an interface. In principle, an interaction between the two fluids is possible. However, in the context of the present study only free surface flows are considered in which the primary fluid, usually a liquid, is not or hardly influenced by the secondary fluid, e.g. a gas. I.e. the primary fluid is not influenced by shear stresses and also no inertial forces are induced by the secondary fluid (Sarpkaya, 1996). Close to the free surface, there is a layer with a free surface normal distance of about 50 wall units, where Reynolds stress and vorticity distributions start deviating from the channel flow distributions (Nagaosa, 1999). In this layer the kinematic boundary of the free surface, $u_3 = 0$, becomes noticeable, vertical velocity fluctuations decrease and get redistributed to horizontal velocity components. Shen *et al.* (1999) called this layer *blockage layer* and inside the blockage layer they further specified a thin surface layer close to the free surface, reflecting the zero shear stress condition. In a first approximation, vortical structures can be distinguished into free surface parallel structures

and structures being normal and/or attached to the free surface. A more detailed categorization was introduced by Sarpkaya (1996), who classified five types of free surface normal vortices. i) a structure connected with both ends to the free surface, ii) whirls, detaching from streamwise/free surface parallel vortices by a centrifugal instability, iii) vortices from below the blockage layer moving towards the free surface, iv) whirls, being attached to the wall, that recirculate around themselves and v) vortices being attached to the free surface and a solid wall.

Some of the above mentioned structures might only be created, if the free surface can be deformed and surface tensions can appear, which is, of course, possible in real flows and physical experiments. However, in numerical simulations assumptions have to be made for the treatment of the free surface, which can suppress the occurrence of some structures. Often the free surface is modeled by a rigid non-deformable wall with a slip condition, which approximates a low Froude number flow. This boundary condition is also applied in the present study, hence, the following literature review focuses mainly on low Froude number flows. Please note that the validity of this approximation is investigated in section 2.1. Further note that the Froude number is defined as the ratio between inertia and gravity forces: $Fr = u_b/\sqrt{gH}$, with u_b as bulk velocity and H being the flow depth.

In a wall-bounded flow with a free surface, turbulent activity is generally not generated in the vicinity of the free surface. Instead, Komori *et al.* (1993), Pan & Banerjee (1995), Grega *et al.* (1995) and Nagaosa (1999) show that turbulent structures that reach the free surface often stem from bursts ejecting from the buffer layer and move towards the free surface. The bursts include low velocity streaks with quasi-streamwise vortices, producing upwellings or so-called *splats* at the free surface. Splats are events of negative vertical pressure strain fluctuations, redistributing vertical velocity mostly to spanwise velocities. Because of continuity also the counterpart exists - *anti-splats* or downwellings, with positive vertical pressure strain fluctuations. Interestingly, streamwise pressure strain fluctuations play only a minor role in this redistribution (Nagaosa, 1999; Komori *et al.*, 1993; Shen *et al.*, 1999). Please note that Perot & Moin (1995) found only very small pressure strain values and explained the redistribution of the splat and anti-splat events via viscosity. Shen *et al.* (1999) discussed the individual terms of the enstrophy budget and found that locally the enstrophy dissipation is increasing for splats and anti-splats in the horizontal components, but free surface-attached structures show little dissipation of enstrophy. Thus, overall the dissipation of enstrophy is an important process at the free surface.

At the boundaries of splats and as transformation from quasi-streamwise vortices free surface-normal vortices being attached to the free surface are generated. As long as they are not disturbed by other structures they decay only very slowly, because of low dissipation (Pan & Banerjee, 1995; Kumar *et al.*, 1998). However, these attached structures have only minor contribution to the inter-component transfer of turbulent kinetic energy (Nagaosa, 1999). Nezu & Nakagawa (1993), Pan & Banerjee (1995) and Kumar *et al.* (1998) state, that a layer of two-dimensional structures is generated at the free surface, however, adjacent to the surface layer the flow structures become three-dimensional and can not be regarded as two-dimensional anymore (Nagaosa, 1999). Another process taking place at the free surface is that vortical structures with the same direction of rotation connect and form larger structures, establishing an inverse energy cascade and vortices with an opposite sign dissolve (Sarpkaya, 1996).

In recent physical experiments by Tamburrino & Gulliver (2007) and Zhong *et al.* (2016) it was found that in addition to splats, anti-splats, and attached vortices some long velocity streaks form streets with a sinusoidal/wavy pattern. This is in agreement with an analysis of numerical simulations by Kevin *et al.* (2019), showing an intermittent pattern, generated by growing vortex systems in a turbulent boundary layer, which get more distinct in the outer flow. Zhong *et al.* (2016) showed via velocity correlations, that there are alternating high and low velocity streaks in streamwise direction that have a width of approximately one flow depth. This was in agreement with the results of a POD of the velocities at the free surface, with the most energetic modes representing the alternating streak pattern. Please note that both experiments (Tamburrino & Gulliver, 2007; Zhong *et al.*, 2016) showed mean secondary cells in the middle of the wide channel, which was not reported for the numerical simulations of Kevin *et al.* (2019). In contrast to numerical simulations with periodic boundary conditions in spanwise direction, they must have had sidewalls introducing new features to the flow, which might explain the difference. Such a geometry with no-slip walls at the bottom and as side walls and a free surface at the top are called open-channel or open-duct flows and will be investigated in the next section.

1.3. Secondary Flow Phenomenon - Literature Review

Secondary flow describes the motion of the fluid perpendicular to the main flow direction. Intuitively it becomes clear, that secondary flow occurs in curved pipes, rivers and ducts, because of fluid's inertia pushing the water to the outside bend of the cross-section. In 1926 Ludwig Prandtl first mentioned on a conference that secondary flow also occurs in straight, non-circular closed ducts (Meier, 2000). Based on this insight, two main categories of secondary flow can be distinguished according to their generation mechanism. In curved channels the centrifugal force serves as source of skewing-induced vorticity which generates the so-called secondary flow of Prandtl's first kind (Blanckaert & De Vriend, 2004). This can appear in laminar and turbulent flows. Secondary flow of Prandtl's second kind is the result of turbulence inhomogeneities (Prandtl *et al.*, 1990). They also appear in curved channels, but are rather weak. But in contrast to the secondary flow of the first kind, they also appear in turbulent flows in straight channels. Such secondary flows are typically generated at corners or edges of the geometry. Although mean secondary flows have a magnitude of only 2-3% of the mean streamwise velocity, they still have a quite huge impact on the general velocity distribution (Nezu & Nakagawa, 1993). In this thesis, turbulent flows in straight, partially filled pipes are considered containing secondary flow of Prandtl's second kind. However, most of the available studies on secondary flow of the second kind investigate straight open-channel flows with a rectangular cross-section. Hence, these publications are the main references for the following review on the secondary flow phenomenon. The case of partially filled pipe flows will be discussed separately in the next section.

Natural rivers and also technical open-channel flows can be defined by their aspect ratio W/H, with W being the width and H the flow depth. Open-channel flows can be classified as *narrow* if the aspect ratio of the cross-section is $W/H \leq 5$ (Nezu & Nakagawa, 1993). In

this case, the complete flow is directly influenced by the secondary currents attached to the side walls, which can reach a spanwise size of approximately $2\,H$. Open-channels with a larger aspect ratio are considered to be wide and in the centre of the channel symmetric circulation cells are established (Nezu & Nakagawa, 1993; Chauvet *et al.*, 2014), which appear to be similar to the experiments of Tamburrino & Gulliver (2007) and Zhong *et al.* (2016) mentioned in subsection 1.2 (*Free Surface Flows*). As secondary flow is predominantly generated at the side wall the intensity of secondary currents in the centre of the cross-section decreases with increasing aspect ratio (Vinuesa *et al.*, 2015; Sakai, 2016).
Within this thesis only flows classified as narrow are investigated, hence, the following review focuses on the flow phenomenon in narrow open-channel flows.

Secondary Currents in Open-Channel Flow

In literature, a common pattern of secondary currents can be detected for rectangular open-channel flow (Nezu, 2005; Tominaga *et al.*, 1989; Joung & Choi, 2009; Blanckaert *et al.*, 2010; Nawroth *et al.*, 2015; Sakai, 2016), as shown in figure 1.2. There is one large surface vortex directed towards the channel centre at the free surface and a less dominant bottom vortex, counter-rotating to the surface vortex. Additionally, another vortex seems to occur in the mixed-corner, again counter-rotating to the free surface vortex, which will be further discussed below. In connection to the wall shear stress distribution, it was observed, that local wall shear stress maxima occur if secondary flow directs high momentum fluid towards the wall. Conversely, local wall shear stress minima occur if the local secondary flow points away from the wall. Thus, the rapid increase of the wall shear stress near the free surface indicates an inner secondary vortex at the mixed-corner as pointed out by Sakai (2016).

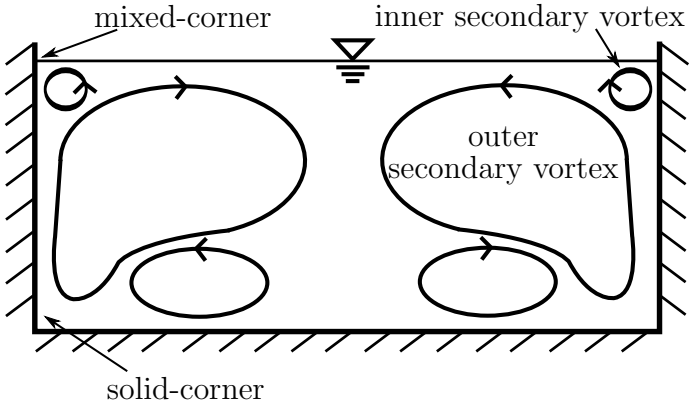

Figure 1.2: Sketch of secondary flow pattern in a rectangular open-channel flow. The sense of rotation of the vortical structures is indicated by small arrows.

Secondary flows are generated at inhomogeneities of the wall, like corners. So far a crucial difference between published experimental and numerical results for open-channel flows can be observed. In direct numerical simulations (DNS) (Joung & Choi, 2009; Lee *et al.*, 2012; Grega *et al.*, 1995; Sakai, 2016), and large eddy simulations (LES) (Broglia *et al.*, 2003), with a rigid slip-condition as free surface, a vortex has been observed, which is directly

in the mixed-corner and in contact with the wall and the free surface. This mixed-corner vortex has been denoted as the inner secondary vortex (Grega *et al.*, 1995) in contrast to the outer secondary vortex, which is strongly dependent on the aspect ratio (cf. Figure 1.2). The inner secondary vortex has a circular shape and its extension has been reported to vary from 40 to 100 wall units (Joung & Choi, 2009; Broglia *et al.*, 2003; Grega *et al.*, 1995; Lee *et al.*, 2012; Sakai, 2016). While the inner secondary vortex points towards the wall at the free surface, the outer secondary vortex points away from the wall and a stagnation point is formed at the free surface between the inner and outer secondary cell. Thus, the corner vortex is counter-rotating to the outer secondary current and transports high-momentum fluid from the free surface towards the side-wall. The outer secondary current is usually reported to be larger in size and depends more on the entire geometry of the channel than on the inner secondary current. Except for very low Reynolds number flows which just maintain a turbulent flow, the inner and outer secondary cell are equal in size and velocity magnitude. For higher Reynolds numbers, the velocity magnitude of the inner secondary flow has been reported to be smaller than that of the outer secondary flow. In addition, Lee *et al.* (2012) also observed the inner secondary vortex in a DNS with non-zero Froude number using a combined level-set/volume of fluid method for the free surface deformations. The inner secondary vortices observed in Froude numbers of $Fr = 0.2$ and $Fr = 0.8$ are consistent with ones observed in other simulations using a rigid slip condition. They are quite similar in shape, position and strength and do not seem to dependent strongly on the Froude number.

In contrast to the simulations, most experiments did not observe the inner secondary vortex. According to Nezu & Nakagawa (1993) and Tominaga *et al.* (1989) there is no inner secondary flow. Grega *et al.* (2002) measured the flow in a mixed-corner with particle image velocimetry (PIV) with a high resolution and a focus on the mixed-corner. Unfortunately, some details of the setup of the experiment do not become fully clear. For measuring the flow, Grega *et al.* (2002) placed a mirror in the channel, which dimensions are not given and might have influenced the flow. The length of the channel is about six flow depths, which is less than a tenth of the channel length a secondary flow usually needs to establish a fully-developed state (Demuren & Rodi, 1984). Nevertheless, Grega *et al.* (2002) claimed to have detected an inner secondary vortex (cf. Figure 1.2). However, in contrast to what has been observed in numerical simulations, no stagnation point can be observed at the free surface. Hence, the measured vortex neither does fully agree with the postulated inner vortex (Grega *et al.*, 1995, 2002) nor with the corresponding simulations mentioned above. Nawroth *et al.* (2015) measured secondary flows in a rectangular channel by stereoscopic (PIV). Unfortunately, their field of view did not provide a near-wall resolution that allowed to render the inner vortex. The same can be concluded for the PIV measurements in partially filled pipes by Ng *et al.* (2018). Thus, clear evidence from experiments for an inner vortex as observed by numerical simulations is still missing to date.

In rectangular cross-sections it has been observed that the secondary flow always points towards the solid corner along the corner bisector and moves away from the solid corner along the walls towards the centers of the side wall (Nezu, 2005; Pinelli *et al.*, 2010; Sakai, 2016). Moreover, Pinelli *et al.* (2010) and Sakai (2016) reported that the vorticity structures in the solid corner scales with wall units for different Reynolds numbers, whereas the secondary flow cells itself scale with bulk units, generating a slightly different

pattern. Moreover, in a squared closed-duct the solid corner vortices generate in total an eight vortex pattern on average. But looking at the instantaneous flow, Uhlmann *et al.* (2007) showed that in marginal Reynolds number flows two four-vortex patterns, shifted by 90°, alternate. Whether such an instantaneous alternating pattern is present in rectangular open-channel flow was investigated by Sakai (2016), who could not find any systematic pattern.
In trapezoidal cross-sections, mixed-corner vortices have been observed in both, simulations and experiments. A three-vortex system has been observed, e.g. by Tominaga *et al.* (1989) and Brosda (2015). The inclination of the side-wall strongly affects the pattern of the secondary currents, which might explain the large extension of the mixed-corner vortex in the trapezoidal configuration (Tominaga *et al.*, 1989; Blanckaert *et al.*, 2010).
Moreover, in wide open-channel experiment Blanckaert *et al.* (2010) observed alternating secondary cells all over the cross-section. They reported a correlation between the TKE and the pattern of the secondary currents. In general, the TKE is larger at the bottom of the channel. In particular, the magnitude of the TKE has peaks where the secondary flow is directed from the wall towards the free surface and lower values where secondary flow points towards the wall. Additionally, also the lateral Reynolds shear stress distribution $\overline{u_1' u_2'}$ is correlated to the pattern of the secondary currents, because of the corresponding variations of the streamwise velocity. Positive $\overline{u_1' u_2'}$ matches counter clockwise turning secondary cells and negative $\overline{u_1' u_2'}$ indicates clockwise rotation. This correlation was not only found in wide channels, but also in narrow experiments and simulations (Nezu & Nakagawa, 1993; Joung & Choi, 2009).

Primary Flow in Open-Channel Flow

Secondary currents considerably influence the distribution of the primary velocity component over the cross section. Like the secondary currents, the primary flow depends on the angle and shape of the side walls and the aspect ratio (Tominaga *et al.*, 1989; Nezu & Nakagawa, 1993; Blanckaert *et al.*, 2010). In wide channels and channels with acute side wall/free surface angles, the location of the maximum mean streamwise velocity occurs at the free surface. However, in rectangular channels with aspect ratios below $W/H \approx 5$ the maximum appears underneath the free surface at about $60 - 80\%$ of the flow depth (Tominaga *et al.*, 1989; Joung & Choi, 2009; Nawroth *et al.*, 2015; Sakai, 2016; Ng *et al.*, 2018). The distance of the maximum streamwise velocity to the free surface scales with outer units (Sakai, 2016). This effect, denoted as *velocity-dip* phenomenon, can be explained by the transport of low-momentum fluid from the side walls towards the center by the secondary surface velocity (Nezu & Nakagawa, 1993; Yang, 2005). Sakai (2016) supports Nezu's conclusion by reporting that the *velocity-dip* phenomenon only occurs, when large-scale low-velocity streaks are ejected from the side walls towards the free surface centre, contributing to lower velocities at the free surface in the channel centre. Moreover, it has been observed that regions exist in which the velocity profiles follow a logarithmic relation (Nezu & Rodi, 1986; Gavrilakis, 1992). In the outer range the log-law has to be adjusted, because of the *velocity-dip* phenomenon. This has been taken into account by a log-wake law (Chiu, 1989; Yang *et al.*, 2004) and further by Guo (2014) in a modified log-wake law.
Another effect of the secondary flow is an inhomogeneously distributed mean wall shear stress

along the circumference (Nezu & Nakagawa, 1993). In the rectangular and narrow open-channel flow experiments of Tominaga *et al.* (1989) a plateau-like maximum of the wall shear stress has been observed at the center of the bottom as global maximum. At the side walls, another local maximum was discovered at approximately 60% of the flow depth. Moreover, they report that the wall shear stress is continuously decreasing from both maxima towards the bottom corner and the free surface (Tominaga *et al.*, 1989). In numerical simulations, the distribution of the bottom shear stress is in agreement with the measurements, but the shear stress distribution at the side walls can differ considerably. In direct numerical simulations, Joung & Choi (2009); Sakai (2016) observed that the wall shear stress sharply increased and reached a global maximum at the mixed-corner. A local minimum was seen at 50 wall units underneath the free surface, scaling with inner units for moderate Reynolds numbers (Sakai, 2016). This is explained by a high velocity streak located directly at the free surface and a subsequent low velocity streak, with a streak diameter of 50 wall units, which is in agreement with the velocity streaks reported in section 1.2 (*Coherent Structures in a Wall-Bounded Flow*). In the solid bottom corner, a high velocity streak is located with subsequent streaks next to it, producing a local wall shear stress maximum at a distance of 50 wall units from the corner (Sakai, 2016). For low Reynolds numbers, only one low velocity streak with a spanwise length of 50 wall units fits in between the corner streaks. This velocity streak pattern corresponds to a minimum Reynolds number just maintaining turbulence. If less velocity streaks fit along the wall, turbulence collapses and laminar flow develops. For a rectangular cross-section with aspect ratio $W/H = 2$, Sakai (2016) reported a minimum Reynolds number of $Re_\tau = 102$. With increasing, still small Reynolds number, the velocity streaks grow in size and at the same time the viscous length scale decreases until a new pair of streaks of regular size (100 wall units) fits in again such that five streaks (300 wall units) are next to each other. With further increasing Reynolds number the size of the velocity streaks in the corner remains approximately constant and further new velocity streak pairs are integrated creating an alternating pattern of velocity streaks (Pinelli *et al.*, 2010; Sakai, 2016).

Generation Mechanism of Mean Secondary Flow

There are still ongoing debates about details of the generation mechanism of secondary flow, especially on the interaction between secondary flow and turbulence (Nikora & Roy, 2012). In 1993 Nezu & Nakagawa (1993) gave a comprehensive review of turbulence in open-channel flows, explaining the mechanism via a simplified mean vorticity equation and the anisotropic turbulence structure. Anisotropy is induced by the geometry and leads to gradients in the Reynolds normal stresses, which are supposed to generate secondary flows. This review was extended and updated by Nezu (2005). Beforehand and in the meanwhile, others have tried to describe the interaction between turbulence and secondary flow from different perspectives, as highlighted by Nikora & Roy (2012). In particular via the (i) *mean vorticity equation* (Einstein & Li, 1958; Nezu & Nakagawa, 1993; Nezu, 2005; Gessner, 1973), (ii) *Reynolds-Averaged Navier-Stokes (RANS)-equations* (Yang *et al.*, 2012), (iii) *energy balance of the mean flow* (Gessner, 1973; Yang & Lim, 1997; Nikora & Roy, 2012), (iv) *mean and turbulent enstrophy* (Nikora & Roy, 2012) and (v) *coherent structures* (Uhlmann *et al.*, 2007; Pinelli *et al.*, 2010; Sakai, 2016). Nikora & Roy (2012) emphasize that

it could be worthwhile to interconnect the different approaches and compare the results, in order to gain new insights into the generation mechanism of secondary currents. Wherever appropriate, more detailed aspects of the various approaches will be discussed within this thesis.

The focus on the processes in the mixed-corner was first put by the experiments of Grega *et al.* (1995), Hsu *et al.* (2000) and Grega *et al.* (2002). Although their results should be treated with caution, see section 1.3 (*Secondary Currents in Open-Channel Flow*), some aspects for the generation mechanism of secondary flow are summarised in the following. Based on the mean vorticity equation, Grega *et al.* (1995) conclude that at the free surface the free surface normal fluctuations are damped and mainly the free surface parallel fluctuations occur which leads to an anisotropy of the turbulent fluctuations in the mixed-corner. Moreover, they reported bursting events generated at the side wall that spread along the free surface that might create the outer secondary cell. Hsu *et al.* (2000) made further experimental measurements with detailed investigations of the Reynolds stresses and the single terms of the energy balance of the TKE in the mixed-corner. They reported that the turbulent production and the dissipation decrease towards the free surface. Please note that their velocity measurements were restricted to several free-surface parallel planes. Grega *et al.* (2002) extended the analysis by investigating the distribution of convection of the streamwise vorticity.

Sakai (2016) applied a vortex eduction technique, using the criteria of Kida & Miura (1998) to define vortex centres and counting the location and sense of rotation of these vortices. The most probable location of streamwise vortices agrees with the mean streamwise vorticity field. The highest probability of vortices rotating in one particular direction is in the mixed-corner, in contrast to the solid corner, which do not have any distinct peak of vortex probability. Sakai (2016) concludes, that the inner secondary cell is generated by quasi-streamwise vortices from the inner layer. Moreover he states, that the outer secondary cell is not present instantaneously as one big structure, but is rather an accumulation of smaller structures evolving mostly from the side wall, which is in agreement with literature reported in section 1.2 (*Free Surface Flows*). For a small free surface layer of about $15\delta_\nu$, Sakai (2016) proposed a sorting mechanism based on the 2D vortex interactions with different boundary conditions by Orlandi (1990). According to this mechanism, streamwise vortices moving towards the free surface move either towards the centre or the mixed-corners depending on their sense of rotation, see figure 1.3. According to the sketch, a vortex rotating counter-clockwise moves towards the mixed-corner giving rise to an accumulation of counter-clockwise rotating vortices in the mixed-corner. Clockwise rotating vortices move towards the pipe's centre, thus, contributing to the outer secondary vortices. The same sorting mechanism occurs for vortices with an opposite sense of rotation for the mixed-corner at the opposite side.

From subsequent instantaneous snapshots of the flow Sakai (2016) statistically analysed the temporal development of coherent structures. This analysis was performed for a flow in a rectangular cross-section with aspect ratio $W/H = 2$ at $Re_\tau = 150$. He reports that the inner secondary flow consists of rather long structures. The flow structures with the largest volume occur in the centre of the cross-section at a height of approximately one third of the flow depth above the bed. However, the longest-living structures are relatively small and dissolve in the centre of the free surface. Sakai (2016) found that a significant part

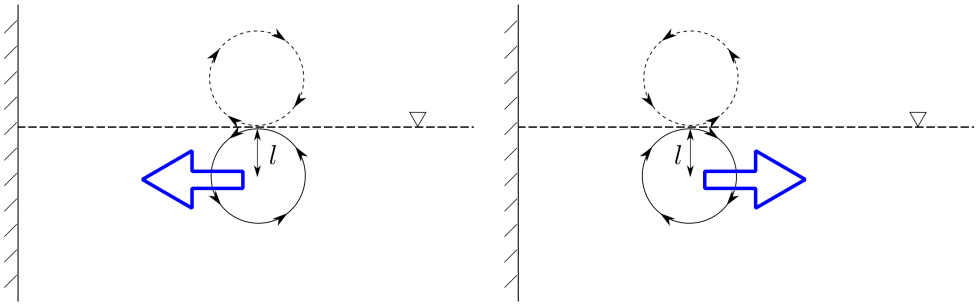

Figure 1.3: Concept of vortex sorting mechanism at the free surface proposed by and from Sakai (2016)

of the structures that grow older move from the side wall to the free surface along the path of the outer secondary cell. In addition, the advection of vortices and its advection-angles were investigated. They resemble the mean secondary flow and slightly support the aforementioned sorting algorithm at the free surface.

1.4. Partially Filled Pipe Flow - Literature Review

The following review is divided into a first part that shows the historical development and background of partially filled pipe flows. The second part gives a brief overview about the state of the art in the field of partially filled pipe flows.

Historical Review of Partially Filled Pipe Flow

As mentioned above, partially filled pipe flows are categorised as open-channel flows, which were subject of investigations from early ages on. The history of technical open-channel flows is strongly connected to the necessity of transporting water over longer distances. This development began around 5,000 B.C. when humans started to settle down and irrigation of agricultural fields became important (Garbrecht, 1987). From that time on, human kind built up engineering knowledge about hydraulics in open-channel flow and more and more sophisticated systems for water supply systems were established, e.g. in the ancient Nineveh (around 700 B.C.) in Mesopotamia (Garbrecht, 1995) or in the ancient Jericho (around 100 B.C.) (Garbrecht & Netzer, 1991). Equally impressive are the buildings that were constructed for transporting water, for example the aqueducts in Roman times (Garbrecht, 1995). It would have been very interesting to understand, which hydraulic considerations were made to realize such projects, but unfortunately, there are no surviving documents from this early period, that describe the knowledge of flows in open-channels at that time.

One of the first known mathematical descriptions for the calculation of the flow velocity in open-channels goes back to 1775, when Chézy came up with an empirical formula for the mean velocity u_b and discharge in open-channel flows $u_b = C_C\sqrt{R_H I_S}$ (Naudascher, 1992),

with C_C being an empirical friction coefficient, the hydraulic radius $R_H = A/U_w$, A the area of the flow cross-section, U_w the wetted perimeter and I_S the bed slope. Further, similar approximations, which relate the flow velocity with the cross-section, the bed slope and the wall roughness, were established in the middle of the nineteenth century by Darcy and Weißbach for pipe flows and the Manning-Strickler equation for rivers with rather rough walls (Hager, 1994). In addition, the Prandtl-Colebrook equation was established in the beginning of the twentieth century. This equation is valid for hydraulically smooth and rough, fully filled pipe flow:

$$\frac{1}{\sqrt{\lambda}} = -2 \cdot log_{10}(\frac{2.51}{\sqrt{\lambda} Re_b} + \frac{k_s}{3.71D}) \tag{1.19}$$

with k_s being the relative wall roughness. An equally universal equation lacks for open-channel flow, but the Prandtl-Colebrook equation can also be applied for partially filled pipe flow, by taking the difference of the cross-section into account (Melhem, 1990; DWA, 2012). However, since there are only a few studies on partially filled pipe flow, see next subsection, the suitability of the Prandtl-Colebrook equation for partially filled pipe flow is not documented in detail.

Review of recent developments in Partially Filled Pipe Flow

As mentioned in section 1.1 and the subsection above, partially filled pipe flows are present in various applications, but detailed investigations of this flow case are rare. In contrast to an open-channel flow in a rectangular cross-section, partially filled pipe flow lacks the solid corner inhomogeneity. Therefore, the generation of secondary flow at a mixed-corner can be studied without the influence of other inhomogeneities in partially filled pipes. Moreover, for flow depths lower than the pipe's radius an acute angle between the pipe's wall and the free surface occurs. Flow depths larger than the radius generate obtuse angles in the mixed-corner. In contrast, for full pipe flow, no mixed-corner occurs and azimuthal symmetry is established, hence, no mean secondary flow is generated. However, for partially filled pipe flow, the free surface breaks the azimuthal symmetry and mean secondary flow is generated. In the following section, various studies on partially filled pipe flow are introduced, which are mostly based on experimentally generated data.

To the author's knowledge, the first more detailed experimental studies of partially filled pipe flows were carried out by Replogle & Chow (1966); Melhem (1990) using Pitot tubes and by Strauß (1978); Sander & Koch (1990) using hydraulic impellers. They reported the velocity distribution in the vertical symmetry line and tried to deduce the bulk velocity and the discharge from it. Kölling (1994) did first numerical simulations of partially filled pipe flows, validating his results on the published measurements. He was able to reproduce the main aspects of the mean streamwise velocity distribution. More recently, velocity distributions were measured by Knight & Sterling (2000) using Pitot and Preston tube, Clark & Kehler (2011) using Acoustic Doppler Velocimetry in partially filled corrugated pipes and Yoon *et al.* (2012) and Ng *et al.* (2018) performing Stereo-PIV measurements. In addition, a LES representing the free surface by a level set method was recently published by Liu *et al.* (2022) for partially filled pipe flow. The main parameters of the more recent experiments are

summarized in table 1.1. Clark & Kehler (2011) and Yoon *et al.* (2012) have an inflow length of $\approx 25D_H$ hydraulic diameters, with $D_H = 4R_H$, which is the same for Tominaga *et al.* (1989), but according to Gessner (1973) $\approx 70D_H$ are needed to establish a fully developed flow, including secondary flow. Knight & Sterling (2000) and Ng *et al.* (2018) have at least $70D_H$ as inflow length.

Author	$H/(2R)$	Re_b	Fr
Knight & Sterling (2000)	0.33	64900	0.52
	0.51	110000	0.50
	0.67	135000	0.44
	0.82	150000	0.37
Clark & Kehler (2011)	0.34	339000	0.40
	0.44	295000	0.25
	0.50	557000	0.39
	0.61	238000	0.15
	0.65	468000	0.28
Yoon *et al.* (2012)	0.3	5693	0.47
	0.40	9766	0.54
	0.50	13541	0.56
	0.60	16088	0.53
	0.70	18326	0.50
	0.80	18974	0.44
Ng *et al.* (2018)	0.44	29300	0.52
	0.52	30100	0.43
	0.62	31000	0.36
	0.70	30300	0.30
	0.80	28500	0.25
Ng *et al.* (2018)	0.25	17020	0.15
	0.52	30100	0.10
	0.75	35020	0.08
	1.00	29020	-

Table 1.1: Parameters for turbulent partially filled pipe flow from recent experiments. $H/(2R)$ filling ratio, $Re_b = u_b \cdot D_H/\nu$ bulk Reynolds number and Froude number $Fr = u_b/\sqrt{gD_m}$ with $D_m = A/W$ and A being the area and W the free surface width of the cross-section.

In the following paragraph the main results for partially filled pipe flow from the experiments listed in table 1.1 are summarised. In the case of semi filled pipe flow and similar filling heights, the location of the maximum streamwise velocity has been reported by Knight & Sterling (2000),Yoon *et al.* (2012) and Ng *et al.* (2018) to be in the pipe centre at about $60 - 70\%$ of the flow depth. Hence, the *velocity-dip* phenomenon known from rectangular cross-sections also occurs for semi filled pipe flow. The maximum streamwise velocity u_{max}/u_b ranges from approximately 1.35 (Knight & Sterling, 2000) to 1.41 (Yoon *et al.*, 2012; Ng *et al.*, 2018). On the one hand, there have been attempts to model the streamwise velocity distribution over the cross-section. Clark & Kehler (2011) and Guo *et al.* (2015) each

established a set of equations based on the log-law, which show a fairly good agreement with their own measurements (high Reynolds number and rough walls). On the other hand, Yoon *et al.* (2012) used their data to generate fitted velocity distributions based on the velocity distribution functions of Chiu & Said (1995). From the fitted velocity distributions Yoon *et al.* (2012) approximated the wall shear stress. The maximum wall shear stress has been found in the centerline of the partially filled pipe, while the minimum wall shear stress has been reported to occur in the mixed-corner. Maxima have been reported to reach about $1.9\tau_0$ (Yoon *et al.*, 2012), with τ_0 being the globally averaged wall shear stress, or $1.1\tau_0$ (Knight & Sterling, 2000), who measured the wall shear stress directly with a Preston tube. Unfortunately, the most recently published results by Ng *et al.* (2018) did not provide any near-wall measurements due to a too coarse spatial resolution of their PIV. Instead Ng *et al.* (2018) extended the former publications with an extensive investigation of different filling heights for $Re_b \approx 30000$. Ng *et al.* (2018) and Clark & Kehler (2011) reported that the secondary flow consist of two big counter-rotating vortices that cover the whole cross-section and are symmetric to the channel mid plane. They did not report any inner secondary cell, which is also reflected in the wall shear stress distributions mentioned above. Ng *et al.* (2018) furthermore investigated flow structures in instantaneous velocity fields and patterns of streamwise velocity correlations in comparison to full pipe flow. Recently, they published further analyses of their data focusing on high energy modes of the flow appearing in the mixed-corner and on pseudo-instantaneous *very large scale motions* (VLSM) (Ng *et al.*, 2021). In 2022, not only the results of this thesis on semi filled pipe flow were published (Brosda & Manhart, 2022), but also the results of Liu *et al.* (2022) performing a LES for various filling ratios. Besides an investigation of the TKE-budget, Liu *et al.* (2022) compare the VLSMs of the flow with those of a full pipe flow. They report the absence of VLSMs for partially filled pipe flow, which is attributed to the presence of secondary flow. Moreover, they state that the missing VLSMs lead to a less developed near-wall turbulence.

1.5. Objectives and Structure

This study provides the first spatially and temporally highly resolved data set for partially filled pipe flow generated by direct numerical simulations. The range of Reynolds numbers covers marginal turbulent to moderate turbulent flows. The aim is to use the data set to validate and complement the existing data on basic flow features by answering the following questions:

- How does the friction factor change with Reynolds number and filling ratio?
- What is the distribution and statistics of the wall shear stress?
- What is the detailed mean secondary flow structure?
- Is there a corner vortex at the mixed-corner? Under which conditions will this vortex be present and how do its extensions scale?
- How do Reynolds stresses interfere with the mean secondary flow?
- How does the primary and secondary flow and other flow quantities change with Reynolds number?
- How does the filling ratio with its acute and obtuse mixed-corner affect the primary and secondary flow and other flow quantities?

With the knowledge of the basic flow quantities and a clear picture of the mean secondary flow different perspectives on the mechanism that generates and maintains secondary flow in partially filled pipe flow are investigated in order to answer the questions below:

- How and where is the streamwise vorticity generated?
- How does the mean secondary flow obtain its kinetic energy?
- What is the size and structure of coherent structures and how do they correlate to the mean secondary currents?
- Which structures are involved in the generation mechanism of mean secondary flow and how do they interact?

The structure of the thesis is the following: in chapter 2, the numerical methods are presented and validated for the present setup. The results of the thesis are separated, similarly to the distinction of the questions above – first the basic flow quantities are described in chapter 3. Their dependencies on Reynolds number for semi filled pipe flow and different filling ratios with a constant Reynolds number are investigated in chapter 3.2 and 3.3, respectively. Chapter 4 contains the analysis of mean flow quantities (chapter 4.1) and coherent structures (chapter 4.2). The results of the previous chapters are concluded in chapter 5, and with an outlook into new approaches to tackle remaining and newly found questions the thesis finishes.

2. Numerical Procedure

In the first part of this chapter, the tools to acquire the turbulent flow data are presented. The computational fluid dynamics code used to conduct the simulations, and its applied methods to solve the governing equations numerically are briefly introduced. As next step, it is shown how the code was applied to the present flow case. Moreover, it is described what kind of data was gathered throughout the simulations. A grid-study and a two-point correlation are presented in section 2.2 to validate the applied methods for the setup of the present flow case. In section 2.3, the Reynolds number for the flow case is defined and discussed. The chapter finishes with the description of the setups for the different simulations carried out for this thesis. Please note that the numerical method, validation and simulation setup are also described in Brosda & Manhart (2022) for the case of a semi filled pipe flow.

2.1. Numerical Method

As shown in Chapter 1, turbulent flows are governed by the Navier-Stokes equations (1.1a) and (1.1b) which are numerically discretised in a flow simulation. Moreover, turbulent flows consist of various – large and small – scales of motions and all of them have to be addressed with a numerical simulation. A DNS resolves all the scales of motion. Hence, DNS provides high accuracy without using any further model, but needs both high spatial and temporal resolution in order to resolve even the smallest scales. Thus, DNS creates large computational costs and needs to be employed carefully with regard to costs and energy consumption.
The simulations were carried out on the *SuperMUC* at the *Leibniz computing Centre* applying the scientific in-house code MGLET (Manhart *et al.*, 2001), which is under constant development, see latest publication by Sakai *et al.* (2019). MGLET is using a finite-volume method with a staggered, Cartesian grid (Harlow & Welch, 1965). Spatial approximation is provided by a second order central difference scheme and time integration is applied by an explicit third order low-storage Runge-Kutta scheme (Williamson, 1980). A conservative second order Immersed Boundary method represents arbitrarily shaped geometry using a ghost-cell method (Peller *et al.*, 2006), (Peller, 2010). Please note in order to achieve a conservative second order immersed boundary method, the momentum and mass balance are treated differently. The velocity in the cells which are intersected by the boundary are set as Dirichlet boundary condition. Therefore, MGLET applies a second order point-wise interpolation for the advective and diffusive terms in the momentum balance (Peller *et al.*, 2006). The mass flux is interpolated by considering the open face areas and used as boundary condition of the Poisson equation. Usually, the interpolated mass flux of a intersected pressure cell is not divergence free, hence, a flux correction was introduced (Peller, 2010). This procedure reduced the mass defect in selected cases by three orders of magnitude (Peller,

2010). Thus, mass conservation is guaranteed cell-wise after the pressure correction cycle. As MGLET employs a finite-volume method, no singularity appears at the mixed-corner, where the free surface and the wall intersect. By applying a multi-grid hierarchy the grid can be refined locally by zonally embedded grids, see Manhart (2004). This enables a simulation with flexible grid refinement along the wall and in the mixed-corner. The code has been used for a large variety of different flow cases: e.g. Manhart (1998), Breuer *et al.* (2009), Schanderl & Manhart (2018), Strandenes *et al.* (2019).

The flow domain is a partially filled pipe with radius R, length L and flow depth H, see figure 2.1. Simulations for three different filling ratios were conducted: $H/R = 0.5$, $H/R = 1.0$ and $H/R = 1.5$. The flow is driven by a constant body force g_1 in streamwise direction, which can also be seen as gravity force or pressure gradient. The constant body force sets the friction velocity $u_\tau = \sqrt{\tau_w/\rho}$ *a priori* via the integral force balance $\tau_w = \rho g_1 R_H$. The volume force g_1 can also be interpreted as a gravity force or as a pressure gradient. Periodic boundary conditions are applied in streamwise direction to model an infinitely long pipe, which enables to develop a statistically steady and fully-developed turbulent flow in a fairly small domain. The wall of the pipe is at rest and modeled by a no-slip boundary condition, i.e. $\mathbf{u}|_{wall} = 0$. At the free surface, there is a slip boundary condition with zero free surface parallel shear stresses, zero free surface normal velocity and no deformation, i.e. no surface waves are modeled. Hence, the Froude number is approximately zero. This limitation is accepted, because on the one hand this study does not aim to document any Froude number dependencies. On the other hand, almost all simulations documented in the literature review (cf. section 1.2 and 1.3) were also employing a rigid slip condition as free surface, thus, comparisons to the existing simulations are possible. Furthermore, Lee *et al.* (2012) simulated an open-duct with moving free surface for three different Froude numbers ($Fr = 0.2, 0.5, 0.8$). The basic flow pattern with an inner and an outer secondary vortex was observed for all Froude numbers and strong differences between the different Froude number simulations were reported for the turbulence statistics and the free surface deformations. However, for $Fr = 0.2$ only small deviations were found compared to a rigid slip condition at the water surface. From experimental studies of a wide open-duct flow, Kumar *et al.* (1998) concluded that a rigid plane with a slip condition is suitable to represent flows with Froude numbers smaller than 0.5. Certainly, the present study cannot be compared to high Froude number flows, but for similar flows with low Froude numbers a good agreement is expected.

Pipe flow simulations are often conducted using a grid with cylindrical coordinates. However, grids with cylindrical coordinates would have cut cells at the free surface for any filling than semi and full pipe flow. In addition, grid cells in the centre of the pipe might become very thin, which might cause problems during the simulations. Hence, for the sake of simplicity and efficiency of the flow solver, a Cartesian grid is applied, see figure 2.2 for semi filled pipe flow of $Re_\tau = 460$. The additional cells outside of the pipe's boundary, which have to be included for the Cartesian grid, can be tolerated, because of the efficiency of the flow solver. For all simulations one grid was applied over the whole cross-section with an equal grid cell size in x_2- and x_3-direction and elongated in streamwise direction (red grid). This is further specified in a following section of this chapter where the simulation parameters are described for all different simulations. For semi filled pipe flow up to $Re_\tau = 230$ and for the

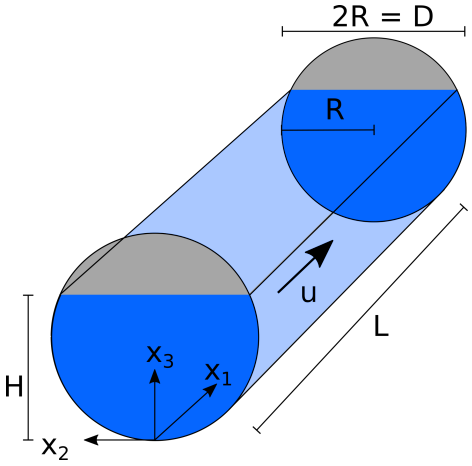

Figure 2.1: Flow domain

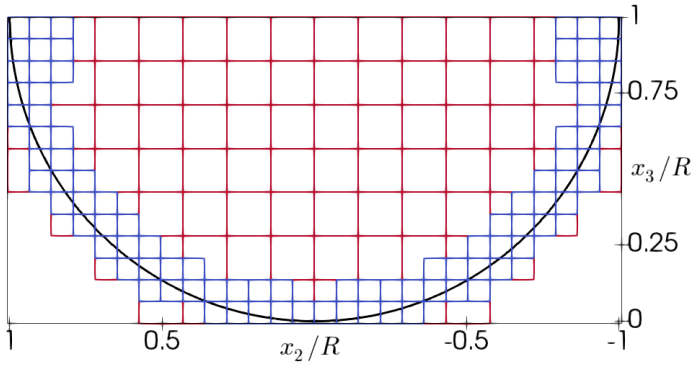

Figure 2.2: Grid configuration for semi filled pipe flow of $Re_\tau = 460$, base grid (red) and local grid refinement (blue)

simulation with a filling ratio of 75% and $Re_\tau = 180$, only one grid level was used. With increasing Reynolds numbers, a finer resolution is required especially where velocity gradients are large. In order to save computational costs, a second grid-level is added improving the grid resolution by a factor of two only in the vicinity of the wall, where large velocity gradients predominantly appear. The area of each mixed-corner is also refined for larger Reynolds numbers, because the flow physics in this area are of special interest for this thesis. This was done for the semi filled pipe flow at $Re_\tau = 460$ and for the case of 25% filling ratio at $Re_\tau = 180$. Please note that for the post-processing only the results of the base grid were used. To obtain a fully-developed turbulent flow, the following procedure by Jiménez & Moin (1991) is applied: a constant flow velocity, a high Reynolds number and a random disturbance are set as initial conditions; once a turbulent boundary layer started to form at the wall, and its turbulence spread over the entire cross-section, the Reynolds number was decreased in steps by adjusting the viscosity of the fluid until the intended conditions of the simulation are reached. After the flow reached a steady state, the flow statistics (e.g. averaged and instantaneous flow fields) were recorded.

2.2. Validation

The numerical flow configuration of the present flow case has not been examined yet, so it is important to validate the simulation setup. This is first of all done by a grid study, checking whether the simulations converge with respect to the grid resolution. In a second step the Cartesian grid configuration is validated by simulating a full pipe flow and comparing the results to validated data from literature, generated by a different numerical method. Whether the length of the domain is long enough is confirmed by means of two-point correlations. Moreover, many previous studies are mentioned in section 1.3 and 1.4, with the most relevant studies Liu *et al.* (2022); Ng *et al.* (2018); Clark & Kehler (2011); Yoon *et al.* (2012) and Sakai (2016), which serve as comparison and reference to the present results, if possible. Finally, as mentioned in section 2.1, the applied numerical methods, boundary and initial conditions were already used in different setups and validated in that respect, which gives

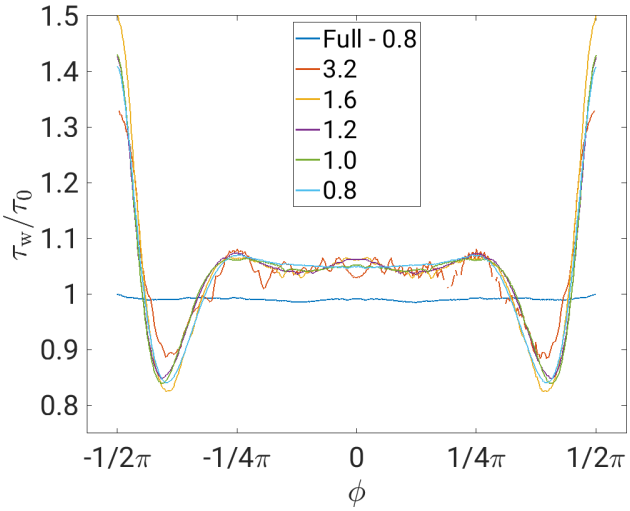

Figure 2.3: Grid-study of wall shear stress τ_w/τ_0 for $Re_\tau = 180$ for semi filled and full pipe flow. Grid-size equal to $\Delta x_2^+ = \Delta x_3^+ = 3.2$, 1.6, 1.2, 1.0 and 0.8 wall units for semi filled and 0.8 wall units for full pipe flow.

confidence for the present simulations.

At first, a grid-study for semi filled pipe flow is presented. It is based on the wall shear stress, which is a highly sensitive parameter for the grid resolution. The Reynolds number was kept constant at $Re_\tau = 180$. A single-grid configuration with constant grid spacings at $\Delta x_2^+ = \Delta x_3^+ = 3.2, 1.6, 1.2, 1.0$ and 0.8 was used. Note that the streamwise spacing was set to $\Delta x_1^+ = 6\,\Delta x_2^+$. Figure 2.3 shows the converging behaviour of the mean wall shear stress. Please note that the wall shear stress is normalised by the average wall shear stress τ_0, obtained from the global force balance. Additionally, the wall shear stress along one half of a full pipe simulation is included from the finest resolution ($\Delta x_2^+ = \Delta x_3^+ = 0.8$ and $\Delta x_1^+ = 6\,\Delta x_2^+$). The wall shear stress was obtained *a posteriori*, i.e. τ_w is not directly obtained from the simulation, but was computed using the velocity gradients at a wall distance of $\Delta r^+ = 2$ in radial, wall normal direction. Therefore, the mean velocities in Cartesian coordinates were interpolated to Polar coordinates. It can be seen for the coarser simulations that there are larger deviations of the maxima in the mixed-corner and the minima at approximately $\pm 3/8\pi$. For the coarsest resolution strong wiggles can be noticed, which is somewhat expected, because the grid resolution is coarser than the distance between the interpolation point of the velocity gradient and the wall. In general, the finer resolutions $\Delta x_2^+ = \Delta x_3^+ \leq 1.2$ agree very well, only small bumps in the centre are visible, which disappear for the finest resolution. The wall shear stress distribution of the finest grid is very smooth over the whole wetted perimeter. The remaining variations in the centre part also occur for the wall shear stress in the full pipe flow at the same grid resolution. The maximum deviation of the wall shear stress of the full pipe flow is less than 1% of the ideal value. Hence, the full pipe flow simulation shows a high azimuthal homogeneity of the wall shear stress.

In order to validate the Immersed Boundary Method (IBM) and the Cartesian Grid configuration, a full pipe flow was computed at three different grids, $\Delta x_2^+ = \Delta x_3^+ = 3.2, 1.6$ and 0.8 for $Re_\tau = 180$. These simulations are compared to a DNS of full pipe flow with

body-fitted grids by El Khoury *et al.* (2013). Looking at the (IBM) in detail, the actual wall distance of the centres of the first momentum cells near the wall are randomly distributed. Converting the Cartesian gridspacing of $\Delta x_i^+ = 0.8$ at $Re_\tau = 180$ into Polar coordinates, it turns out that the mean wall distance of the momentum cell centres is $\Delta r^+ = 0.7871$ with a root mean square (rms) of $\Delta r_{rms}^+ = 0.8135$. This spatial variability in the cell centre position produces numerical errors, which are represented in the variations of the wall shear stress distribution. The grid-study of the full pipe flow mostly shows the influence of the boundary condition on the homogeneity of the computed wall shear stress and its azimuthal symmetry. For completeness of the description of the implemented IBM, please note that only fluid cells, which are not intersected by the wall, receive the driving body force. This reduces the global volume force that acts on the fluid, because it is not applied on the complete round pipe but on a smaller volume. The differences in the volume are 0.5% at $\Delta x_i^+ = 0.8$, 1.4% at $\Delta x_i^+ = 1.6$ and 2.6% at $\Delta x_i^+ = 3.2$. The differences are small for the finest resolution, but the Reynolds numbers Re_τ given in table 2.2 (see section 2.4) are actually by about 0.4% smaller than given. For the flow case of a predicted friction Reynolds number of $Re_\tau = 180$ this means, that the predicted value is actually $Re_\tau \approx 179.3$. Moreover, from the results of the simulation it is possible to obtain a friction Reynolds number *a posteriori*, which is equal to 181.3. However, the differences between the predicted and the obtained friction Reynolds number are small. Thus, in the following it will be related to the friction Reynolds number based on the idealized prediction, hence, in the present example $Re_\tau = 180$.

In addition to the grid-convergence study, figure 2.4 (left) shows a comparison between the streamwise velocity averaged in both time and space (azimuthal direction) of the full pipe flow simulation and data from El Khoury *et al.* (2013). This is done to further assess the possible drawbacks of a Cartesian grid compared to a body-fitted grid. The averaged streamwise velocity profile (left figure) converges in the viscous layer towards the law of the wall, but it only shows satisfying agreement for the finest grid of 0.8 wall units. While the velocity of the coarse grid is slightly lower in the centre than the one of El Khoury *et al.* (2013), the finer grid velocity converges at a somewhat higher magnitude already at the medium grid with 1.6 wall units. Between the finest and second finest grid u_τ/u_b differs by 0.6% and compared to El Khoury *et al.* (2013) a slightly larger difference of 1.1% can be reported.

In figure 2.4 (right) the convergence behaviour of the rms of the velocity fluctuations in full pipe flow are shown and compared to the profiles of El Khoury *et al.* (2013). The finest grid matches the reference very well for all components. While for $u_{1,rms}^+$ and $u_{\theta,rms}^+$ the finest resolution is needed, $u_{r,rms}^+$ seems to be converged already in the coarsest simulation. Please note that there is no distortion of the Reynolds stresses visible near the wall. Thus, it is concluded, that the IBM is able to represent the pipe's wall at the chosen grid resolution.

Overall, the convergence study indicates that the grid resolution of $\Delta x_2^+ = \Delta x_3^+ = 0.8$ and $\Delta x_1^+ = 6\Delta x_2^+$ is sufficiently fine. Note that at the two highest Reynolds numbers, a grid cell aspect ratio of $\Delta x_1/\Delta x_2 = 4$ was used.

A second important aspect is that the length of the domain with its periodic boundary condition in streamwise direction should be long enough in order to avoid unphysical constraints on the largest flow structures. The pipe length is approximately $8\pi H$ for $Re_\tau = 180$. A

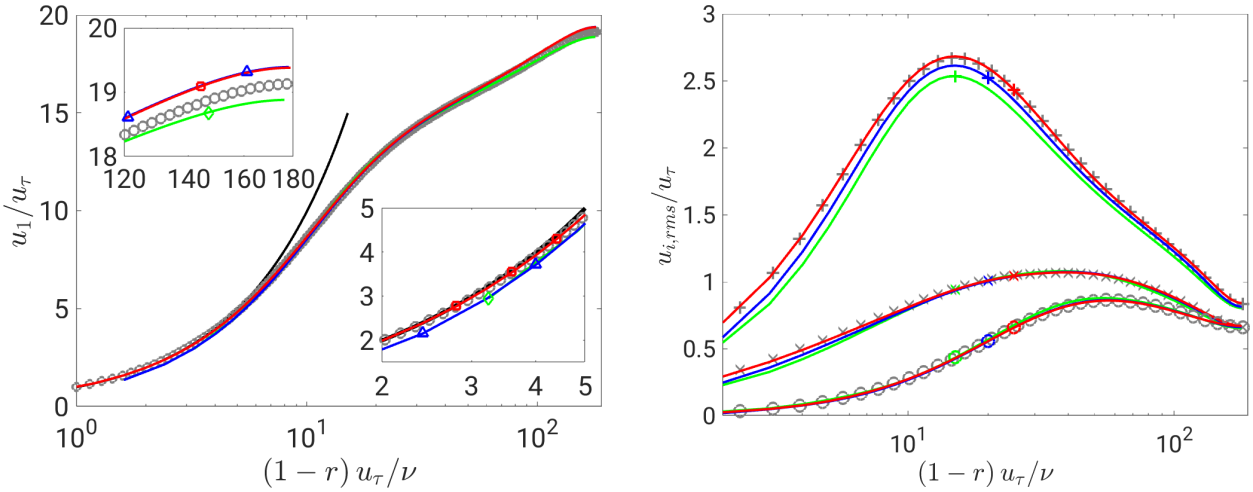

Figure 2.4: Azimuthally averaged streamwise velocity u_1/u_τ in wall-normal direction x_n for full pipe flow of $Re_\tau = 180$ for different grid resolutions (left). Red represents $\Delta x_2^+ = \Delta x_3^+ = 0.8$, blue corresponds to 1.6 and green to 3.2. For comparison, data from El Khoury *et al.* (2013) is included as grey circles and the black line shows the linear law of wall $u_1^+ = x_r^+$. The boxes include details of the near-wall and centre region. Rms of velocity fluctuations $u^+_{1,\mathrm{rms}}$ (+) , $u^+_{\mathrm{r,rms}}$ (∘) and $u^+_{\theta,\mathrm{rms}}$ (×) in inner units for the full pipe flow simulation of $Re_\tau = 180$ averaged in azimuthal direction (right). Lines correspond to the present simulation and every fifth data point of El Khoury *et al.* (2013) is included as circles for comparison.

standard two-point correlation (Sillero *et al.*, 2014)

$$\kappa_{ij}(\mathbf{x}-\mathbf{x}') = \frac{\overline{u_i(\mathbf{x},t)u_j(\mathbf{x}',t)}}{\sigma(u_i(\mathbf{x},t))\sigma(u_j(\mathbf{x}',t))}, \tag{2.1}$$

is applied for all three velocity components to assess the streamwise correlation for points across the whole cross-section. The slowest decay of the correlation κ_{ij} appears in the mixed-corner ($x_2/R = -0.97$,$x_3/R = 0.97$), see figure 2.5 (left), where half of the domain length is shown. The correlation for the streamwise velocity κ_{11} needs the longest distance of about a quarter of the pipe length to sufficiently decay. Note that for $Re_\tau < 140$ the pipe length was enlarged to $\approx 12\pi H$ in order to satisfy the criteria of decaying two-point correlations (see figure 2.5 (right)).
From the streamwise two-point correlation an integral length scale L_{11} can be computed for each point of the cross-section:

$$L_{11} = \int_0^{L/2} \kappa_{11}(x_1 - x_1')\, d(x_1 - x_1'). \tag{2.2}$$

The distribution of L_{11} over the cross-section is shown in figure 2.6. High values of L_{11} can be found along the wall and especially in the mixed-corner. Hence, the decay of the two-point correlations is much faster in most of the cross-section than in the mixed-corner, which was shown in figure 2.5. The investigations of the two-point correlation were done for

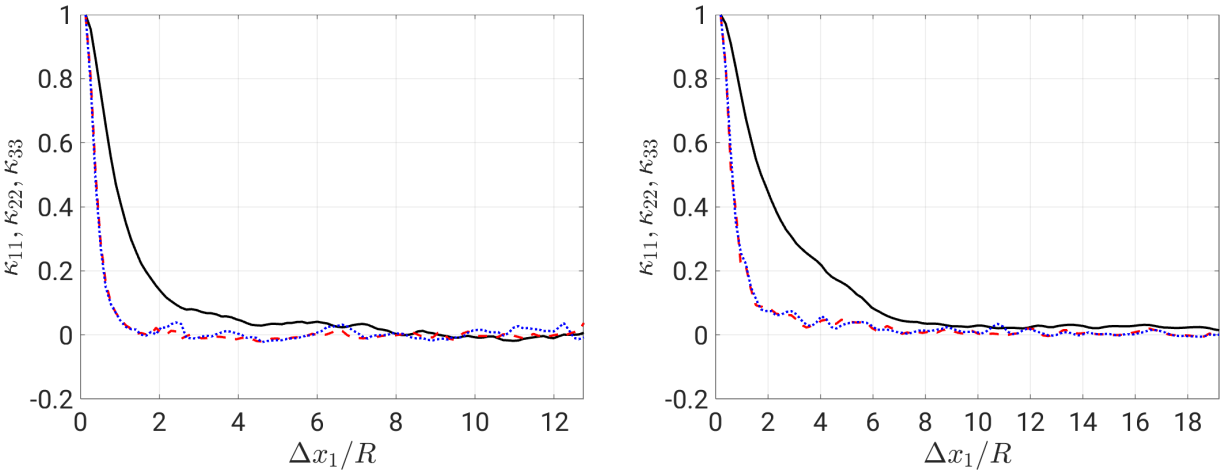

Figure 2.5: Streamwise-temporal 2-point correlation κ_{ij} for all three velocity components in the mixed-corner at position $x_2 = -0.97$, $x_3 = 0.97$ for 50% filling ratio and $Re_\tau = 180$ (left) and $Re_\tau = 115$ (right). Black solid line represents κ_{11}, red dashed line κ_{22} and blue dotted line κ_{33}.

all simulations.

In the framework of very-large-scale motions in open-channel flows even longer domains might be required as Zampiron *et al.* (2020) observed very-large-scale motions of lengths up to 25 flow depths. Such structures could not be represented in the present simulation setup. However, Feldmann *et al.* (2018) reported that 14 radii are sufficiently long to obtain converged second-order statistics in a full pipe flow and Ng *et al.* (2021) reported a maximal length of structures of approximately $11R$ in partially filled pipe flow, which is the same flow case as this thesis deals with. In addition, Liu *et al.* (2022) report an absence of VLSMs for a LES with similar Reynolds numbers as Ng *et al.* (2021). The flow domain in this study is more than twice as large as structures reported by Ng *et al.* (2021), which had Reynolds numbers twice as large than the maximum Reynolds number of this study. Moreover, it is also longer than what has been used in other recent, comparable numerical studies, e.g. (Pirozzoli *et al.*, 2018). Another aspect is that the phenomenon of secondary flow is well developed and occurs in a similar manner as in other literature, see section 3.2. Last point to mention is, that very-large-scale motions are usually considered in the context of large Reynolds number (Monty *et al.* (2009), $Re_\tau = 3000$), whereas this study deals with comparably small Reynolds numbers with a maximum of $Re_\tau = 460$. However, for channel flow the influence of very-large-scale motions starts to be recognisable in the energy spectrum from $Re_\tau = 550$ on (del Álamo & Jiménez, 2003).

Based on the aforementioned, it is assumed, that the simulation domain is sufficiently long and the grid resolution is fine enough to study the phenomenon of secondary flow in partially filled pipe flow.

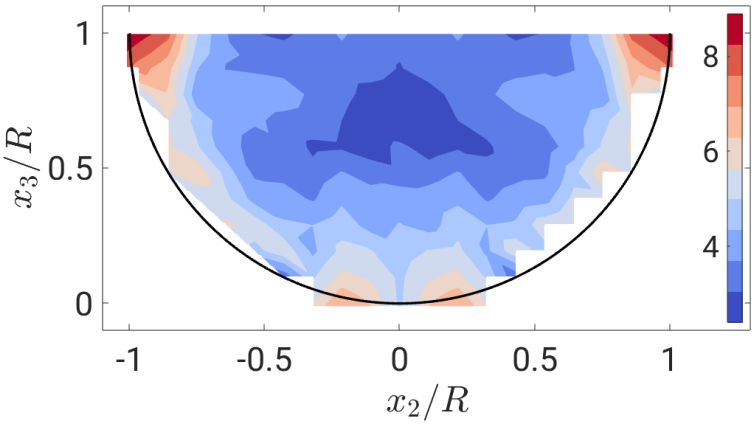

Figure 2.6: Integral length scale L_{11} of the streamwise-temporal 2-point correlation κ_{11} over the cross-section for $Re_\tau = 180$ and 50% FR.

2.3. Definition of Reynolds Number

The definition of the Reynolds number Re is important to be able to compare the simulations between each other and to literature. So far partially filled pipe flows were only studied by experiments. For comparison to numerical simulations one can only refer to full pipe flow and open-channel flows with various aspect ratios. On the one hand the experimental community commonly uses a bulk Reynolds number $Re_b = \frac{u_b D_H}{\nu}$, with u_b being the bulk velocity, D_H being the hydraulic diameter $D_H = 4 \cdot R_H$ and ν the kinematic viscosity. On the other hand the numerical community is used to work with the friction Reynolds number $Re_\tau = \frac{u_\tau \ell}{\nu}$, with u_τ being the friction velocity and $\ell = \delta$ being the boundary layer thickness. For full pipe flows, ℓ is considered to be the pipe radius R and for open-channel flows to be the water height H.

Using Re_b as reference Reynolds number would be intuitive, but as u_b is a result of the simulation, Re_b can only be roughly estimated *a priori*. On the other hand, for a steady flow, the wall shear stress is in balance with the driving body force, see the integral force balance $\tau_w = \rho g_1 R_H$, thus, the friction velocity u_τ and therefore also Re_τ can be calculated *a priori*. Hence, Re_τ is used as reference Reynolds number and Re_b is calculated *a posteriori* to be able to compare to experiments.

If the friction Reynolds number for a partially filled pipe flow was defined the same way as for full pipe flows, with $\ell = R$, one viscous length scale δ_ν/R would be constant across all filling rates, leading to the same length of the viscous layer for all filling rates. Hence, there would be a smaller number of wall units per flow depth for low filling ratios compared to high filling ratios. In contrast, if $\ell = H$ is set the same number of wall units per flow depth occur for the different filling ratios, but δ_ν/R gets larger with increasing filling ratio. Compare table 2.1, which shows δ_ν normalised by the radius R for the three different fillings for $Re_\tau = 180$. Another possibility is to set $\ell = 2R_H$ resulting in a δ_ν/R that is the same as in the semi filled pipe case where $\ell = R$ and reflecting the global geometry settings for other filling ratios. In the first three approaches the viscosity was adjusted to equal the assumed Reynolds number, as ℓ and u_τ are set by definition. The last considered approach is to keep the viscosity constant for each Reynolds number for all filling ratios. The constant viscosity

is set according to the viscosity of the semi filled case, where $\ell = R$ (e.g. for $Re_\tau = 180$ ν is kept constant at $0.0556/(Ru_\tau)$). ℓ can then be calculated by $\ell = \frac{Re_\tau \nu}{u_\tau}$. This leads to a decreasing ℓ for an increasing flow depth, which is counter-intuitive, see table 2.1. In contrast, for the cases $\ell = H$ and $\ell = 2R_H$ the resulting wall unit lengths are increasing as the filling rate increases.

Filling ratio H/(2R)	$\ell = R$	$\ell = H$	$\ell = 2R_H$	$\ell = \frac{Re_\tau \nu}{u_\tau}$
25 %	0.005556	0.002778	0.003258	0.007254
50 %	0.005556	0.005556	0.005556	0.005556
75 %	0.005556	0.008333	0.006704	0.005057

Table 2.1: Wall unit length δ_ν/R for different definitions of ℓ; $Re_\tau = 180$

The aspects that are expected to be strongly responsible for the secondary flow pattern are the geometry and the mixed-corner vortex, which scales with wall units (Sakai, 2016). Hence, $\ell = 2R_H$, including both aspects, is used as length scale for the reference Reynolds number $Re_\tau = \frac{u_\tau 2R_H}{\nu}$. The bulk Reynolds number $Re_b = \frac{u_b D_H}{\nu}$, with $D_H = 4R_H$, can be used to conveniently compare to most experimental publications.

2.4. Simulation Setup

For this study various different flow set-ups were simulated. Within the first simulation series the Reynolds dependency was studied for a semi filled pipe flow. For the second simulation series the friction Reynolds number was kept constant at 180 and the filling ratio was varied from $H/(2R) = 25\%$ over 50% to 75%. In the upper part of table 2.2, the different simulations and the corresponding parameters for the semi filled pipe are listed. The main parameter is the friction Reynolds number $Re_\tau = \frac{u_\tau 2R_H}{\nu}$. It ranges from 115, which is just maintaining turbulence, to 460, a moderately turbulent flow. Accordingly, a bulk Reynolds number $Re_b = u_b D_H/\nu$ can be calculated. Please note that for the semi filled cases Re_b is based on the pipe diameter, because $D_H = 2R$, being in line to the full pipe flow definition and is equal to a Reynolds number based on the hydraulic diameter D_H as used by e.g. Ng *et al.* (2018). As mentioned in section 2.1 and 2.3, Re_τ was fixed for each simulation run *a priori* and Re_b was resulting from the simulation. The lower part of table 2.2 contains the simulations with different filling heights and constant friction Reynolds number. For the different filling ratios the simulations were set up such that $Re_\tau = 180$. The bulk Reynolds number is, as mentioned above, a result from the simulations and it can be seen that the resulting Re_b's for different filling ratios and constant Re_τ only have small deviations.

The following data was gathered: Instantaneous three-dimensional flow fields were captured each time after the bulk flow had passed the pipe once. Instantaneous values of all three velocity components and of the pressure were gathered at 38000 single points at 200 cross-sections that were equally distributed along the length of the pipe. At the individual cross-sections, the points were spread in a Cartesian equidistant manner. The data was collected every ten viscous time units. To be able to investigate the wall shear stress, further single

$H/(2R)$	Re_τ	Re_b	L/R	$\mathrm{N_{total}} \times 10^6$	Δx_1^+	$\Delta x_2^+ = \Delta x_3^+$	Δt_b	Δt^+
0.5	115	3239	38.46	48	4.38	0.73	11489	93058
0.5	120	3363	38.46	48	4.56	0.76	9053	76898
0.5	140	3875	25.91	43	4.74	0.79	11486	115395
0.5	180	5198	25.54	90	4.74	0.79	5068	62849
0.5	230	6874	25.36	242	3.32	0.83	5511	84424
0.5	460	15452	25.36	749	3.32 - 6.64	0.83 - 1.66	4958	135489
0.25	180	5332	14.85	118	3.2 - 6.4	0.80 - 1.6	5048	52296
0.75	180	5318	30.53	102	3.16	0.79	6058	91790

Table 2.2: Simulation parameters for turbulent partially filled pipe flow. $H/(2R)$ filling ratio. $Re_\tau = u_\tau\, 2R_H/\nu$, $Re_b = u_b\, D_H/\nu$ friction and bulk Reynolds number. Total number of grid points $\mathrm{N_{total}}$. Δx_i^+ grid spacing in wall units (close to wall - bulk region). $\Delta t_b = \Delta t u_b/R$, $\Delta t^+ = \Delta t u_\tau^2/\nu$ averaging time for statistics in bulk time units and viscous time units.

points were placed two wall units above the wall in wall normal direction. Along the wetted perimeter, 2.5 wall units were between the single points and in streamwise direction the points had a distance of 1/10 of the pipe length. The instantaneous data at these points was also gathered at an interval of ten viscous time units. For various flow parameters, like velocity and its statistical moments or spatial gradients of the fluctuating velocity, ensemble-averaged values were gathered with respect to time, see equation (1.7). Similar to Sakai (2016), ensemble-averaged quantities were accumulated approximately every single viscous time unit for over at least $4950\, u_b/R$ bulk time units to ensure a sufficient number of samples. During the post-processing, the samples were further averaged over the domain length and advantage was taken of the half plane symmetry of the flow by mirroring the averaged values.

3. Basic Flow Description for Partially Filled Pipe Flows

In this first chapter of results, the flow in partially filled pipes is examined applying basic statistical concepts, hence, the main flow parameters are presented.
The flow will be explored over two main parameters. First, the Reynolds number, i.e. the degree of turbulence, is adjusted from marginally turbulent to moderately turbulent flow. Second, for a fully-turbulent state different filling ratios are analysed. For both varying parameters following the main flow quantities are investigated: the mean streamwise velocity, the secondary flow, the wall shear stress and the turbulence intensities. With the help of the various analysis the following questions are addressed.

- How does the friction factor change with Reynolds number and filling ratio?
- What is the distribution and statistics of the wall shear stress?
- What is the detailed mean secondary flow structure?
- Is there a corner vortex at the mixed-corner? Under which conditions, will this vortex be present and how do its extensions scale?
- How do Reynolds stresses interfere with the mean secondary flow?
- How does the primary and secondary flow and other flow quantities change with Reynolds number?
- How does the filling ratio with its acute and obtuse mixed-corner affect the primary and secondary flow and other flow quantities?

Moreover, for the case of semi filled pipe flow, the minimum turbulent Reynolds number and the minimal domain length are reported.
In this chapter 3, there are already first comments on the generating and maintaining processes of secondary flows. However, in the following chapter 4, a detailed analysis on the generation mechanism of secondary currents is examined based on the main flow parameters of this chapter.
Please note that the section 3.1 (*Friction Factor* λ) for the case of semi filled pipe flow and the section 3.2 (*Reynolds Dependency for Semi Filled Pipe Flow*) are mostly already published in Brosda & Manhart (2022). If additional results, that were not part of the publication, are presented, it will be emphasized in the beginning of the paragraphs.

3.1. Friction Factor

Please note that the results for the 25% and 75% filled case are first published in this thesis.

The friction factor is an important parameter for engineering problems. In order to estimate the friction losses within a pipe system, one needs to know λ for the different parts of the flow system. Moreover, the role of friction can be compared for different geometries, roughness and Reynolds numbers via the dimensionless friction factor λ.

For turbulent flows in pipes and open-channels, a relation between wall shear stress τ_w and the friction factor λ is defined as follows, e.g. (Oertel, 2012):

$$\tau_\mathrm{w} = \lambda \cdot \frac{\rho u_\mathrm{b}^2}{8} \tag{3.1}$$

As τ_w and u_b are results from the simulations λ can be calculated. Equation (3.1) can be further transformed to $\lambda = (8 g_1 R_H) / u_b^2$, with g_1 being the constant volume force. In addition, one can define the friction coefficient as $C_\mathrm{f} = \lambda/4$ Pope (2000). In 1932, Prandtl has defined an empirical function (eq. (3.2)) between the Reynolds number Re_b and the friction factor λ for a turbulent flow in fully filled smooth pipes with $Re_\mathrm{b} < 10^6$ (Oertel, 2012). Please note, equation (3.2) can be extended to hydraulically rough flows, see eq. 1.19. The wall of the pipe of the present simulations is smooth as well, thus, a comparison to smooth, full pipe flow should give reasonable results.

$$\frac{1}{\sqrt{\lambda}} = 2 \cdot log_{10}(\sqrt{\lambda} Re_\mathrm{b}) - 0.8 \tag{3.2}$$

In figure 3.1 (left), the relation between Re_b and λ is shown for laminar and turbulent flows in semi filled pipes like in the Moody-diagram. The red pluses represent semi filled pipe flows of the present study which are compared to measurements for semi filled pipe flow by Ng *et al.* (2018) (×) and Yoon *et al.* (2012) (♦) and a LES of Liu *et al.* (2022) (+). In addition, data of full pipe flows are included: present simulation (○), measurements from Schlichting & Gersten (2017) (○) and Ng *et al.* (2018) (○). The relation between Re_b and λ for full pipe flows follows the black line, i.e. the Prandtl-equation (3.2).

While the measurements of Ng *et al.* (2018) and Yoon *et al.* (2012) suggest a large increase of the friction factor in semi filled pipe flow compared to full pipe flow, the present simulations show a good agreement with the full pipe flow. The LES of Liu *et al.* (2022) lies slightly underneath the Prandtl's relation for hydraulically smooth pipe flows. One has to bear in mind that both measurements are affected with large uncertainties. Yoon *et al.* (2012) performed stereoscopic PIV from which they were not able to compute the wall gradient directly. Thus, they estimated the wall shear stress on the basis of a fitted streamwise velocity, based on the method proposed by Chiu & Said (1995). Unfortunately, it is unclear, how accurate this procedure is. Ng *et al.* (2018) obtained the friction factors from a global force balance for which they measured the slope of the water surface. They rate this indirect method as associated with "relatively large uncertainty". Ng *et al.* (2018) also plotted the relation with an equivalent length scale, taking the flow cross-section into account, which made their results match the full-pipe flow distribution better. However, based on the validation and grid study presented in section 2.2, it seems that the large increase of the friction factor as

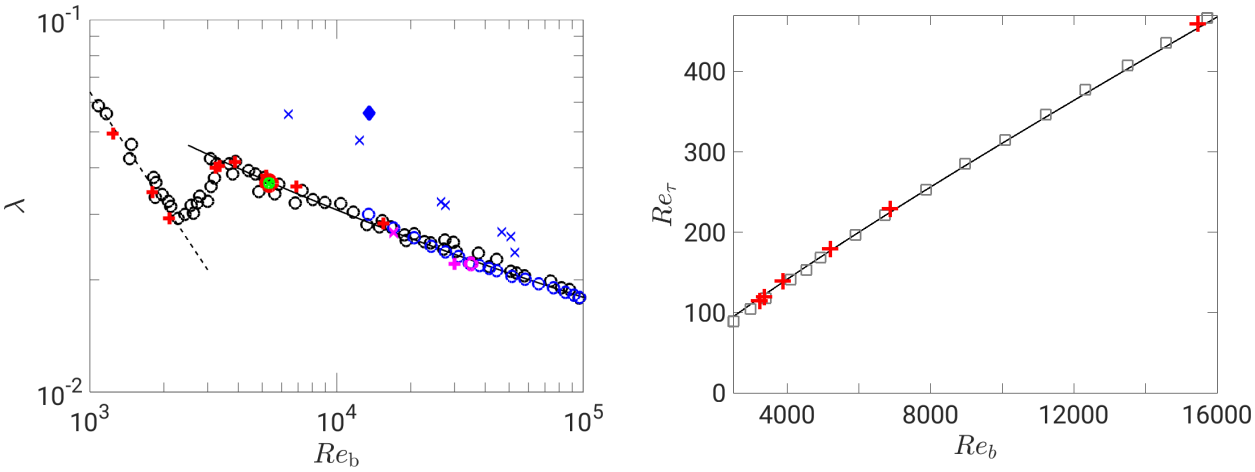

Figure 3.1: Bulk Reynolds dependency of friction factor λ (left). Friction Reynolds number Re_τ over bulk Reynolds number Re_b (right). + indicate present semi filled pipe flow simulations. ○ represent present full-pipe flow simulation. × and ○ represent present 25% and 75% filled pipe flow, respectively. Grey ○ are measurements for full pipe flow extracted from textbook of Schlichting & Gersten (2017). × show data for 52% filled pipe by Ng *et al.* (2018), ○ show data for full-pipe by Ng *et al.* (2018), and ♦ represents a measurement by Yoon *et al.* (2012). In magenta the results of the LES of Liu *et al.* (2022) is included: ×, + and ○ represent 25%, 52% and 75% filling ratio, respectively. Solid line follows equation (3.2) and dashed line follows $\lambda = 64/Re_b$. □ show Sakai (2016)'s data for rectangular open-channel flow.

inferred from the two experiments is unrealistic.

In addition to the data of semi filled and full pipe flow, the data for the quarter filled × and three-quarter filled ○ flow cases of the present study are also included in figure 3.1 (left), as well as the data from the LES of Liu *et al.* (2022) for higher Reynolds numbers ($H/(2R) = 0.25$: × and $H/(2R) = 0.75$: ○). In general, it seems like they also agree with Prandtl's friction law for smooth pipes. The non-semi fillings of the present study have slightly smaller friction factors, deviating $5-7\%$ from the semi filled flow case. In contrast, Ng *et al.* (2018) reported higher global values for λ and a correlation to the filling height. The higher the flow depth the higher the friction factor, deviating about 14% for smaller fillings and up to 50% for greater fillings. Please note in order to further validate the post-processing for the friction factor, three laminar simulations were simulated additionally. These low Reynolds number cases match the laminar relation for a fully filled pipe flow $\lambda = 64/Re_b$ (dashed line). This is expected and consistent to the analytical solution of a fully symmetric flow.

Figure 3.1 (right) shows the ratio between Re_τ and Re_b. Red pluses show the results of the present semi filled pipe flow and as black squares data of Sakai (2016) for an open-duct flow with an aspect ratio of $W/H = 2$ is included. The two data sets agree very well for all Reynolds numbers. By combining Prandtl's friction law for smooth pipes (eq. (3.2)) with the relation between τ_w and λ (eq. (3.2)), the definition of the friction velocity (eq. (1.15)) and the definitions of Re_τ and Re_b, a relation between Re_τ and Re_b can be deduced for smooth full pipe flow (black solid line). Both data sets follow the black solid line, hence, the

friction factors of the two different geometries do hardly differ from full pipe flow. Moreover, this comparison gives further confidence that the friction factor is not underestimated by the present simulations. Please note to be able to compare the two different flow cross-sections, the Reynolds numbers of the rectangular cross-section were calculated by using an equivalent length scale H_{eq} as characteristic length scale. By assuming an equally large cross-sectional area for both geometries H_{eq} has been defined as $H_{eq} = H\frac{2}{\sqrt{\pi}}$, with H being the flow depth (Sakai, 2016).

3.2. Reynolds Dependency for Semi Filled Pipe Flow

Please note that most of the results have been published in Brosda & Manhart (2022), otherwise it is emphasized in the beginning of the paragraph.

3.2.1. Mean Flow

Mean Streamwise Velocity and Velocity-Dip Phenomenon

Although the rotational symmetry of the pipe is broken, radial profiles in laminar flow are invariant with respect to rotations about the pipe axis. This does not hold true for turbulent flows. In figure 3.2, the normalised mean streamwise velocity is shown for $Re_\tau = 115, 140, 180$ and 460. The distribution of the mean streamwise velocity is Reynolds number dependent. For $Re_\tau \geq 140$, the so-called *velocity-dip* phenomenon can be observed, i.e. the maximum velocity – indicated by a plus in the plots – is not at the free surface, but below on the vertical symmetry line. The distance of the velocity maximum from the free surface increases within this Reynolds number range, which is further investigated below. These velocity distributions differ significantly from rotational symmetry. The general picture is in accordance with findings from higher Reynolds numbers in partially filled pipe flows (Knight & Sterling, 2000; Clark & Kehler, 2011; Yoon *et al.*, 2012; Ng *et al.*, 2018) and rectangular open-duct flow (Tominaga *et al.*, 1989; Joung & Choi, 2009; Sakai, 2016). For the very low yet fully turbulent Reynolds number $Re_\tau = 115$ the velocity distribution is much closer to full pipe flow and no *velocity-dip* phenomenon can be detected. The same behaviour was observed by Sakai (2016) for a turbulent rectangular open-duct flow at marginal Reynolds numbers.

The distance of the maximum mean streamwise velocity from the free surface is shown in figure 3.3 in inner units. For comparison, the data of a rectangular open-duct flow are shown (Sakai, 2016), taking the difference in cross-sectional area into account via the equivalent length scale H_{eq} as introduced in section 3.1. For the very low Reynolds numbers, there is a slight difference, which can be explained by the different geometry and the vortex pattern, but for higher Reynolds numbers both cases match well. The distance in outer units can be compared to several other measurements of semi filled pipe flows (Knight & Sterling, 2000; Clark & Kehler, 2011; Yoon *et al.*, 2012; Ng *et al.*, 2018) at higher Reynolds numbers, see figure 3.4. The experiment of Yoon *et al.* (2012), which is in the same Reynolds number range as the present simulation, deviates with more than 20% from the data of this study. Maybe their inflow length of $25D_H$ is too short to have fully-developed secondary flow structures. Note that on the one hand Demuren & Rodi (1984) reported a fully developed secondary flow in a rectangular channel not before $70D_H$ from the inlet. On the other hand, the high Reynolds number cases would approximately follow the trend of the current data. Taking all data into account, after a strong increase for small Reynolds numbers, the distance from the velocity maximum to the free surface $\Delta z/R$ seems to settle for larger Reynolds numbers between 0.3 and 0.4.

The magnitude of the normalised maximum mean streamwise velocity decreases with Reynolds number when normalised by u_b, see figure 3.5. This means that the momentum is more evenly

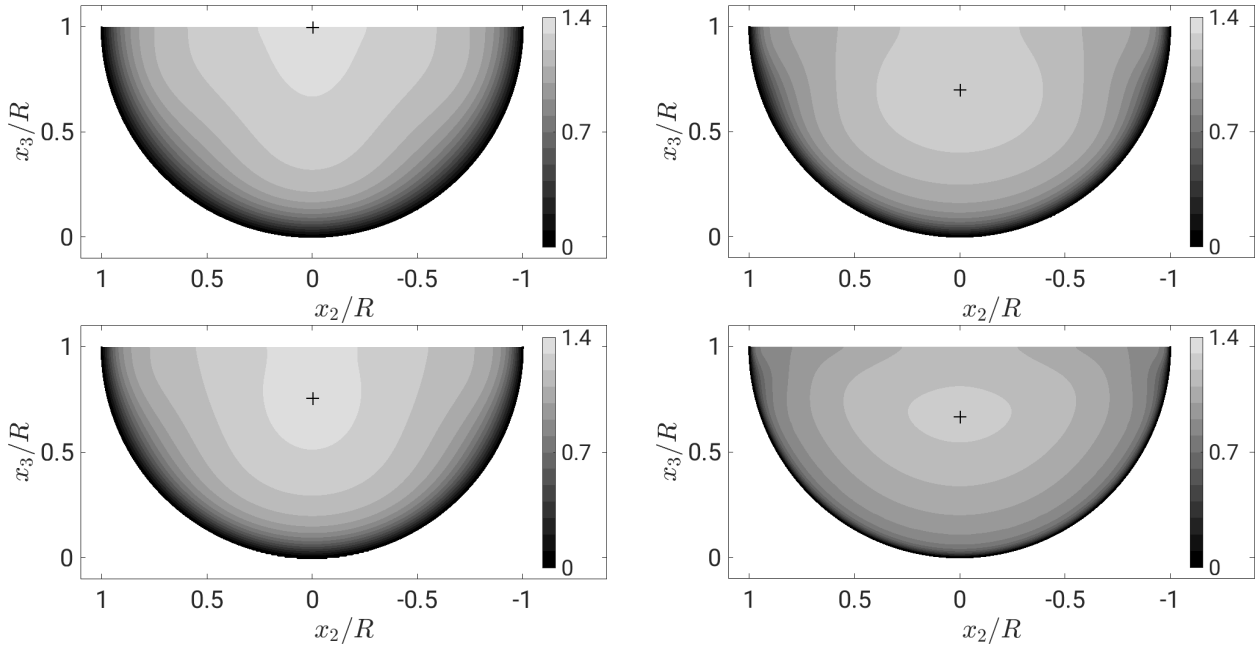

Figure 3.2: Mean streamwise velocity $\overline{u}/u_b$ of $Re_\tau = 115, 140$ (left column) and $180, 460$ (right column, top to bottom). + indicates the position of the velocity maximum. Please note, that the distributions were symmetrized using the half-plane symmetry.

distributed with higher Reynolds number, hence, the velocity distribution is more balanced and its peak, the maximum velocity, is less distinct. The data for $\overline{u}_{\max}/u_b$ reported in the literature do not show a distinct trend. While the maximum velocity measured by Ng *et al.* (2018) agrees with this study, the older measurements by Yoon *et al.* (2012),Clark & Kehler (2011) and Knight & Sterling (2000) largely deviate.

The *velocity-dip* phenomenon can also be seen in figure 3.6 (left), which shows the mean velocity profiles in the symmetry plane in inner units. Please note that for this plot, the *local* wall shear stress was used, obtained by the velocity gradient at the wall, see section 3.2.2 figure 3.13. Near the wall, all profiles collapse to the linear law of the wall. For $Re_\tau \leq 140$, the profiles do not develop a logarithmic layer, whereas for $Re_\tau = 180$ and 230 a logarithmic layer can be observed, which reaches up to the *velocity-dip* but the slopes are decreasing with increasing Reynolds number. Overall, the Reynolds numbers seem to be too low to describe a clear logarithmic behaviour, like known from higher Reynolds number pipe flows (El Khoury *et al.*, 2013). However, the standard log-law $u^+ = 0.41^{-1} ln(x_3^+) + 5.2$ is approached for $Re_\tau = 460$. At this Reynolds number, a pronounced wake region develops beneath the velocity maximum. With increasing Reynolds number, the wake region becomes more distinct, which appears also in experiments and simulations of full pipe flow (Zagarola & Smits (1997) and El Khoury *et al.* (2013)), but has not been reported in experiments of semi filled pipe flow so far (Ng *et al.*, 2018).

The results of the following small paragraph have not been included in Brosda & Manhart (2022) and are first published in this thesis. In figure 3.6 (right) the distribution of the mean streamwise velocity is shown at approximately 8 wall units below and parallel to the free surface. All the velocities of the different Reynolds numbers follow the linear relation until

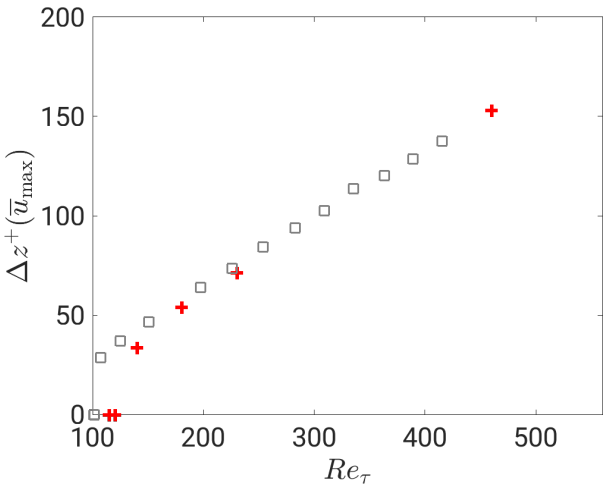

Figure 3.3: Distance $\Delta z/R$ from the free surface to the maximum mean streamwise velocity of $Re_\tau = 115, 120, 140, 180, 230, 460$ (+). □ represent data for rectangular open-duct flow from Sakai (2016).

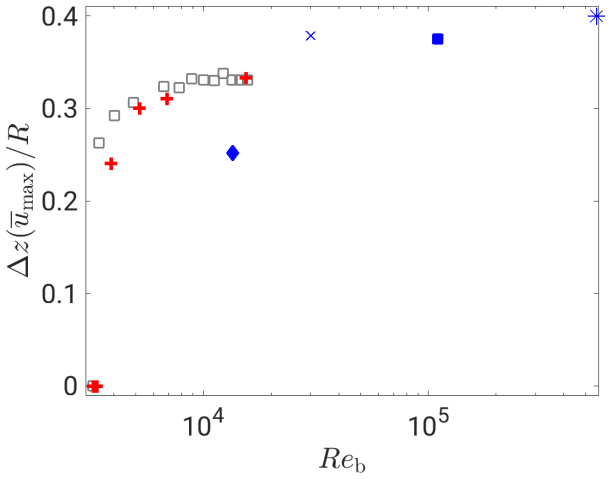

Figure 3.4: Distance $\Delta z/R$ from the free surface to the maximum mean streamwise velocity of $Re_b = 3274, 3414, 3924, 5254, 6935, 15630$ (+). □ represent data for rectangular open-duct flow from Sakai (2016). Including data from experiments: ♦ (Yoon *et al.*, 2012), × (Ng *et al.*, 2018), ∗ (Clark & Kehler, 2011) and ■ (Knight & Sterling, 2000).

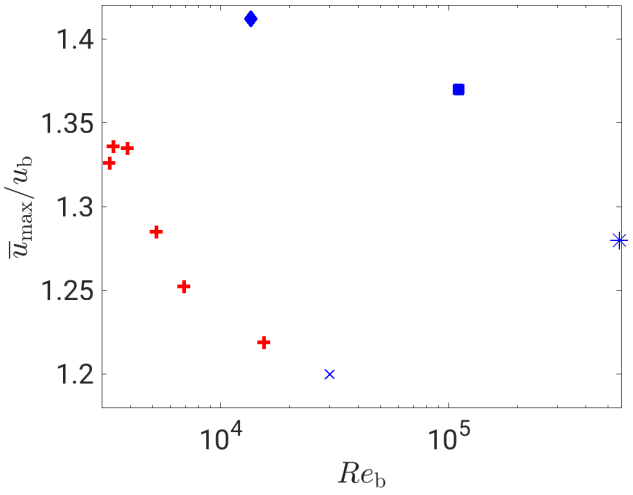

Figure 3.5: Maximum mean streamwise velocity $\overline{u}_{\max}/u_b$ of $Re_b = 3274, 3414, 3924, 5254, 6935, 15630$. Including experimental data: ♦ (Yoon *et al.*, 2012), × (Ng *et al.*, 2018), ∗ (Clark & Kehler, 2011) and ■ (Knight & Sterling, 2000).

approximately $x_2^+ = 11$, from where they start separating. Velocities of $Re_\tau \leq 140$ further increase before aligning with the logarithmic layer until the vertical bisector of the pipe. For larger Reynolds numbers the distribution is more complex. After 11 wall units, the increase of velocity becomes less strong and the velocities stay smaller until the centre is reached. For $Re_\tau = 460$, the velocity almost stagnates in the buffer layer and from approximately $x_2^+ = 70$ on the velocity increases slightly stronger again.

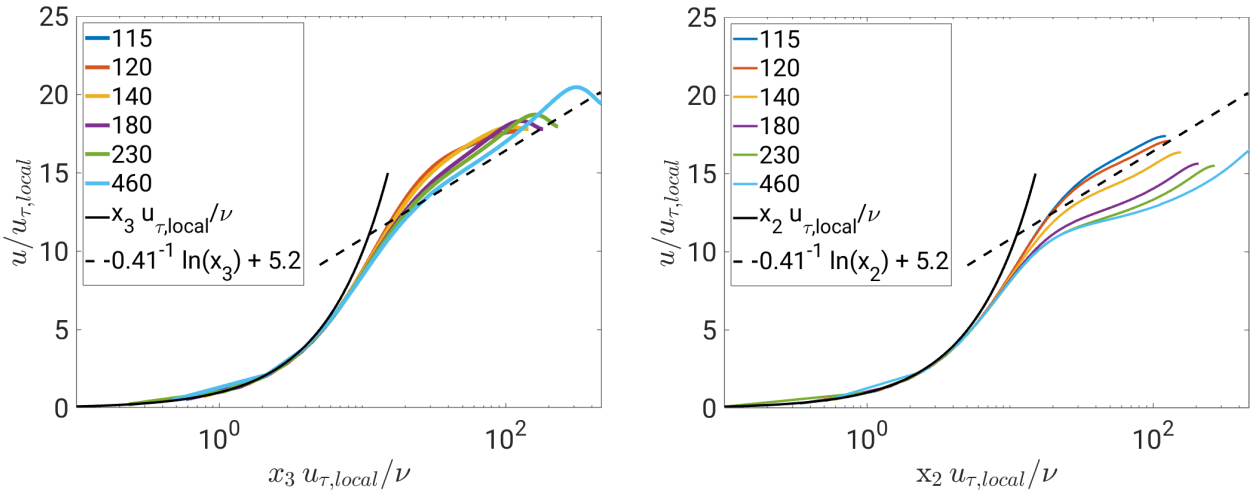

Figure 3.6: Mean streamwise velocity distribution $\overline{u}/u_{\tau,\text{local}}$ from the wall to the pipe centre at the vertical symmetry line (left) and from the wall to the pipe centre horizontally along the free surface ≈ 8 wall units below (right) of $Re_\tau = 115, 120, 140, 180, 230, 460$.

In outer units, the distribution of the mean streamwise velocity shows that the velocity gradient gets steeper close to the wall as Reynolds number increases (fig. 3.7, left). For low Reynolds numbers, u/u_b increases monotonically and reaches higher magnitudes. At high Reynolds numbers, the velocity distribution is more complex. They have a less steep gradient from a wall distance of $x_3/R = 0.1$ on and the *velocity-dip* phenomenon in the bulk region. The velocity profiles show a similar distribution as the experimental results of Ng *et al.* (2018) and Yoon *et al.* (2012). The latter, however, does not indicate an as pronounced *velocity-dip* phenomenon as the results of this study and the velocities are much higher when normalised by u_b. The velocity magnitude of the experiment by Ng *et al.* (2018) fits quite well to the present data and they also found a gradient close to zero when approaching the free surface. For the data of Yoon *et al.* (2012) this feature appears less clear. If choosing the maximum streamwise velocity u_{max} as normalisation (fig. 3.7 (right), not yet published in Brosda & Manhart (2022)), the different distributions lie on top of each other in the bulk region. Moreover, this normalisation shows more clearly that the *velocity-dip* phenomena is more distinct for the large Reynolds number simulations of this study than for the experiments. The deviations in the vicinity of the wall are similar for both normalisations.

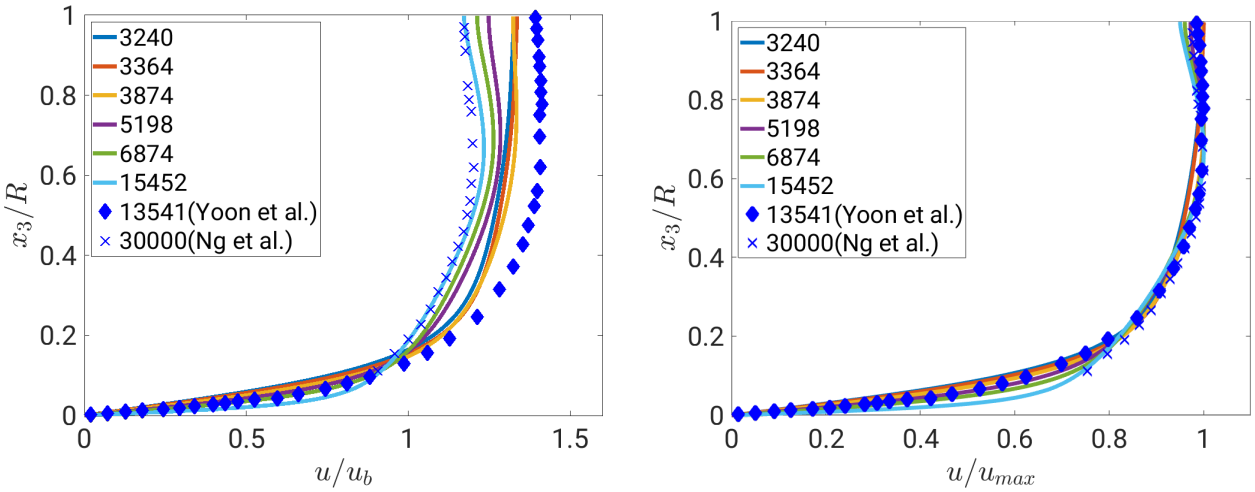

Figure 3.7: Mean streamwise velocity distribution $\overline{u}/u_b$ (left) and $\overline{u}/u_{max}$ (right) from the wall to the pipe centre at the vertical symmetry line of different Re_b (right). Including experimental data: ♦ (Yoon *et al.*, 2012), × (Ng *et al.*, 2018).

Mean Secondary Flow

The mean secondary flow is formed by the in-plane velocity components u_2 and u_3. The geometry and the position of the vortical structures generated by the secondary flow are described especially with respect to the Reynolds number dependence, and compared with known flow patterns from literature.
In order to visualize the streamlines of the mean secondary flow the stream function is evaluated for the mean in-plane velocities. The stream function ψ is two-dimensional and is defined as

$$\mathbf{u} = \nabla \times \psi, \tag{3.3}$$

which is equal to equation (3.4) for Cartesian coordinates.

$$u_2 = \frac{\partial \psi}{\partial x_3}; \qquad u_3 = -\frac{\partial \psi}{\partial x_2} \tag{3.4}$$

Along the Cartesian grid the change in ψ can be calculated by

$$\Delta\psi = u_2 \Delta x_3 - u_3 \Delta x_2. \tag{3.5}$$

Moreover, the stream function in the cross-section is directly linked to the streamwise vorticity by $\nabla^2\psi = -\omega_1 = -(\partial u_3/\partial x_2 - \partial u_2/\partial x_3)$.
Throughout two streamlines, a constant mass flux is transported. The step between two streamlines is kept constant for all stream function visualisations. Hence, more streamlines for a vortex means more mass flux by a vortex. Basically it also means, that the higher the peak value of ψ of a vortex the higher the mass flux between the wall and the vortex centre. In addition, the circulation of a vortex Γ can be described by the integrated velocity along the structure's boundary, which can be defined by an iso-contour line. Having the same velocity

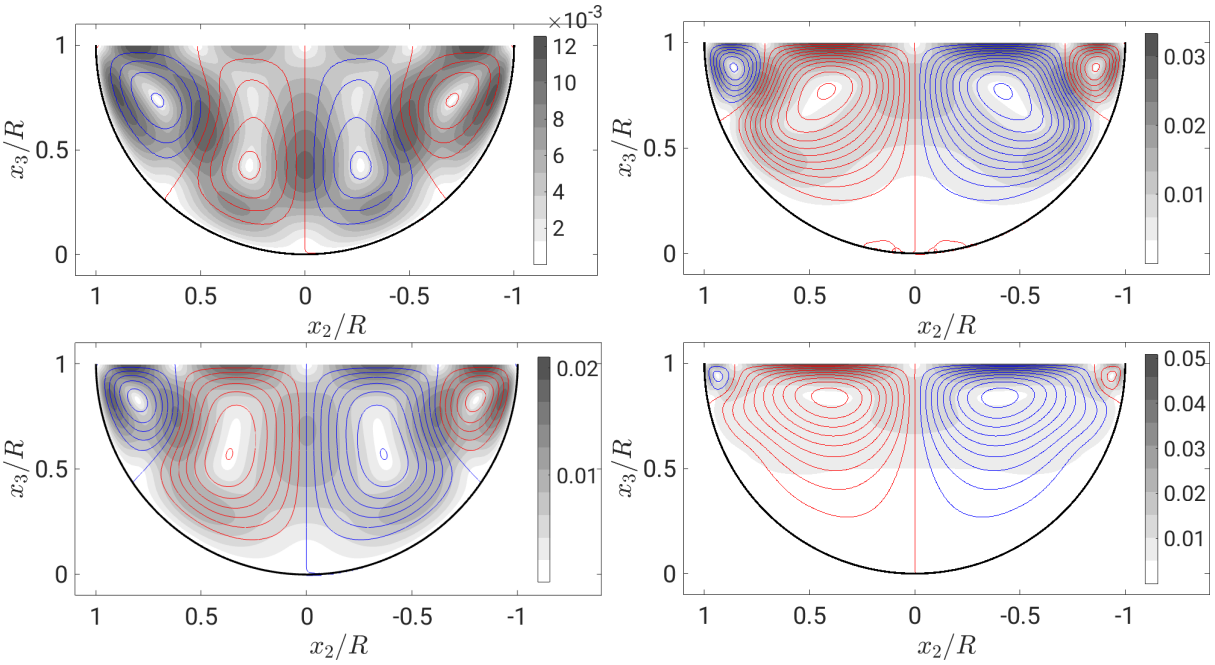

Figure 3.8: Contours of stream function ψ of mean crossflow velocities $\overline{u}_2$ and $\overline{u}_3$ and as greyscale the velocity magnitude of $\sqrt{\overline{u}_2^2 + \overline{u}_3^2}/u_b$ for $Re_\tau = 115, 140$ (left column) and $180, 460$ (right column, top to bottom). The increments for the contourlines of ψ are 0.003. For clarity, the increments of $Re_\tau = 460$ are doubled. Please note, that the distributions were symmetrized using the half-plane symmetry.

threshold limiting the boundary of a structure leads to the length of the perimeter as crucial parameter for the circulation's magnitude. Thus comparing the perimeter of streamlines gives a relative measure of the circulation. The circulation can also be expressed as the vorticity integrated over the vortex area A_S.

$$\Gamma \equiv \int_S \boldsymbol{u}(s) ds = \int_{A_S} \boldsymbol{\omega} \boldsymbol{n} dA_S \tag{3.6}$$

Looking at the distribution of streamlines of the secondary flow over the cross section, an alternating pattern of clock-wise (red) and anti-clockwise (blue) rotating vortices can be found, which are symmetrically arranged with respect to the vertical bisector, see figure 3.8. The basic pattern does not change with Reynolds number. According to Grega *et al.* (2002), the vortex in the mixed-corner is also called *inner secondary cell* and the centre vortex *outer secondary cell*. For very low Reynolds numbers, the vortices are almost equally strong and distributed over the whole circumference. The inner secondary cell gets smaller and moves towards the mixed-corner when the Reynolds number increases. In contrast, the centre vortex enlarges and is shifted towards the free surface. For higher Reynolds numbers, the outer secondary cell has a negligible effect in the bottom region of the pipe. These observations are in line with the distribution of the in-plane velocity magnitude $\sqrt{\overline{u}_2^2 + \overline{u}_3^2}/u_b$, shown as greyscale in figure 3.8. For friction Reynolds numbers smaller than 180, the in-plane velocities are active over the whole cross-section. With higher Reynolds numbers,

the activity in the bottom region becomes less and the areas with high in-plane velocities concentrate at the free surface. The maximum in-plane velocity magnitude increases with Reynolds number from 1.3% to 5.7% of u_b, see table 3.1 (note, that the grey scales in the plot do not represent the exact range). This agrees well with data found in the literature for similar geometries (Tominaga *et al.*, 1989; Sakai, 2016; Ng *et al.*, 2018; Liu *et al.*, 2022). Table 3.1 also indicates the position of the maximum secondary flow, which is always at the free surface. For $Re_\tau \leq 140$, the inner secondary cell contains the maximum at about $0.8R$. For higher Reynolds numbers, the secondary flow is stronger in the outer cell at $x_2/R \approx 0.42$, hence, the outer secondary cell obtains more energy with increasing Reynolds number.

Re_τ	$\sqrt{\overline{u}_2^2 + \overline{u}_3^2}\vert_{max}/u_b$	$\pm x_2/R$	x_3/R
115	0.0126	0.7993	1.0
120	0.0145	0.7993	1.0
140	0.0208	0.8374	1.0
180	0.0331	0.3991	1.0
230	0.0448	0.4310	1.0
460	0.0566	0.4446	0.9982

Table 3.1: Maximum magnitude of secondary flow and its position for different Reynolds numbers

The *velocity-dip* appears as soon as the outer secondary cell moves towards the free surface. For $Re_\tau = 115$, the outer secondary cell circulates more fluid in the lower half of the cross-section, whereas there is already more convection in the upper half for $Re_\tau = 140$, transporting high momentum fluid from the free surface towards the centre bottom. This can also be observed in the data of Sakai (2016).

The pattern of the mean streamwise vorticity is similar to the one of the stream function, but does not exactly reflect the mean vortex pattern, see figure 3.9. As it is the Laplacian of the stream function, the vorticity describes a smaller structure than the stream function. This is especially visible for the shear layers at the wall. As the Reynolds number increases, the vorticity maxima are even further shifted towards the free surface than the vortex centres deduced from the streamlines. Similar to the stream function, the mean streamwise vorticity is almost zero in the bottom region for higher Reynolds numbers, hence, the influence of the mean secondary flow is very small in the lower part of a semi filled pipe.

The distance of the vortex centres to the free surface (red) and the mixed-corner (blue) are shown in outer units over the bulk Reynolds number in figure 3.10 (left). In general, for both vortices, the distances to the free surface and the mixed-corner decrease with increasing Reynolds numbers. However, for the outer secondary cell the distance to the mixed-corner is approximately constant at $\Delta s/R \approx 0.6$ for the higher Reynolds numbers, whereas the other distances are further decreasing. In wall units, the outer secondary cell (+) does not scale, whereas both distances of the inner secondary cell (∘) scale well (figure 3.10, right) especially at higher Reynolds numbers. Its distances range from 20 to 50 wall units. This is in agreement with the findings of Sakai (2016) for rectangular open-channel flow in a similar range of Reynolds numbers. If the inner vortex continues to scale with inner units at

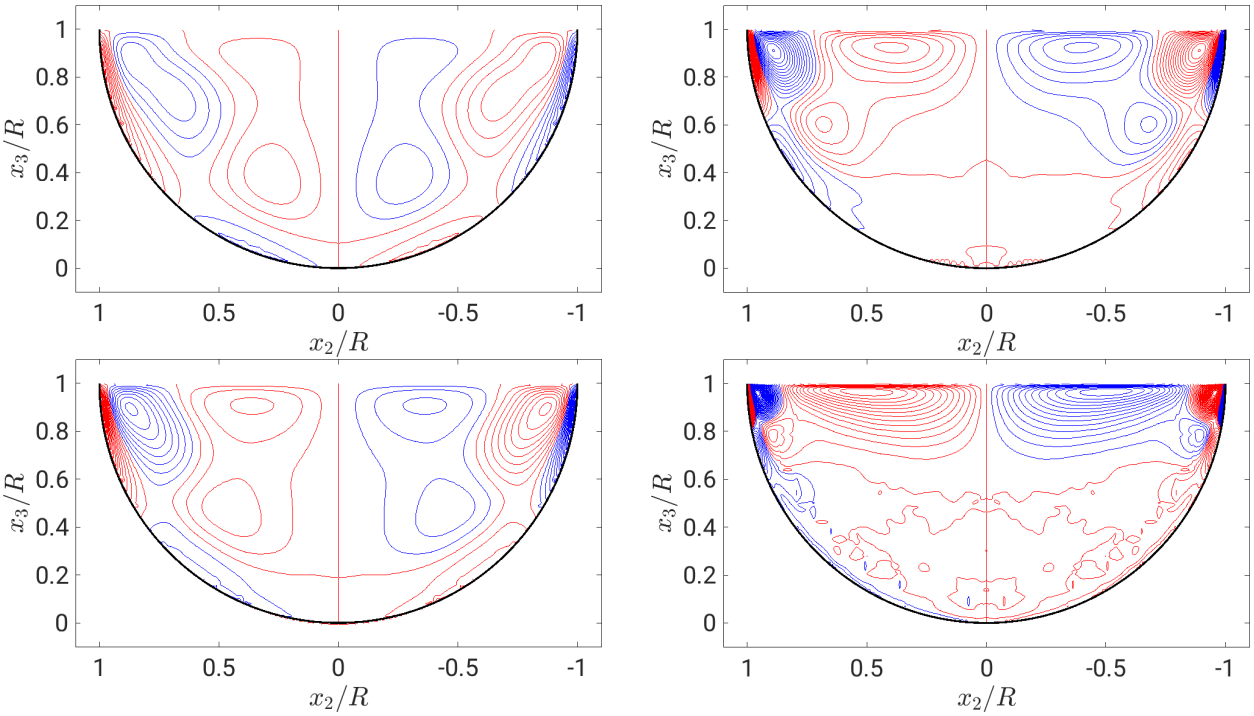

Figure 3.9: Mean streamwise vorticity $\overline{\omega}_1 \cdot R/u_b$ of $Re_\tau = 115, 140$ (left column) and $180, 460$ (right column, top to bottom). The increments for the contourlines of $\overline{\omega}_1 R/u_b$ are 0.04. Please note, that the distributions were symmetrized using the half-plane symmetry.

higher Reynolds numbers one can expect that the inner secondary cell becomes very small compared to the radius of the pipe. Consequently, it would be more and more difficult to detect it by measurements with limited spatial resolution. This could explain why previous measurements in partially filled pipe flow only reported the outer secondary vortex (Clark & Kehler, 2011; Ng *et al.*, 2018). Unfortunately, no detailed visualisation of the mixed-corner flow is provided by Liu *et al.* (2022). Hence, it is unclear whether they observed the inner secondary vortex. However, the outer secondary vortex is in good agreement for all publications.

The results of the following paragraph have been published in Brosda & Manhart (2022) apart from the parameter circulation Γ. This parameter was first included in this thesis. As a measure for the strength of the secondary vortices, the peak values of the stream function in the inner and outer secondary cells are documented in figure 3.11 in red and the magnitudes of the circulation in blue, defined by equation (3.6). At the lowest two Reynolds numbers, both vortices exhibit the same amount of volume flux between the free surface and the vortex centre. At higher Re_τ, the peak of the stream function reaches larger values in the outer vortex than in the inner vortex. While the stream function seems to saturate for larger Reynolds numbers in the outer vortex, it appears to attain its maximum at between $Re_\tau = 230$ and 460 in the inner vortex. Both circulation and stream function peaks agree very well, only the circulation peak of $Re_\tau = 460$ shows instead of a slight decrease a small increase, however, it still seems to indicate a beginning saturation for larger Reynolds numbers in this study.

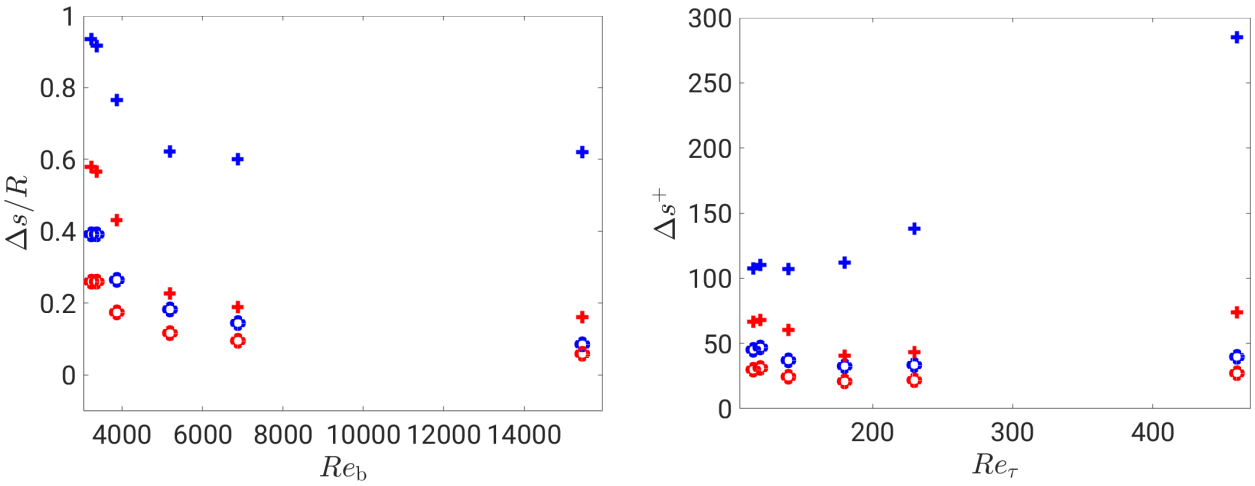

Figure 3.10: Normalised distance Δs from the mixed-corner (blue) and free surface (red) to the minimum and maximum of the stream function ψ in outer (left) and inner units (right) over Re_b and Re_τ, respectively. $\circ$ corresponds to the inner secondary vortex and $+$ to the outer secondary vortex.

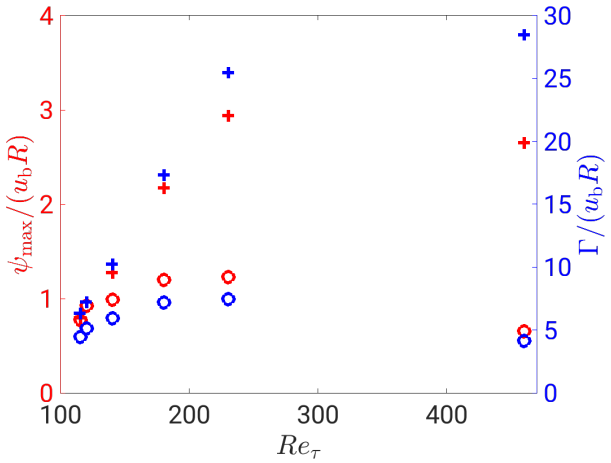

Figure 3.11: Normalised peak values of the stream function $\psi/(u_\tau R)$ (red) and circulation $\Gamma/(u_b R)$ (blue) of the inner ($\circ$) and the outer secondary cell ($+$) of $Re_\tau = 115, 120, 140, 180, 230, 460$.

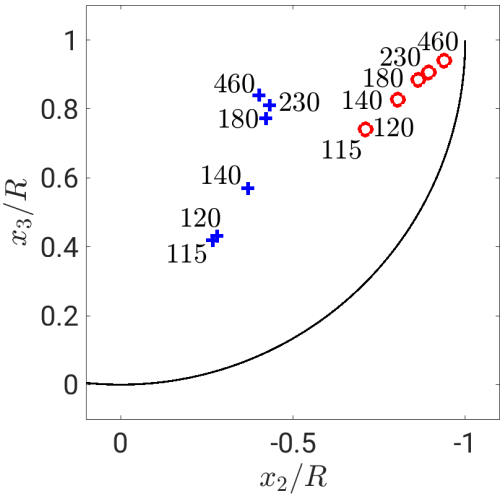

Figure 3.12: Positions of the inner and outer secondary cell centres for $Re_\tau = 115, 120, 140, 180, 230, 460$. Cell centres are defined as local minima and maxima of the stream function ψ. $\circ$ corresponds to the inner secondary vortex and $+$ to the outer secondary vortex.

The Reynolds dependency of the positions of the inner and outer secondary cells within the cross-section is shown in figure 3.12 by the locations of the vortex centres in one half of the duct. The vortex centres are defined as minima and maxima of the stream function, thus, in agreement to the stream function distribution (cf. figure 3.8) the vortex centres move upwards as Reynolds number increases. The inner secondary cell does always cover the position in the mixed-corner and with decreasing size it further moves into the mixed-corner. For small Reynolds numbers, the outer vortex centre is located close to the bottom and its circulation is similar to the one of the inner vortex. For moderate Reynolds numbers, its position and the covered area changes quickly. As the inner vortex becomes smaller, the size of the outer secondary cell becomes larger and moves to the centre. While the vorticity of the inner vortex strongly increases with Reynolds number (figure 3.9), its peak stream function remains bounded (figure 3.11). The peak values of the stream function in the outer cell grow stronger with Reynolds numbers than the one of the inner cell, whereas its vorticity only moderately increases. For higher Re_τ, the position and the intensity of the outer secondary cell seems to stabilise, whereas the intensity of the inner secondary cell even decreases. Apparently, with increasing Reynolds number, the outer secondary cell becomes more and more the dominating vortex. A similar observation has been made by Pirozzoli *et al.* (2018) for the case of a closed square duct. They observe a corner-circulation with inner scaling and a core-circulation scaling with the duct half height, the latter becomes more and more dominant with increasing Reynolds number.

3.2.2. Wall Shear Stress

The local wall shear stress τ_w is an important parameter in terms of sedimentation and resuspension in sewage pipes. Its distribution over the perimeter can be seen as footprint of the secondary flow. The wall shear stress is obtained by near wall velocity gradients, see section 2.2. In figure 3.13 (left), the distribution of the time-averaged wall shear stress τ_w/τ_0 around the wetted perimeter is shown for various Reynolds numbers, τ_0 being the perimeter- and time-averaged wall shear stress. The maxima can be found at the mixed-corners independent of the Reynolds number. A local minimum can be found at $\pm\pi/4$ for the lower Reynolds numbers and moves towards the mixed-corners with increasing Reynolds number. At small Reynolds numbers ($Re \leq 140$), the distribution is nearly harmonic with a clear local maximum in the symmetry plane of the pipe. This local peak flattens and its magnitude decreases towards $\tau_\mathrm{w} \approx \tau_0$ when the Reynolds number is increased. Eventually, secondary local maxima form between the flat region and the minima. For small Reynolds numbers, the maxima in the corners and in the symmetry plane have approximately the same magnitude. For increasing Reynolds numbers, the difference between maxima and minima becomes larger, while in the symmetry plane, the wall shear stress tends to be $\tau_\mathrm{w} \approx \tau_0$, reflecting the low activity of the secondary flow in the lower part of the pipe, cf. figure 3.8. The wall shear stress distribution can be directly linked to the secondary flow. In regions with a secondary flow pointing towards the wall, τ_w is high and when the secondary flow is directed away from the wall τ_w is small.
In figure 3.13 (right), the current results are compared with the high Reynolds number experiments of Knight & Sterling (2000) ($Re_b = 110,000$) and Clark & Kehler (2011) ($Re_b = 557,000$, only data for one side available). They both match each other fairly

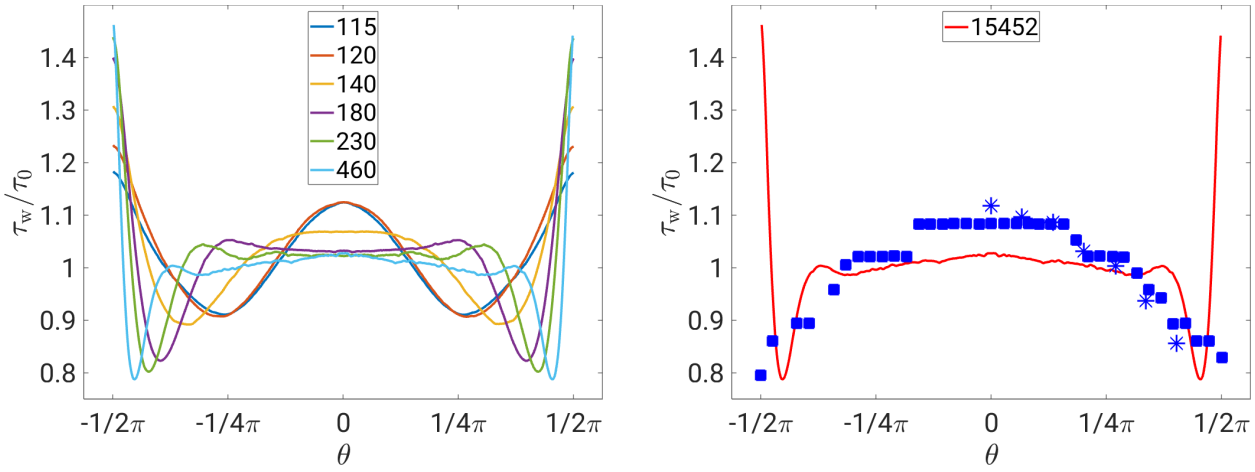

Figure 3.13: Normalised mean wall shear stress τ_w/τ_0 of $Re_\tau = 115, 120, 140, 180, 230, 460$ (left). Normalised mean wall shear stress τ_w/τ_0 of $Re_b = 15452$ and including experimental data: $*$ (Clark & Kehler, 2011) ($Re_b = 557000$) and ■ (Knight & Sterling, 2000) ($Re_b = 110000$) (right). Please note, that the distributions of the present data were symmetrized using the half-plane symmetry.

well, but as they could not detect the inner secondary cell within their measurements, they also do not show a global wall shear stress maximum at the mixed-corner. Instead, they found the global minimum at the mixed-corner and the global maximum at the centre bottom.

The results of the following small paragraph have not been published in Brosda & Manhart (2022) and are first published in this thesis. In order to get a first impression of the instantaneous wall shear stress, its local values along the perimeter were obtained from velocities interpolated to a wall distance of $\Delta r^+ = 2$. The probability density functions (PDF) of the instantaneous wall shear stress are presented for different positions in figure 3.14: close to the mixed-corner (left); at the minimum value of the time-averaged τ_w (middle); and where the plateau-like region starts (right) for $Re_\tau = 180$. It can be seen that in the mixed-corner a wide range of wall shear stresses are equally likely to occur and even values larger than

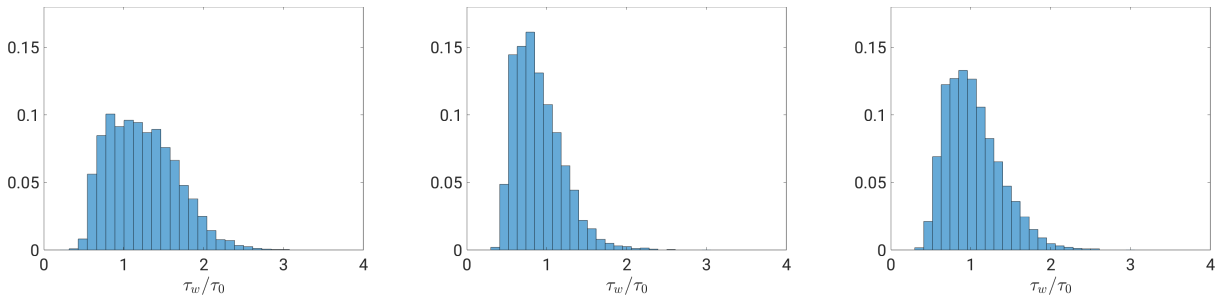

Figure 3.14: PDF of the instantaneous wall shear stress for $Re_\tau = 180$ at the positions $-1.514 \approx 0.48\pi, -1.359 \approx 0.43\pi$ and $-1/4\pi$ (from left to right).

$2\tau_w/\tau_0$ have a probability greater than 1%. Values below 1 are more unlikely in the mixed-corner than at the position of minimum wall shear stress. The PDF at the position of the minimum wall shear stress seems to be more confined to values around $\tau_w/\tau_0 = 0.85$ as the standard deviation is only $\sigma = 0.30$ in comparison to $\sigma = 0.42$ for the position at the mixed-corner. When the plateau-like region is reached, the mean of the distribution is equal to one τ_w/τ_0 and the PDF has a slightly larger standard deviation ($\sigma = 0.34$) than the PDF at the minimum. Overall, strong wall shear stress events ($\tau_w > \tau_0$) are likely to appear almost all over the perimeter.

In addition, the root-mean-squares (rms), skewness and flatness of the wall shear stress fluctuations are plotted along the perimeter in figure 3.15, enabling a quantitative assessment of the wall shear stress fluctuations. In general, the distribution of the rms resembles the mean wall shear stress distribution with its maxima at the mixed-corners, followed by a minimum and a plateau in the centre. Hence, the largest fluctuations in wall shear stress occur in the mixed-corner. With increasing Reynolds number the local minimum moves towards the mixed-corner as it was observed for the mean wall shear stress. The rms-level in the centre increases with Reynolds number and nearly reaches $\tau_{w,rms}/\tau_0 \approx 0.4$, a value that was observed in channel and pipe flows at high Reynolds numbers (Alfredsson *et al.*, 1988; El Khoury *et al.*, 2013). The local fluctuations in the mixed-corners are about $1.2-1.7$ times stronger than in the centre of the perimeter. Moreover, they reach approximately the value by which the time-averaged wall shear stress exceeds the perimeter-averaged one. The skewness and the flatness have similar distributions. Close to the mixed-corner a minimum occurs, where the distributions are closest to a Gaussian distribution (S = 0; F = 3). The minimum is followed by a maximum and in the centre of the perimeter a plateau establishes, which increases with increasing Reynolds number. At the plateau, the skewness approaches a value of $S(\tau_\mathrm{w}) \approx 0.9-1.1$ and the flatness a value of $F(\tau_\mathrm{w}) \approx 4-5$, which resembles the values reported for a channel flow of $Re_\tau = 180$ by Kim *et al.* (1987).

In the mixed-corner, the secondary flow points towards the pipe's wall transporting high momentum fluid to the wall and generating the large wall shear stress values in the mixed-corner. The first wall shear stress minimum is found close to the location where the secondary flow separates from the perimeter and marks the end of the inner vortex. This is demonstrated in figure 3.16 in which both locations are plotted in dependence of the Reynolds number.

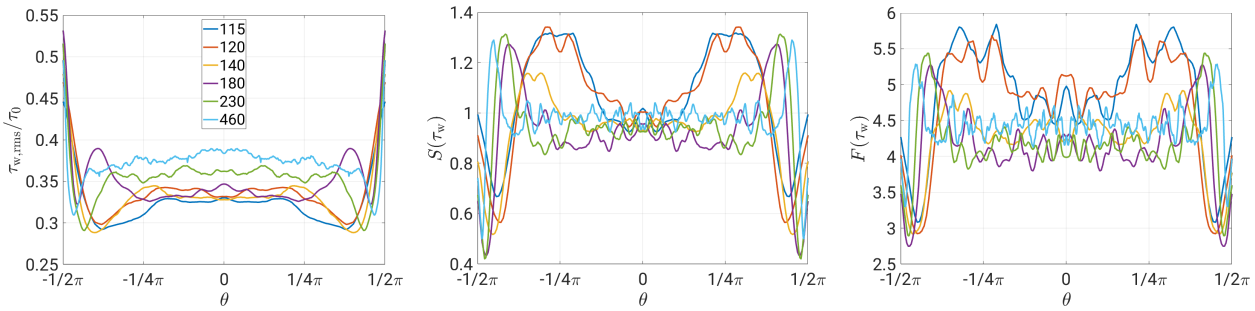

Figure 3.15: Normalised root-mean-square of wall shear stress fluctuations $\tau_{\mathrm{w,rms}}/\tau_0$ (left), skewness (middle) and flatness (right) of the wall shear stress fluctuations over the perimeter for $Re_\tau = 115, 120, 140, 180, 230, 460$. Please note, that the distributions were symmetrized using the half-plane symmetry.

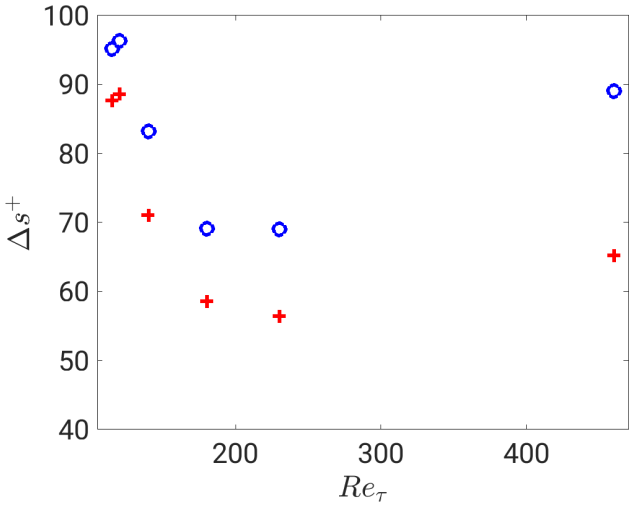

Figure 3.16: Azimuthal distance in wall units Δs^+ from mixed-corner to first minimum of wall shear stress (+) and to the separation point of the secondary flow (∘) for $Re_\tau = 115, 120, 140, 180, 230, 460$.

At the lower Reynolds number, the separation point is about ten wall units further away from the mixed-corner than the wall shear stress minimum. The distance from the mixed-corner to the first wall shear stress minimum and the separation point has its minimum at $Re \approx 230$. At $Re_\tau = 460$ the distance to both points increases and reaches approximately 90 and 65 wall units, respectively. More data at higher Reynolds numbers would be necessary to elucidate a scaling here. In comparison to a flow in a rectangular cross-section, the location of the wall shear stress minimum is in agreement for low Reynolds numbers with the results from Pinelli *et al.* (2010) and Sakai (2016) (cf. section 1.3 (*Primary Flows in Open Channels*)).

The combination of the wall shear stress maximum, minimum and the inner secondary flow resembles the near-wall turbulence concept of high and low velocity streaks and the quasi-streamwise vortices. In canonical pipe flow, the wall shear stress fluctuations are linked to the appearance of streaks in instantaneous near-wall streamwise velocities, which are plotted in figure 3.17 at a constant distance from the wall of 10 wall units. An alternating pattern of low- and high-speed streaks can be detected independently of Re. In outer units, individual streaks become smaller with increasing Reynolds number, as they scale with inner units, having an average spacing of 100 wall untis in channel flow (Kim *et al.*, 1987). This streak spacing would give rise to about 3.5 high-speed streaks fitting in the perimeter at $Re_\tau = 115$ and to 14.5 streaks at $Re_\tau = 460$. The instantaneous velocity distributions do not contradict such a spacing. The wall shear stress peak in the mixed-corners, i.e. at $\pm\frac{1}{2}\pi$, can hardly be seen as increased levels in the instantaneous velocity distribution. There are strong fluctuations of the streamwise velocity at $10\delta_\nu$ wall distance which do not seem to differ in the mixed-corners from the centre of the channel.

The observation that the time-averaged wall shear stress distribution is not visible in instantaneous velocity distributions is supported by figure 3.18 in which cross-sectional distributions of the instantaneous streamwise velocity are plotted. The uplift of low-speed fluid from the wall can be clearly seen at several spots along the circumference. With increasing

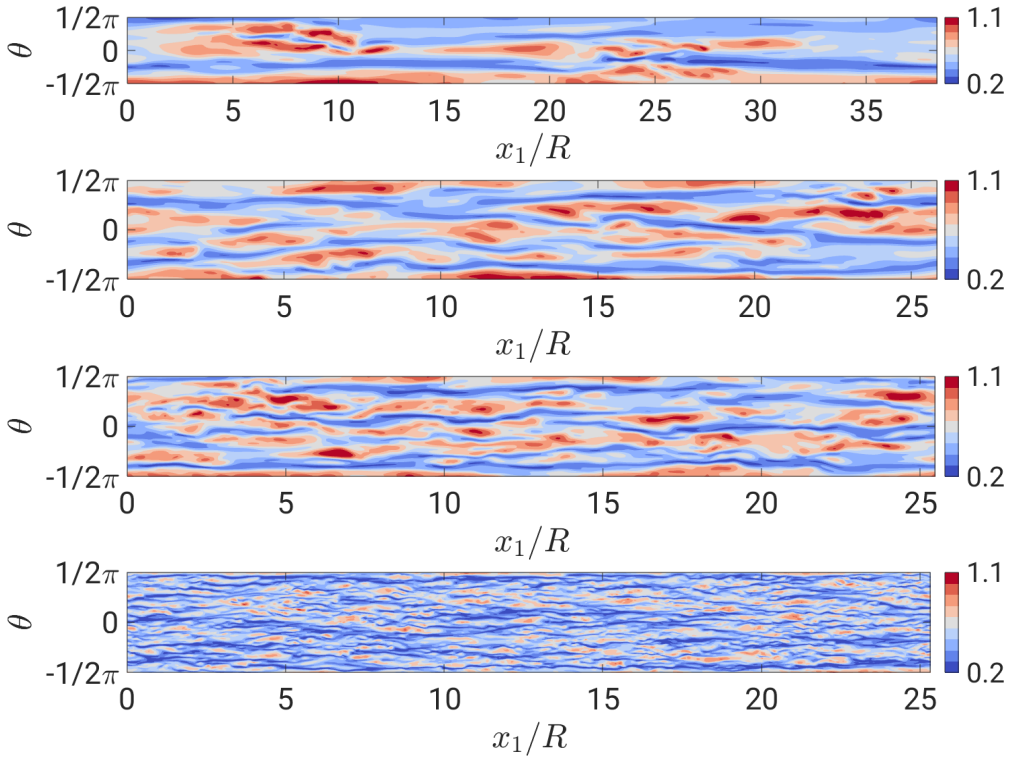

Figure 3.17: Instantaneous normalised streamwise velocity u_1/u_b at a constant distance of 10 wall units from the wall over the channel length for $Re_\tau = 115, 140, 180, 460$ (top to bottom).

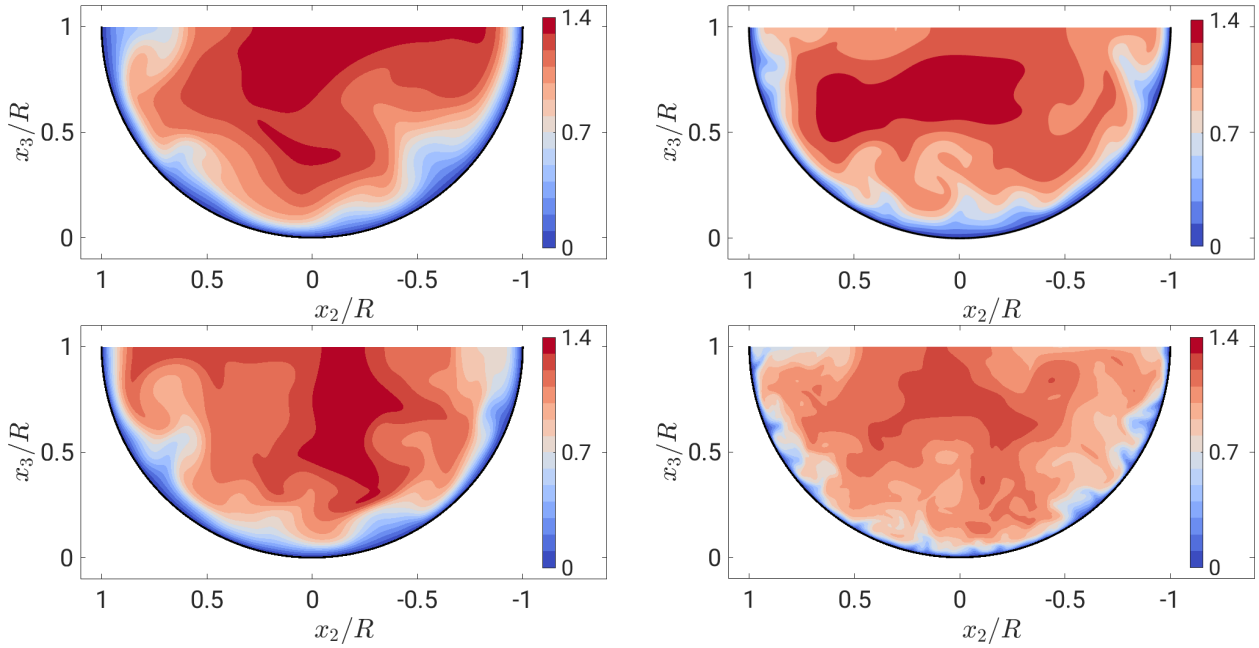

Figure 3.18: Instantaneous, cross-sectional slice of normalised streamwise velocity u_1/u_b for $Re_\tau = 115, 140$ (left column) and $180, 460$ (right column, top to bottom).

Reynolds number, more and smaller uplift events can be seen, as expected. There is no specific structure visible in the mixed-corners. However, for the higher Reynolds numbers, the *velocity-dip* is clearly visible.

In order to evaluate the characteristics of the wall shear stress distribution, running averages of the wall shear stress were computed at a fixed streamwise position using an averaging time of one flow-through time L/u_b. These are plotted for $40 \cdot L/u_b$ (figure 3.19). In this representation, the short-time fluctuations which obscured the long-term variations of the wall shear stress are not visible. It becomes obvious that the running averages reveal large wall shear stresses in the mixed-corners for most of the time. In addition to these wall shear stress maxima in the mixed-corners, local minima occur next to them. The variations in the centre appear more randomly and only few extreme values occur. In a similar manner, Pinelli *et al.* (2010) investigated the velocity streak behaviour for the solid corner in a rectangular closed-duct with a local wall shear stress minimum appearing in the vicinity of the solid corner. The Reynolds dependency of their velocity streaks is analogous to the one of the present study, with the only difference that in the current case the fixed peak is not in the solid corner, but at the free surface. Overall, the evaluation of the wall shear stress and near wall velocity streaks suggests that the mixed-corner vortex is not a stable vortex – in the sense that it rotates constantly in the same direction – but results from an averaging of many individual uplift and downwash events which are present in wall-bounded turbulence. However, figure 3.17 indicates that the structures contributing to the inner secondary cell are rather long structures of up to approximately $10\,R$. This is in good agreement with the findings of Sakai (2016), who did a statistical analysis on the probability of vortex positions in rectangular open-channel flow. He showed that in the mixed-corner mostly vortices are present that rotate towards the wall at the free surface, which would generate a similar wall shear stress pattern like the running averaged wall shear stress distribution in figure 3.19.

The results of the following paragraph have not been included in Brosda & Manhart (2022) and are first published in this thesis. To assess whether the wall shear stress near the left and right mixed-corner are correlated, the joint probability density function is displayed in figure 3.20. It shows that there is hardly any correlation between the left and right instantaneous wall shear stresses. Combinations of low and high magnitudes are equally likely to occur, implying that wall shear stress events on the left and right mixed-corner are independent of each other.

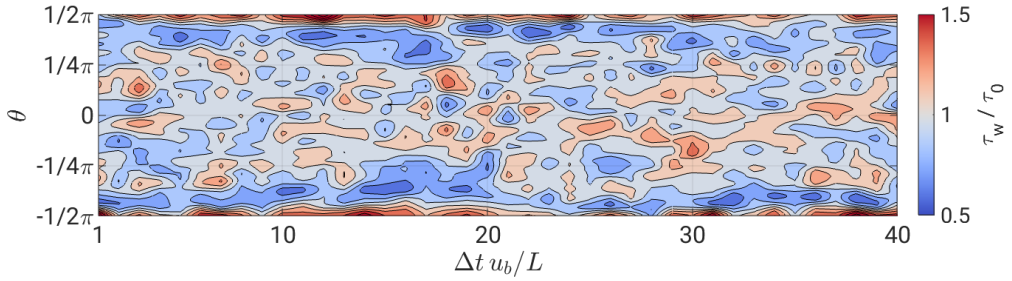

Figure 3.19: Temporal distribution of the normalised, short-time averaged, mean wall shear stress τ_w/τ_0 over the perimeter for $Re_\tau = 180$. One time instant equals to the averaged τ_w over a period of L/u_b. The total time interval is 40 L/u_b.

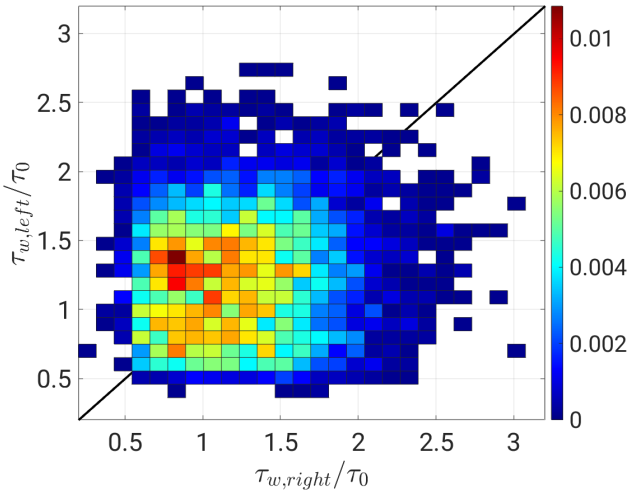

Figure 3.20: Normalised joint PDF of τ_w/τ_0 taken from the vicinity of the left and right wall for $Re_\tau = 180$.

It seems that low- and high-speed streaks appear for all Reynolds numbers. These structures can be associated to quasi-streamwise vortices and they scale in inner units, i.e. with a streak spacing of around 100 wall units. In the low Reynolds number cases ($Re_\tau \leq 140$), they fill the whole cross-section and their movement is restricted. It seems that in this range, only four streaks fit into the semi filled pipe. This leads to a preferential position of the streamwise vortices which can explain the mean secondary flow cells and the harmonic distribution of the mean wall shear stress. At higher Reynolds numbers ($Re_\tau \geq 180$), the time-averaged secondary cells seem to be lifted from the lower part of the semi filled pipe towards the free surface (see figure 3.8). This might be a result of a larger variability of the streaks in circumferential direction which leads to averaging effects of the low- and high-speed zones in a statistical sense. This can explain the plateau in the wall shear stress. Similar observations for a comparable range of Reynolds numbers were made by Pinelli *et al.* (2010) for a rectangular closed-duct flow. In the mixed-corners, there is always a low- or a high-speed streak, since, at the free surface, the in-plane velocity vector always points towards or away from the corner for kinematical reasons, thus fixing the streak there. From figure 3.19, it can be inferred that high-speed fluid is transported towards the corners, thus, the secondary flow preferentially points towards the mixed-corners.

The results of the following paragraphs in this section have not been published in Brosda & Manhart (2022) and are first published in this thesis. The following analysis was inspired from Pinelli *et al.* (2010), who investigated turbulent flows of low Reynolds numbers in a closed square duct. Samples of the wall shear stress were taken every 10 viscous time units with sampling points along the perimeter with approximately two wall units apart from each other at one fixed streamwise position.

Figure 3.21 shows the temporal development of the global minima of the wall shear stress. For all Reynolds numbers, two pronounced clusters of wall shear stress minima can be detected that form roughly a line, however, with increasing Reynolds number, the temporal distribution of minima get less coherent. At $Re_\tau = 115$, the branches of the minima meander in separate sides of the pipe and it seems that one can follow the two separated minima in

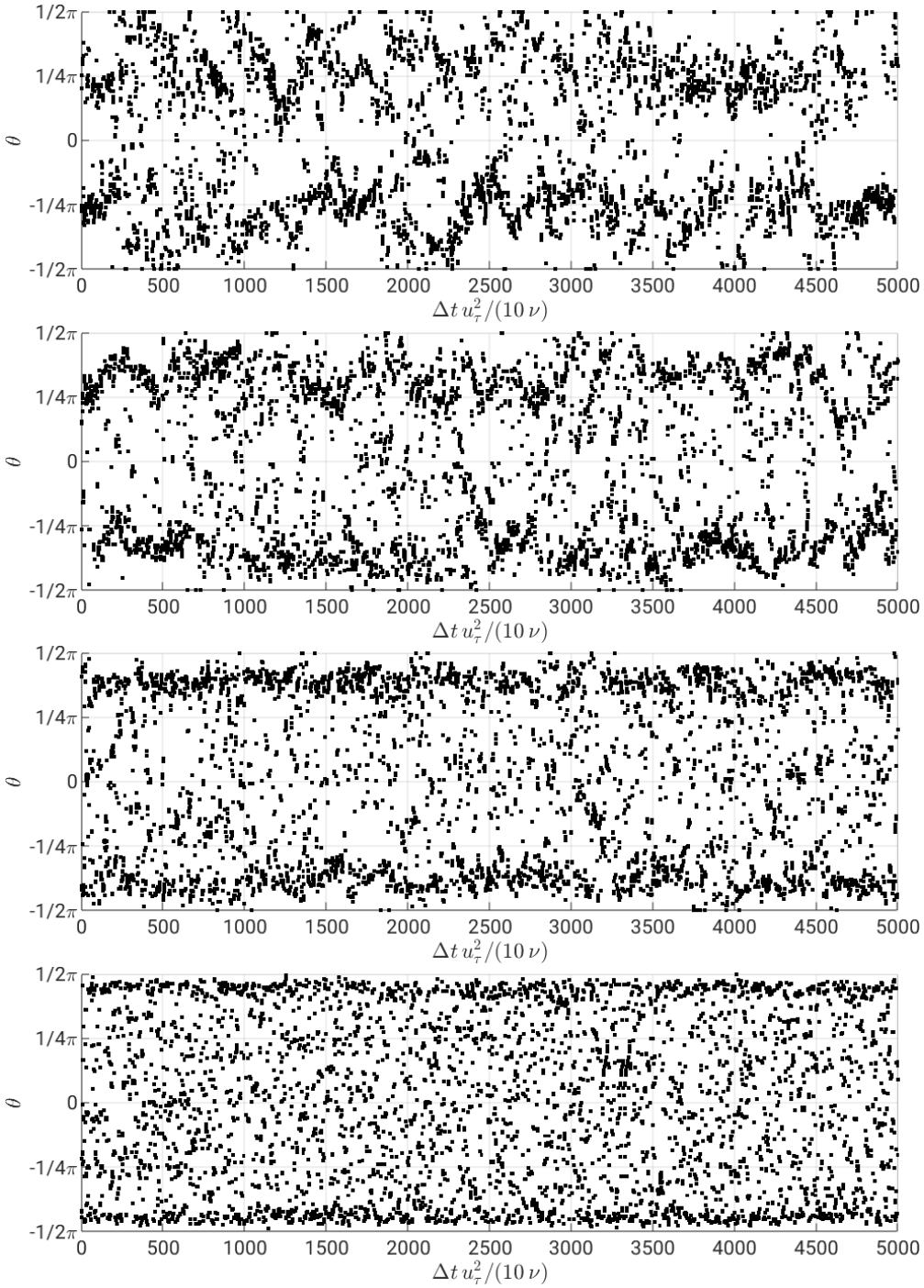

Figure 3.21: Development over time of the position of the instantaneous global minimum value of wall shear stress for $Re_\tau = 115, 140, 180$, and 460 (top to bottom).

time. For larger Reynolds numbers, also two pronounced lines can be identified. Their spatial variations decrease as Reynolds number increases, but the number of minima not directly related to these two lines increase and mostly appear in between the two lines, rarely at the mixed-corner. For $Re_\tau = 460$, the distribution is almost homogeneous apart from a layer with only few minima directly in the mixed-corner and a following region with stronger accumulation of minima right next to it. This behaviour is consistent to the Reynolds-number dependent distribution of the mean wall shear stress.

These positions of the wall shear stress minima are plotted as PDF in figure 3.22(left), and the general pattern of the negative part of the mean wall shear stress becomes apparent. With increasing Reynolds number, the high minimum τ_w probabilities shift from $\pm 1/4\pi$ towards the mixed-corner and they become higher and more concentrated. In the centre of the perimeter the probability of a minimum slightly increases for higher Reynolds numbers. The PDF of the maxima of the wall shear stress (fig. 3.22, right) shows that the maximum is located most likely directly at the mixed-corner and only single events are found in the rest of the perimeter. It is striking that the distribution of the maxima reveals two distinct peaks at the mixed-corner with a strong decrease towards the centre of the pipe. This indicates that the maxima are much more persistent for all Reynolds numbers, thus, a high-speed streak is most of the time present in the mixed-corner, but the following low speed streak varies.

Thus far, only the dominating component – the streamwise component – of the wall shear stress was studied, however, for the secondary flow, the in-plane components also play an important role, as they are the direct footprint of the secondary flow at the wall. As the distribution of wall shear stress is along the perimeter, the Cartesian in-plane components are transformed into polar coordinates applying the transformation in appendix A. Hence, an azimuthal wall shear stress component $\tau_{w,\theta} = \mu \frac{\Delta u_\theta}{\Delta x_r}$ can be defined. Moreover, the near-wall pressure p_w can be interpreted as normal stress in the wall normal direction. The inner secondary cells in the mixed-corners are the strongest secondary flow close to the wall, which is present in the mean distribution of the azimuthal wall shear stress and the pressure, see figure 3.23. $\tau_{w,\theta}$ has a magnitude up to 9% and p_w up to 44% of the globally averaged wall shear stress τ_0. In the bottom of the cross-section, from $-\pi/4$ to $\pi/4$ magnitudes around zero

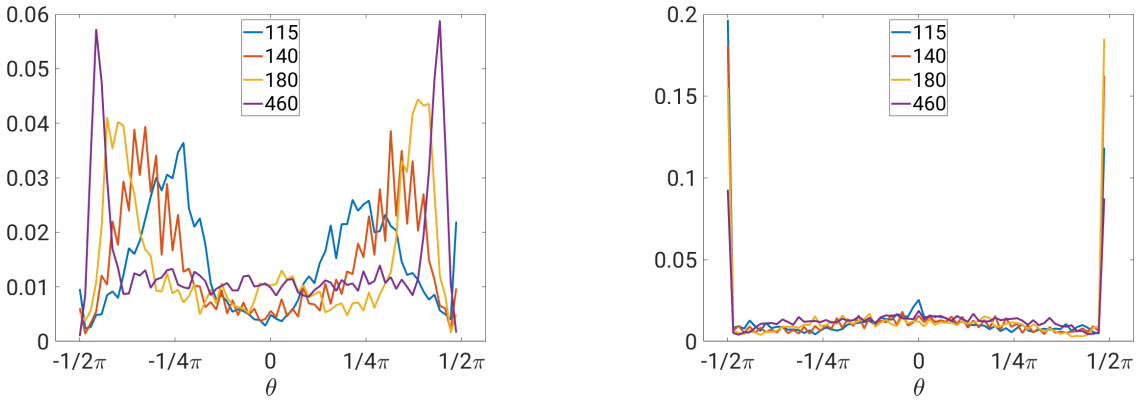

Figure 3.22: Probability density function of the instantaneous position of the global minimum (left) and maximum (right) value of wall shear stress for $Re_\tau = 115, 140, 180$, and 460.

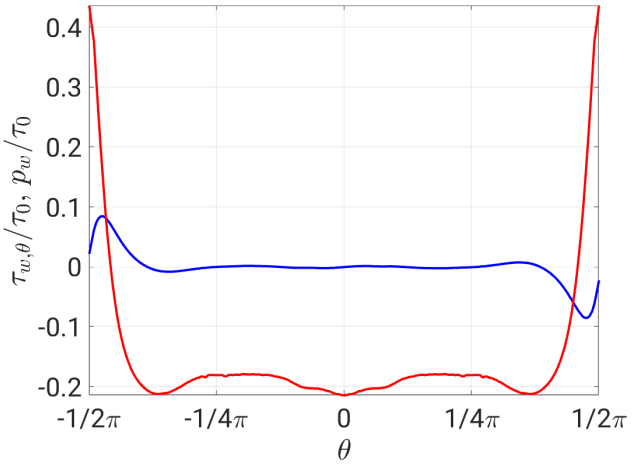

Figure 3.23: Azimuthal component of the normalised mean wall shear stress $\tau_{w,\theta}/\tau_0$ (blue) and the normalised normal stress at the wall p_w/τ_0 (red), respectively, for $Re_\tau = 180$. Please note, that the distributions were symmetrized using the half-plane symmetry.

occur for the azimuthal component. The peak of the azimuthal wall shear stress is about 15 wall units away from the mixed-corner, where the secondary flow is strongest coming from the free-surface and decreases as the wall friction decelerates the secondary flow. p_w is in line with the azimuthal wall shear stress component and the secondary flow. It has its maximum at the mixed-corner, where secondary flow is directed towards the wall. From the mixed-corner on, the magnitude decreases strongly until a local minimum is reached at about 75 wall units from the wall, where the separation point of the secondary flow is located. Next to the local minimum the pressure slightly increases before the magnitude decreases in the symmetry plane again to the same value as the other local minimum.
In figure 3.24, the PDF of the positions of the maxima (dashed line) and minima (solid line) with a bin size of four wall units are shown for $\tau_{w,\theta}$ (left) and p_w (right). The azimuthal component has the highest peaks in the mixed-corner, where a maximum means flow in positive azimuthal direction and a minimum denotes a flow in negative azimuthal direction. The mixed-corner peak overlaps with a small peak of the opposite direction, and agrees with the distribution of the streamwise component, when keeping in mind the connection between velocity streaks and quasi-streamwise vortices. In addition, there is another wide, local peak in the bottom between $-1/4\pi$ and $1/4\pi$, where many maxima and minima of the azimuthal component appear. Apparently, this accumulation of peaks is not present in the mean wall shear stress distribution of the azimuthal component, hence, the flow is very active in the bottom part of the pipe, but the various peaks must balance each other over time. At about $\pm 1/4\pi$, almost no minima nor maxima occur. This separates surprisingly strictly the upper flow, where secondary flow is present, from the lower, bottom flow. Apart from the mixed-corner, the two distributions of minima and maxima of the pressure are very similar to each other. An almost constant amount of maxima and minima is present over the perimeter with a hardly detectable peak at the very bottom. Compared to the mean distribution these peaks seem to balance each other, thus, the peaks do not have a strong influence on the mean distribution. In the mixed-corner the minima occur less, however, about 8 times more maxima appear, which is in line with the global maximum in the mixed-corner of the mean

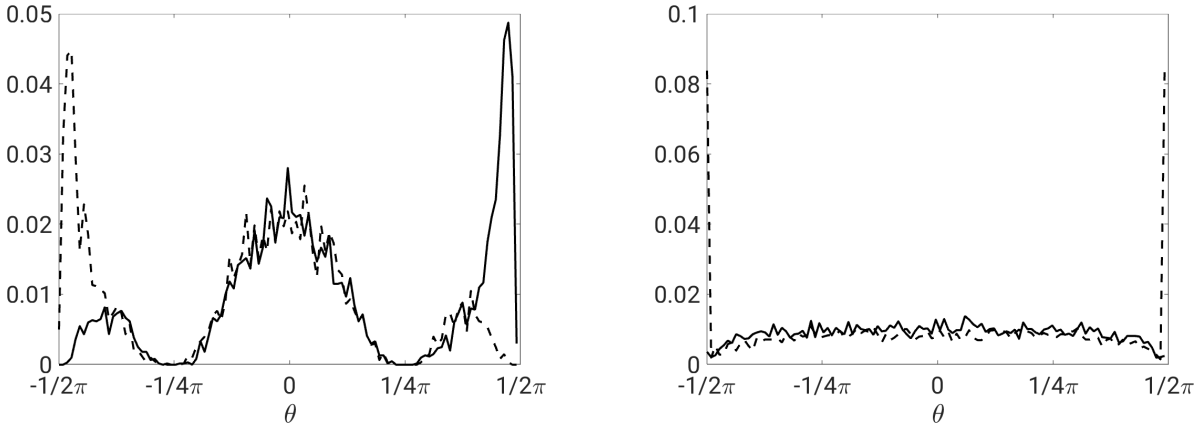

Figure 3.24: Probability density function of the instantaneous position of the global maximum (dashed line) and minimum (solid line) value of the azimuthal wall shear stress component (left) and the pressure at the wall (right) for $Re_\tau = 180$.

pressure distribution.

3.2.3. Reynolds Stresses

In this section, the spatial distribution of the Reynolds stresses is investigated. The Reynolds number dependence of the Reynolds stress profiles in the symmetry plane (figure 3.25) is shown first. For the normal stresses, the rms of the velocity fluctuations is plotted. Between their maxima and the wall, all profiles share a high degree of similarity with those found in full pipe flow, which are shown from the wall until the pipe's centre. The streamwise normal stresses $\overline{u_1'^2}$ are largest and peak at around $x_3^+ \approx 15$. The peak position is rather independent of the Reynolds number while its magnitude slightly increases. Similarly to observations of El Khoury *et al.* (2013), there is a strong increase of the peaks from the other Reynolds stresses with Reynolds number. Note, that in the symmetry plane, u_3 is the radial component and u_2 is the azimuthal component. The most prominent difference to the Reynolds stress distributions in full pipe flow is found near the free surface at which the velocity component perpendicular to the surface u_3 is strongly damped and the other two components are amplified. At a similar position as the mean streamwise velocity maximum, minima of $u_{1,rms}$ occur with an intensity of about $0.75u_\tau$ and the one of $u_{2,rms}$ is slightly smaller. The distances of these minima from the free surface seem to coincide in inner units while the thickness of the damping layer of $u_{3,rms}$ to the free surface is much thinner. The free surface layer thickness of 50 wall units reported by Nagaosa (1999) is not in accordance with the present findings, because the distance between the free surface and the minima of the x_1- and x_2- components neither scale in inner nor in outer units. The shear stress $\overline{u_1'u_3'}$ approaches zero at the free surface, but changes its sign beforehand and shows a small positive maximum close to the free surface. Unlike the full pipe flow profile, which follows a linear trend above the minimum, the Reynolds shear stress of the semi filled pipe flow does not follow the linear trend. This difference is caused by the momentum transport of the secondary flow.

The Reynolds stress distributions presented by Ng *et al.* (2018) are similar to the current

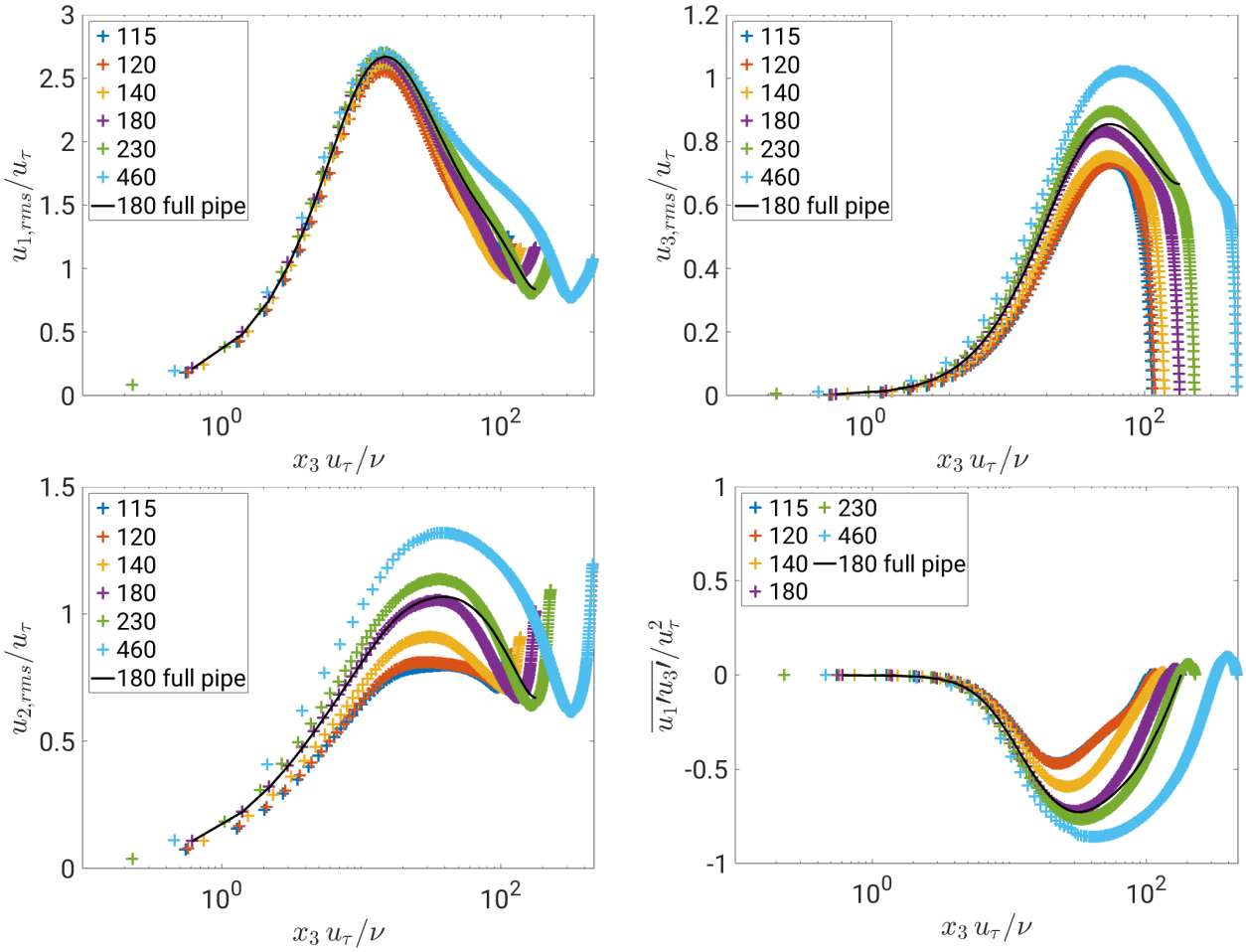

Figure 3.25: Root mean square of the velocity fluctuations $u_{1,\mathrm{rms}}/u_\tau, u_{2,\mathrm{rms}}/u_\tau, u_{3,\mathrm{rms}}/u_\tau$ and Reynolds shear stress $\overline{u_1'u_3'}/u_\tau^2$ in inner units in the vertical symmetry line of $Re_\tau = 115, 120, 140, 180, 230, 460$. The solid black lines represent full pipe flow from present DNS. Please note that for the shown data along the vertical symmetry line the Cartesian coordinates in x_2- and x_3-direction are equal to the Polar coordinates θ and r, respectively.

data. Unfortunately, they didn't provide their results in inner units. However, their measured maxima seem to be smaller than the present maxima when normalized by bulk units (Ng *et al.* (2018): $\overline{u_1'^2}/u_b^2 \approx 0.01$; present study, $Re_\tau = 460$: $\overline{u_1'^2}/u_b^2 \approx 0.025$).
Looking at the cross-sectional distribution of the Reynolds stresses reveals that there are equally high turbulence intensities around the perimeter except at the area of the mixed-corner, see figure 3.26 showing the Reynolds normal and shear stresses for $Re_\tau = 180$ in polar coordinates. The applied transformation can be found in appendix A. Since the single distributions of $u_{r,rms}$ and $u_{\theta,rms}$ show artefacts of the coordinate system in the centre of the pipe, the sum of the cross-stream normal stresses is plotted. Please note that the individual terms are shown in the appendix B. The streamwise stresses have considerably larger values than the other stresses, demonstrating that the TKE (shown in section 4.1.3) is dominated by $\overline{u_1'^2}$. The minimum of $\overline{u_1'^2}$ appears approximately at the location of the mean streamwise velocity

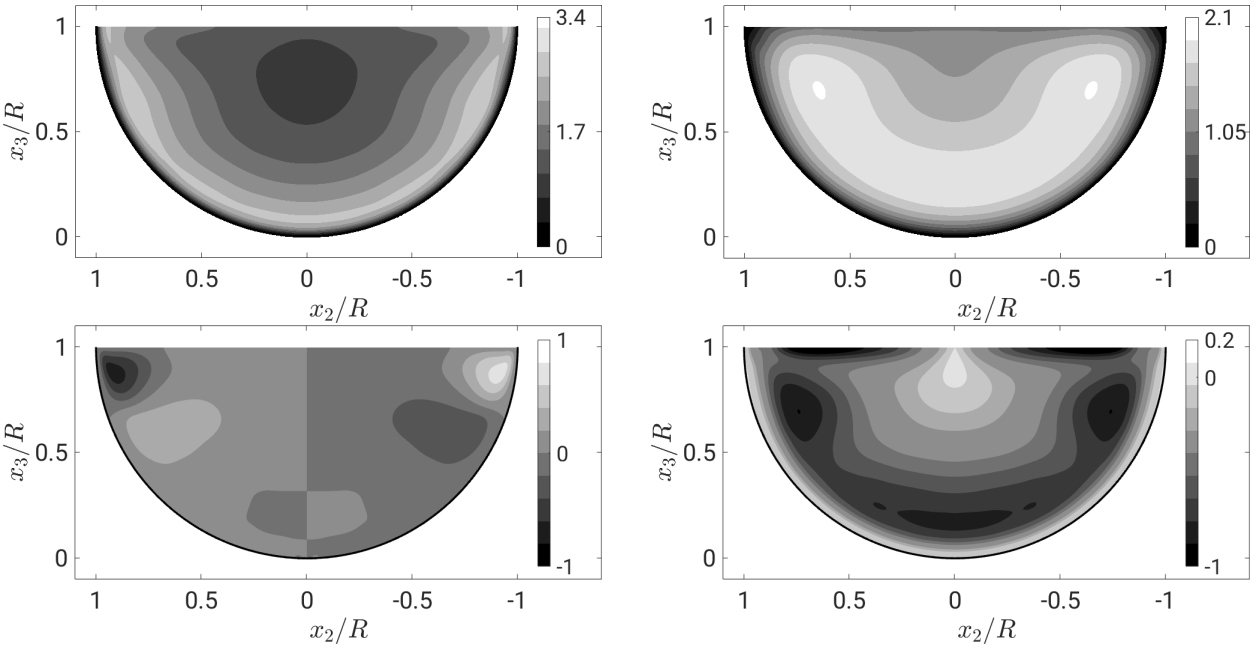

Figure 3.26: Normalised root mean square of velocity fluctuations $u_{1,\mathrm{rms}}/u_\tau$, $(u_{\mathrm{r,rms}} + u_{\theta,\mathrm{rms}})/u_\tau$ (top left and right) and Reynolds shear stresses $\overline{u_1' u_\theta'}/u_\tau^2$, $\overline{u_1' u_r'}/u_\tau^2$ (bottom left and right) for $Re_\tau = 180$. Please note, that the distributions were symmetrized using the half-plane symmetry.

maximum. The layer of large values of $\overline{u_1'^2}$ around the perimeter has local minima where the secondary flow of the inner vortex is parallel to the wall. A local maximum occurs at the location where the secondary flow points away from the wall.

The streamwise Reynolds stress and the sum of the cross-stream stresses are nearly homogeneous in the azimuthal direction in the lower part of the pipe within $\pm 45^o$ from the vertical bisector. This is consistent with the observation that the secondary flow is weak in the lower part of the flow and suggests that the flow near the lower wall could behave like a normal, full pipe flow. This conjecture is partly supported by the shear stress $\overline{u_1' u_\theta'}$ which is essentially zero in the lower part. In agreement to Nezu & Nakagawa (1993), Blanckaert *et al.* (2010) and Joung & Choi (2009), positive $\overline{u_1' u_\theta'}$ matches clockwise rotation and negative Reynolds shear stress occurs where counter-clockwise rotation is present. Please note that the wall parallel coordinate of the references is defined inversely, hence, positive $\overline{u_1' u_\theta'}$ matches counter-clockwise rotation and *vice versa*. The distribution of $\overline{u_1' u_r'}$ shows a distribution of minima along the wall that is not fully homogeneous in the lower part. Additionally, minima occur at the free surface. The distribution $\overline{u_r' u_\theta'}$ is omitted as the values are very small in the entire cross-section compared to the other stress components.

The sum of the cross-stream components shows its maximum at about $0.25R$ from the wall with a stronger contribution of the azimuthal component at the bottom and along the wall, whereas the radial component has its maximum at the free surface. The mixed-corner has predominantly a damping effect on the normal stresses $\overline{u_1'^2}$ and $(u_{\mathrm{r,rms}} + u_{\theta,\mathrm{rms}})$. The shear stresses, however, are strongly affected near the mixed-corner. The magnitude of $\overline{u_1' u_r'}$ peaks in the area below the inner vortex where the secondary flow points away

from the wall. The magnitude of $\overline{u_1' u_\theta'}$ peaks in the region where the corner vortex flow is parallel to the wall. Both of those peaks could be linked to strong fluctuations of the corner vortex associated with the dynamics of the near wall streaks discussed in the previous section.

In order to better understand the Reynolds stress distribution, the anisotropy of the Reynolds stress tensor will be evaluated by the so-called Lumley triangle, which is also known as turbulence triangle. The state of anisotropy is described by its invariants ζ and ξ. They are defined by the eigenvalues of the Reynolds stress tensor ζ (eq. (3.7)) and ξ (eq. (3.8)) (Pope, 2000).

$$\zeta^2 = \frac{1}{3}(\lambda_1^2 + \lambda_1\lambda_2 + \lambda_2^2) \tag{3.7}$$

$$\xi^3 = -\frac{1}{2}(\lambda_1\lambda_2(\lambda_1 + \lambda_2)) \tag{3.8}$$

The Lumley triangle, defined in the eigenvalue space, assigns to its corners different turbulent states, see figure 3.27 (left). The upper right corner describes turbulence that consists only of fluctuations in one component (x_{c1}), e.g. the streamwise component. In the upper left corner a two-component turbulence state (x_{c2}) is indicated, hence, the fluctuations of two different components are equally intense. Whereas in the lower corner, the fluctuations of all three components are equally contributing to the turbulence (x_{c3}). In between the corners, all kinds of intermediate states are possible.

In figure 3.27 (left), the turbulence state in the symmetry line is shown. Starting from the wall (indicated in figure 3.27 (left) by $x_3^+ = 1$), the general behaviour first follows the distribution of a channel flow, see (Pope, 2000). At the wall, the streamwise component is dominant and the azimuthal component is weakly present. At a wall distance of 10 wall units, the flow tends towards the one-component state. This is more pronounced at lower Reynolds numbers. With increasing wall distance, the Reynolds stresses move towards the isotropic state until they reach a sharp turning point, which is closer to the isotropic state when the Reynolds number is higher. This turning point is the point at which the boundary condition of the free surface starts to damp the vertical component and which is marked by a local minimum in the streamwise and spanwise Reynolds stresses. Upwards from this point, the Reynolds stresses have to move towards the two-component state as the vertical component is zero at the free surface. For Reynolds numbers ≥ 140, the two-components at the free surface are equally strong, whereas for lower Re_τ the second component is less dominant. Hence, at the free surface, the anisotropy is shaped elliptical for $Re_\tau = 115$ and 120, and for higher Reynolds numbers the anisotrpoy appears like a disk. For $Re_\tau = 460$, an oblate-spheroid shaped anisotropy appears underneath the free surface.

In Brosda & Manhart (2022), the distributions over the cross-section were reported only for $Re_\tau = 180$. For the other Reynolds numbers the results are first published in this thesis. Emory & Iaccarino (2014) proposed to link the position in the anisotropy map to a colour code, which can be used to visualise the different turbulence states over the entire cross-section (figure 3.28). The specific colourmap is defined in figure 3.27 (right). Red corresponds to a one-component, green to a two-component and blue to a three-component turbulent

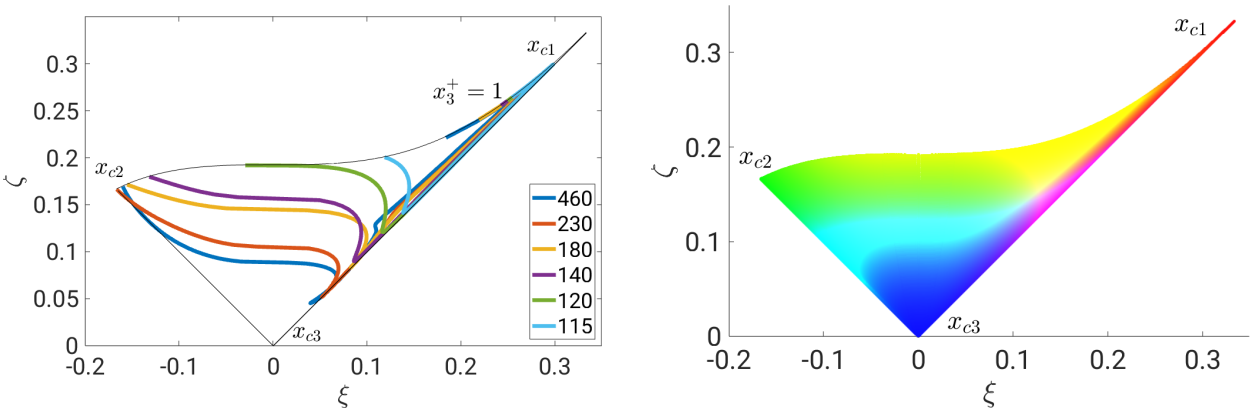

Figure 3.27: Lumley triangle of the Reynolds stress tensor in the vertical symmetry line for $Re_\tau = 115, 120, 140, 180, 230, 460$ (left) and colourmap according to non-linear anisotropy invariant map (right). $x_3^+ = 1$ indicates the location of the wall for the distribution along the vertical symmetry line.

state. Yellow, turquoise and pink describe intermediate states. The nearly one-component turbulence (red colour) spreads along the whole perimeter including the inner vortex region. From the Reynolds stress plots, it becomes clear that the streamwise component is dominant in this region. With increasing Reynolds number, this wall layer shrinks. The shift to orange colour for larger Reynolds numbers still indicates a mostly one-component behaviour. Further away from the wall there is another ring-like area in which the Reynolds stresses move towards the three-component state (magenta). The area of the velocity maximum is characterised by a state which is near the three-component limit (blue). For $Re_\tau = 115$, this three-component area misses, whereas it grows with larger Reynolds numbers. At the free surface, a layer behaves different. Here, the damping of the vertical fluctuations changes the flow state to a two-component limit (yellow and green). When moving from the mixed-corner to the centre, the state changes gradually from a one-component (red) to two-component (green) state. Again for $Re_\tau = 115$, only a yellow state is reached, which is in between one- and two-component state.

The results of the following small paragraph have not been published in Brosda & Manhart (2022) and are first published in this thesis. In figure 3.29, the anisotropy only according to the x_2- and x_3-components is shown, where the dominating effect of the streamwise component is excluded. The one-component turbulence (red) is at the wall and at the free surface. The intermediate two-component turbulence (yellow) reaches into the mixed-corner. In the centre, both components are equally intense. Again, as Reynolds number increases, the one-component layer shrinks and the two component area increases and further reaches to the wall and to the free surface.

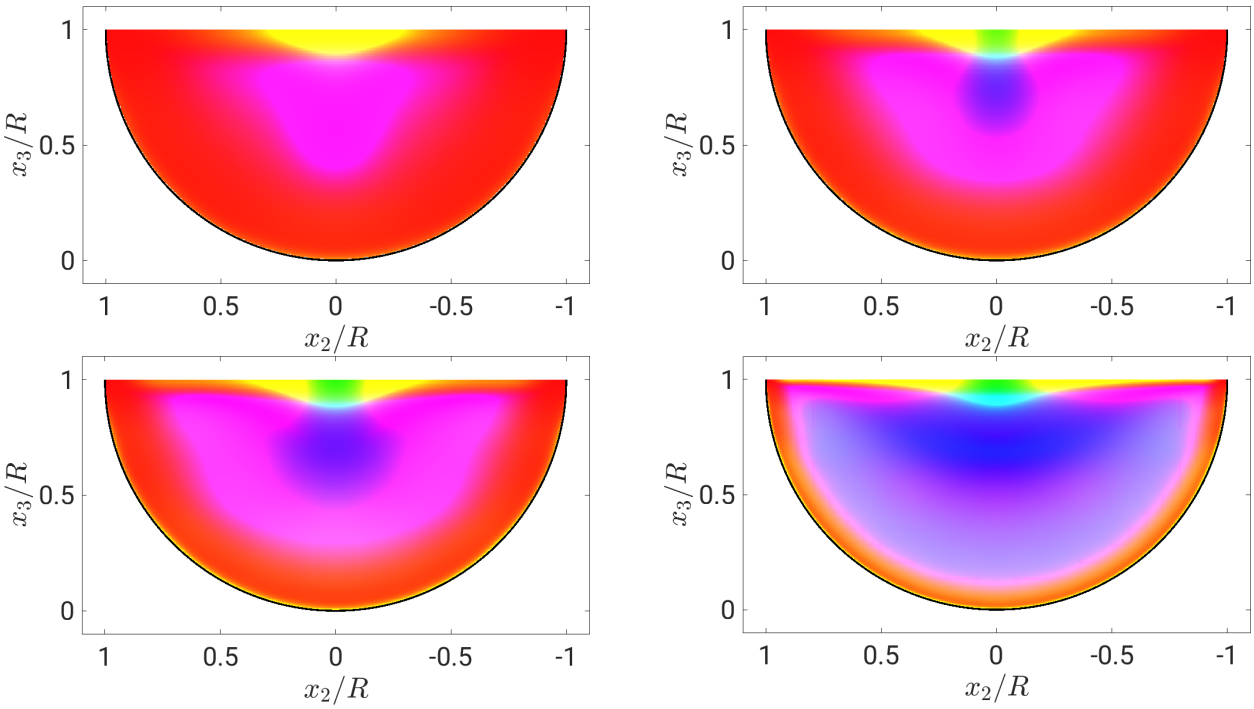

Figure 3.28: Anisotropy componentiality of Reynolds stresses over the cross-section for $Re_\tau = 115, 140$ (top) and 180 and 460 (bottom, from left to right). Please note, that the distributions were symmetrized using the half-plane symmetry.

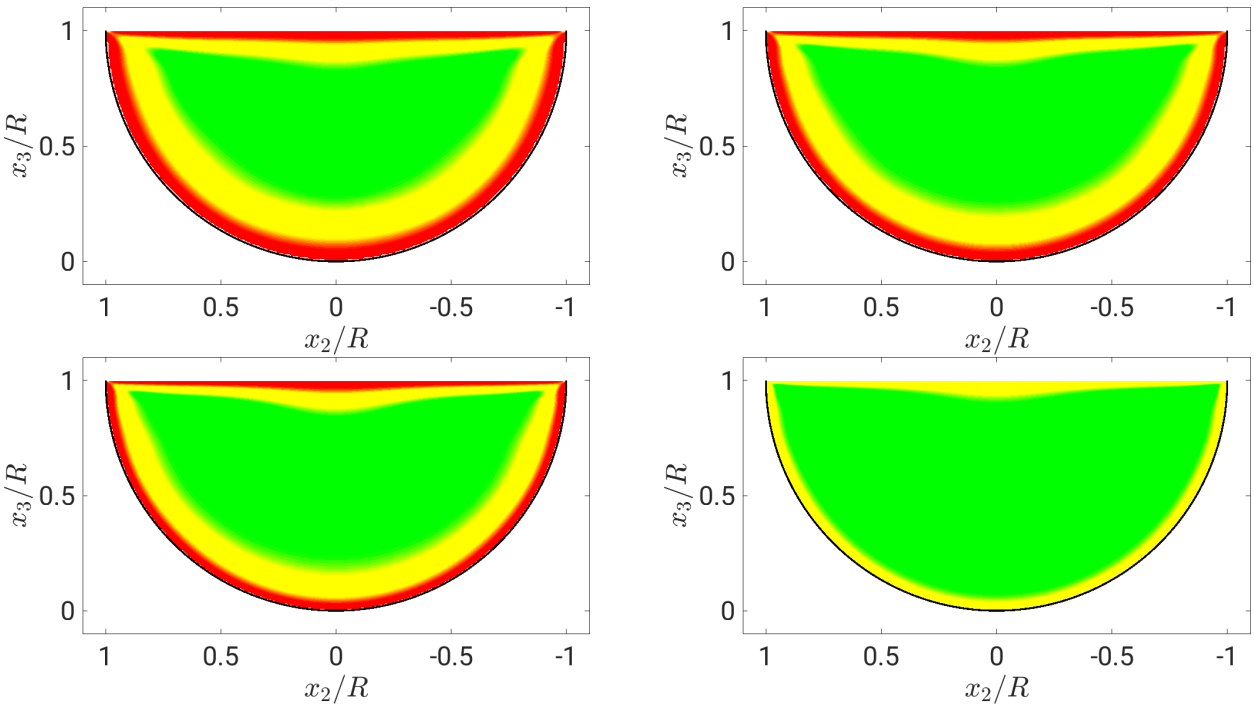

Figure 3.29: Anisotropy componentiality only for the in-plane components of Reynolds stresses over the cross-section for $Re_\tau = 115, 140$ (top) and 180 and 460 (bottom, from left to right). Please note, that the distributions were symmetrized using the half-plane symmetry.

3.2.4. Minimum Turbulent Reynolds Number / Minimum Box Size

Please note that the results of the following section have not been published in Brosda & Manhart (2022) and are first published in this thesis.
The intention of this section is to address the following two questions: (i) which is the lowest Reynolds number, and (ii) what is the minimum domain size, to still sustain a turbulent semi filled pipe flow? Most probable the spatial resolution of the present simulations is not fine enough to really study transitional effects, hence, only superficial evaluations are made and these have to be taken with care. Moreover, these simulations are also not taken into account for the analysis of the Reynolds-dependency compared to the integral friction coefficient (cf. figure 3.1). Uhlmann *et al.* (2007) stated that the marginally turbulent flow at minimal Reynolds number or minimum box size should contain structures, which are part of the buffer-layer, but their sizes are in the order of magnitude of the duct geometry.
The lowest Reynolds number with a turbulent flow was $Re_\tau = 110$. The procedure to reach this low Reynolds number was the same as mentioned in chapter 2.1 and slightly adapted in the same manner as Uhlmann *et al.* (2007): A fully-turbulent, high Reynolds number simulation was established and if a turbulent flow was still present after 2000 bulk time units, the Reynolds number was decreased step-by-step. The flow at $Re_\tau = 110$ kept being turbulent over 8000 bulk time units, whereas for $Re_\tau = 109$ the flow completely laminarised, which was indicated by the magnitude of turbulent kinetic energy, and by the fact that the flow field qualitatively matched the laminar and symmetric distribution of a full pipe flow. Like Uhlmann *et al.* (2007) reported for their marginal flow, also the flow at $Re_\tau = 110$ shows periods of apparently fully-turbulent flow and also sections of quasi-laminar flow. This resembles the flow structure of transient flow the so-called "puffs" (Avila & Hof, 2013). A detailed description of the flow is not provided as the grid resolution is not satisfactory for transient flows. In the flow of $Re_\tau = 115$, no puff events were found, either the flow does not contain any, or they are so rare that they were not spotted. Sakai (2016) reported a minimal Reynolds number of $Re_\tau = 102$ that is based on the flow depth for a rectangular open-duct with a width to height aspect ratio of $W/H = 2$. This small difference is probably due to the different geometry including solid corners, creating a larger total area. The larger total area provides more space for the vortices to exist and to move. For the closed rectangular duct the minimal friction Reynolds number, based on the half duct height, is even smaller ($Re_\tau = 77$). Overall, it seems that the solid corners of the rectangular duct have a significant impact on the generation of turbulence on the one hand, and structures can move in a larger area on the other hand.
The other parameter, which was studied, is the minimal box size. For each domain size, the same procedure, as reported in chapter 2.1, was undertaken to establish a turbulent flow. The Reynolds number was kept constant at $Re_\tau = 180$ for the different domain sizes. For a domain size of $L^+ = 170$, turbulence could still be sustained, but for $L^+ = 141$, turbulence disappeared and a laminar flow profile could be detected. This agrees well with the limit reported by Uhlmann *et al.* (2007) for a quadratic closed duct.

3.3. Filling Ratio Dependency for Partially Filled Pipe Flow of $Re_\tau = 180$

Similar to section 3.2, the basic flow quantities are described. In this section the Reynolds number is kept constant and different filling ratios (FR), namely 25%, 50% and 75% filling ratio, are compared to each other.

3.3.1. Mean Flow

Mean Streamwise velocitiy and velocity-dip phenomenon

As already known from section 3.2.1, the rotational symmetry is broken for all partially filled pipe flows. Hence, depending on the filling ratio, the mean streamwise velocity deviates from a homogeneous distribution in azimuthal direction, see figure 3.30. The deviations are strongest for 25% FR with larger deviations at approximately $x_2 = \pm 0.5R$. This bump is also visible for 50% FR, but less strong. For 75% FR, the distribution is almost homogeneous in azimuthal direction and no large deviations are visible anymore. However, the location of the maximum velocity, marked with a black plus, is below the pipe centre at about $x_3 = 0.9R$. Hence, the *velocity-dip* phenomenon also occurs for 75% filled pipe flow, as it deviates from the location with the largest distance to the wall, i.e. the centre of the pipe. The smaller the filling ratio gets, the more a partially filled pipe flow resembles a open-channel flow. The maximum velocity for 25% FR appears at the free surface, which is surprising, because if one would approximate the cross-section as rectangular cross-section, it would be classified as narrow cross-section (cf. section 1.3), and in narrow rectangular cross-sections the *velocity-dip* phenomenon occurs.
For different pipe fillings, the distance between the position of the maximum mean streamwise velocity $\Delta z(\overline{u}_{max})/2R$ to the free surface is plotted over the filling ratio (fig. 3.31, left). Besides the present study, also experimental and numerical data are included for various Reynolds numbers from $Re_b = 5700$ to $560,000$ (Clark & Kehler, 2011; Yoon *et al.*, 2012; Ng *et al.*, 2018; El Khoury *et al.*, 2013). In addition, the fully filled pipe flow is also taken into account with the maximum mean streamwise velocity in the pipe centre. It becomes clear, that especially for $H/2R > 0.5$ the position of the maximum mean streamwise velocity moves with increasing filling ratio towards the centre of the pipe. The distance strongly depends on the filling ratio and seems to be independent of the Reynolds number. Moreover, the data show a linear trend of the type $\Delta z/(2R) = 0.6754(H/(2R)) - 0.1642$, which was fitted using the method of least-square. The upper limit is defined by the full pipe flow, however, the lower limit, i.e. at which filling ratio no *velocity-dip* phenomenon occurs anymore, is not known *a priori*. The reported distances imply that up to a filling ratio of 25%, the maximum mean streamwise velocity occurs at the free surface. For higher filling ratios the *velocity-dip* phenomenon was observed. Please note that for filling ratios larger than $H/2R = 0.8$, a spontaneous transition from a free surface flow to a pressurised flow can take place, which is not taken into account in this consideration, see Trajkovic *et al.* (1999) for example.
The distribution of momentum can be described by $\overline{u}_{max}/u_b$, see figure 3.31 (right). In the present study this ratio appears to be independent of the filling ratio and is approximately

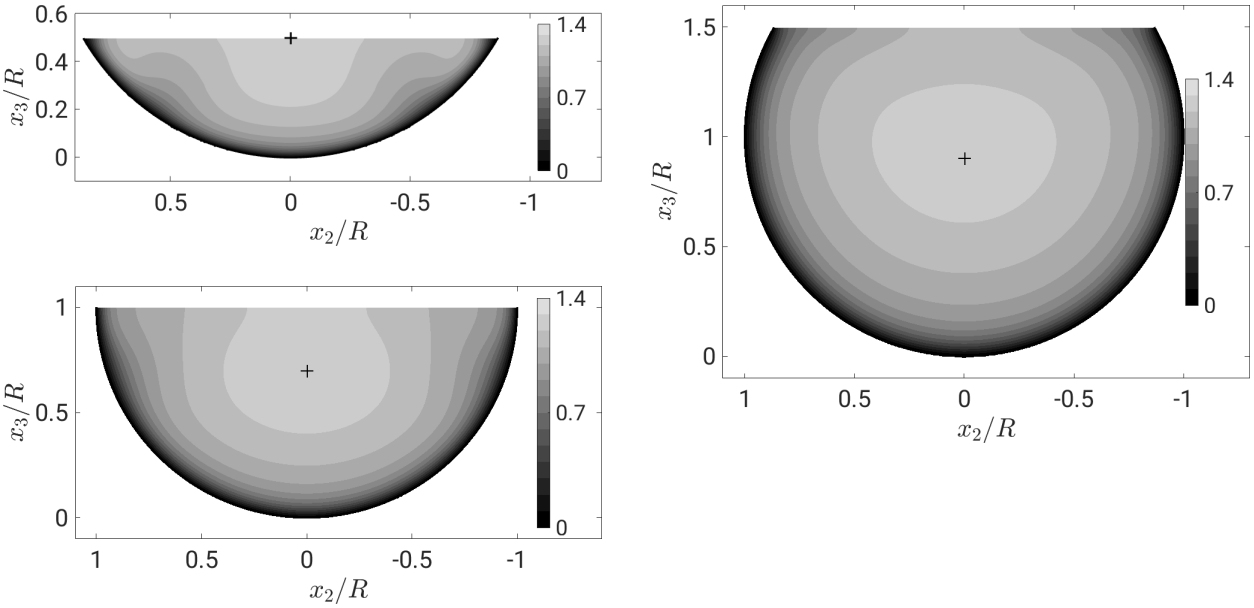

Figure 3.30: Mean streamwise velocity $\overline{u}/u_b$ of $Re_\tau = 180$ for 25%, 50% (left, top and bottom, respectively) and 75% filling (right). The cross indicates the position of the velocity maximum. Please note, that the distributions were symmetrized using the half-plane symmetry.

equal to the value of the full pipe flow. The data of Yoon *et al.* (2012) show larger values, hence, a stronger concentration of momentum, and a decrease of $\overline{u}_{max}/u_b$ for increasing filling ratios. In contrast, the results of Ng *et al.* (2018) increase with the filling ratio, and show good agreement with the results of El Khoury *et al.* (2013) for the full pipe flow case. The deviation between Ng *et al.* (2018) and the present results for the semi filled pipe flow can be explained, by the different Reynolds numbers (cf. figure 3.5). Hence, the Reynolds effects seem to become stronger with decreasing filling ratio.

The distribution of the mean streamwise velocity in the symmetry plane (fig. 3.32) is best suited to compare with the full pipe flow, because the secondary flow has the smallest influence in this plane, especially in the near-wall and buffer layer. This holds true in particular up to a wall distance of approximately 30 wall units, where a very good match to full pipe flow occurs for all filling ratios. Then slight differences occur: for 75% FR the gradient is slightly steeper, whereas for 25% FR it is slightly less steep. Only for the FRs 50% and 75%, a logarithmic layer is possibly established, but for the lowest flow depth no distinct logarithmic layer can be observed. Stronger deviations occur where the velocity maximum occurs. For 75% FR, the velocity maximum is closer located to the pipe centre than for the semi filled pipe flow and the velocity decrease afterwards is also stronger by a factor of two. The normalised velocity at the free surface is approximately the same for 25% and 50% FR.

In outer units, the mean streamwise velocity can be compared to the experimental results of Yoon *et al.* (2012) and Ng *et al.* (2018), see figure 3.33. As already known from figure 3.32, the maximum velocity is approximately the same for the different filling heights of this study. The gradient of the distributions at the wall gets slightly less steep with increasing

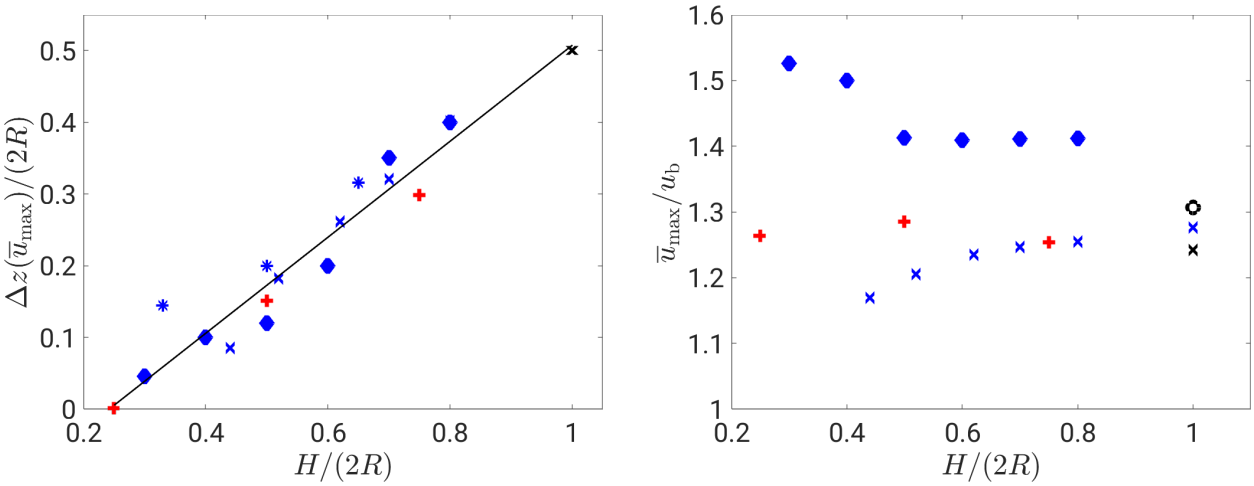

Figure 3.31: Distance $\Delta z/(2R)$ from the free surface to the maximum mean streamwise velocity dependent on the filling ratio $H/(2R)$ for various Re_b (left). Maximum mean streamwise velocity $\overline{u}_{\max}/u_b$ dependent on the filling ratio $H/(2R)$ for various Re_b (right). Present study + ($Re_b \approx 5350$); Experiments: ♦ (Yoon *et al.*, 2012)($Re_b \approx 5700 - 19000$), × (Ng *et al.*, 2018)($Re_b \approx 30000$), ∗ (Clark & Kehler, 2011)($Re_b \approx 340000 - 560000$). × and ∘ are simulations from El Khoury *et al.* (2013) with $Re_b = 5300$ and $Re_b = 37700$, respectively. (—) represents linear least-square fit following $\Delta z/(2R) = 0.6754(H/(2R)) - 0.1642$.

filling ratio. The distribution for 25% FR is monotonically increasing, but the distributions for higher filling ratios are more complex, because they include the *velocity-dip* phenomenon and a zero gradient at the free surface. Ng *et al.* (2018) reports smaller velocities for small filling ratios, whereas for a high filling ratio the velocities match well with the present simulation, only in the upper half of the flow depth the velocities are slightly smaller. This filling ratio dependent behaviour is in accordance with the Reynolds effects discussed for figure 3.31 (right). For all filling ratios, Yoon *et al.* (2012) found larger velocities for the scaling with u_b. However, the different distributions agree in general with each other for each filling ratio.

Based on a modified log-wake-law (Guo, 2014), Guo *et al.* (2015) developed a set of equations (eq. (3.9)–(3.11)) approximating the mean streamwise velocity distribution $u(x_2, x_3)$ for partially filled circular and other conic cross-sections with rough walls. This is interesting especially as the velocity distribution might help to estimate the bulk velocity or discharge in e.g. sewage pipes by a small number of measurements and input parameters. The velocity distribution $u(x_2, x_3)$ is defined as

$$u(x_2, x_3) = -\frac{u_\tau}{\kappa}[ln\frac{x_3}{x_{3,0}} - \frac{1}{3}(\frac{x_3}{\Delta z})^3] - u_\tau \phi(x_2, x_{2,b}), \tag{3.9}$$

which requires the following input parameters: the global friction velocity u_τ, which can be determined from $u_\tau = \sqrt{\tau_w/\rho}$ and the global force balance $\tau_w = \rho g I_s R_H$ that requires the slope I_s and the flow depth H as further input; the von Kármán constant $\kappa = 0.41$; the position Δz of the maximum mean streamwise velocity, for which the linear least-square fit

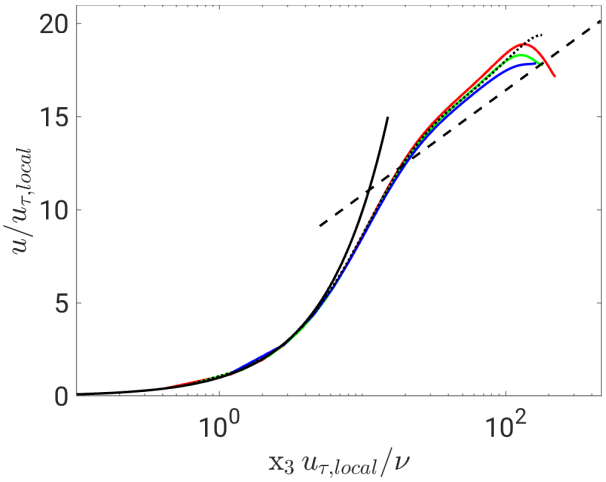

Figure 3.32: Mean streamwise velocity distribution from the wall to the free surface at the vertical symmetry line of $Re_\tau = 180$ for 25% (—), 50% (—) and 75% FR (—), and full pipe flow (·····) normalised with the local friction velocity. The solid, black line represents the linear relation and the dashed, black line the standard log-law $u^+ = 0.41^-1ln(x_3) + 5.2$.

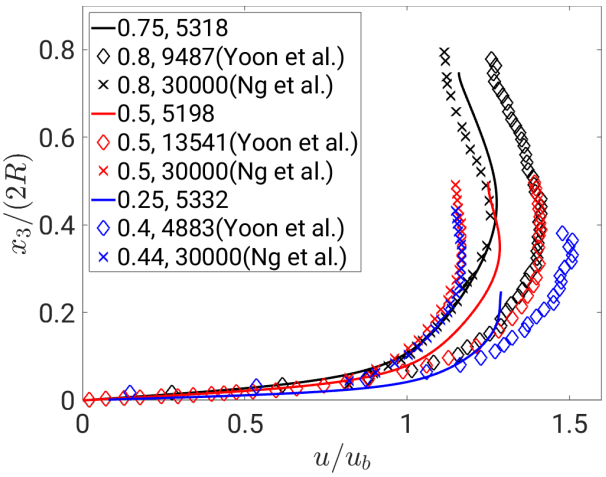

Figure 3.33: Mean streamwise velocity distribution from the wall to the pipe center at the vertical symmetry line of different Re_b for 25% (blue), 50% (red) and 75% (black). Present study is represented by solid lines, including symbols: ◊ (Yoon *et al.*, 2012), × (Ng *et al.*, 2018)(each lowest, highest and semi filled pipe flow). Legend shows the filling ratio and Re_b.

from fig. 3.31 (left), following $\Delta z = 1 - (0.6754H - 0.1642(2R))$, can be used. The two missing terms $x_{3,0}$ and $\phi(x_2, x_{2,b})$ are defined by the equations (3.10) and (3.11), respectively. $x_{3,0}$ represents, depending on the wall roughness, the location of the zero-velocity in the symmetry line at the wall and is defined as

$$\frac{1}{\Delta z^3} = \frac{3}{I_2}(I_1 - \frac{A\,ln(x_{3,0})}{2} - \frac{3A}{8u_{\tau,centre}/u_\tau} - \frac{\kappa u_b A}{2u_{\tau,centre}}). \tag{3.10}$$

Equation (3.10) requires further input: I_1 and I_2 are geometry-dependent constants (Guo *et al.*, 2015); the area of the cross-section A; the bulk velocity u_b; and the local friction velocity in the symmetry line $u_{\tau,centre}$, which can be estimated from the present data (with $u_{\tau,centre} \approx 1.025u_\tau$) or from Clark & Kehler (2011) ($u_{\tau,centre} \approx 1.1u_\tau$). The second missing term $\phi(x_2, x_{2,b})$ defines the spanwise velocity distribution as follows

$$\phi(x_2, x_{2,b}) = -\frac{1}{\kappa}\left[ln\left(1 - |\frac{x_2}{x_{2,b}}|\right) + \frac{1}{3}\left(1 - \left(1 - |\frac{x_2}{x_{2,b}}|\right)^3\right)\right], \tag{3.11}$$

with $x_{2,b}$ being the horizontal distance to the closest wall.
The simulated and the modeled mean streamwise velocity distributions are shown in figure

3.34 for filling ratios of 25%, 50% and 75%. The positions of the maximum velocity are indicated by + and ×, referring to the present simulation and the approximation by Guo *et al.* (2015), respectively. For the two higher filling ratios the maximum velocity position of Guo *et al.* (2015) is a little bit lower compared to the simulations. Furthermore, the modeled distributions are more flat over the centre for a filling ratio of 50% and 75%, and there is a stronger velocity gradient at the wall. The variations due to the inner secondary vortex around the mixed-corner cannot be reproduced by the suggested approximation. Nevertheless, a fair overall agreement can be reported. By checking the hydraulic regime according to the Moody-diagram based on the backwards-calculated roughness k_s and the Reynolds number a hydraulically smooth regime can be reported, being in line with the friction factors derived from the simulations. This approximation offers a good estimate for fully developed flows, in order to approximate the bulk velocity or the discharge in partially filled pipes from a small number of measurement points.

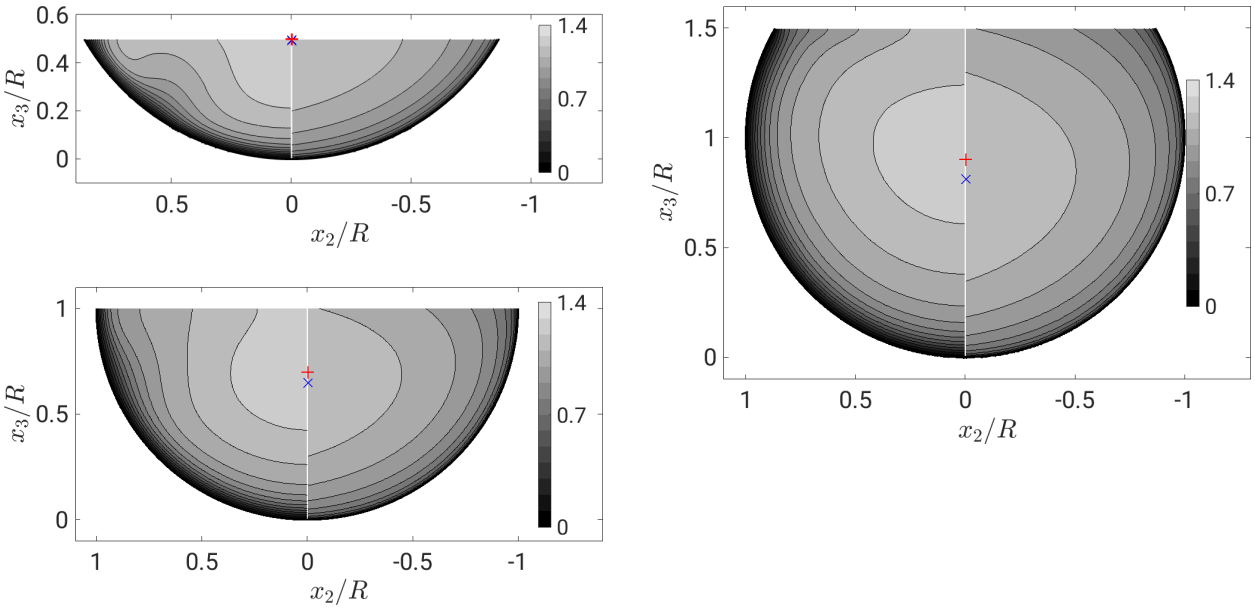

Figure 3.34: Mean streamwise velocity $\overline{u}/u_b$ of $Re_\tau = 180$. The cross-sections are divided into two halves. Left: present simulations; right: approximation by method of Guo *et al.* (2015). + and × indicates the position of the velocity maximum for the present data and the estimation by method of Guo *et al.* (2015), respectively.

Mean Secondary Flow

Mean secondary flow occurs in all partially filled pipe flows. Figure 3.35 shows the stream function ψ and the velocity magnitude of $\sqrt{\overline{u_2}^2 + \overline{u_3}^2}/u_b$ for a 25%, 50% and 75% FR of $Re_\tau = 180$. For 25% FR, the inner secondary cell is stronger and covers around one third of the cross-sectional area. With increasing FR the inner secondary cell becomes smaller and less strong until it almost vanishes for 75%. In contrast, the outer secondary cell changes from a less dominant (25% FR) to a more dominant vortex with increasing FR. For 75% FR, it covers almost the complete cross-section. The in-plane velocity intensities are more

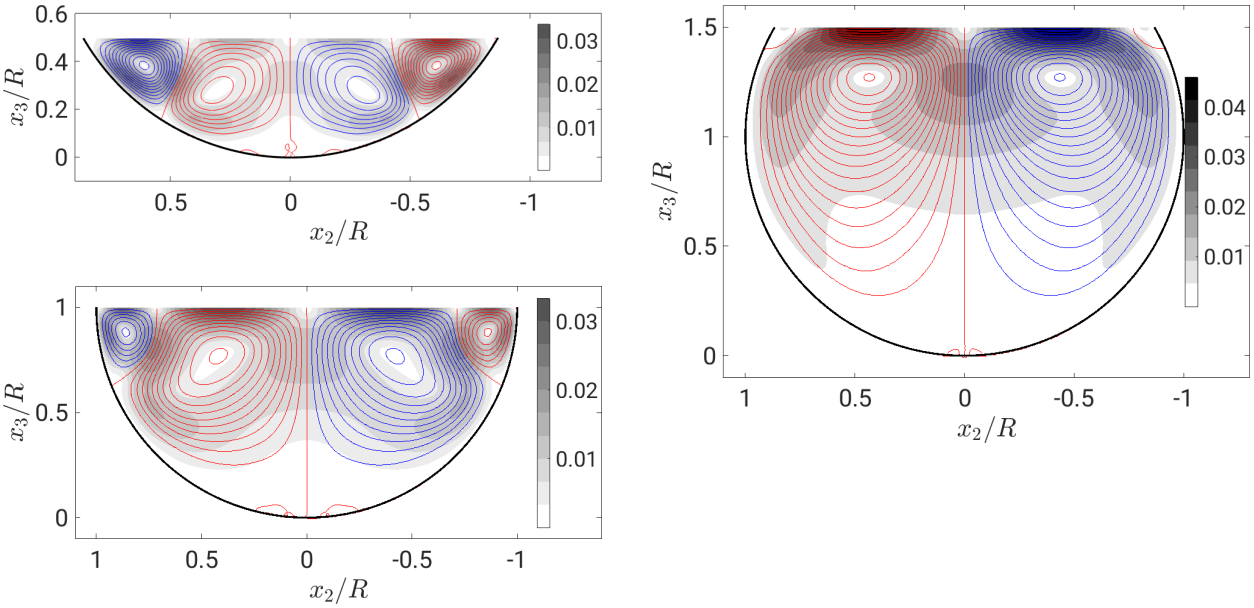

Figure 3.35: Contours of the stream function ψ of mean in-plane velocities $\overline{u}_2$ and $\overline{u}_3$ and as greyscale the in-plane velocity magnitude of $\sqrt{\overline{u}_2^2 + \overline{u}_3^2}/u_b$ for $Re_\tau = 180$. Left column 25% and 50% filling, right column 75% filling. The increments for the contourlines of ψ are 0.003. Please note, that the distributions were symmetrized using the half-plane symmetry.

concentrated towards the free surface with increasing FR. For 25% filling ratio, only a small area in the bottom centre shows no secondary flow. The area with low secondary flow gets larger for 50% FR and covers a third of the cross-section when the pipe is 75% filled. Moreover, the absolute area covered by stronger secondary flow increases with increasing filling ratio, but relative to the total cross-section it decreases (the area $A_{2,3}$ of $\sqrt{\overline{u}_2^2 + \overline{u}_3^2}/u_b > 0.01$ relative to the total cross-section A decreases from $A_{2,3}/A = 0.39$ (25%), over 0.36 (50%) to 0.34 (75% FR)). The in-plane velocities have higher intensities in the mixed-corner vortex for lower filling ratios, for semi filled it is almost equal and for higher filling there is almost no in-plane velocity for the inner, but high magnitudes for the outer secondary cell. Looking from a kinematics point of view, a vortex can have different shapes, such as circular, elliptical or arbitrarily deformed. In any case, however, it is a somewhat 'round' structure. Moreover, the maximum diameter of vortices in rectangular (Sakai, 2016), trapezoidal (Tominaga *et al.*, 1989; Brosda, 2015) or partially filled pipe flow (Ng *et al.* (2018) and present study) is proportional to the flow depth. Its horizontal extent is approximately of the same size. Hence, the vortices of a certain size can not reach into the mixed-corner enabling another vortex to evolve in the mixed-corner, see 25% filling ratio. This effect becomes less strong for 50% filling ratio and the inner secondary cell gets much smaller compared to the outer secondary vortex. For 75% filling ratio, the outer secondary cell gets even larger and completely fits to the upper half, leaving hardly any space for the inner secondary cell. As the mixed-corner has an obtuse angle, the big centre vortex can fill out this mixed-corner almost completely and no small vortex can develop. The mean secondary flow field of 75% filling indicates that if vortices are present in the mixed-corner, the big centre vortex could flush them away, preventing the generation of a stable mixed-corner vortex. In the lower half, the

flow is similar to a pipe flow without any mean secondary flow. The secondary flow pattern agrees well with Ng *et al.* (2018) for the outer cell at 50% and 75% FR. However, for all filling ratios, they do not show any inner secondary cell. In the case of 25% FR the inner secondary cell is more dominant and it would be more likely that the mixed-corner vortex could be detected by measurements. Unfortunately, the lowest filling ratio of Ng *et al.* (2018) is 44%, hence, no comparison of the secondary flow pattern is possible for the small filling ratio.

The relation between the secondary flow and the vorticity was introduced in section 3.2.1. Like for the secondary flow, the general pattern of the vorticity distribution is similar for the different filling ratios, see figure 3.36. Two symmetric, counter-rotating centre-structures are present for all filling ratios and the mixed-corner structure becomes less dominant with increasing filling ratio. For 25% FR, the vorticity is active over the whole cross-section apart from a small region at the bottom and as the filling height increases this inactive region is growing until, for 75% FR, 2/3 of the cross-section are not affected by larger vorticity and high magnitudes gather around the free surface. For 25% and 50% FR, the shear layer at the wall from the outer secondary cell and the inner secondary cell itself are clearly two different structures, connected by a saddle point, i.e. the location where the contourlines of $\overline{\omega}_1$ cross. Please note that the term saddle point is used in the context of describing the scalar field $\overline{\omega}_1$, not in terms of flow topography. The condition of a saddle point is met, as the hessian matrix of $\overline{\omega}_1$ is indefinite at the location of the saddle point. For 75% FR, this distinction is not so clear anymore, as the shear layer of the inner secondary cell is very small and the shear layer of the outer secondary vortex and the vortictiy of the inner secondary vortex merge into each other. However, a saddle point, dividing the shear layer of the outer secondary vortex and the vorticity of the inner secondary vortex, is also present. The pattern of vorticity of the centre structure consists of two peaks for the 25% and 50% FR, one near the free surface and one closer to the wall, whereas for 75% FR, only one peak at the free surface exists.

Table 3.2 summarises the magnitudes and positions of the secondary flow maxima. It is obvious that secondary flow is present for all filling ratios. The magnitude of the maximum mean secondary flow is similar for 25% and 50% FR, whereas it is approximately 1.5 times larger for 75% FR. The maximum is always located at the free surface, but for 25% FR, it is present in the inner vortex, like for small Reynolds numbers, whereas for filling ratios of 50% and 75%, the maximum velocity occurs in the outer secondary cell.

Filling rate	$\sqrt{\overline{u}_2^2 + \overline{u}_3^2}\|_{max}/u_b$	$\pm x_2/R$	x_3/R
25 %	0.0345	0.6400	0.4974
50 %	0.0331	0.3991	1.0000
75 %	0.0512	0.4319	1.4974

Table 3.2: Magnitude and position of maximum in-plane velocity for different filling ratios; $Re_\tau = 180$

The distance between the peak values of the stream function and the free surface is compared between the present study and the experiments of Ng *et al.* (2018) (fig. 3.37, left). The distances agree quite well for the outer secondary cell when normalised in bulk units.

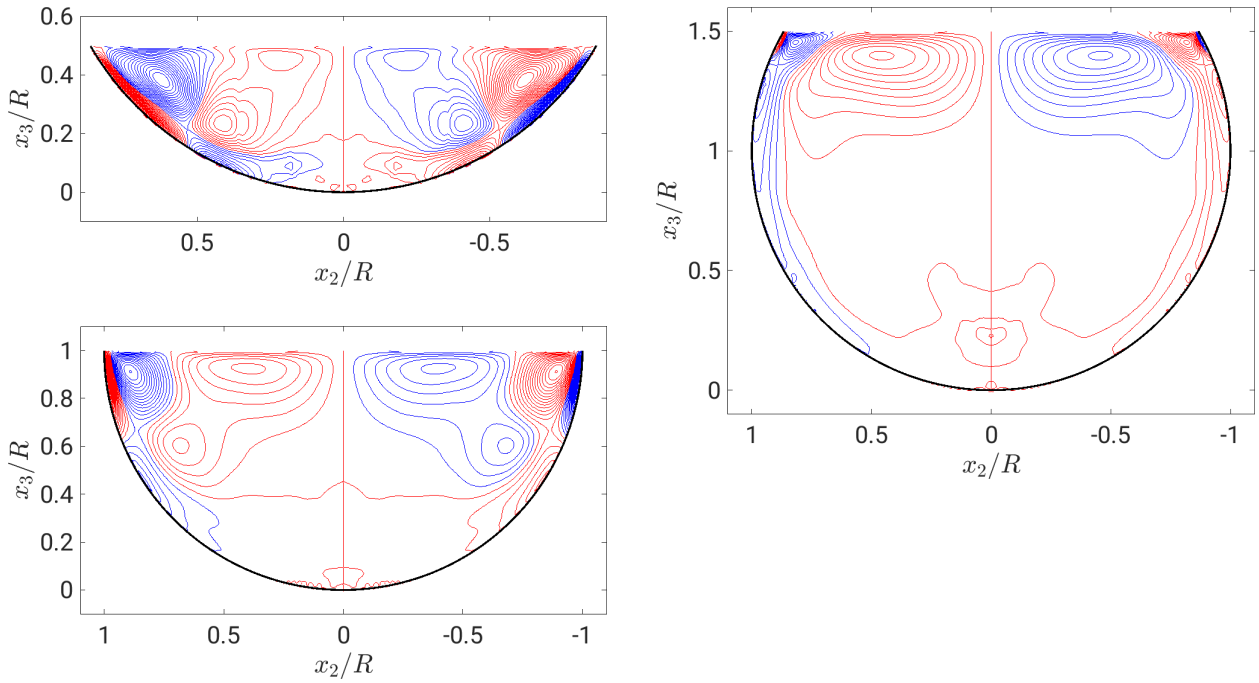

Figure 3.36: Mean streamwise vorticity $\overline{\omega}_1 \cdot R/u_b$ of $Re_\tau = 180$. Left column 25% and 50% filling, right column 75% filling. The increments for the contourlines of $\overline{\omega}_1 R/u_b$ are 0.04. Please note, that the distributions were symmetrized using the half-plane symmetry.

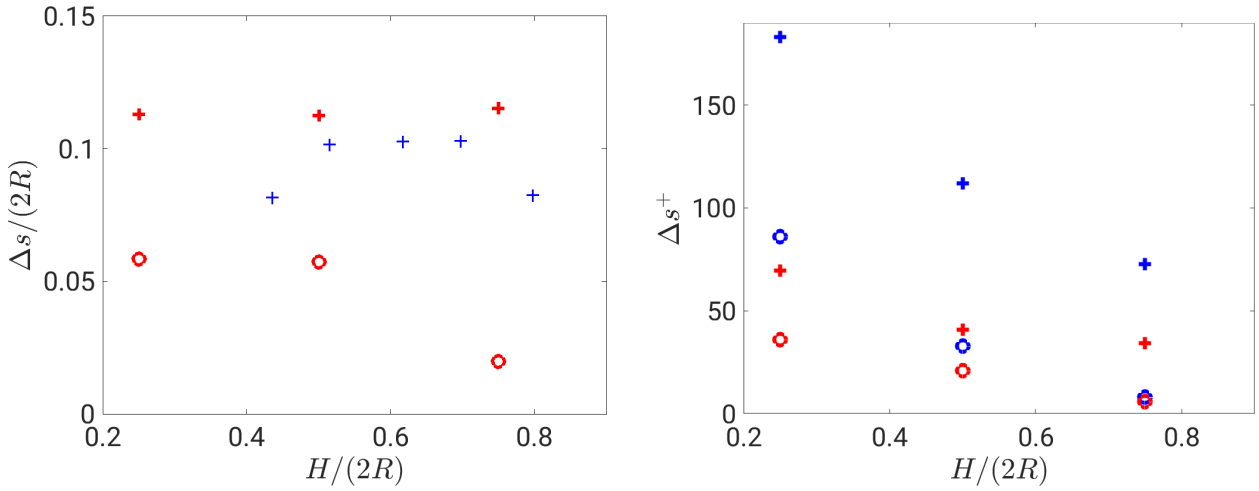

Figure 3.37: Left: Distance $\Delta s/R$ in outer units from the free surface to the minimum and maximum of the stream function ψ for $Re_\mathrm{b} = 5254$. Red colour shows the present study, blue symbols correspond to Ng *et al.* (2018), $Re_\mathrm{b} = 30000$. Right: Distance Δs^+ in wall units from the free surface (red) and the mixed-corner (blue) to the minimum and maximum of the stream function ψ for $Re_\tau = 180$. For both plots $\circ$ corresponds to the inner secondary vortex and $+$ to the outer secondary vortex.

Its distances appear to be constant around $0.1/(2R)$ independent of the filling height and independent of Re in the range of $Re_b = 5000$ to $30,000$. The distance of the inner secondary cell is constant for 25% and 50% FR around $0.05/(2R)$ and drops for the 75% FR by a factor of two. The distances of the inner and outer secondary cells to both the free surface and to the mixed-corner decrease in wall units with increasing filling ratio, see figure 3.37, right. Especially for the 75% filling ratio, the distance of the inner secondary flow does not follow the scaling of the Reynolds-dependence of semi filled pipe flows (section 3.2.1), which has a lower limit of 20 wall units. Almost all distances have a filling ratio dependency, only the distance from the free surface to the centre of the outer secondary cell does hardly change from 50% to 75% FR. As mentioned above, these results cannot be extrapolated to filling ratios higher than 80%, because the phenomenon of transition to a pressure flow can occur.

The peak values of the stream function agree very well with the circulation of the inner and outer secondary cell and display the same trends in figure 3.38, left. The inner secondary cell becomes weaker with increasing filling height, whereas the outer secondary cell gets stronger. The peak values of the stream function increase (outer) and decrease (inner) approximately linearly. The distribution of the circulation is slightly more complex: it has a strong rise between 25% and 50% FR for the outer secondary cell and only moderately increases in the 75% case. This is in good agreement with the qualitative plot of the secondary flow, see figure 3.35. When summing up the circulation of the inner and outer secondary cell, an increase from 25% to 50% FR can be reported and then it stays approximately the same from 50% to 75% FR. A similar observation can be drawn from the intensity of the stream function. In figure 3.38 (right), the position of vortex centres are extracted and compared between the different fillings. The outer vortex centre moves slightly outwards from the centre and is always lower than the inner vortex. The inner vortex centre moves closer to the wall into the mixed-corner. The distance between the vortex centres is smallest for 25% FR $\Delta s = 0.32R$ and is similar for 50% and 75% FR with $\Delta s \approx 0.44R$.

Apparently, the in-plane circulation, i.e. the secondary flow, is as strong or even stronger for the 75% filling than for the lower filling ratios, but the inner secondary cell has almost vanished for the 75% filling. Hence, the outer secondary cell becomes more dominant, which is similar to when increasing the Reynolds number in the semi filled case. This poses the question, whether the mixed-corner vortex is really as important for the generation and maintenance of the secondary flow as it seems when looking at the results of the semi filled pipe flow. Possible conclusions from the 75% filled pipe flow are that either the inner vortex is not as stable as for the semi filled flow and the obtuse shape of the mixed-corner is not able to keep the vortices, but still it appears and plays its role in the generation process, or a different, not known process needs to take place, where the outer vortex plays the major role. These questions are addressed in chapter 4, where the generation process of secondary flow will be investigated in detail.

3.3.2. Wall Shear Stress

As mentioned in section 3.2.2, the wall shear stress is very important for engineering applications. Besides a Reynolds number dependency the development of wall shear stress with different filling ratios is also of interest. The mean wall shear stress indicates areas, where

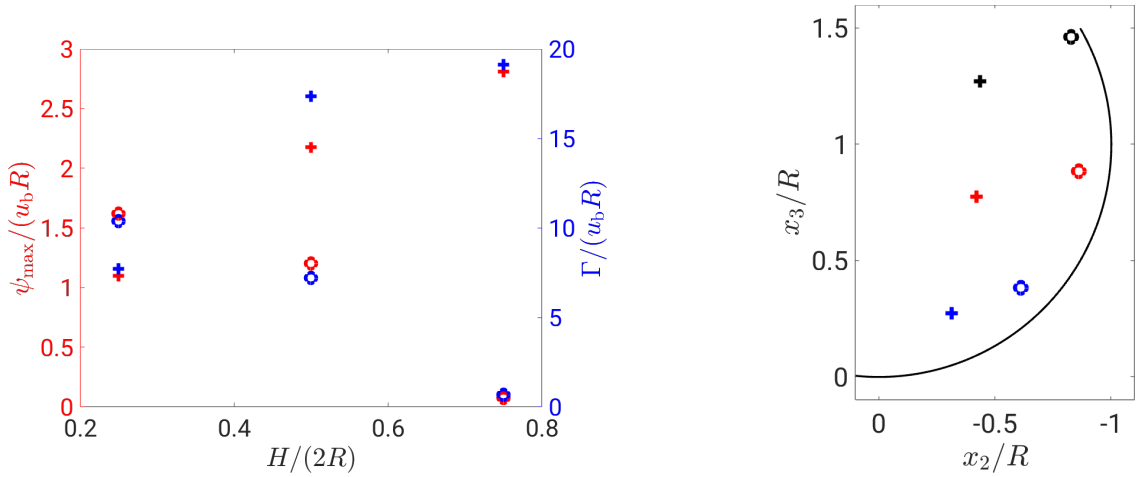

Figure 3.38: Left: Normalised peak values of the stream function $\psi/(u_\tau R)$ (red) and normalised circulation $\Gamma/(u_b R)$ (blue) over the filling ratio for $Re_\tau = 180$. Right: Position of inner and outer secondary cell for $Re_\tau = 180$. Colours represent the filling ratio: 25%(blue), 50%(red), 75%(black). For both plots ∘ corresponds to the inner secondary vortex and + to the outer secondary vortex.

strong shear stresses act on the wall on average. The mean wall shear stress distributions of 50% and 75% FR have a similar pattern – a global maximum in the mixed-corner followed by a global minimum, see figure 3.39 (left). Near the vertical bisector, the wall shear stress is constant for most part of the perimeter with $\tau_w \approx \tau_0$. When comparing 50% and the 75% FR, the maximum is stronger by a factor of 1.2 for 75% FR, whereas the minimum value is lower for the 50% FR by a factor of 1.15. The maximum and minimum together appear much closer to the mixed-corner for 75% than for 50% filling ratio. This is surprising as the wall shear stress distribution was found to be linked to the mean secondary flow for the 50% FR and the mean secondary flow of the inner vortex is much weaker for 75% FR, still the wall shear stress maximum is higher. This can be understood, by looking at the boundary condition of the free surface. The impact of the slip condition at the free surface can be imagined as a mirror, i.e. the velocity field and the wall are mirrored at the free surface and the sign of the x_3-component of the velocity is switched. Hence, for 50% FR a regular full pipe can be imagined, see figure 3.39 (right). For 75% FR a strongly obtuse angle larger than 180 degrees would be generated by the present and the mirrored wall, thus, the influence of the wall friction on the velocity in the vicinity of the mixed-corner is smaller than for the 50% FR. Hence, a higher velocity at the wall and therefore also a higher wall shear stress is generated. In contrast, the mean wall shear stress distribution of 25% FR shows a minimum in the mixed-corner, because the velocities are smaller, as the acute angle generates a narrow section at the mixed-corner. The global minimum in the mixed-corner is followed by a local maximum and a minimum which can be directly linked to the secondary flow. The small plateau in the centre has a slightly higher level of magnitude than the local maximum at the side. At the bottom of the pipe, the secondary flow shows higher intensities than in the case of the higher filling ratios, which results in a larger wall shear stress. The distribution of wall shear stress in the 25% case resembles the distribution of a flow through a trapezoidal cross-section (Tominaga *et al.*, 1989; Brosda, 2015), as the cross-sectional shape is similar

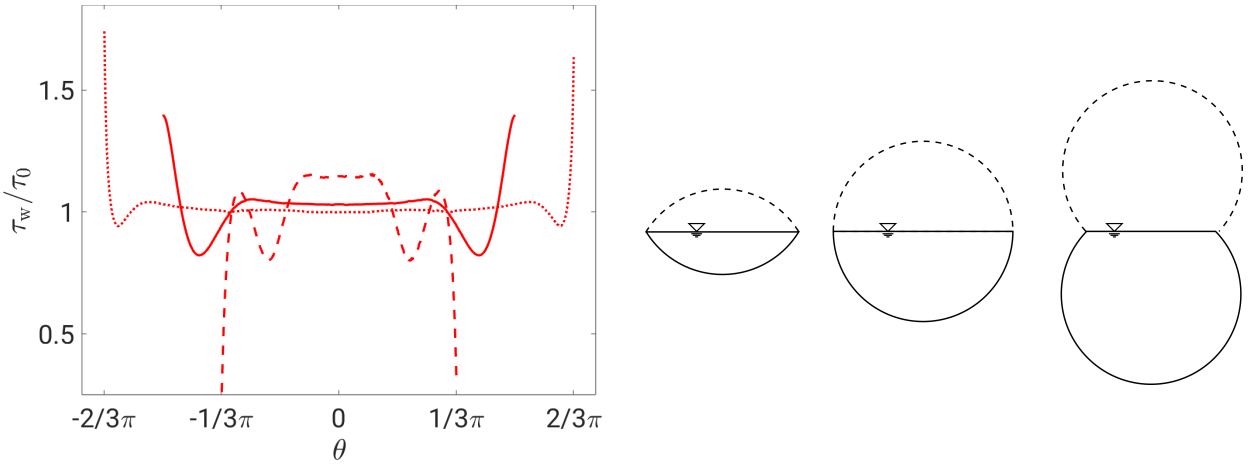

Figure 3.39: Left: Normalised mean wall shear stress τ_w/τ_0 of $Re_\tau = 180$ for 25%(- - -), 50%(——) and 75%(·····). Right: present wall (solid line) and mirrored wall (dashed line) due to the slip boundary condition at the free surface. Please note, that the distributions were symmetrized using the half-plane symmetry.

except the solid corners.

The wall shear stress distributions can be compared to experimental data of Knight & Sterling (2000), however, their Reynolds numbers are much larger than those of the present study. Surprisingly, the distributions agree well, see figure 3.40. Of course the experiments were not able to measure the inner secondary cell, as it scales with wall units. But the magnitudes of the plateau in the centre of the perimeter match very well. Moreover, the magnitude of the minimum in the mixed-corner is similar to the magnitude of the minimum between the inner and outer secondary cells of the present simulations. For 50% FR, only the maximum in the mixed-corner misses. The 75% FR is compared to 66% and 83% FR of Knight & Sterling (2000). The transition of the wall shear stress distribution from 50% FR over 66% to 83% FR is explained by the particular structure of the secondary flow that shifts towards the upper part of the cross-section with increasing flow depth, and therefore, less high-momentum fluid is transported onto the lower part of the pipe. The 83% filled pipe

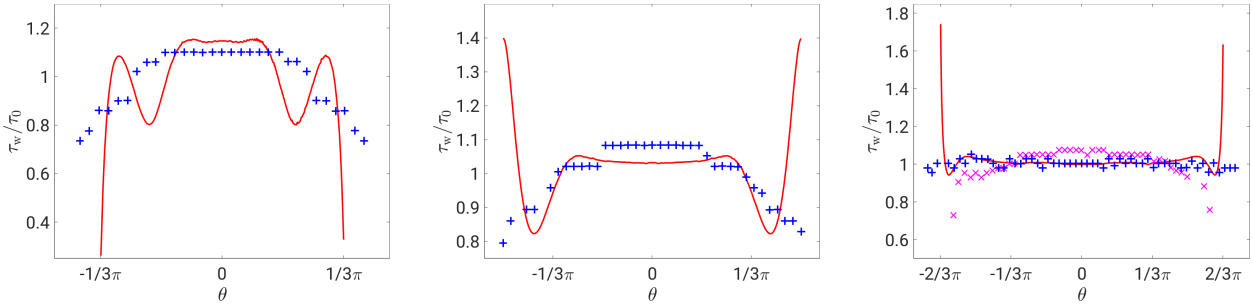

Figure 3.40: Normalised mean wall shear stress τ_w/τ_0 of $Re_b \approx 5300$ (——) for 25% (left), 50% (middle) and 75% FR (right), including τ_w/τ_0 as + for 33% (left), 50% (middle) and 83% and as × for 66% (right) by Knight & Sterling (2000) of $Re_b = 64,000 - 150,000$.

flow shows an almost constant wall shear stress over the perimeter, just like the simulation for 75% filling ratio, except for the small minimum and the stronger maximum at the mixed-corner, which is hard to detect in experiments. For 25% FR the comparison is made to a 33% filled pipe-flow, which does already show a *velocity-dip* phenomenon. Moreover, the wall shear stress distribution of Knight & Sterling (2000) shows a similar pattern as the 50% FR with one maximum in the centre and minima at the sides. Translated into secondary flow, it would mean that two counter-rotating vortices transport high-momentum fluid from the centre of the free surface towards the pipe's bottom. No additional maxima or minima are reported by Knight & Sterling (2000), hence, there are no more footprints of secondary flow documented. For the other filling ratios the inner vortex is relatively small and therefore difficult to detect by measurements, but for the 25% FR, and therefore also for 33% FR, the inner secondary vortex covers such a large area of the cross-section, that measurements should detect it. Unfortunately, Knight & Sterling (2000) did not measure any in-plane velocities. As mentioned above, it seems that the present wall shear stress distribution of 25% FR is much more resembled by the trapezoidal cross-section (Tominaga *et al.*, 1989). Their measurements reported an inner secondary cell, which covers most of the area between the side wall and the free surface, for even higher Reynolds numbers, however, the geometry is slightly different.

The root-mean-square of the wall shear stress fluctuations gives an idea how large the fluctuations deviate from the local mean value. Figure 3.41 shows that the basic pattern of the rms of the wall shear stress fluctuations is similar for all fillings. There is a maximum in the mixed-corner, a small minimum next to it and a plateau-like mid-section. For the 25% and the 50% FR, another local maximum occurs next to the minimum. The maxima of 25% and 75% FR are higher than for 50% filling ratio by a factor of approximately 1.2 and 1.3, respectively. The rms-maximum in the mixed-corner corresponds to 0.3-0.5 of the mean wall shear stress maximum. The minima are lowest for 25% FR and similar for 50% and 75% FR and the plateau is for all three filling-ratios around $\tau_{w,rms}/\tau_0 \approx 0.35$. It implies that extreme events mostly occur at the mixed-corner.

The azimuthal distance from the mean wall shear stress minimum to the mixed-corner is in a range of 55-90 wall units for different Reynolds numbers of semi filled pipe flow. For the different filling ratios at $Re_\tau = 180$, figure 3.42 shows that this range only holds true for low filling ratios. For the 75% FR, the distance drops to 20 wall units. The azimuthal distance to the first minimum of the wall shear stress distribution and separation point of secondary flow have a similar trend: in general the distance gets smaller as the filling ratio increases. For 25% FR, the azimuthal distance to the first minimum of the wall shear stress distribution agrees very well with the distance of the separation point of streamlines. For 50% filling ratio, the distance is about 10 wall units larger than for the wall shear stress, whereas it is about ten wall units smaller for 75% filling ratio. This shows that the wall shear stress and the secondary flow are linked and describe a similar flow structure.

In order to get an impression of the instantaneous near-wall flow a snapshot of the streamwise velocity located at a constant wall distance of 10 wall units is shown in figure 3.43 for different filling ratios. For 25% FR, there are small velocities in the mixed-corner, followed by a small layer where only few extreme values occur and in the middle part streaks with very high and very low intensities alternate. For 50% filling ratio, an alternating pattern of velocity streaks with very high and very low intensities are all over the cross-section, which is also the

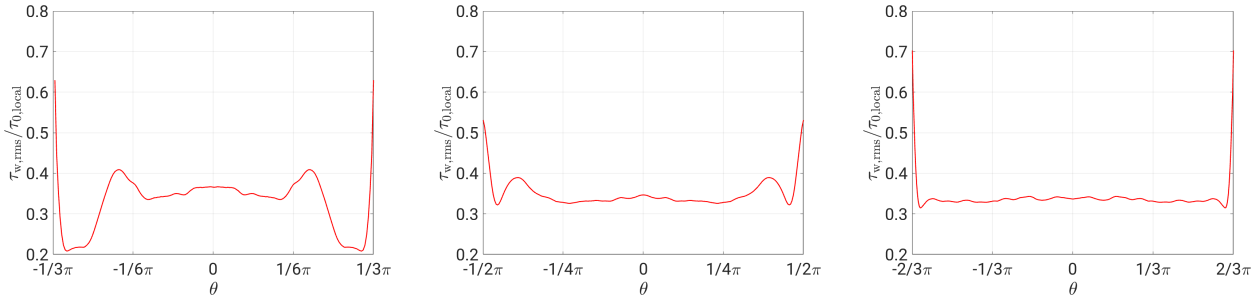

Figure 3.41: Root-mean-square of local, normalised wall shear stress fluctuations $\tau_{w,rms}/\tau_0$ over the perimeter for $Re_\tau = 180$ for 25%, 50% and 75% filling ratio (left to right). Please note the different ticks and limits of the horizontal axis. Please note, that the distributions were symmetrized using the half-plane symmetry.

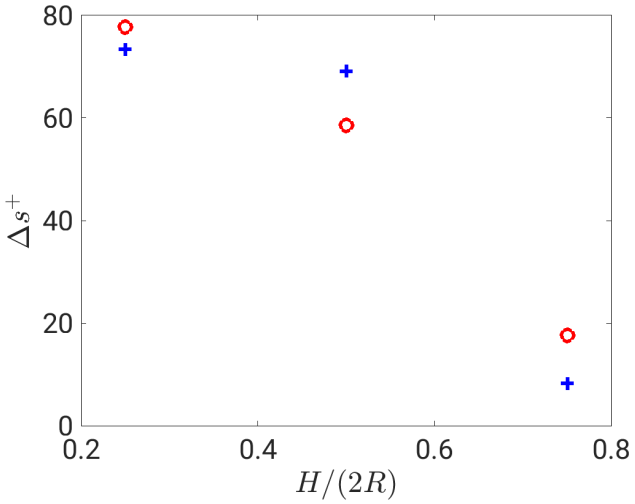

Figure 3.42: Azimuthal distance in wall units Δs^+ from mixed-corner to first minimum of wall shear stress (○) and to the separation point of the secondary flow (+) for $Re_\tau = 180$.

case for 75% FR. The size of the streaks seems to be increasing as the filling ratio increases, which also controls the number of streaks fitting along the perimeter. Please note, that as the streaks are scaling in wall units, this should be in direct relation to the definition of the friction Reynolds number, which was kept constant $Re_\tau = \frac{u_\tau 2R_H}{\nu} = 180$. The hydraulic radius for the 25% FR is approximately half of R_H of the 75% filled pipe flow. Hence, the wall units of 75% FR are twice as large as for 25% FR, but its wetted perimeter is also twice as long. The number of high velocity streaks included are approximately four for 75% FR and five for 25% and 50% FR.

From the instantaneous streamwise velocity distribution in the cross-section no particular pattern can be found in order to distinguish between the inner and outer secondary vortex, as the different minima and maxima are not distributed in a sorted manner, see figure 3.44. This implies, that the secondary flow is rather a product of many different single events than a mean flow only slightly fluctuating over time. Moreover, the *velocity-dip* phenomenon can

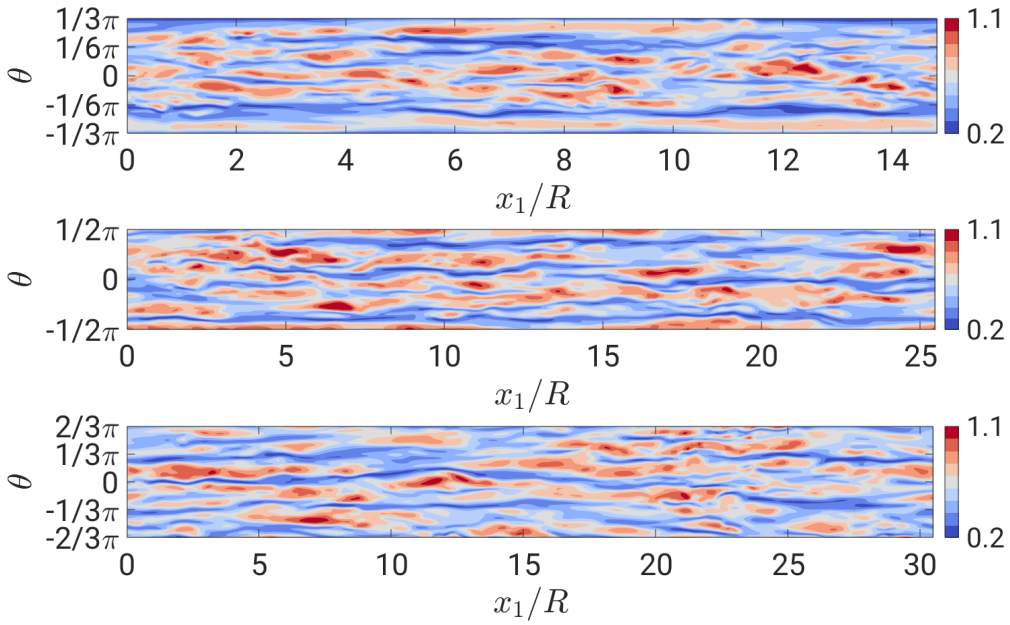

Figure 3.43: Instantaneous normalised streamwise velocity u_1/u_b at a constant distance of 10 wall units from the wall over the channel length for $Re_\tau = 180$ for 25%, 50% and 75% filling ratio (top to bottom).

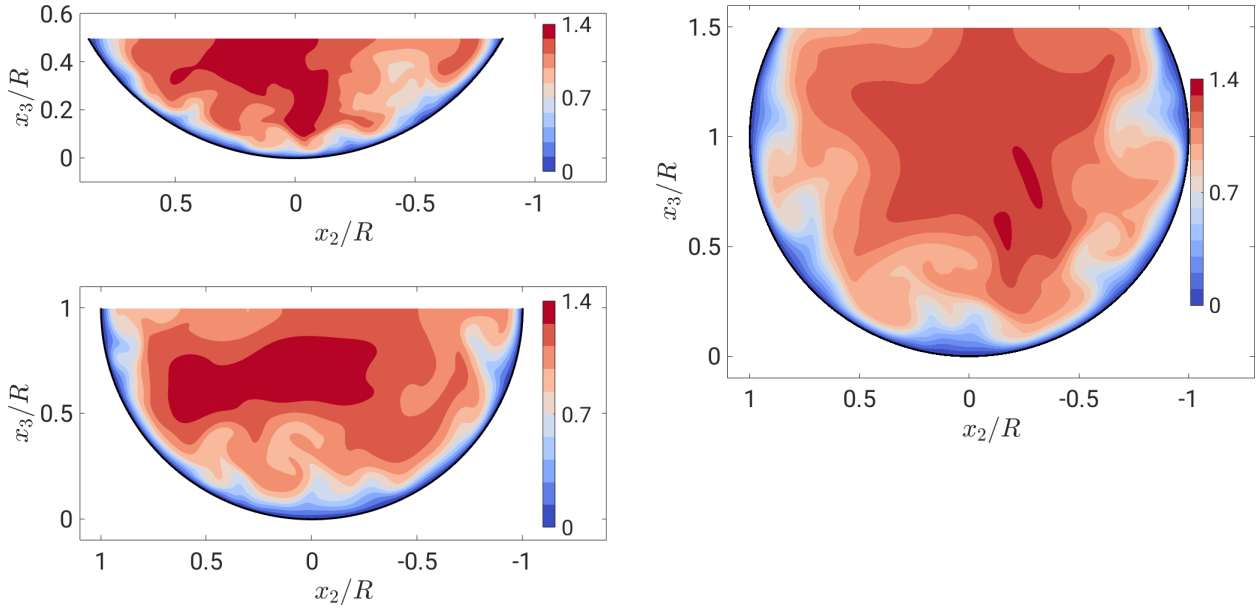

Figure 3.44: Instantaneous normalised streamwise velocity u_1/u_b over the cross-section for $Re_\tau = 180$. Left column 25% and 50% FR, right column 75% FR.

be detected for 50% and 75% FR, whereas for 25% FR the velocity maximum is closer to the free surface.
For figure 3.45, the azimuthal wall shear stress distribution was short-time averaged at a fixed streamwise position. The averaging interval was one flow-through time L/u_b and in total $40\,L/u_b$ intervals are shown. In this representation, the short-time fluctuations which obscured the long-term variations of the wall shear stress are not visible. For 25% FR, a small layer of low intensity with the extent of only a few wall units that is hardly visible in this representation occurs directly in the mixed-corner. It is followed by an area of moderately high wall shear stress. Then a strong minimum appears almost throughout the 40 snapshots. In the middle, an alternating pattern of high and medium intensities occurs. The distribution of the 50% filling ratio starts with highest wall shear stresses in the mixed-corner and next low τ_w occur. The area of randomly distributed, moderately high and low wall shear stresses covers more than half of the perimeter. Similar to 25% filling ratio, a very small layer of a few wall units directly in the mixed-corner exists also for 75% FR, however, it consists of very high intensities. It is followed by a minimum and an alternating pattern over most of the perimeter, but in this case almost without any extreme events. This goes hand in hand with the impression from the instantaneous velocity streaks, see figure 3.43, and the mean wall shear stress distribution which can be extrapolated from this short-time average behaviour. Similar to the results of the Reynolds-dependency this short-time average is already able to capture most of the general features of the mean wall shear stress distribution.

3.3.3. Reynolds Stresses

This section investigates the Reynolds stresses for different filling ratios in the partially filled pipe flow. In figure 3.46, the different components of the root-mean-square of the velocity fluctuations of the different fillings are compared with each other in the symmetry plane. Near the wall, the distributions of all FRs lie almost on top of each other for $u_{1,rms}$, $u_{3,rms}$ and $\overline{u_1' u_3'}$, only for $u_{2,rms}$, the first peak is filling ratio dependent. With decreasing FR the peak increases, however, full pipe flow matches semi filled pipe flow. In the outer layer stronger deviations appear for the different Reynolds stress distributions. At approximtely 100 wall units $u_{1,rms}/u_\tau$ has a minimum of 0.94 for 25% and 50% FR, and approximately 0.8 for the 75% FR. The maximum afterwards, towards the free surface increases with filling height. The transverse component $u_{2,rms}$ also has a minimum with a following maximum at the free surface. With increasing filling ratio, the magnitude of the minimum and the maximum both increase. For $u_{3,rms}$, the 25% FR shows a monotonical decrease, whereas 50% and 75% FR have a less steep gradient after the initial maximum. The 75% FR has a region of almost constant $u_{3,rms}$. Nevertheless, a steep decrease occurs towards the free surface, where all free surface normal fluctuations are damped. The Reynolds shear stress $\overline{u_1' u_3'}$ is also consistent in the outer layer for the different fillings, only the full pipe flow slightly deviates. On the one hand, the full pipe flow and the 25% FR distribution end without a change of sign at zero shear stress. On the other hand, the 50% and 75% FR have a layer at the free surface with positive shear stress, which is stronger for 75% filling ratio. At the free surface these two distributions also come back to zero.
It is obvious, that the free surface has a strong impact on the Reynolds shear stresses. To

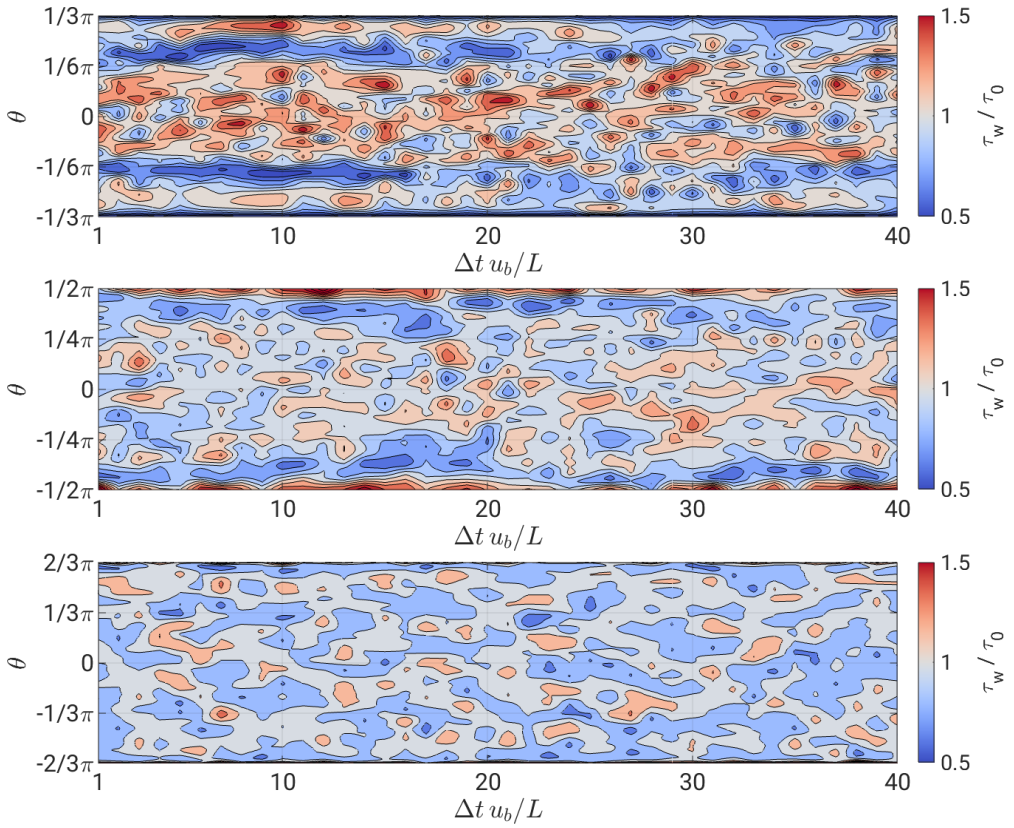

Figure 3.45: Temporal distribution of the normalised averaged wall shear stress τ_w/τ_0 over the perimeter for $Re_\tau = 180$ and a filling ratio of 25%, 50% and 75% (top to bottom). One time instant equals the averaged τ_w over a period of L/u_b. Total time interval is 40 L/u_b.

define exactly the thickness of this layer and where it begins is difficult, since small deviations are present all over the distribution. A change of sign in gradient in comparison to the full pipe flow serves as an estimate of the starting point of influence. For $u_{1,rms}$ and $u_{2,rms}$, the influence can be noticed from approximately 50 wall units away from the free surface and for $u_{3,rms}$ it is difficult to say. The Reynolds shear stress changes sign about 40 wall units away from the free surface. These observations agree with the results of Nagaosa (1999), defining a free surface layer with a size of 50 wall units. However, as mentioned in section 3.2.3, no scaling could be found for different Reynolds numbers of semi filled pipe flow.

The Reynolds stresses can be compared to the experiment by Ng *et al.* (2018) only in outer units, see figure 3.47. First focusing at the bulk region, the qualitative pattern of the distributions of the present study agree well with the experiments, however, the magnitudes of the experiments deviate. At the free surface the experiments underestimate the magnitudes for $u^+_{1,\mathrm{rms}}$ and $u^+_{2,\mathrm{rms}}$ and for $u^+_{3,\mathrm{rms}}$ they do not meet the boundary condition that the vertical component is damped to zero. These deviations occur probably because they could not measure directly at the free surface. On the other hand, their free surface is able to move, hence, a different pattern of Reynolds stresses is possible. In order to assess the free-surface behaviour the Reynolds stresses are compared to the data of Lee *et al.* (2012). They inves-

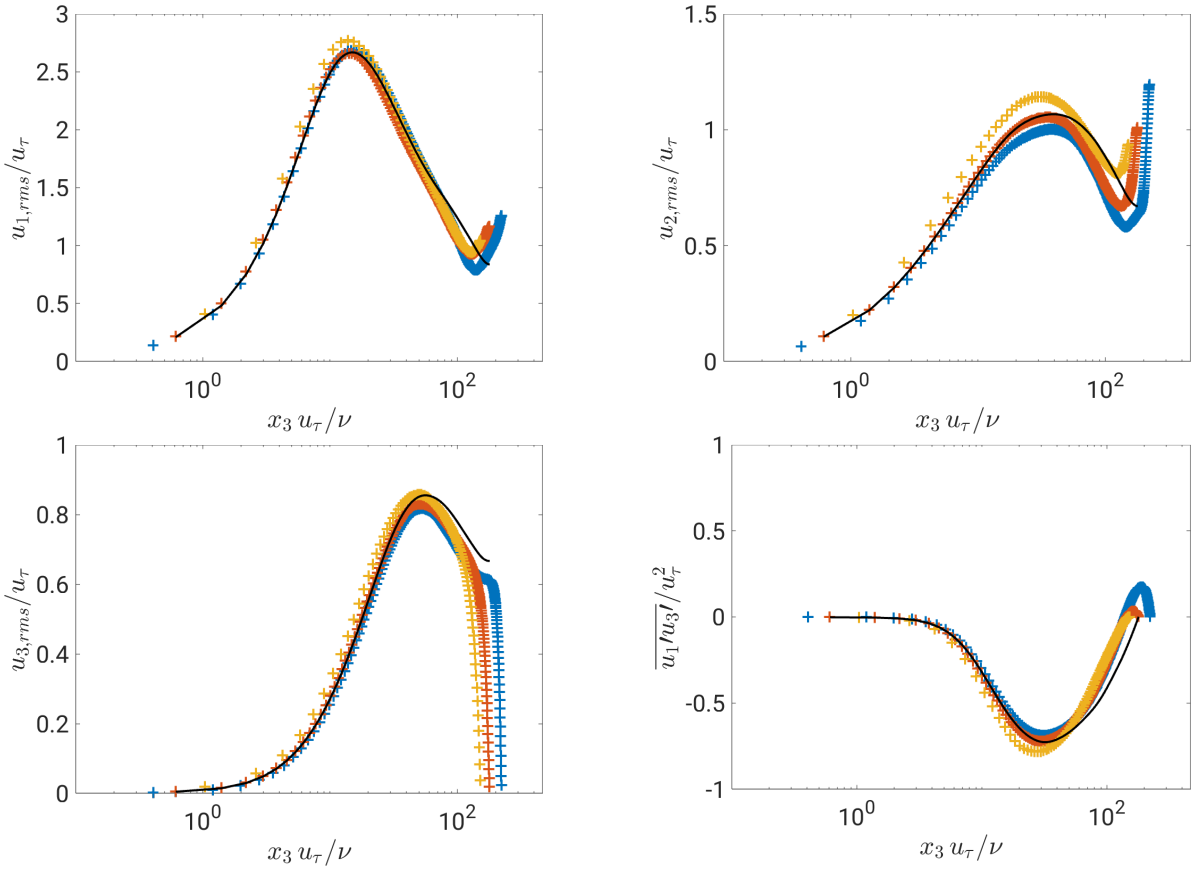

Figure 3.46: Root mean square of velocity fluctuations $u^+_{1,\mathrm{rms}}, u^+_{2,\mathrm{rms}}$ (top), $u^+_{3,\mathrm{rms}}$ and Reynolds shear stress $\overline{u_1'u_3'}/u_\tau^2$ (bottom) in inner units in the vertical symmetry line of $Re_\tau = 180$ for 25% (+), 50% (+) and 75% (+) filling ratio. (—) represents the full pipe flow from present DNS ($Re_\tau = 180$). Please note that in the vertical symmetry line, the Cartesian coordinates in x_2- and x_3-direction are equal to the Polar coordinates θ and r, respectively.

tigated the free surface movement in the mixed-corner using a Direct Numerical Simulation and compared it to experiments. They simulated a rectangular cross-section with an aspect ratio of 1:1. Because of their small aspect ratio and rectangular cross-section the Reynolds stresses show deviations especially near the wall, however, close to the free surface their results show a good agreement with the present study. Please note that their domain length is rather small with $L = 2\pi$. Further note that the flow depth was set to be equal to semi filled pipe flow, however, this is only an assumption to enable the comparison for the free-surface region. Coming back to the experiments of Ng *et al.* (2018), all Reynolds stresses have much lower magnitudes near the wall than the current results. Measuring Reynolds stresses using PIV can be biased by a low-pass filter (Adrian & Westerweel (2011), p. 449), which reduces the actual fluctuations and therefore the Reynolds stresses. This is also mentioned by Ng *et al.* (2018). In addition, due to surface reflections measurements near the wall become even more difficult. Nevertheless, of course there are deviations, but still their data captures most of the main details, like peaks, minima, plateaus and change of sign. The agreement

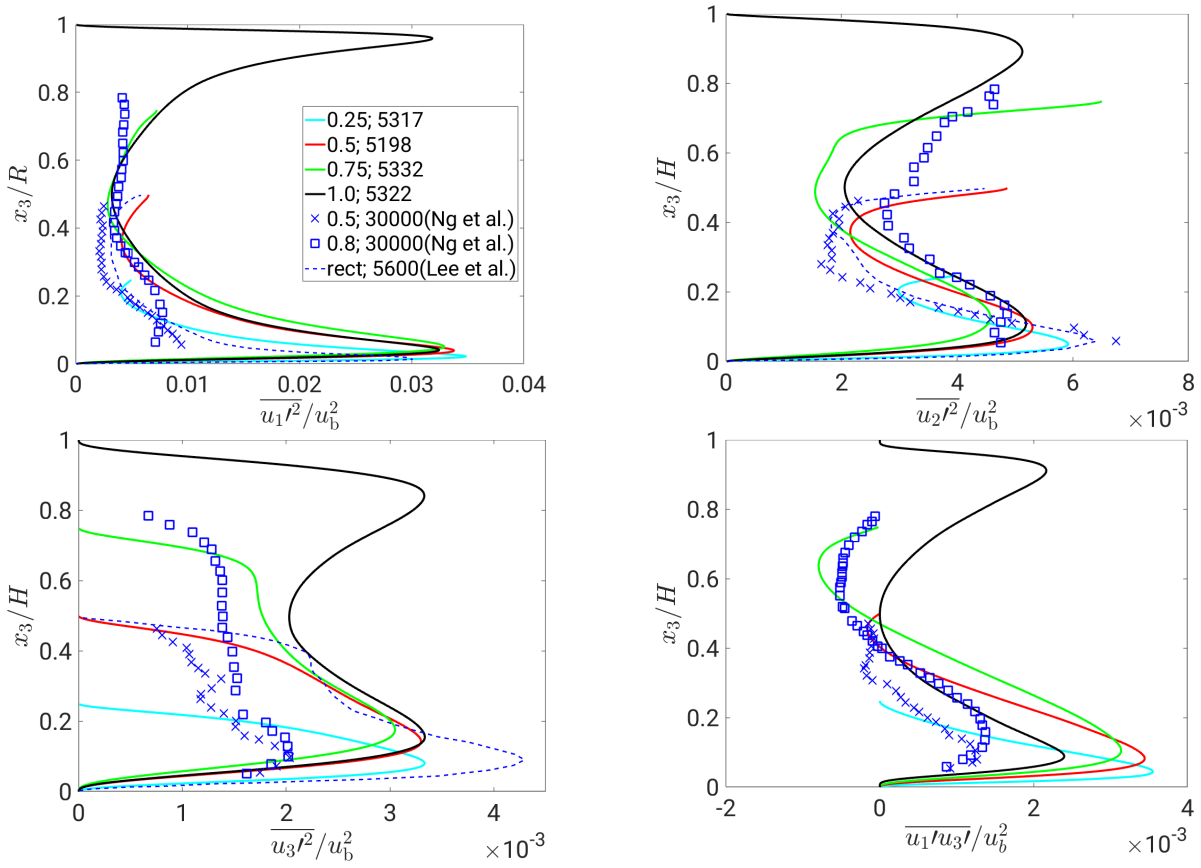

Figure 3.47: Reynolds stresses $\overline{u_1'^2}/u_b^2$, $\overline{u_2'^2}/u_b^2$, $\overline{u_3'^2}/u_b^2$ and $\overline{u_1'u_3'}^2/u_b^2$ in outer units in the vertical symmetry line of $Re_\tau = 180$ for 25%, 50% and 75% filling ratio. Blue data is from experiments of Ng *et al.* (2018) and simulations of Lee *et al.* (2012) for a rectangular cross-section with aspect ratio $W/H = 1$ and a moving free surface.

of the present study with full-pipe flow DNS is very good near the wall. However, in the bulk region, secondary flow and free surface effects influence the present profiles, see figure 3.46.

The distributions of the turbulence intensities over the whole cross-section are shown in figures 3.48. In the left plot the streamwise component and in the right plot the sum of the in-plane components are shown. For 50% and 75% FR, $u_{1,rms}$ is homogeneously distributed in azimuthal direction with some deviations in the upper part of the cross-section due to the secondary flow. In the bottom part the distribution of 25% FR is similar to the higher filling ratios, but shows small intensities in the mixed-corner. All fillings show a minimum in the centre, which is further moving away from the free surface with increasing filling. Similar to the streamwise component, the sum of the in-plane components show high intensities along the perimeter, however, they decrease for all filling ratios approaching the free surface. Furthermore, low intensities occur along the free surface. Both distributions, $u_{1,rms}$ and $u_{\mathrm{r,rms}} + u_{\theta,\mathrm{rms}}$, are homogeneous along the perimeter as long as the secondary flow intensity is low. This homogeneous area becomes larger with increasing filling ratio.

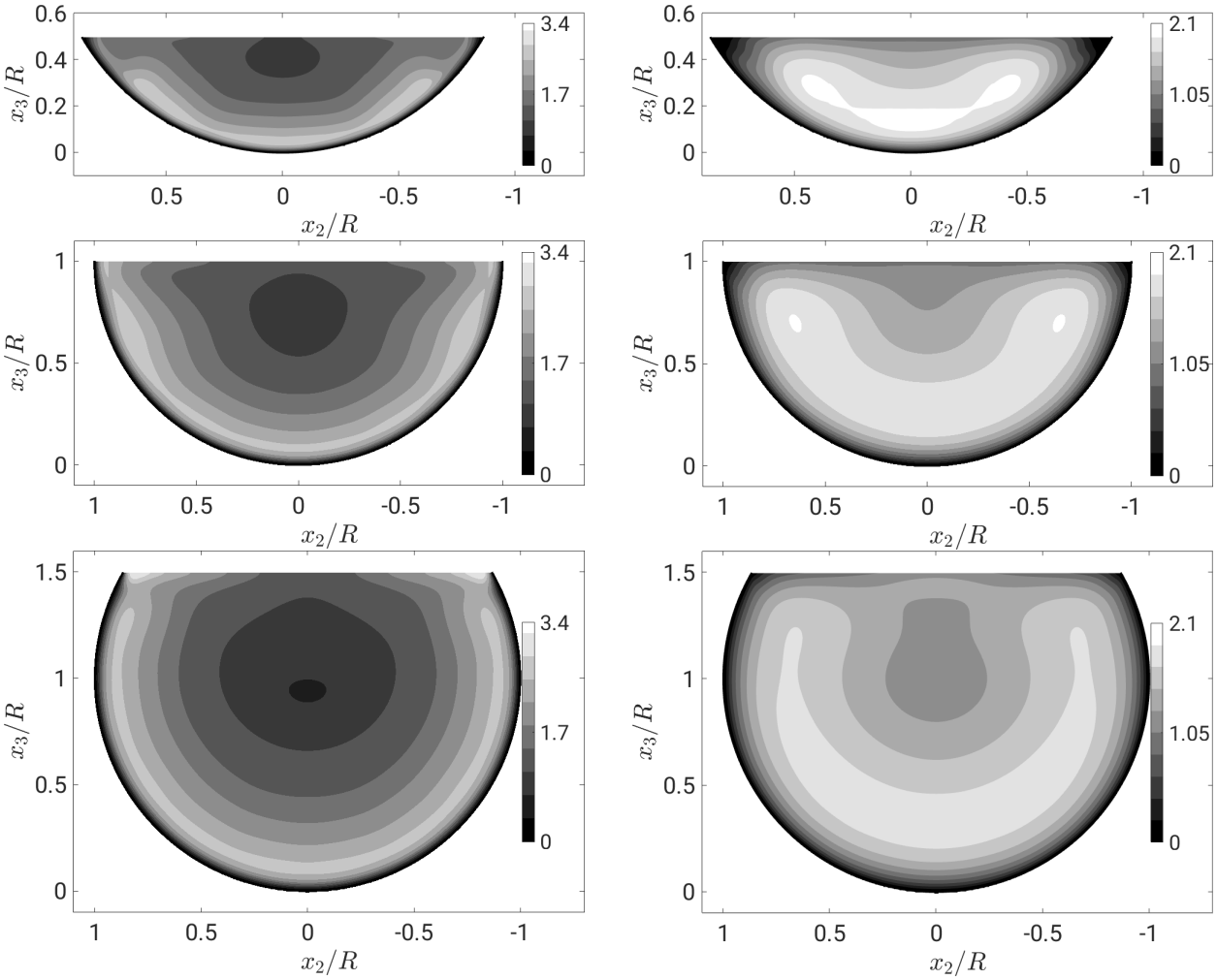

Figure 3.48: Normalised root mean square of velocity fluctuations $u_{1,\mathrm{rms}}/u_\tau$ (left), $(u_{\mathrm{r,rms}}+u_{\theta,\mathrm{rms}})/u_\tau$ (right) for $Re_\tau = 180$ and each filling ratio: 25%, 50% and 75% (top to bottom). Please note, that the distributions were symmetrized using the half-plane symmetry.

The Reynolds shear stresses are shown in Polar and Cartesian coordinate system, see figures 3.49 and 3.50, respectively. Similar to the normal components, $\overline{u_1' u_r'}$ shows a homogeneous layer of high intensities along the perimeter and minima in the top centre of the flow. Peaks can be observed where the secondary flow is directed away from the wall. In addition, the 25% filling has a change of sign with small intensities in the mixed-corner. $\overline{u_1' u_\theta'}$ appears to be small over the cross-section where secondary flow is small and peaks occur where the inner secondary cell is located. Especially for the 75% FR, high intensities concentrate at the free surface, which are only $\overline{u_1' u_2'}$ shear stresses, because the free surface normal component is damped, see figure 3.50. Overall, with increasing filling ratio, the intensities along the free surface become more intense, whereas they become less intense in the bottom part of the pipe.

Corresponding to the colour-mapping of turbulence anisotropy for the Reynolds number dependent cases (see section 3.2.3), figure 3.51 displays the occurrences of one- (red), two-

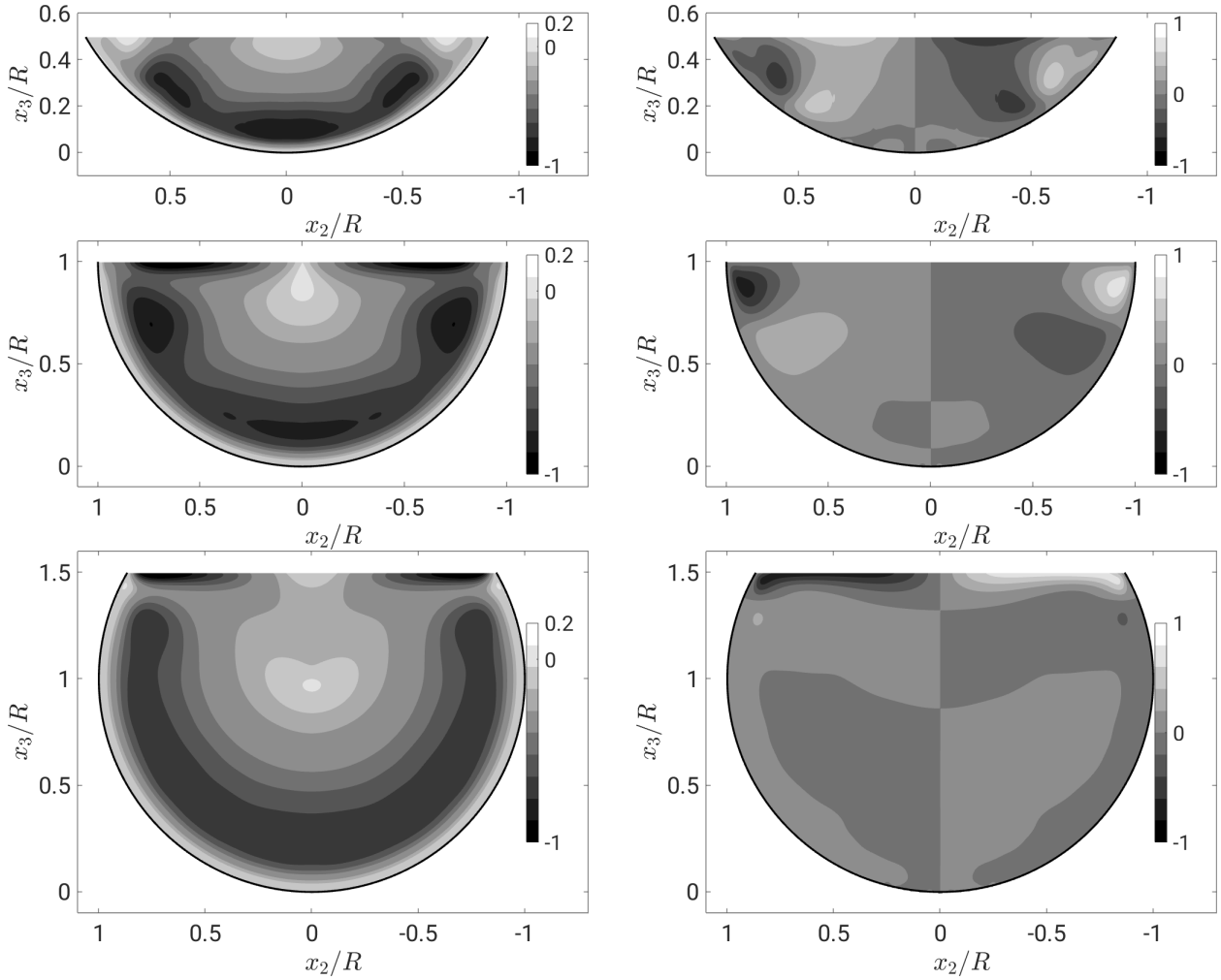

Figure 3.49: Normalised Reynolds shear stresses $\overline{u_1' u_r'}/u_\tau^2$ (left) and $\overline{u_1' u_\theta'}/u_\tau^2$ (right) for $Re_\tau = 180$ and each filling ratio: 25%, 50% and 75% (top to bottom). Please note, that the distributions were symmetrized using the half-plane symmetry.

(green) or three-component (blue) turbulence. As in section 3.2.3, the colourmap is defined according to the Lumley triangle in the lower right. The turbulence anisotropy of the different fillings have many similar aspects: The one-component layer (orange/red) along the perimeter and the transition to three components (blue) where the streamwise velocity maximum is located. Along the free surface, the one-component layer reaches further into the centre with increasing filling height. The transition along the free surface from the state of one- to two-component turbulence (green) takes a longer distance for the lower filling ratio. However, the area of two-component turbulence is similar for different fillings.

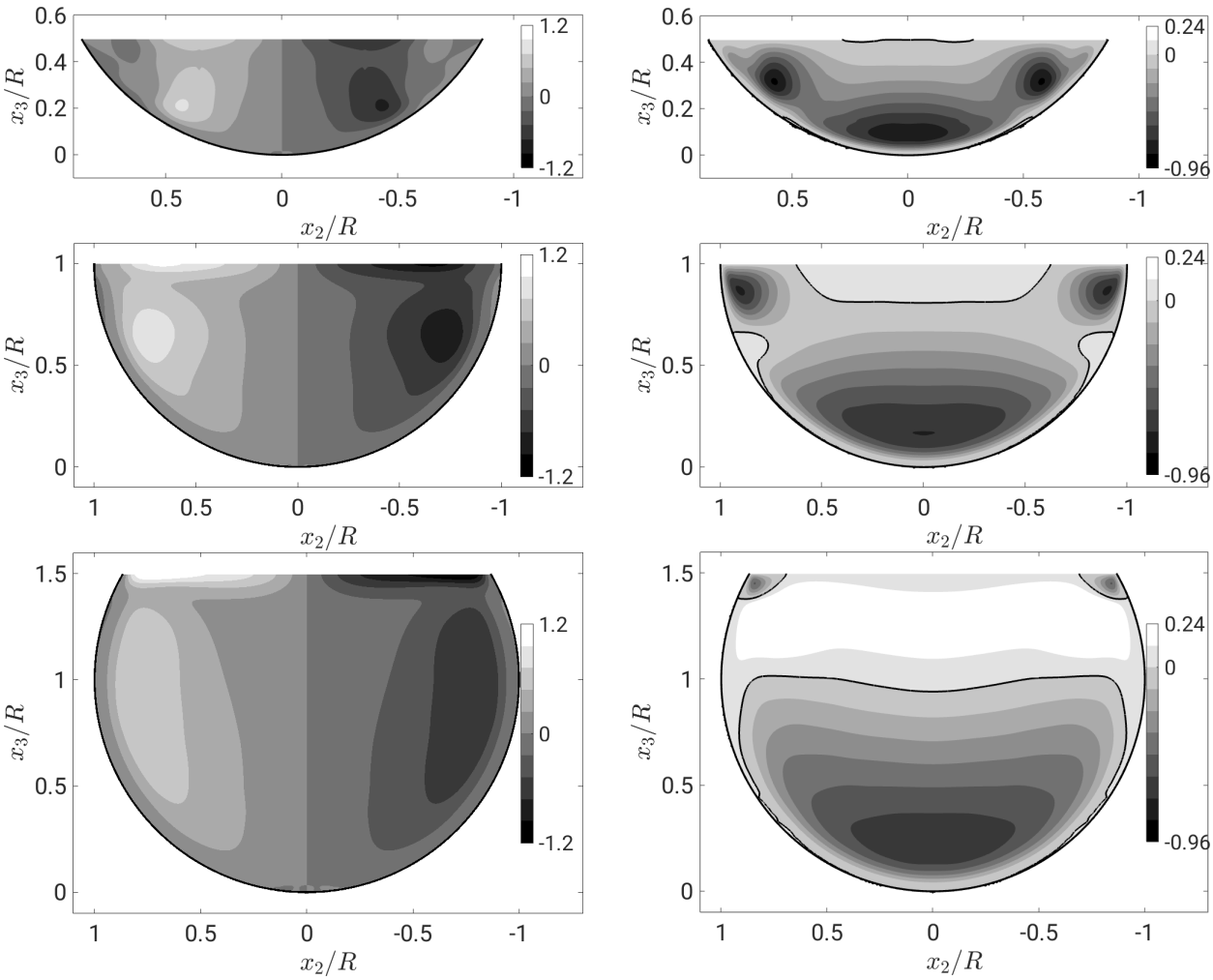

Figure 3.50: Normalised Reynolds shear stresses $\overline{u_1' u_2'}/u_\tau^2$ (left), $\overline{u_1' u_3'}/u_\tau^2$ (right) for $Re_\tau = 180$, 25%, 50% and 75% filling ratio. For a better distinction the zero stress line (black solid line) is added for $\overline{u_1' u_3'}/u_\tau^2$. Please note, that the distributions were symmetrized using the half-plane symmetry.

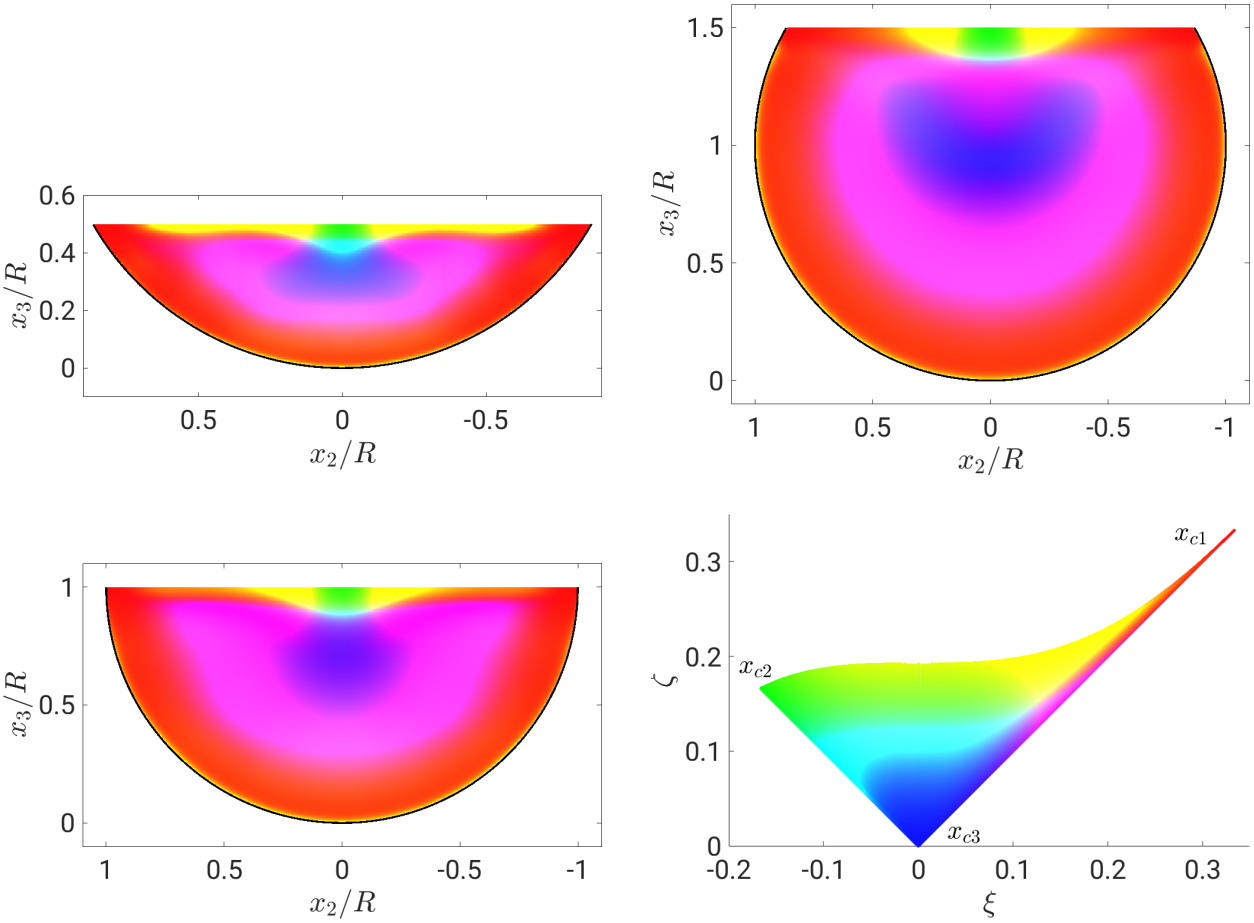

Figure 3.51: Anisotropy componentiality of Reynolds stresses over the cross-section for $Re_\tau = 180$. Left column 25% and 50% filling, right column 75% filling; colourmap according to non-linear anisotropy invariant map. Please note, that the distributions were symmetrized using the half-plane symmetry.

3.4. Conclusion

The computed friction coefficient in the present study for quarter-, semi- and three-quarter filled pipe flow are in good accordance to Prandtl's relation for smooth full pipe flows. This finding establishes an update to previously published experimental results in which the friction factors were reported to lie above the full pipe's values.

For the mean streamwise velocity in general, a good agreement to existing experiments was obtained, however, important details of the flow were found to be different. The analysis of semi filled pipe flow for different Reynolds numbers reports that the appearance and position of the maximum streamwise velocity are Re-dependent and seem to settle at a distance of $0.3 - 0.4/R$ from the free surface for the highest simulated Reynolds number. This is very similar to values found by Sakai (2016) for a rectangular open-channel flow and within the range of values measured by Yoon *et al.* (2012) and Ng *et al.* (2018) for a similar Reynolds number range. In the symmetry plane, the velocity in the lower half of the domain seems to move towards the standard log-law and matches well with the profile measured by Ng *et al.* (2018) at a slightly higher Reynolds number. In combination with all data available in literature on the position of the maximum streamwise velocity Δz, the present results indicate a linear relation between Δz and the FR. It follows $\Delta z/(2R) = 0.6754(H/(2R)) - 0.1642$, providing an easy estimation for the position of the maximum streamwise velocity. Moreover, this relation was used to approximate the streamwise velocity distribution applying the procedure of Guo *et al.* (2015). Good agreement was found between the approximation and the present study, however, the effects of the secondary flow could not be represented by this estimation.

The secondary flow pattern is organised in four vortices which are arranged symmetrically to the vertical bisector in two counter-rotating pairs. Thus, the existence of the so-called *inner secondary cell* appearing in the mixed-corner of partially filled pipe flow, postulated by Grega *et al.* (2002), was confirmed for the investigated range of Reynolds numbers and the different filling ratios. This was already confirmed for rectangular open-duct flows by simulations of Joung & Choi (2009) and Sakai (2016) for low Reynolds numbers. While the geometry of the outer secondary cell scales in bulk units, the position and size of the inner secondary cell in semi filled pipe flow scale with wall units. This could explain, why it has not yet been found in experiments performed at much higher Reynolds numbers as it becomes smaller with increasing Reynolds number. With decreasing filling ratio, the inner secondary cell grows in size, whereas it almost vanishes for a high filling ratio (75%). Hence, the outer secondary cell becomes more dominant with increasing filling ratio. Under which conditions the mixed-corner vortex is present, not only in an averaged sense, but also in instantaneous flow fields, is addressed in the next chapter.

The inner secondary vortex has strong implications on the distribution of the wall shear stress over the perimeter. The inner vortex transports high-momentum fluid from the free surface towards the wall, which results in a global maximum of the wall shear stress in the mixed-corner. For semi filled pipe flow, an almost harmonic wall shear stress distribution can be observed for the lowest Reynolds numbers with a local maximum in the centre of the perimeter. At Reynolds numbers above $Re_\tau \approx 140$, a plateau is formed in the centre of the perimeter, which becomes wider as Reynolds number increases. At the highest simulated Reynolds number, the wall shear stress in the centre is only slightly above the global wall

shear stress, whereas in the mixed-corner, it is more than 40% larger. With increasing filling ratio, the region of constant wall shear stress in the centre enlarges, and despite the less intense inner secondary cell for high filling ratios, the maximum in the mixed-corner increases. For the 25% filling ratio, there is a minimum of wall shear stress directly in the mixed-corner. This is due to the narrow flow section in the mixed-corner, where the wall friction has a stronger impact on the flow than in the other regions. So far, the wall shear stress variations in the mixed-corner, presented in this study, have not been reported in literature for partially filled pipe flow yet.

Instantaneous near-wall streamwise velocities are organised in a streaky pattern like in a standard, full pipe flow. The increased near-wall velocities in the mixed-corner can not be seen in instantaneous distributions. By applying running time averages on the wall shear stress over time intervals of L/u_b, the large wall shear stress fluctuations occurring in the mixed-corner are smoothed, and the mean wall shear stress distribution becomes detectable.

The Reynolds stresses in the symmetry plane behave similarly to the full pipe flow, apart from a narrow layer at the free surface in which the vertical component is damped and the horizontal components are amplified. In the lower part of the pipe, the Reynolds stresses are nearly homogeneously distributed in azimuthal direction. At the free surface and especially at the mixed-corner, this homogeneity is broken by the fact that local maxima or minima occur in and around the corner vortex. An anisotropy map highlights the prominent role of the free surface and the corner vortex for the Reynolds stresses and infers a Reynolds stress anisotropy. Moreover, it gives rise to the generation of mean streamwise vorticity which – according to the classical picture – is a necessary condition for the generation of secondary flow, which will be discussed in the next chapter.

4. Generation Mechanism of Secondary Flow

Chapter 3 revealed that the mean secondary flow has a much smaller magnitude than the streamwise velocity, but its influence on the streamwise velocity and on the wall shear stress distribution is profound. In general, two counter-rotating vortices occur on each side of the symmetry plane. One vortex is located in the mixed-corner, scaling with wall units, and the second vortex is attached to the free surface, which becomes more dominant with increasing filling ratio and increasing Reynolds number. The *velocity-dip* phenomenon occurs for $Re_\tau \geq 140$ for semi filled pipe flow and 75% FR. The 25% filled pipe flow does not show the *velocity-dip* phenomenon and resembles a trapezoidal open-channel flow. Except for 25% FR, the wall shear stress has a maximum in the mixed-corner followed by a minimum which is fully compatible with the secondary flow pattern. From the literature survey and the results of chapter 3 following questions arise:

- Under which conditions is the mixed-corner vortex present?
- How and where is the streamwise vorticity generated?
- How does the mean secondary flow obtain its kinetic energy?
- What is the size and structure of coherent structures and how do they correlate to the mean secondary currents?
- Which structures are involved in the generation mechanism of mean secondary flow and how do they interact?

As mentioned in section 1.3, different approaches exist which try to explain the mechanism of secondary flow. However, there is no comprehensive answer yet. One very important aspect was mentioned by Nikora & Roy (2012) that the different explanations for secondary flow are different perspectives on the same phenomenon, which all accentuate other aspects of the flow based on the Navier-Stokes equations. The aim should be to bring the different perspectives in agreement to obtain a full picture of the secondary flow mechanism (Nikora & Roy, 2012). In the following chapter approaches to the secondary flow mechanism, such as the mean vorticity equation, the mean and turbulent kinetic energy budgets and proper orthogonal decomposition, are applied to partially filled pipe flow. Moreover, new methods that provide additional perspectives are introduced: Gaussian filtering and conditional averaging of the flow field. By interpreting the results in combination, the above mentioned questions are tackled.

4.1. Balances of the Reynolds-Averaged Flow Statistics

There are various approaches to explain the secondary flow mechanism by analysing the Reynolds-averaged flow (cf. section 1.3), which is appealing, because the secondary flow is a mean flow phenomenon by definition. At first, some of the existing approaches are examined in more detail in order to be able to assess, which of them may offer insights into the secondary flow mechanism in partially filled pipe flows.
One of the approaches was introduced by Yang & Lim (1997) and Yang *et al.* (2012), who analysed secondary flow in rectangular and trapezoidal open-channel flows and open channels with longitudinal ridges. They used the RANS-equations and simplified versions for the near-wall and bulk flow in order to explain the generation and appearance of the mean secondary flow. However, some of their conclusions can neither be completely applied to the DNS data of Sakai (2016) nor to the present data of partially filled pipe flow. For example, Yang & Lim (1997) and Yang *et al.* (2012) introduced the concept of division lines, which only applies for larger Reynolds numbers and does not take the mixed-corner vortex into account. In the vicinity of solid corners, they concluded that secondary flow points towards stronger wall shear stress. This can be applied to the vortices directly in touch with the solid corner, however, not for the inner secondary cell at the mixed-corner. Moreover, they have argued that the place where secondary flow is generated should be where secondary flow is strongest. In the case of longitudinal ridges, the strongest secondary flow can be found in the vicinity of the ridges themselves. While for Sakai (2016) and the present flow case, the maximum of mean secondary flow can be found at the free surface, which makes a comparison difficult. Nevertheless, at the free surface, where the maximum intensities of the secondary flow can be found for partially filled pipe flows, the production of mean secondary flow via the MKE-budget, which will be discussed in section 4.1.2, shows a peak as well. In conclusion, the concepts of Yang & Lim (1997) and Yang *et al.* (2012) can hardly be used to explain the generation processes of secondary flow occurring in partially filled pipe flows. Mainly, because they were set up for different geometries and a different scope, as they have described high Reynolds number flows, hence, they did not consider the inner secondary cell, which is a main focus of this study.
The other approaches examining the Reynolds-averaged flow, that seem to be promising to get insights into the secondary flow mechanism, are the analysis of the mean vorticity equation and the budget equations of the MKE and TKE (Nikora & Roy, 2012). The investigation of the mean vorticity equation is the classical approach to analyse the secondary flow mechanism (Nezu & Nakagawa, 1993). It enables to assign the generation of streamwise vorticity to terms based on the anisotropy of the Reynolds stresses and to localize the process of vorticity generation. The two budget equations of MKE and TKE form a framework to understand how the incoming kinetic energy is transformed within the flow and how secondary flow obtains its kinetic energy. In the following section, the mean vorticity equation and the budget equations of MKE and TKE are introduced and analysed in detail and, in addition, possible connections between the different perspectives shall be highlighted.

4.1.1. Mean Vorticity Equation

Please note that the results and conclusions for semi filled pipe flow in this section have been partly published in Brosda & Manhart (2022). Results for different filling heights are first published in this thesis.
Einstein & Li (1958) were the first to derive that secondary flow of Prandtl's second kind is present in straight turbulent flows, if anisotropy of the in-plane Reynolds stresses occurs. This conclusion can be drawn from the equation for the mean streamwise vorticity (eq. 1.14), which simplifies for a straight and steady flow to

$$\bar{u}_2\frac{\partial\bar{\omega}_1}{\partial x_2}+\bar{u}_3\frac{\partial\bar{\omega}_1}{\partial x_3}=\frac{\partial^2}{\partial x_2\partial x_3}\left(\overline{u_3'^2}-\overline{u_2'^2}\right)+\left(\frac{\partial^2}{\partial x_3^2}-\frac{\partial^2}{\partial x_2^2}\right)\left(-\overline{u_3'u_2'}\right)+\frac{\partial}{\partial x_2}\left(\nu\frac{\partial\bar{\omega}_1}{\partial x_2}\right)+\frac{\partial}{\partial x_3}\left(\nu\frac{\partial\bar{\omega}_1}{\partial x_3}\right) \tag{4.1}$$

The convection terms on the left hand side are balanced by gradients of the Reynolds shear and normal stress terms and a vorticity dissipation term. The Reynolds shear and normal stress terms have been denoted as *vorticity dissipation* and *generation*, respectively (Nezu & Nakagawa, 1993; Nikora & Roy, 2012). However, the delimitation between the two processes is not accurate. Firstly, because this denomination is not invariant with respect to coordinate transformations. Only as a sum, they are invariant and can be interpreted as generation of streamwise vorticity (Einstein & Li, 1958; Nezu & Nakagawa, 1993). Secondly, positive values of the sum of the Reynolds stress terms generate streamwise vorticity of counter-clockwise rotation. In contrast, negative values do not describe the dissipation of vorticity, they generate streamwise vorticity with the opposite sense of rotation (clockwise) compared to positive values. Thus, if anisotropy of the in-plane Reynolds stresses occurs, streamwise vorticity is generated and, therefore, turbulence-induced secondary flow. In figure 4.1 one can see the sum of the Reynolds stress terms, which is approximately zero over the whole cross-section apart from a small region at the mixed-corners and a layer at the free surface in case of high Reynolds numbers. Please note that for the highest Reynolds number artifacts from the grid refinement are present. These artifacts occur because the boundary of fine to coarse grids is only first order accurate and only conserves mass but not momentum.
For different filling heights, see figure 4.2, the general distribution of the vorticity generation term is similar, the peaks are gathered in the mixed-corner, where always the same sense of rotation is induced. However, in detail they differ: the peak is attached to the side wall for 25%, whereas with higher filling the Reynolds stress anisotropy gets concentrated more and more in the mixed-corner and reaches out along the free surface. The change of sign of the distribution does not perfectly match the separation of inner and outer secondary cell, but it matches fairly well with the vorticity itself, which is shown as contours in the right half of the cross-sections. A large area of high intensity of vorticity generation covers the shear layer at the wall, especially for 25% and 50% filling. Another part is covered by the mixed-corner vortical structure with the opposite sign as the shear layer. A similar pattern can be found in Brosda (2015) for rectangular and trapezoidal open-duct flows and in Kara *et al.* (2012) for compound open-channel flows. In these studies vorticity generation also occurs in the vicinity of the solid-solid corners, nevertheless, the total secondary flow generated is similarly strong as for semi filled pipe flow. This could mean that the mixed-corner alone is

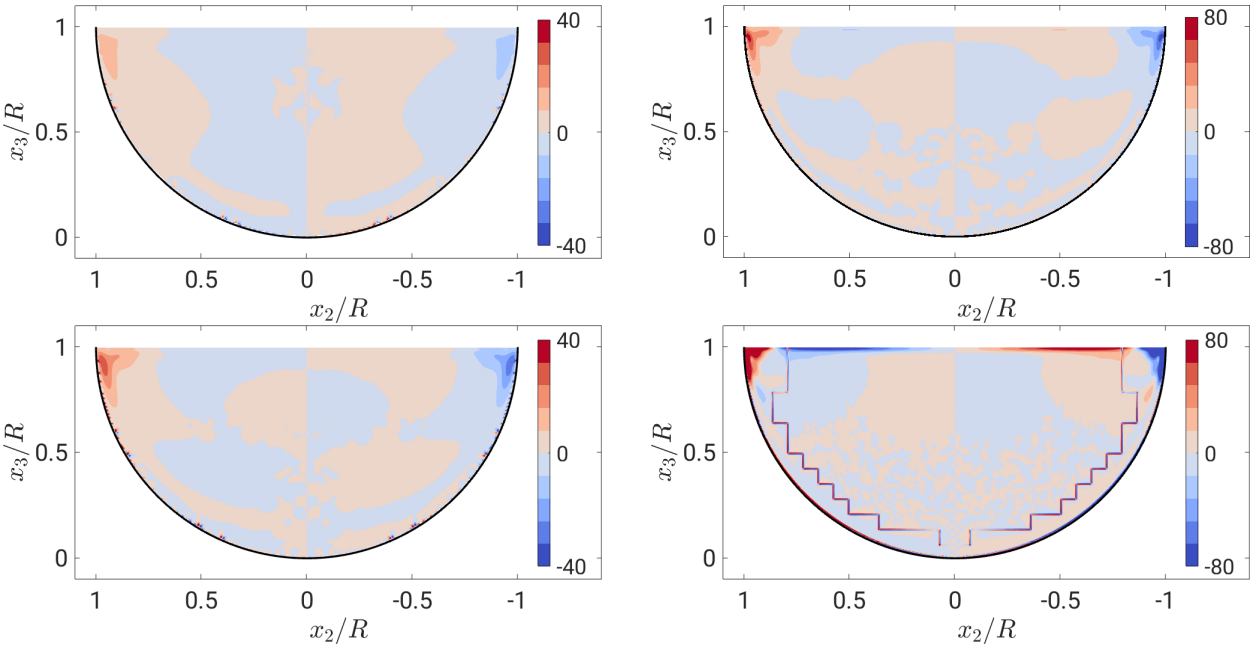

Figure 4.1: Sum of normalised vorticity generation $\left(\left(\frac{\partial^2}{\partial x_3^2} - \frac{\partial^2}{\partial x_2^2}\right)\left(-\overline{u_3' u_2'}\right) + \frac{\partial^2}{\partial x_3 \partial x_2}\left(\overline{u_3'^2} - \overline{u_2'^2}\right)\right) R^2/u_\tau^2$ of $Re_\tau = 115, 140$ (left column) and $180, 460$ (right column, top to bottom). Please note that the range of the colourmap of the left column is smaller by a factor of two. Further note, that the distributions were symmetrized using the half-plane symmetry.

able to produce a secondary flow as strong as generated by a mixed-corner and a solid-corner together. Hence, following the derivation of Einstein & Li (1958) and Nezu & Nakagawa (1993), it can be concluded that the mixed-corner region is responsible for the generation of the mean secondary flow in partially filled pipe flow, which also emphasizes the role of the inner secondary cell.

4.1.2. Mean Kinetic Energy (MKE) Budget

Please note that the results and conclusions for semi filled pipe flow in this section have been partly published in Brosda & Manhart (2022). Results for different filling heights are first published in this thesis.

Theory of MKE-Budget

Nikora & Roy (2012) have proposed a path of kinetic energy highlighting the perspective of the MKE-budget on the generation of mean secondary flow. It is based on the component-wise MKE-budget for steady, straight and uniform flow. The MKE-budget equations are split up into the streamwise component $\overline{u}_1^2$ (eq. (4.2)) and the sum of the secondary components $\overline{u}_2^2 + \overline{u}_3^2$ (eq. (4.3)).

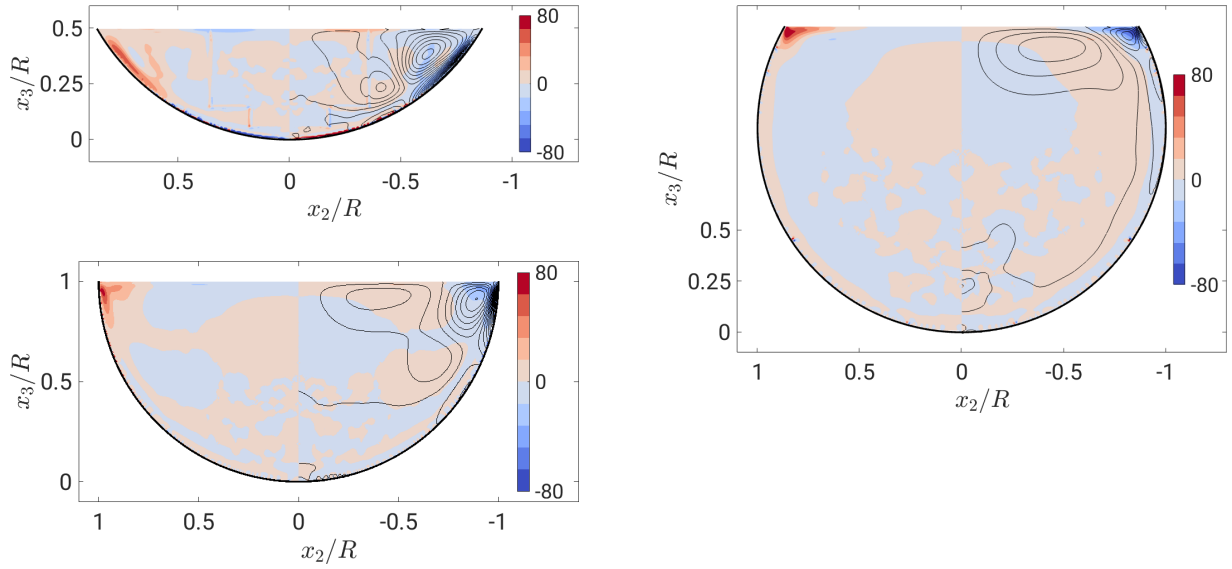

Figure 4.2: Sum of normalised vorticity generation $\left(\left(\frac{\partial^2}{\partial x_3^2}-\frac{\partial^2}{\partial x_2^2}\right)\left(-\overline{u_3'u_2'}\right)+\frac{\partial^2}{\partial x_3 \partial x_2}\left(\overline{u_3'^2}-\overline{u_2'^2}\right)\right) R^2/u_\tau^2$ of $Re_\tau = 180$ for filling ratio 25%, 50% (left, top and bottom, respectively) and 75% (right). In the right half, black contours indicate the distribution of $\overline{\omega}_1$. Please note, that the distributions were symmetrized using the half-plane symmetry.

$$0 = \underbrace{-\ \overline{u}_j \frac{\partial}{\partial x_j}\left(\frac{\overline{u}_1^2}{2}\right)}_{\substack{\text{convection}\\ C_1}} \underbrace{+\ \nu \frac{\partial^2}{\partial x_j^2}\left(\frac{\overline{u}_1^2}{2}\right) - \frac{\partial}{\partial x_j}\left(\overline{u}_1 \overline{u_1' u_j'}\right)}_{\substack{\text{transport}\\ T_1 = T_{1,visc} + T_{1,turb}}} \underbrace{+\ g_1 \overline{u}_1}_{\substack{\text{energy input}\\ \text{by gravity}\\ E_{\text{in}}}}$$
$$\underbrace{+\ \overline{u_1' u_j'} \frac{\partial \overline{u}_1}{\partial x_j}}_{\substack{\text{MKE-production}\\ P_1}} \underbrace{-\ \nu \left(\frac{\partial \overline{u}_1}{\partial x_j}\right)^2}_{\substack{\text{dissipation}\\ \overline{\epsilon}_1}}, \qquad \text{with j} = 2,3 \tag{4.2}$$

$$0 = \underbrace{-\ \overline{u}_j \frac{\partial}{\partial x_j}\left(\frac{\overline{u}_2^2 + \overline{u}_3^2}{2}\right)}_{\substack{\text{convection}\\ C_{2,3}}} \underbrace{-\frac{1}{\rho}\left(\frac{\partial \overline{p}}{\partial x_2}\overline{u}_2 + \frac{\partial \overline{p}}{\partial x_3}\overline{u}_3\right) - \frac{\partial}{\partial x_j}\left(\overline{u}_2 \overline{u_2' u_j'} + \overline{u}_3 \overline{u_3' u_j'}\right) + \nu \frac{\partial^2}{\partial x_j^2}\left(\frac{\overline{u}_2^2 + \overline{u}_3^2}{2}\right)}_{\substack{\text{transport}\\ T_{2,3} = T_{2,3,press} + T_{2,3,turb} + T_{2,3,visc}}}$$
$$\underbrace{+\ \overline{u_2' u_j'} \frac{\partial \overline{u}_2}{\partial x_j} + \overline{u_3' u_j'} \frac{\partial \overline{u}_3}{\partial x_j}}_{\substack{\text{MKE-production}\\ P_{2,3}}} \underbrace{-\ \nu \left(\frac{\partial \overline{u}_2}{\partial x_j}\right)^2 - \nu \left(\frac{\partial \overline{u}_3}{\partial x_j}\right)^2}_{\substack{\text{dissipation}\\ \overline{\epsilon}_{2,3}}}, \qquad \text{with j} = 2,3 \tag{4.3}$$

Please note since the steady volume force driving the flow g_i acts only in streamwise direction ($g_2 = g_3 = 0$), the energy input E_{in} appears only in the MKE-budget for the streamwise component. In a gravity-driven flow, the term $g_3\overline{u_3}$ would be in equilibrium with the hy-

drostatic pressure, hence no energy input would occur in the velocity component u_3. The supplied kinetic energy is redistributed in space by the convection term C_1 and the turbulent and the viscous transport terms T_1. Parts of the energy are directly dissipated ($\overline{\epsilon}_1$) and other parts are transferred to the TKE via the production P_1. Please note that there is no direct inter-component transfer term from the streamwise to the secondary velocity components. The kinetic energy enters the mean secondary flow in a two-step process. First the MKE-production terms P_1 transfer energy to TKE, where it is partly dissipated, redistributed in space and spread among the fluctuation components, see section 4.1.3. Second, some of the remaining part is transferred to the secondary flow ($\overline{u_2}^2 + \overline{u_3}^2$) by the terms $\overline{u_2' u_j'} \frac{\partial \overline{u}_2}{\partial x_j}$ and $\overline{u_3' u_j'} \frac{\partial \overline{u}_3}{\partial x_j}$ ($P_{2,3}$). The secondary MKE is redistributed in space, directly dissipated or transferred back to TKE by the other terms in equation (4.3). In order to verify the suggested path of kinetic energy and to explicitly apply it to the partially filled pipe flow, all important terms of the path will be analysed in the following.

Analysis of MKE-Budget

First of all, the distributions of the primary and secondary MKE and TKE themselves are introduced, see figure 4.3 and 4.4. The distribution of the primary MKE, $\overline{u}_1^2$, is similar to the distribution of the streamwise velocity (figure 3.2) displaying large values of MKE in the pipe's centre and below where the velocity maximum can be found. In the vicinity of the wall, a large bump in the primary MKE distribution can be found for 25% filling and a small bump for 50% filling. These bumps occur, where secondary flow is pointing away from the wall, transporting low momentum fluid to the centre. The distribution of 75% filling is almost homogeneous along the wall. The secondary MKE has peak values less than one per mille of the primary MKE. Two peaks can be found at the free surface symmetrically between the pipe axis and the mixed-corners. Smaller local peaks can be found around the corner vortex. For 75% filling these local peaks miss, because the inner secondary cell is very weak.
The largest values of primary TKE, $\overline{u_1'^2}$, can be found in a band along the perimeter at a wall distance of approximately $x_n^+ \approx 15$, see figure 4.4 (left). For 25% filling a minimum occurs in the mixed-corner, where the influence of friction seems to be strong. In contrast, 75% filling has maximum of primary TKE in the mixed-corner. The maxima of the secondary TKE are distributed along the perimeter at larger wall distances than the maxima of the primary TKE. For 75% filling another local maximum can be found in the centre of the free surface, where TKE is produced, which is discussed later in this section, see figure 4.10.
Table 4.1 provides a quantitative comparison between the primary and secondary of MKE and TKE. The individual energy shares are shown for all different Reynolds numbers and filling ratios. The mean kinetic energy is partitioned into 99.99% of primary kinetic energy and only 0.01% of secondary kinetic energy, which does hardly change for different Reynolds number or filling ratios. The TKE is partitioned into 85% ($Re_\tau = 115$) to 60% ($Re_\tau = 460$) of the primary component and 15% ($Re_\tau = 115$) to 40% ($Re_\tau = 460$) of the secondary components. Different filling ratios do not change the partition, but with increasing Reynolds number the secondary components get more energy, which is in agreement with the Reynolds-dependent observations of the Reynolds stress anisotropy in section 3.2.3.

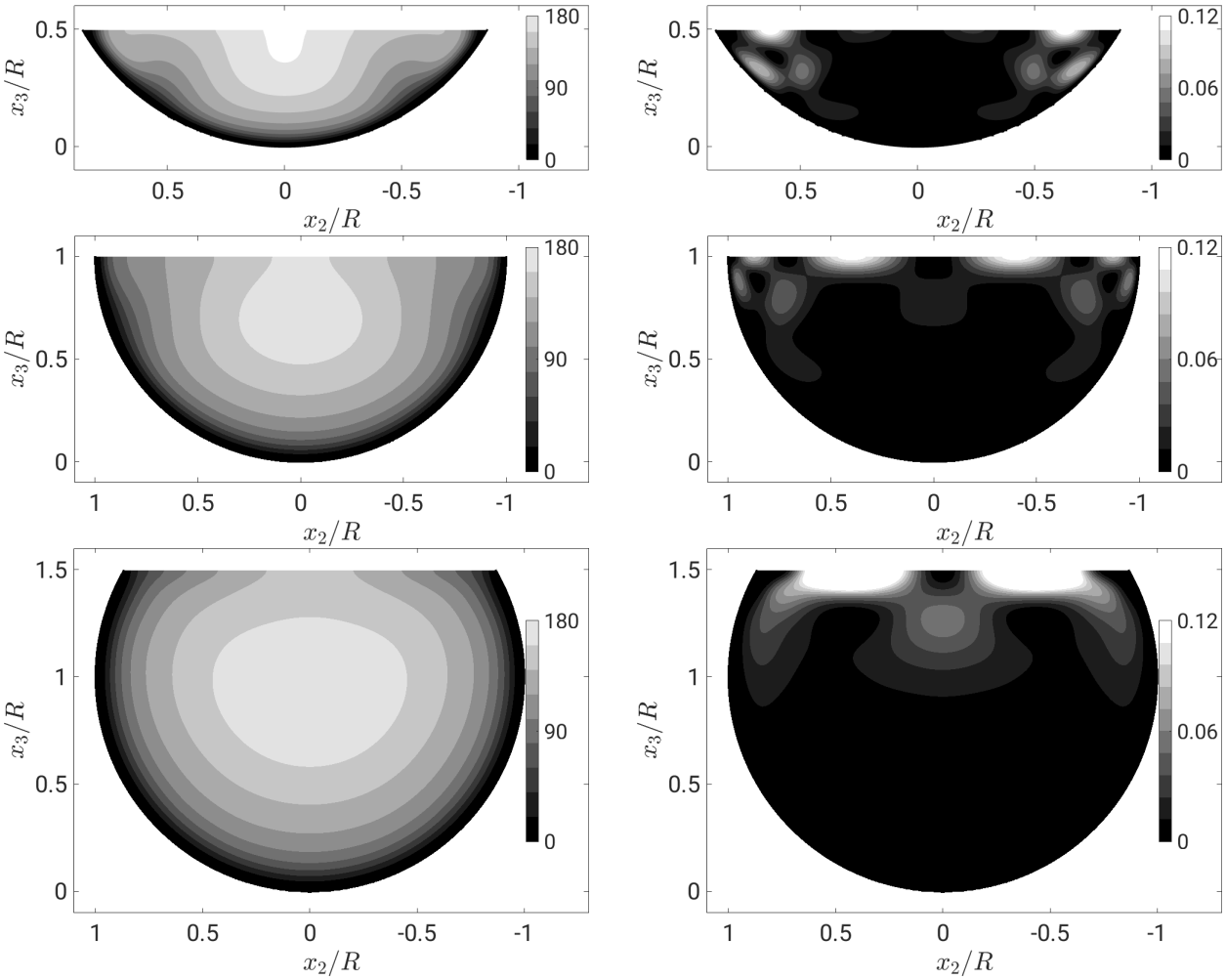

Figure 4.3: Primary (left) and secondary (right) components of MKE of $Re_\tau = 180$ normalised by u_τ^2 for filling ratio 25%, 50% and 75% (top to bottom). Please note, that the distributions were symmetrized using the half-plane symmetry.

Filling ratio	Re_τ	MKE_1	$MKE_{2,3}$	TKE_1	$TKE_{2,3}$
50 %	115	0.99996	0.00004	0.856	0.144
50 %	120	0.99995	0.00005	0.841	0.159
50 %	140	0.99994	0.00006	0.798	0.202
50 %	180	0.99989	0.00011	0.736	0.264
50 %	230	0.99987	0.00013	0.682	0.318
50 %	460	0.99986	0.00014	0.595	0.405
25 %	180	0.99987	0.00013	0.731	0.269
75 %	180	0.99985	0.00015	0.742	0.258

Table 4.1: Partition of total kinetic energy into primary and secondary components for different Reynolds numbers

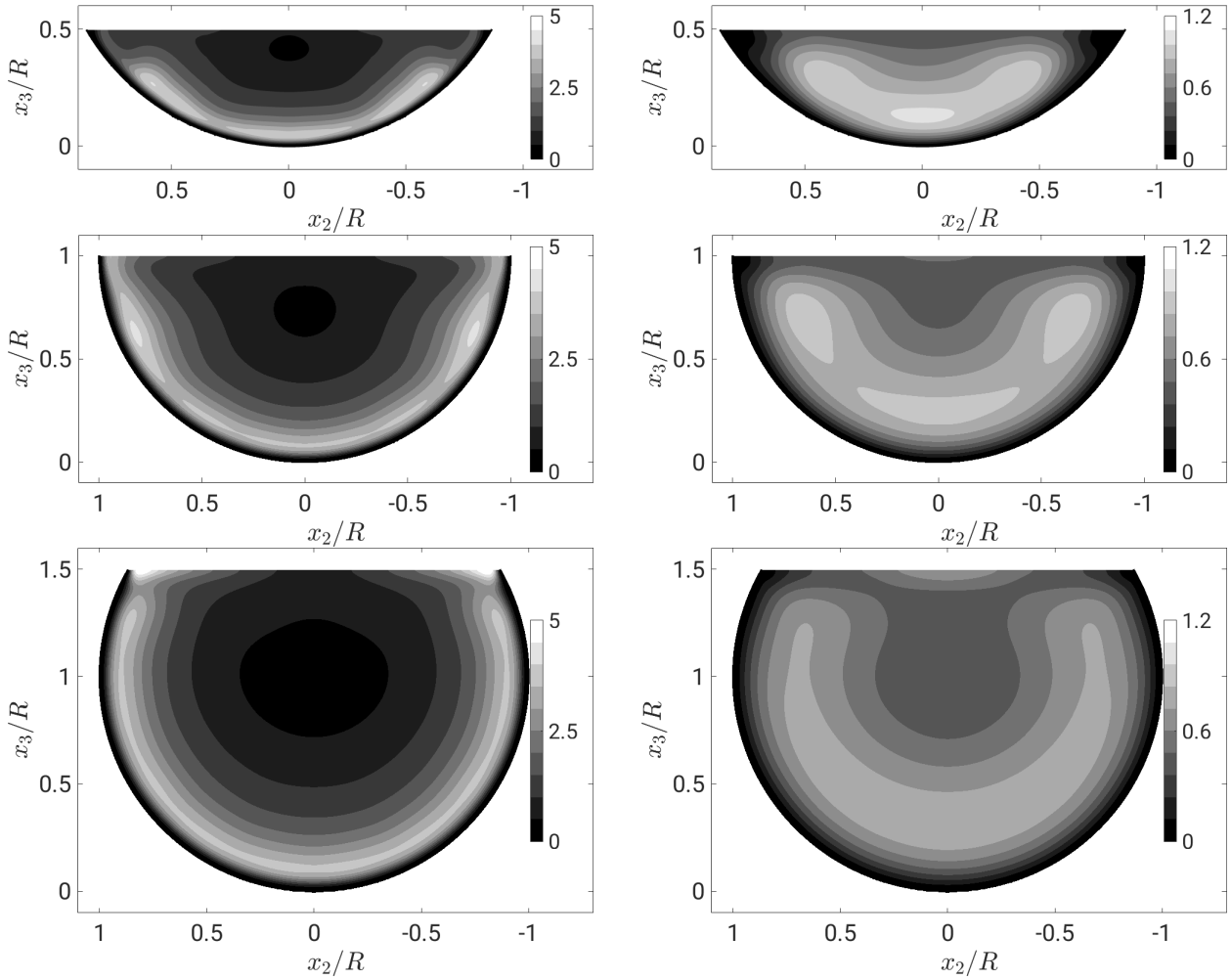

Figure 4.4: Primary (left) and secondary (right) components of TKE k of $Re_\tau = 180$ normalised by u_τ^2 for filling ratio 25%, 50% and 75%(top to bottom). Please note, that the distributions were symmetrized using the half-plane symmetry.

In a next step, the budget of the MKE shall be validated by checking the residuum of the primary and in-plane components of the MKE-budget at the free surface, where strong convection is present. The residuum is the black solid line in figure 4.5 and 4.6. Hence, for the primary MKE-budget the maximum residuum is less than 2% of the maximum of other terms, apart from the very first cell at the wall. For the secondary components the residuum is also less than 2% compared to the other terms apart from the first cells at the wall. Only for $Re_\tau = 460$ a higher residual disturbance at the boundary of grid refinement can be noticed, for the same reason as described in section 4.1.1.

Looking at the magnitude of the budgets, it is obvious that the primary MKE is highly dominating the total MKE budget. Please note that a positive MKE-production P corresponds to a transfer from TKE to MKE and a negative MKE-production P from MKE to TKE. Very close to the wall the viscous transport and the dissipation balance each other. Going further away from the wall the MKE-production, convection and turbulent transport also contribute to the budget. In the bulk region the energy input is mainly balanced by the

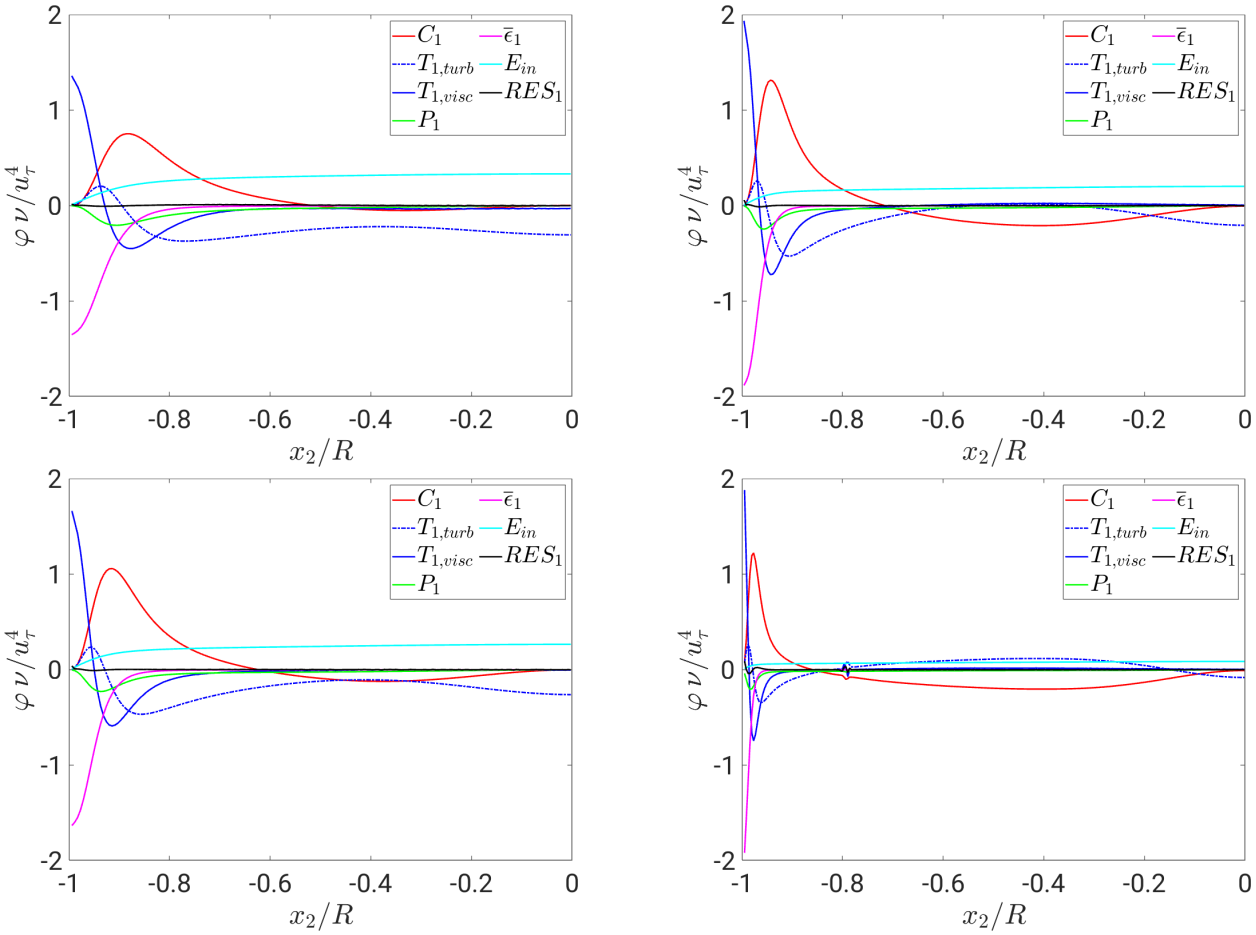

Figure 4.5: Primary terms of MKE budget terms taken four wall units below and parallel to the free surface of $Re_\tau = 115, 140$ (left column) and $180, 460$ (right column, top to bottom).

convection and the turbulent transport. For the primary terms a Reynolds-dependency can be noticed. With increasing Reynolds number the global maxima of all peaks move closer to the wall, $x_2/R = -1$. Moreover, the peaks gain magnitude with increasing Reynolds number and seem to saturate for higher Reynolds numbers. Focusing on the secondary component mostly the terms of MKE-production, convection, pressure and turbulent transport balance each other. Their development with changing Reynolds number is similar to the primary terms. The magnitudes increase and seem to settle for higher Reynolds numbers and the peaks shift towards the wall. A more detailed look on the budget is presented via the expansion of each term over the whole cross-section.

Before describing each term in detail, please note that the visualisations of the primary and secondary components have different scales. Let us start with the terms that redistribute the incoming kinetic energy, thus, the convection and the transport terms. The primary convection is strongly connected to the mean secondary flow. It has high intensities in the mixed-corner, negative at the upper side of the inner secondary cell and positive at the lower side of the vortex and reaching to the centre of the flow (see figure 4.7, left). This means that the secondary flow transports high energetic fluid into the mixed-corners and low energetic fluid from below the inner vortex into the bulk region. Within the area in which

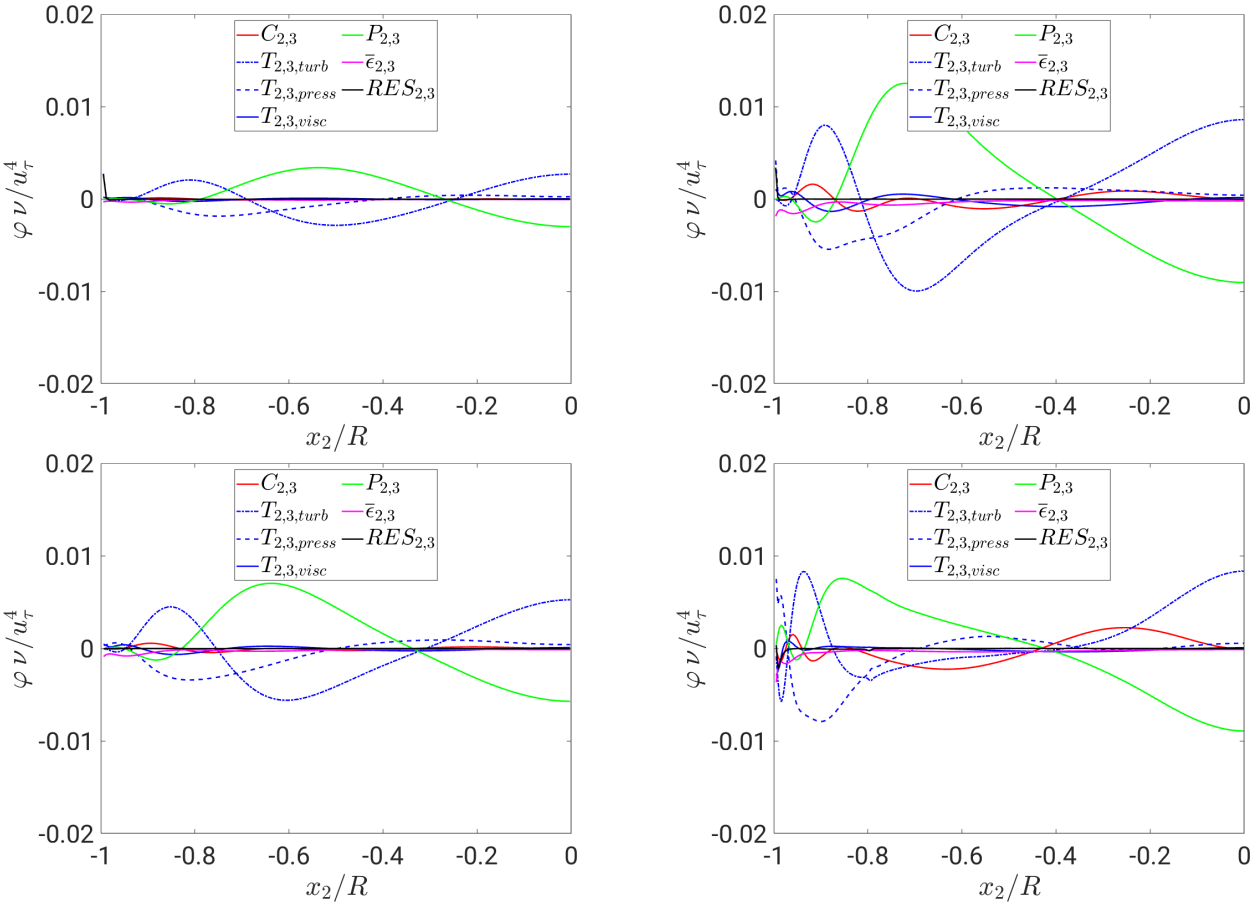

Figure 4.6: Secondary terms of MKE budget terms taken four wall units below and parallel to the free surface of $Re_\tau = 115, 140$ (left column) and $180, 460$ (right column, top to bottom).

the convection term is positive (marked as red) the streamwise velocity and, therefore, the primary MKE increases along the streamlines. The area with negative values in the mixed-corner becomes smaller as the FR increases, similar to the secondary flow. Moreover, for all fillings the convection changes its sign at the position of the *velocity-dip*. The secondary components of the convection are negligible small over the cross-section in comparison to the other terms (see figure 4.7, right). Only for 75% filling small contributions directly at the free surface are noticeable. Integrated over the whole cross-section the convection is approximately 0. Hence, it describes a transport of energy, which does not change the amount of energy over the entire cross-section.

Like convection, each transport term of the MKE-budget integrated over the cross-section equals approximately zero. Therefore, MKE is transported and redistributed by the transport terms, but they cannot produce or dissipate energy, because of their flux divergence form. Overall, the primary transport terms T_1 carry primary MKE from the pipe centre (negative) towards the walls (positive), where it is either dissipated or transferred to TKE (see figure 4.8, left). In other words, the turbulent transport $T_{1,turb}$ acts like a diffusion of kinetic energy. In the vicinity of the wall the viscous transport is responsible for the transport of kinetic energy towards the wall, where the viscous effects dissipate the kinetic

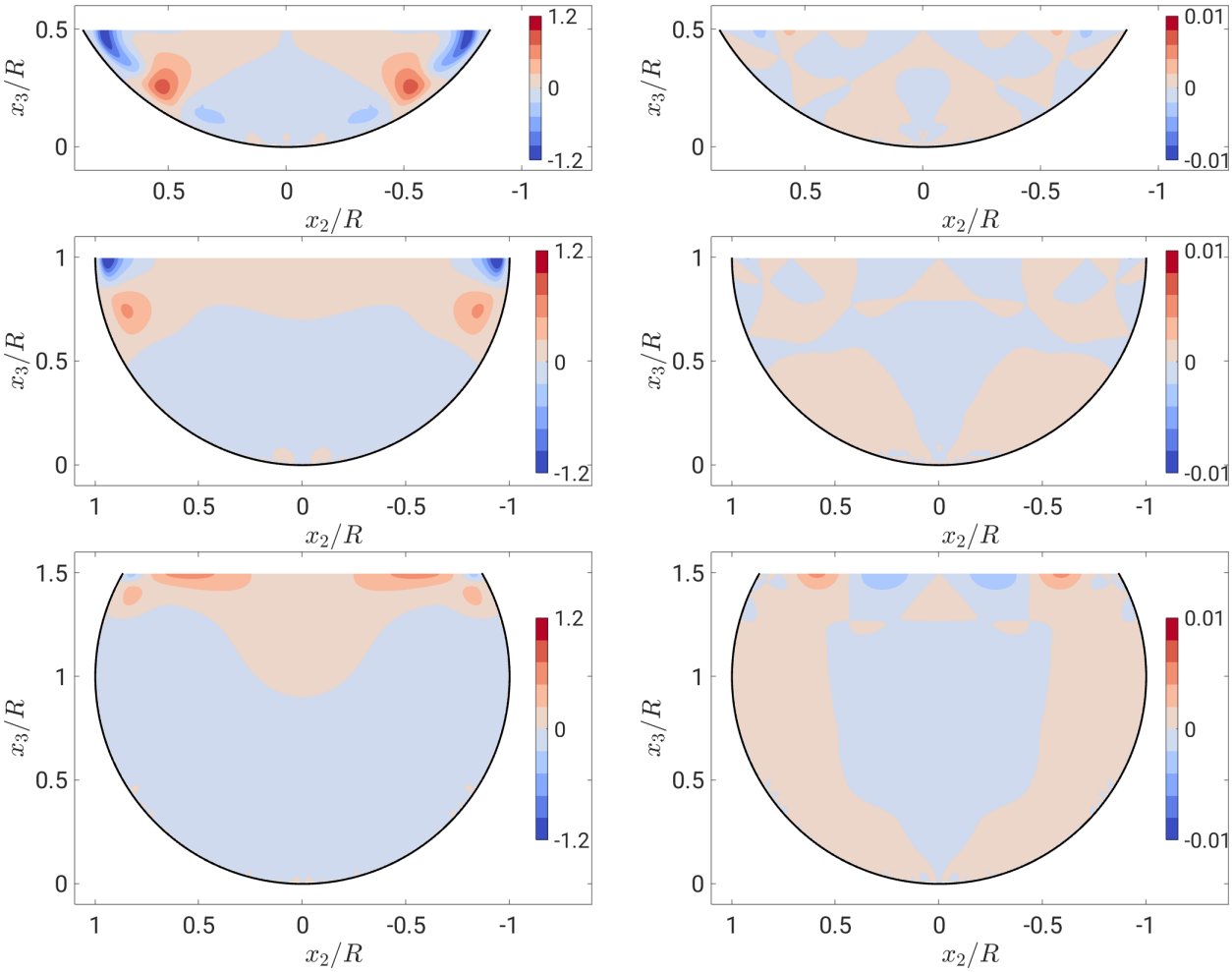

Figure 4.7: C_1 (left) and $C_{2,3}$ (right) of $Re_\tau = 180$ normalised by ν/u_τ^4 for filling ratio 25%, 50% and 75% (top to bottom). Please note, that the distributions were symmetrized using the half-plane symmetry.

energy. This is shown by the small layer of high positive intensities along the perimeter. In addition, the high positive intensities reach further to the centre, where secondary flow flows away from the wall. In contrast, for 25% and 50% FR a minimum of the transport terms appears in the mixed-corner, where secondary flow transports high momentum towards the wall. For high filling ratio, no minimum is detectable in the mixed-corner, because of the very small inner secondary vortex. However, the positive layer further spreads along the free surface, being aligned with the outer secondary vortex.

The extreme values of the secondary transport terms $T_{2,3}$ are smaller than the primary extreme values by a factor of approximately 100 (see figure 4.8, right). They are mostly active in the mixed-corner and in the centre of the free surface, negative where stagnation and positive where separation points of the mean secondary flow exist. $T_{2,3}$ mainly consists of pressure and turbulent transport, whereas viscous transport is negligible. Moreover, the distribution of $T_{2,3}$ is strongly related to the secondary MKE-production $P_{2,3}$, which are described later in this section.

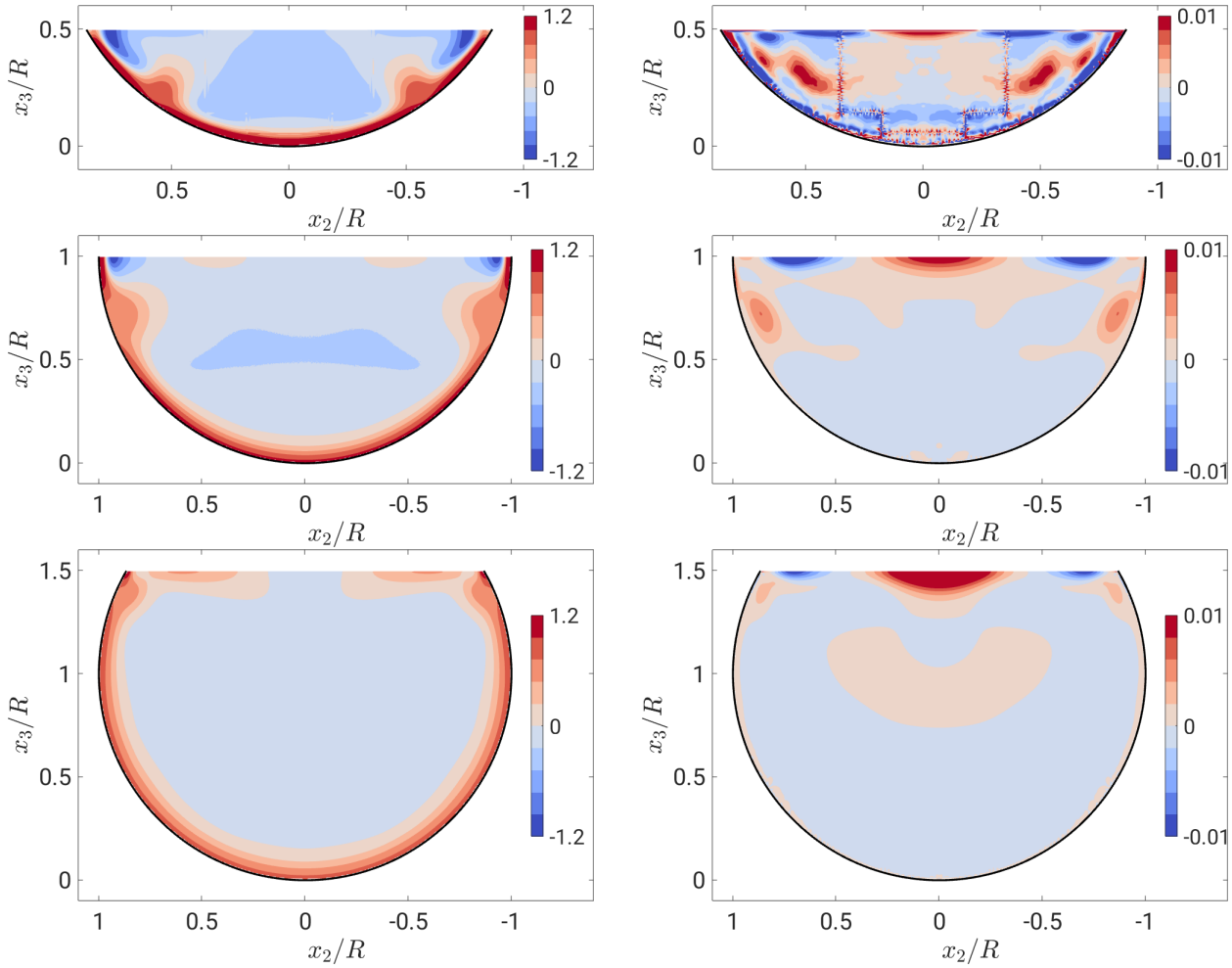

Figure 4.8: T_1 (left) and $T_{2,3}$ (right) of $Re_\tau = 180$ normalised by ν/u_τ^4 for filling ratio 25%, 50% and 75% (top to bottom). Please note, that the distributions were symmetrized using the half-plane symmetry.

As mentioned above, the convection and transport terms integrated over the cross-section are approximately zero, hence, the incoming energy is in equilibrium with the MKE-production and the mean dissipation, which are examined next. Let us first focus on the dissipation of MKE. The primary dissipation $\bar{\epsilon}_1$ dissipates energy in the vicinity of the wall with its highest intensities in the mixed-corner, see figure 4.9 (left). For 75% filling the peak in the mixed-corner is less strong. The distribution of $\bar{\epsilon}_{2,3}$ has only a very small layer along the wall where the inner secondary cell is located, a little region at the bisector of the mixed-corner or a small area at the free surface with a rather small impact, see figure 4.9 (right).

The last puzzle piece of the MKE-budget is the MKE-production displayed in figure 4.10, which mostly transfers MKE to TKE. The primary MKE-production P_1 is similarly distributed as the primary TKE itself. It seems to be very similar to the distribution in a standard turbulent pipe flow with a nearly homogeneous distribution around the perimeter apart from the mixed-corner, where lower values occur for 25% and higher values for 75%

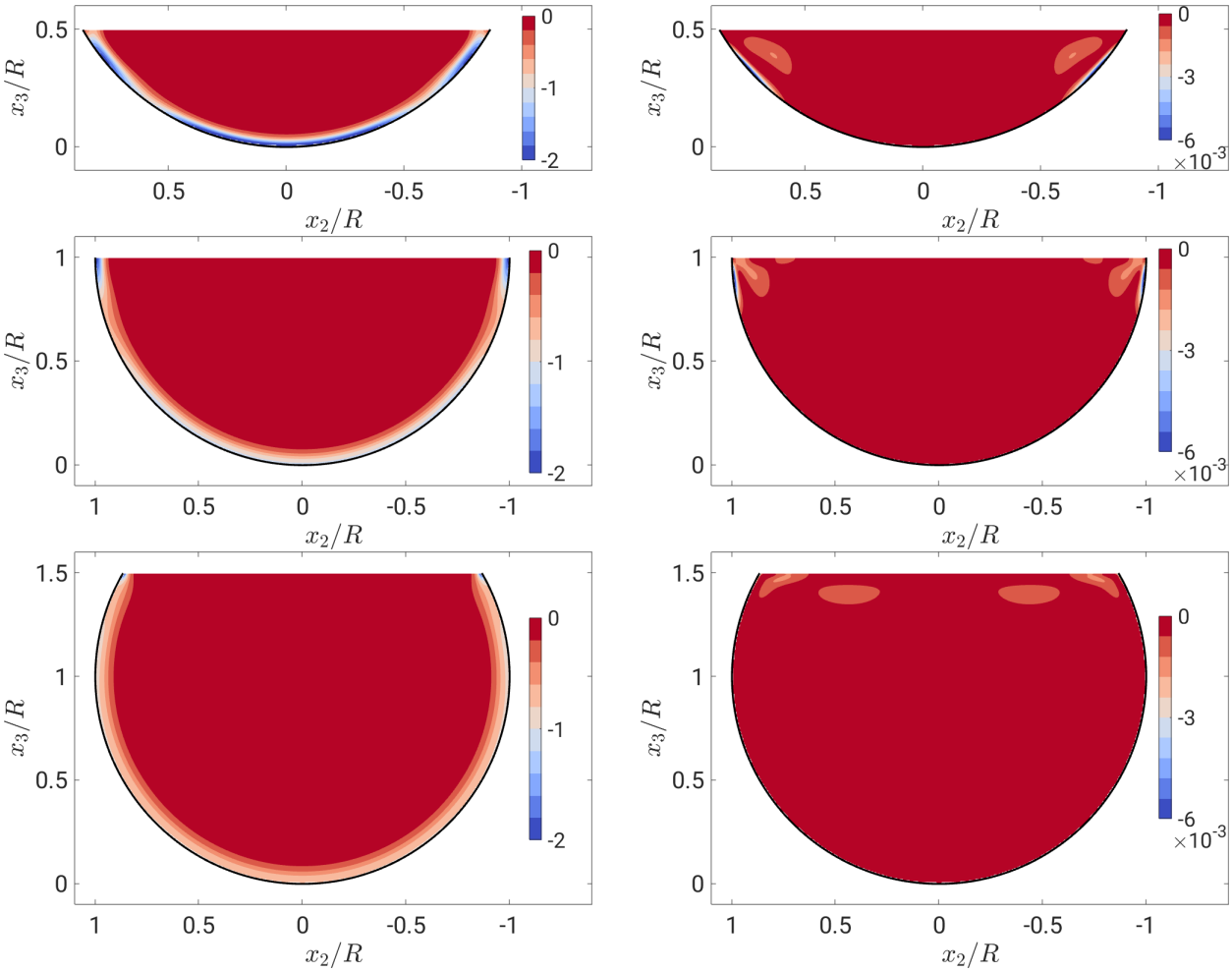

Figure 4.9: $\bar{\epsilon}_1$ (left) and $\bar{\epsilon}_{2,3}$ (right) of $Re_\tau = 180$ normalised by ν/u_τ^4 for filling ratio 25%, 50% and 75% (top to bottom). Please note, that the distributions were symmetrized using the half-plane symmetry.

filling ratio. In contrast, the secondary MKE-production $P_{2,3}$ is strong at the free surface, where the secondary MKE has its maxima, see figure 4.10. In addition for 25% and 50% filling local peaks appear at the upper wall, again, where secondary MKE also has local maxima. While P_1 is consistently negative in the MKE balance equation (energy is transferred from MKE to TKE), its counterpart $P_{2,3}$ changes sign. This means that in the regions where the MKE-production is positive, energy is transferred from the fluctuations to the mean secondary flow (TKE $\rightarrow$ MKE) and where $P_{2,3}$ is negative: MKE $\rightarrow$ TKE. Comparing $P_{2,3}$ to the secondary transport terms $T_{2,3}$, they balance each other, hence, where $P_{2,3}$ is positive MKE is transported away and where $P_{2,3}$ is negative secondary MKE is brought to that location by $T_{2,3}$.

It can be observed that kinetic energy is essentially transferred to the mean secondary flow only in two regions symmetrically located about the vertical symmetry plane at the stagnation point at the free surface that marks the boundary between the inner and the outer vortex. The mean secondary flow points away from this stagnation point, thus, giving

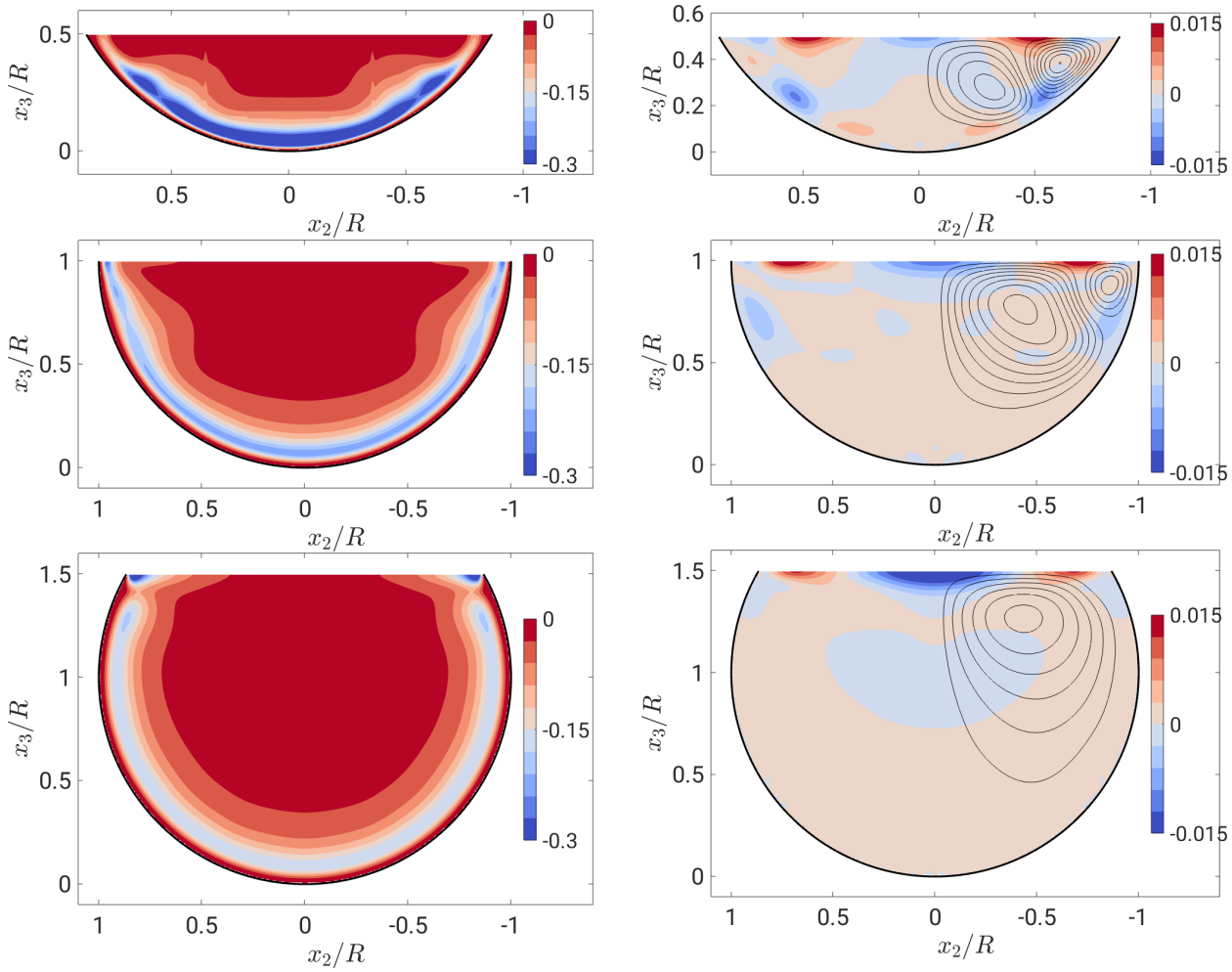

Figure 4.10: P_1 (left) and $P_{2,3}$ (right) of $Re_\tau = 180$ normalised by ν/u_τ^4 for filling ratio 25%, 50% and 75% (top to bottom). Please note, that the distributions were symmetrized using the half-plane symmetry. For secondary components the stream function ψ of secondary flow has been included in one half of the cross-section.

rise to a positive MKE-production $\overline{u_2' u_2'} \frac{\partial \overline{u_2}}{\partial x_2}$ in the MKE balance. In the pipe centre, the secondary flow points towards each other from both sides and is redirected downwards. This situation generates a negative production term in the MKE balance and kinetic energy is transferred back from the secondary MKE to the secondary TKE. A similar effect can be observed at the lower boundary of the inner vortex where the secondary flow is directed away from the wall. Here as well, transfer from secondary MKE to TKE is indicated by a negative $P_{2,3}$. Therefore, it can be deduced that a part of the kinetic energy that the mean secondary flow receives at the free surface is passed back to the turbulent secondary flow.

A condition of having a non-zero transfer between secondary MKE and TKE is that the vertical fluctuations are damped near the free surface. This can be seen by rewriting the secondary MKE-production $P_{2,3}$ in equation (4.3) neglecting the shear production – which is small –

and using the continuity equation ($\partial\overline{u}_2/\partial x_2 = -\partial\overline{u}_3/\partial x_3$):

$$\overline{u_2'u_2'}\frac{\partial\overline{u}_2}{\partial x_2} + \overline{u_3'u_3'}\frac{\partial\overline{u}_3}{\partial x_3} \approx \left(\overline{u_2'u_2'} - \overline{u_3'u_3'}\right)\frac{\partial\overline{u}_2}{\partial x_2} \quad . \tag{4.4}$$

At the free surface, the vertical fluctuations u_3' are damped and the horizontal fluctuations u_2' are amplified, compare figures 3.48 and 3.46. Thus, in contrast to an isotropic turbulence structure the normal stress difference in equation (4.4) increases at the free surface enabling exchange of kinetic energy between the mean and the fluctuating velocities.
In figure 4.10 (right) the stream function of the secondary flow is plotted in addition to the MKE-production of secondary components. For the different fillings, the production of mean secondary flow ($P_{2,3} > 0$) at the free surface (red area) is split up into a contribution to the inner and outer secondary cell. For the semi filled case the produced secondary MKE seems to be shared equally between inner and outer vortex. For 25% most of the energy seems to be shifted into the inner secondary cell, whereas for 75% almost everything is provided for the outer secondary cell. This distribution shows which vortex gets more energy, hence, is the more dominant vortex. This is in good agreement with the filling-dependency reported for the circulation in section 3.3.1.
In the next paragraph, the above mentioned findings shall be discussed in combination with the results of section 4.1.1, which had shown that the sum of gradients of the Reynolds stresses, which are responsible for generating streamwise vorticity, are located in the mixed-corner. From the perspective of the MKE-budget, it can be deduced that mostly at the free surface energy is transferred from TKE to the secondary MKE into its horizontal component $\overline{u}_2^2$. This generates a flow towards the mixed-corner, where the flow is directed downwards. The downward flow creates a shear flow along the wall until it meets the outer secondary vortex. At this point the flow is again redirected away from the wall and most of the secondary MKE is transferred back to TKE. It is clear that this partial circle goes hand in hand with rotation, i.e. streamwise vorticity, that occurs in the mixed-corner. Thus, the two perspectives describe two different generation mechanisms of secondary flow, which do not contradict each other. Furthermore, at least for 25% and 50% filling, where the inner secondary cell plays an important role, one could argue that the two mechanisms strengthen each other. Whereas for 75% FR, it is difficult to draw a similar conclusion, as the inner secondary cell is very weak, but vorticity generation still occurs in the mixed-corner. Hence, it is not clear whether the processes are similar to the other fillings. In conclusion, no clear and convincing connection could be found between the two different approaches of secondary flow generation mechanisms.

The path of kinetic energy is further illustrated by the cross-section integrated terms of the MKE- and TKE-budget in figure 4.11 for semi filled pipe flow with $Re_\tau = 180$. Terms redistributing kinetic energy in space, such as convection and the transport terms, vanish after integration. About two thirds of the kinetic energy input are dissipated directly, which can be explained by the relatively low Reynolds number ($Re_\tau = 180$). One third is transferred to TKE and mainly dissipated by the turbulent dissipation ϵ'. Only a very small fraction, less than one per mill of the total kinetic energy flux is fed back to the secondary flow via the term $P_{2,3}$ in an absolute sense.

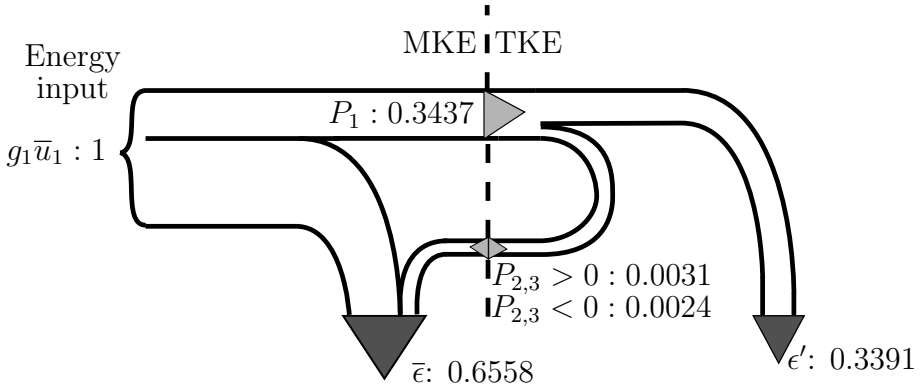

Figure 4.11: Path of kinetic energy for $Re_\tau = 180$. Cross-section integrated values normalised by the energy input $g\overline{u}_1$.

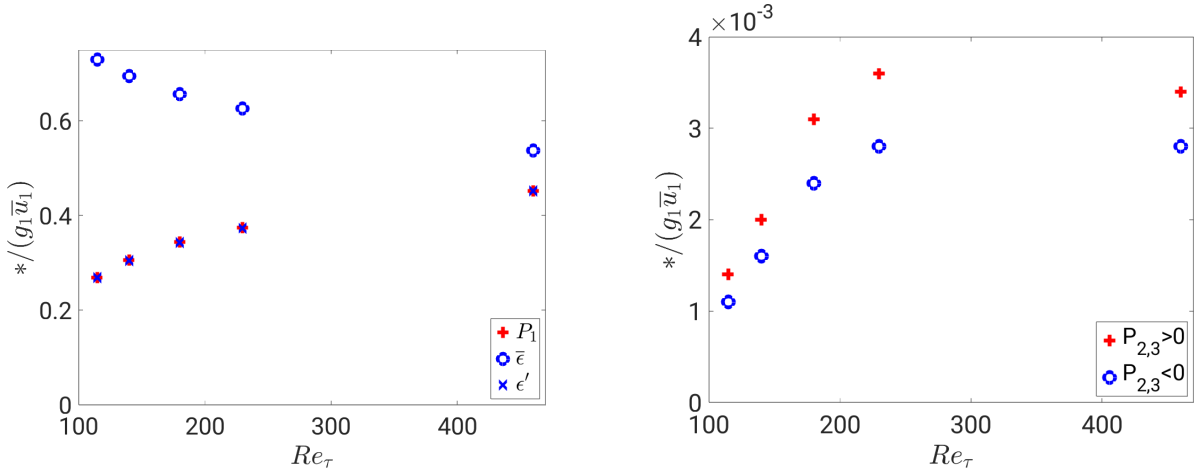

Figure 4.12: Cross-section integrated values of P_1, $\overline{\epsilon}$ and ϵ' (left) and $P_{2,3>0}$ and $P_{2,3<0}$ (right) for $Re_\tau = 115, 140, 180, 230, 460$ normalised by the energy input $g_1\overline{u}_1$.

The path of the kinetic energy in figure 4.11 is complemented with values for other Reynolds numbers in figure 4.12. As expected, with increasing Reynolds number direct dissipation $\overline{\epsilon}$ decreases and the share of energy transferred to TKE increases. It can be seen that independent of the Reynolds number the turbulent dissipation is nearly equal to the MKE-production. The energy exchange between turbulence and secondary flow, $P_{2,3}$ gets stronger with increasing Reynolds number and seems to saturate for larger Re_τ. This behaviour is similar to the behaviour of the peak values of the stream function, see figure 3.11. The transfer from the turbulence to the mean secondary flow ($P_{2,3} > 0$) is always larger than the transfer in reverse direction ($P_{2,3} < 0$). The difference is the energy dissipation by the secondary flow which has a nearly invisible share of the total energy balance.
Finally, the PDF of the cross-section integrated $\int_\Omega P_{2,3}$ is shown in figure 4.13. The absolute values of $\int_\Omega P_{2,3}$ are displayed in the left plot. The PDF is nicely Gaussian distributed, with a slightly non-zero mean value, equal to the absolute secondary MKE-production in figure 4.11. For the plot on the right, two different PDF's were created. The red PDF is

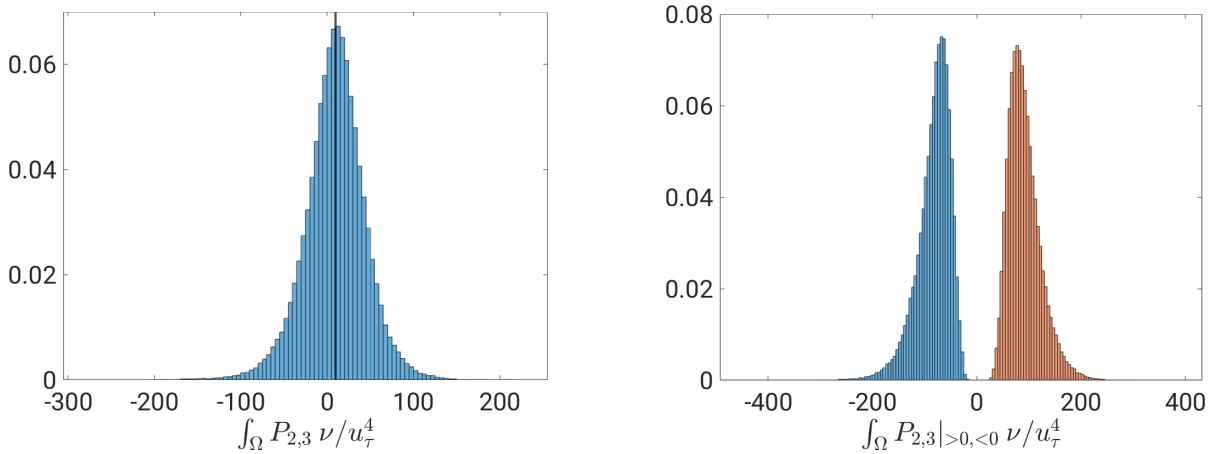

Figure 4.13: Left: Integrated $P_{2,3}$ over all values for each cross-section of all snapshots. The black line indicates the mean value (≈ 9). Right: Histogram of minimum and maximum of sign-separated integration of $P_{2,3}$ over each cross-section of all snapshots. Both for $Re_\tau = 180$ and 50% filling.

generated by only taking the positive values of the secondary MKE-production into account for creating a cross-section integrated PDF $\int_\Omega P_{2,3}|_{>0}$, whereas the blue PDF only considers the negative values $\int_\Omega P_{2,3}|_{<0}$. Both PDF's are included in the right plot. Each of the two sign-separated distributions shows a skewed distribution with the highest magnitude close to zero and a long tail of large values. The extreme values are larger than for the absolute secondary MKE-production, hence, if, for example, an event of strong positive $P_{2,3}$ occurs in a cross-section it is at least partly balanced by an event of negative $P_{2,3}$. Moreover, the sign-separated distribution shows that there are no occurrences with zero secondary MKE-production. Thus, there is always a minimum amount of secondary MKE-production occurring in each instantaneous cross-section.

Conclusion

Concluding this section, each individual distribution, primary and secondary terms, of convection, transport, dissipation and MKE-production have in common, that their high intensities are mostly along the perimeter, in the mixed-corner and along the free surface. There are no high intensities where the mean streamwise flow has its maximum, the *velocity-dip* phenomenon.

The mean secondary flow obtains its kinetic energy from the secondary fluctuations in a small area around the stagnation point located at the free surface, separating the inner and the outer secondary flow cells. From this point, one part of the secondary kinetic energy is transported by turbulent transport towards the pipe's centre, where its main part is fed back to the secondary fluctuations. The largest values of secondary kinetic energy can be found midway between the maximum (positive) and minimum (negative) of the MKE-production. Another part of the secondary kinetic energy is transported towards the mixed-corner where the majority of the direct dissipation of mean secondary kinetic energy takes place. With

increasing filling ratio the amount of energy directed towards the centre also increases. For 75% filled pipe flow most of the secondary kinetic energy is directed towards the centre and the inner secondary cell almost vanishes.
The share of direct dissipation by the primary flow decreases with increasing Reynolds number while the transfer to TKE increases. The levels of energy fluxes to the secondary flow are very small compared to the primary MKE-production and seem to saturate within the Reynolds number range considered.
Comparing the processes occurring within the MKE-budget and the mean vorticity equation shows that they are compatible with each other for 25% and 50% filling ratio. The intensity and location of vorticity generation is sensible in connection with the location and division of secondary MKE-production, however, no causality can be concluded. For 75% filled pipe flow the location of vorticity production is in conflict with the results from the MKE-budget. The mixed-corner region obtains only little secondary kinetic energy and the strong outer secondary cell rotates in the opposing direction, but still strong vorticity production takes place. However, on the one hand, the statistics of the secondary MKE-production obviously do not incorporate the full turbulent dynamics. On the other hand, the streamwise vorticity generation does only indicate, where a turbulence anisotropy exists and if there is any mean secondary flow is generated, however, it does hardly provide any information about what process takes place.

4.1.3. Turbulent Kinetic Energy (TKE) Budget

Theory of TKE-Budget

The turbulent kinetic energy budget links the transfer from MKE to TKE via P_1 and the exchange processes of kinetic energy via $P_{2,3}$ described in section 4.1.2. The TKE-budget equation (4.5) contains similar terms as the MKE-budget, but describes the turbulent processes in a Reynolds decomposition sense, as mentioned in section 1.2.

$$0 = \underbrace{-\ \bar{u}_j \frac{\partial}{\partial x_j} \frac{\overline{u_i' u_i'}}{2}}_{\substack{\text{convection} \\ C'}} \underbrace{-\ \frac{\partial}{\partial x_j}\left[\frac{1}{\rho}\overline{p' u_j'} + \frac{\overline{u_i' u_i' u_j'}}{2} - \nu \overline{u_i'\left(\frac{\partial u_i'}{\partial x_j} + \frac{\partial u_j'}{\partial x_i}\right)}\right]}_{\substack{\text{transport} \\ T'=T'_{press}+T'_{turb}+T'_{visc}}} \underbrace{-\ \overline{p' \frac{\partial u_j'}{\partial x_j}}}_{\substack{\text{intercomponent transfer} \\ \Pi'}}$$
$$\underbrace{-\ \overline{u_i' u_j'} \frac{\partial \bar{u}_i}{\partial x_j}}_{\substack{\text{TKE-production} \\ P}} \underbrace{-\ \frac{\nu}{2} \sum_{i,j} \overline{\left(\frac{\partial u_i'}{\partial x_j} + \frac{\partial u_j'}{\partial x_i}\right)^2}}_{\substack{\text{dissipation} \\ \epsilon'}} \quad \text{, with } i,j = 1,2,3 \tag{4.5}$$

In the same manner as the MKE, the TKE can be decomposed into a part containing the primary component and a part containing the secondary components. The corresponding budget equations are given in eqs. (4.6) and (4.7), respectively. Please note that the intercomponent transfer term Π' cancels out in equation (4.5), because of its divergence form, however, for the component-wise budgets, the individual intercomponent transfer terms Π_1' and $\Pi_{2,3}'$ are non-zero. Please keep in mind that the production term P appears in both in the MKE-

budget equations (eq. 4.2 and 4.3) and in the TKE-budget equation (eq. 4.5), but with an opposite sign. This means that according to its sign, its meaning is inverted. Hence, within this section on the TKE-budget, a positive P means transfer from MKE to TKE and a negative P TKE to MKE. Therefore, P is called TKE-production.

$$0 = \underbrace{-\ \bar{u}_j \frac{\partial}{\partial x_j} \frac{\overline{u_1' u_1'}}{2}}_{\text{convection } C_1'} \underbrace{-\ \frac{\partial}{\partial x_j} \left[\frac{\overline{u_1' u_1' u_j'}}{2} - \frac{\nu}{2} \left(\frac{\partial \overline{u_1' u_1'}}{\partial x_j} \right) \right]}_{\text{transport } T_1'} \underbrace{-\ \overline{p' \frac{\partial u_1'}{\partial x_1}}}_{\substack{\text{intercomponent transfer} \\ \Pi_1'}}$$
$$\underbrace{-\ \overline{u_1' u_j'} \frac{\partial \bar{u}_1}{\partial x_j}}_{\text{TKE-production} P_1} \underbrace{-\ \frac{\nu}{2} \overline{\left(\frac{\partial u_1'}{\partial x_j} \right)^2}}_{\text{dissipation } \epsilon_1'} \quad \text{, with } j = 2, 3 \tag{4.6}$$

$$0 = \underbrace{-\ \bar{u}_j \frac{\partial}{\partial x_j} \frac{\overline{u_i' u_i'}}{2}}_{\text{convection } C_{2,3}'} \underbrace{-\ \frac{\partial}{\partial x_j} \left[\frac{1}{\rho} \overline{p' u_j'} + \frac{\overline{u_i' u_i' u_j'}}{2} - \nu \overline{u_i' \left(\frac{\partial u_i'}{\partial x_j} + \frac{\partial u_j'}{\partial x_i} \right)} \right]}_{\text{transport } T_{2,3}'} \underbrace{-\ \overline{p' \frac{\partial u_j'}{\partial x_j}}}_{\substack{\text{intercomponent transfer} \\ \Pi_{2,3}'}}$$
$$\underbrace{-\ \overline{u_i' u_j'} \frac{\partial \bar{u}_i}{\partial x_j}}_{\text{TKE-production} P_{2,3}} \underbrace{-\ \frac{\nu}{2} \sum_{i,j} \overline{\left(\frac{\partial u_i'}{\partial x_j} + \frac{\partial u_j'}{\partial x_i} \right)^2}}_{\text{dissipation } \epsilon_{2,3}'} \quad \text{, with } i, j = 2, 3 \tag{4.7}$$

Nikora & Roy (2012) have mentioned an analysis of the TKE-budget, which was applied by Anderson *et al.* (2015), who studied the TKE budget for a open-channel flow with streamwise ridges. By following the derivation of Hinze (1967, 1973), they could show that secondary flow needs to be generated for their flow configuration. The assumptions of Hinze (1967, 1973) are a steady, turbulent and fully developed flow in a straight uniform geometry. Furthermore, a high Reynolds number flow is assumed, in which the turbulent transport terms T' can be neglected, as they are supposed to be small except near the wall. This leads to $C' \approx P' - \epsilon'$, where locations with an imbalance between TKE-production and dissipation need to generate convection, which also implies a non-zero secondary flow, see C_1' in equation (4.6). Unfortunately, Anderson *et al.* (2015) did not further investigate the processes of the secondary flow mechanism. For the present study the assumption of large Reynolds numbers does not hold. Hence, the transport terms cannot be neglected. Nevertheless, energy needs to be transported from TKE-production to the location, where it is either dissipated or transferred back to MKE. In the present study, this transport is provided not only by convection but also by the transport terms.

Analysis of TKE-Budget

In figure 4.14 the individual terms of the complete TKE-budget (eq. 4.5) and their residual are shown, in order to validate the analysis. Apart from the very first cells in the mixed-

corner the residual does not become larger than 5%. Moreover, a good agreement can be found in comparison to full pipe flow, only the convection term C' plays a more important part, which needs to be balanced by the other terms.

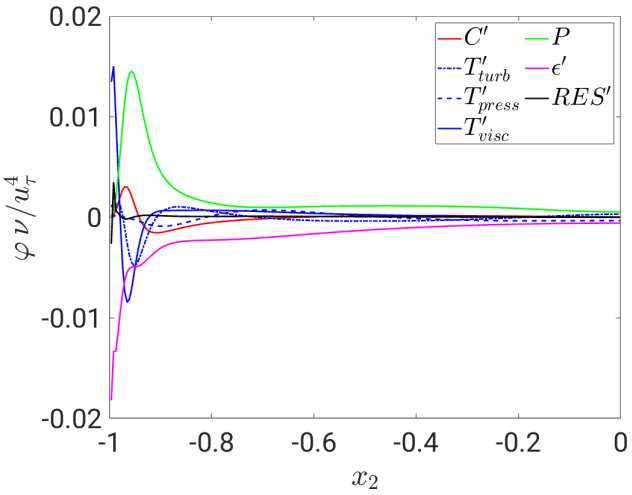

Figure 4.14: TKE budget terms taken four wall units below and parallel to the free surface of $Re_\tau = 180$ for semi filled pipe flow. Terms are defined in equation (4.5).

In figure 4.15 all terms of the primary terms of the TKE-budget for a semi filled pipe flow of $Re_\tau = 180$ are shown. In general, there must be a transfer from locations with high TKE-production P_1 to dissipation ϵ'_1. It is shown that P_1 and ϵ'_1 are large in similar regions, but do not match exactly. Moreover, because the components are split, an intercomponent transfer Π'_1 occurs, which acts like a sink of TKE for the primary components. C'_1 and T'_1 are responsible for the transport of TKE. Please note that the peaks of the convective term are much smaller than the transport term and occur in similar locations, hence, as mentioned above, the latter cannot be neglected for this flow case. The transport T'_1 is strongly active only in the vicinity of the wall, as expected. It transports TKE from the peaks of P_1 towards the wall, where it is dissipated. However, the dissipation occurs not only very close to the wall, but in a larger band along the wall. Moreover, a small part of the primary TKE is directly transferred to the secondary components by Π'_1 at the same location, where it enters the TKE.

The secondary components are presented in figure 4.16. Most of the primary TKE enters the secondary components via $\Pi'_{2,3}$, which is mostly directly dissipated, see distribution of $\epsilon'_{2,3}$. Moreover, TKE enters and leaves the budget via $P_{2,3}$ at the free surface and the upper wall. Therefore, the transport terms and the convection provide the local redistribution, which have their maxima in the surrounding of the mixed-corners. Hence, in the lower part of the flow, the distributions resemble a full pipe flow, whereas the upper part of the flow is strongly influenced by the free surface.

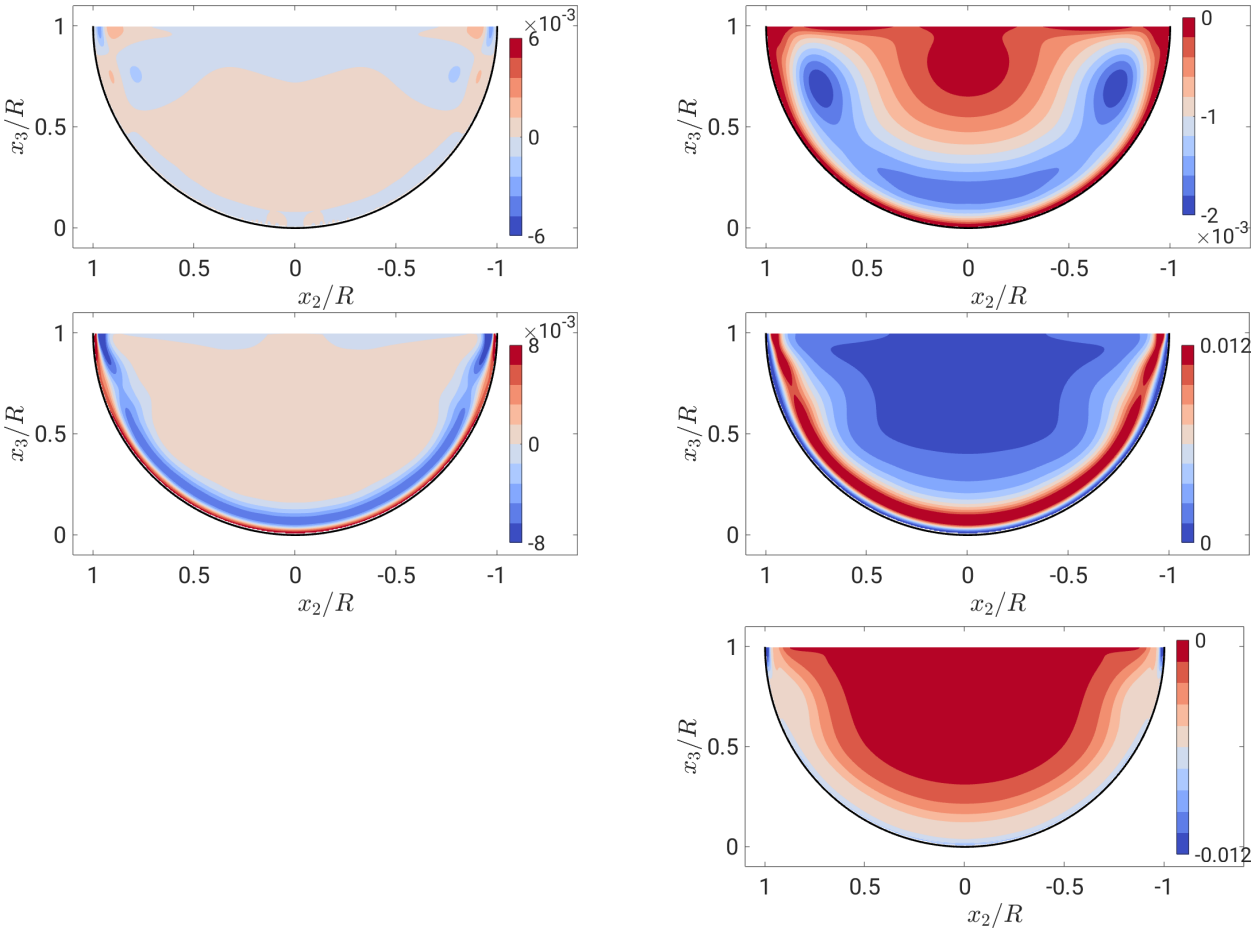

Figure 4.15: Primary components of TKE-budget terms for $Re_\tau = 180$ and 50% FR normalised by ν/u_τ^4. C_1', T_1' (left column) and Π_1', P_1, ϵ_1' (right column, top to bottom). Please note, that the distributions were symmetrized using the half-plane symmetry.

Conclusion

To the end of this section, the investigations of the MKE- and TKE-budget shall be concluded. Therefore, let us recall the schematic flux of energy presented in figure 4.11. It illustrates that most of the incoming energy is directly dissipated and the generation of secondary flow is a subtle process. Energy is transferred from MKE to TKE predominantly via P_{12} and P_{13} mostly along the wall. In order to transfer energy back to secondary MKE, a transition to $P_{2,3}$ needs to take place within the TKE-budget. This intercomponent transfer takes place via Π'. Hence, the path of kinetic energy from the incoming energy to the secondary flow is completed and a crucial term, the secondary production $P_{2,3}$, is identified. However, the perspective of the mean flow analysis provides an incomplete picture of the secondary flow mechanism, because the flow is obviously turbulent. It is not clear, how the secondary flow appears instantaneously, especially the flow in the mixed-corner. Furthermore, it is still unclear what kind of coherent structures are involved in the secondary flow mechanism and how they interact. This missing knowledge shall be addressed in the following section, which deals with the dynamics of coherent structures.

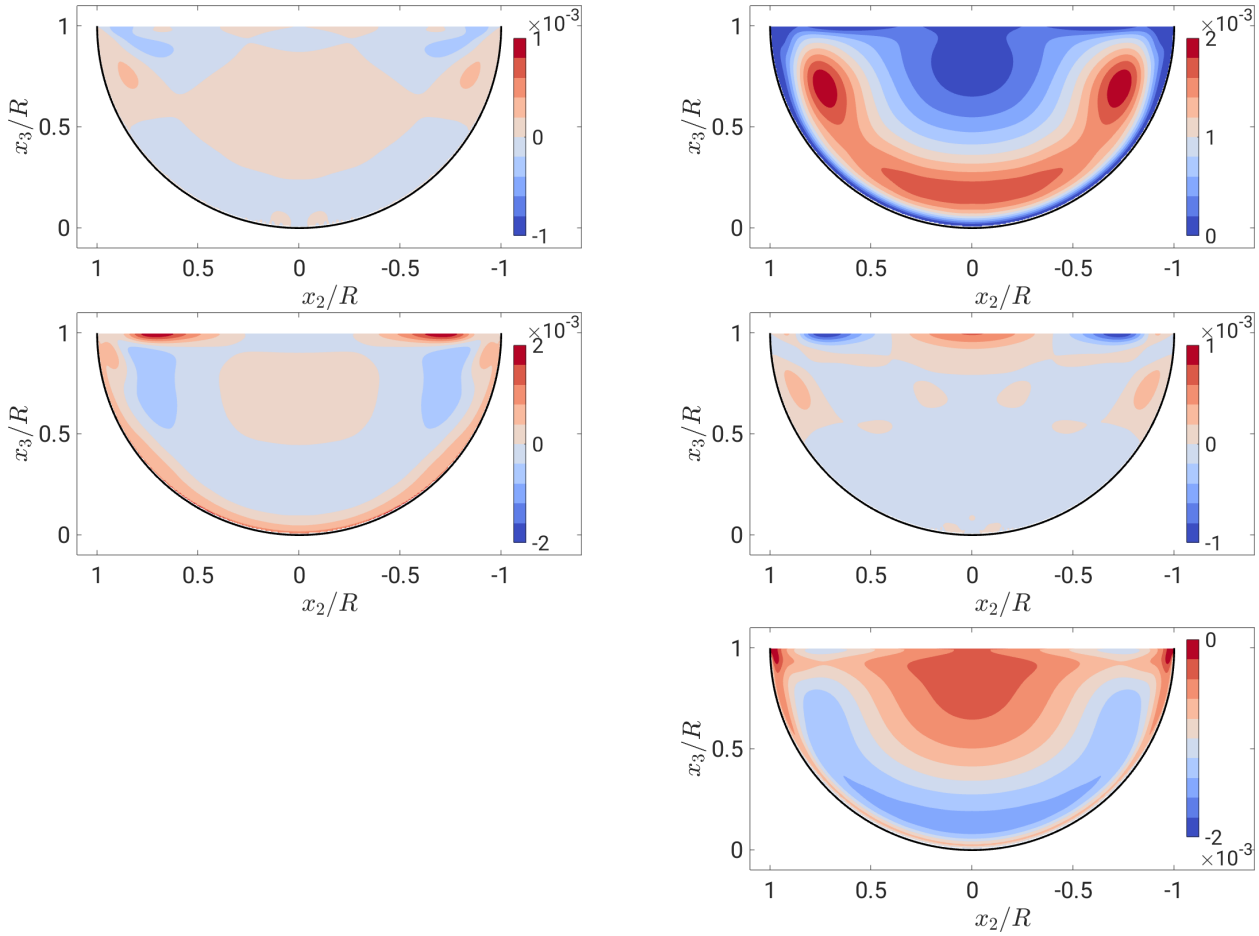

Figure 4.16: Secondary components of TKE-budget terms for $Re_\tau = 180$ and 50% FR normalised by ν/u_τ^4. $C'_{2,3}$, $T'_{2,3}$ (left column) and $\Pi'_{2,3}$, $P_{2,3}$, $\epsilon'_{2,3}$ (right column, top to bottom). Please note, that the distributions were symmetrized using the half-plane symmetry.

4.2. Analysis of Coherent Structures

The path of kinetic energy, how it reaches the mean secondary flow in a time-averaged sense, became more clear with the analysis in section 4.1. The energy transfer term $P_{2,3}$ is responsible for the energy transfer to the mean secondary flow. However, the mean flow analysis only shows an average of the process, but not the possible variance of the process in an instantaneous view. Whether similar mechanisms take place in the mean and in the instantaneous flow is studied in the following sections. In addition it is investigated, how this can be connected to classical structures occurring in turbulent channel flow like velocity streaks, quasi-streamwise vortices, as described in section 1.2. The role of the mixed-corner, which was already emphasized in all previous sections, continues to be of special interest.

In order not to be overwhelmed by the complexity of instantaneous flow fields, different features of the flow are accentuated by applying three different filters: the proper orthogonal decomposition (POD), Gaussian filtering (GF) and conditional averaging. All three approaches are introduced and their individual perspectives on the secondary flow mechanism are compared to each other and to literature, which is briefly summarised in the following. Sakai (2016) has a strong focus on coherent structures for rectangular open-channel flow, educing vortices and analysing their spatio-temporal behaviour. For partially filled pipe flow Ng *et al.* (2018) have investigated instantaneous flow fields and streamwise structures extracted from velocity correlations. This analysis was extended by Ng *et al.* (2021) looking at the TKE decomposed by a POD and at very large scale motions occurring in high Reynolds number flows. The following analysis is mainly compared to these three publications, which will be referred to in more detail, where appropriate.

Please note that in this section the production terms P_1 and $P_{2,3}$ always refer to the MKE-production. Hence, positive P corresponds to transfer from TKE to MKE and negative P corresponds to transfer from MKE to TKE.

Please further note that the coherent structure analysis in the following section is mostly focused on the model case of 50% filling and $Re_\tau = 180$. However, the various investigations were done for all different Reynolds numbers and filling ratios, which is taken into account and contributes to the drawn conclusions. Moreover, if instantaneous flow fields are shown, they always show the same instantaneous three-dimensional snapshot. In figure 4.17 this snapshot is averaged in streamwise direction, which roughly reproduces the globally averaged mean secondary flow. The inner secondary cell is weaker on the left side compared to the right side, thus, more events that contribute to the secondary flow are expected on the right side in negative x_2-direction. Overall, it is assumed that this snapshot should include the processes that generate the secondary flow.

Lastly, please further note that the author is aware that, as introduced in section 1.2 (*Coherent Structures in a Wall-Bounded Flow*) and mentioned by Robinson (1991), there is not one unique definition of coherent structures. Many researchers agree on the conceptual idea of a coherent structure (Robinson, 1991) that there is a quantity correlated to itself or a different quantity over a significant space and time interval. In addition, it is also still under ongoing discussion (e.g. Haller (2005)) which mathematical criterion describes vortices or coherent structures best.

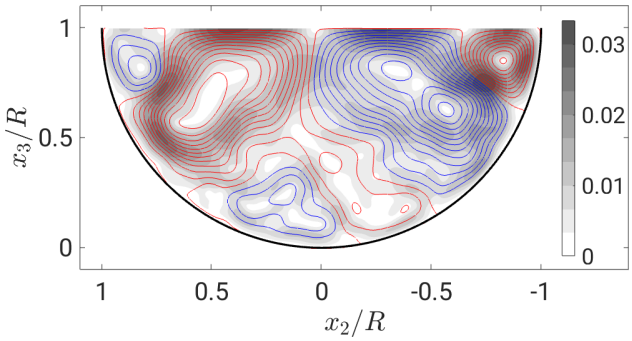

Figure 4.17: Flow fields averaged over streamwise direction of one snapshot: Contours of stream function ψ of crossflow velocities $\overline{u}_2$ and $\overline{u}_3$ (red indicates clockwise and blue represents counter-clockwise rotation) and as greyscale the velocity magnitude of $\sqrt{\overline{u}_2^2 + \overline{u}_3^2}/u_b$ for $Re_\tau = 180$. The increments for the contourlines of ψ are 0.003.

4.2.1. Proper Orthogonal Decomposition (POD)

The proper orthogonal decomposition is a tool to extract coherent structures in turbulent flows. It was first introduced to fluid mechanics by Lumley (1967). The POD can decompose a spatio-temporal process like turbulent flows into its individual – spatial and temporal – components. Therefore, the flow is decomposed into statistically independent basis functions, also called modes. These modes can be divided into spatial modes and their corresponding temporal modes, also called time coefficients. The sum of all modes represent the complete spatio-temporal process. The spatial basis functions are, in contrast to a Fourier transformation, not given *a priori* and show their own, individual temporal behaviour. But for homogeneous directions the POD acts like a Fourier transformation. For partially filled pipe flow, the POD was used by Ng *et al.* (2021) in order to describe high energy structures, which are reported mostly in the vicinity of the mixed-corner.
In a first step the POD will be introduced and its basic parameters will be presented. In a second step the decomposition will be used to filter the flow field and see how the energy transfer towards secondary flow can be described, see section 4.2.3.

Theory of POD

Based on the POD approach described by Lumley (1967), Sirovich (1987) and Aubry (1991) introduced the so-called Snapshot POD, which is applied in this study. The basic idea is to linearly decompose the flow field into a discrete number N_k of temporal coefficients a^k and spatial modes Φ_i^k, see equation (4.8). Please note that because of the limitation to discrete distributions, the relations can be also expressed in the instructive matrix form.

$$u_i(\mathbf{x}, t) \approx \sum_{k=1}^{K} a^k(t)\Phi_i^k(\mathbf{x}) \qquad , \qquad \mathbf{U} = \mathbf{A}\mathbf{\Phi} \tag{4.8}$$

With $\mathbf{U}$ being a velocity matrix, which is set up in the following manner. The velocities

$u_i(\mathbf{x},t)$ are given at N_P discrete points distributed over the two-dimensional cross-section Ω and at N_T discrete points in time that are stored in $\mathbf{U}$:

$$u_i(\mathbf{x},t) \rightarrow \mathbf{U}^T = \begin{pmatrix} u_1(x_1,t_1) & \cdots & u_1(x_1,t_{N_T}) \\ \vdots & \ddots & \vdots \\ u_1(x_{N_P},t_1) & \cdots & u_1(x_{N_P},t_{N_T}) \\ u_2(x_1,t_1) & \cdots & u_2(x_1,t_{N_T}) \\ \vdots & \ddots & \vdots \\ u_2(x_{N_P},t_1) & \cdots & u_2(x_{N_P},t_{N_T}) \\ u_3(x_1,t_1) & \cdots & u_3(x_1,t_{N_T}) \\ \vdots & \ddots & \vdots \\ u_3(x_{N_P},t_1) & \cdots & u_3(x_{N_P},t_{N_T}) \end{pmatrix} \tag{4.9}$$

With $\mathbf{U}^T$ being the transposed matrix of $\mathbf{U}$. More than 8000 instantaneous cross-sectional slices were used as input. By taking advantage of the half plane symmetry the instantaneous slices were mirrored, leading to more than $N_T \gtrapprox 16000$ samples as input for the correlation matrix and creating a symmetric set of samples. Please note that this enforces symmetric spatial modes, which has to be taken into account for interpretation and comparison to modes reported by other authors. Moreover, the number of points in time N_T equals the number of modes N_k that are generated by the POD.
The matrix of the temporal coefficients $\mathbf{A}$ is defined as

$$a^k(t) \rightarrow \mathbf{A} = \begin{pmatrix} a^1(t_1) & \cdots & a^{N_k}(t_1) \\ \vdots & \ddots & \vdots \\ a^1(t_{N_T}) & \cdots & a^{N_k}(t_{N_T}) \end{pmatrix} \tag{4.10}$$

and describes the temporal dynamics of the spatial modes $\mathbf{\Phi}$, which are defined in matrix form as follows

$$\Phi^k(\mathbf{x}) \rightarrow \mathbf{\Phi} = \begin{pmatrix} \Phi^1(x_1) & \cdots & \Phi^1(x_{N_P}) \\ \vdots & \ddots & \vdots \\ \Phi^{N_k}(x_1) & \cdots & \Phi^{N_k}(x_{N_P}). \end{pmatrix} \tag{4.11}$$

The spatial modes Φ shall be derived for the best correlation to $u(t)$ by maximising $\frac{\overline{|\mathbf{u}\cdot\Phi|^2}}{\|\Phi\|^2}$, with $\|\varphi\|$ being the L^2-norm. Hence, the spatial modes are maximised for high kinetic energy. This maximisation problem can be rewritten as the Fredholm integral of a spatial correlation matrix that correlates the velocities in space, and the spatial modes Φ as eigenfunctions. As a high spatial resolution can strongly enlarge the spatial correlation matrix, Sirovich (1987) and Aubry (1991) developed the snapshot POD, which correlates the velocities in time. For the snapshot POD the above mentioned Fredholm integral including the spatial correlation matrix is transformed into a similar equation (eq. 4.12), but based on the temporal correlation matrix $C(t,t')$ (For details of the transformation the reader is referred to either Sirovich

(1987) or Aubry (1991)):

$$\int_T C(t,t')a^k(t')dt' = \lambda^k a^k(t) \qquad , \qquad \mathbf{CA} = \mathbf{A\Lambda} \tag{4.12}$$

with the eigenvalues $\mathbf{\Lambda} = \lambda^k \delta_{kl}$ being associated to with the amount of kinetic energy. The eigenvalue problem enforces orthogonality of the individual modes in order to properly separate the kinetic energy. As mentioned above, the input for the eigenvalue problem is the temporal correlation matrix $C(t,t')$:

$$C(t,t') = \frac{1}{N_T}\int_\Omega u_i(\mathbf{x},t)u_i(\mathbf{x},t') \qquad , \qquad \mathbf{C} = \frac{1}{N_T}\mathbf{U}\mathbf{U}^T. \tag{4.13}$$

The spatial modes are then calculated from the eigenvalues and eigenvectors of equation (4.12) as:

$$\Phi_i^k(\mathbf{x}) = \frac{1}{N_T\lambda^k}\int_T a^k(t)u_i(\mathbf{x},t) \qquad , \qquad \mathbf{\Phi} = \frac{1}{N_T}\mathbf{\Lambda}^{-1}\mathbf{A}^T\mathbf{U}. \tag{4.14}$$

For a more detailed description the reader is referred to Sirovich (1987).
A brief summary of POD analysis for similar flows is provided in the following. For full pipe flow Hellström *et al.* (2011); Hellström & Smits (2014); Hellström *et al.* (2015, 2016) applied a POD to analyse the flow structures. They found VLSMs, which they could describe with the first 4 to 10 modes (Hellström *et al.*, 2011). These first modes appeared as pairs, which were all attached to the wall. Moreover, the first ten modes are responsible for 43% of the Reynolds shear stress $-\overline{u_1' u_r'}$, especially in the outer flow region (Hellström & Smits, 2014). From mode 15 on, the spatial modes consist not only of structures attached to the wall but also of structures detached from the wall. Hence, reconstructing the flow field with the high energy modes up to mode 15 does only recreate wall-attached structures. Including further low-energy modes, enables to reconstruct also wall-detached structures. Moreover, they reported that the previously found VLSM can be described by a superposition of several modes and can also experience transitions between modes (Hellström *et al.*, 2015). Hellström *et al.* (2016) found a self-similarity in the structures according to a length scale dependent on the distance between the peaks of the low order modes and the wall. For narrow open-channel flows with longitudinal ridges at the bottom, Vanderwel *et al.* (2019) state that they could reconstruct large scale motions that are responsible for most of the secondary flow in this flow case by the first six modes. From the literature of different, but similar flow cases it can be concluded that the high-energy modes represent the most important flow features of streamwise and in-plane components. As mentioned above, Ng *et al.* (2021) did snapshot POD for their PIV-data of partially filled pipe flow, which will be compared to the results of the present study.

Before coming to the results of POD, the general partitioning of the kinetic energy of par-

tially filled pipe flow into primary and secondary component is introduced and its implications on the POD are discussed. Obviously, the streamwise component is the dominating component, see figure 4.18, which makes it difficult to identify the subtle influence of the cross-stream components. Only 1-2% of the streamwise kinetic energy are turbulent energy, whereas the kinetic energy of the secondary flow consists of approximately 97-99% TKE, see figure 4.18. Please keep in mind table 4.1, for the ratio between primary TKE to secondary TKE ($TKE_1 : TKE_{2,3} \approx 3 : 1$), showing the importance of the mean streamwise flow.

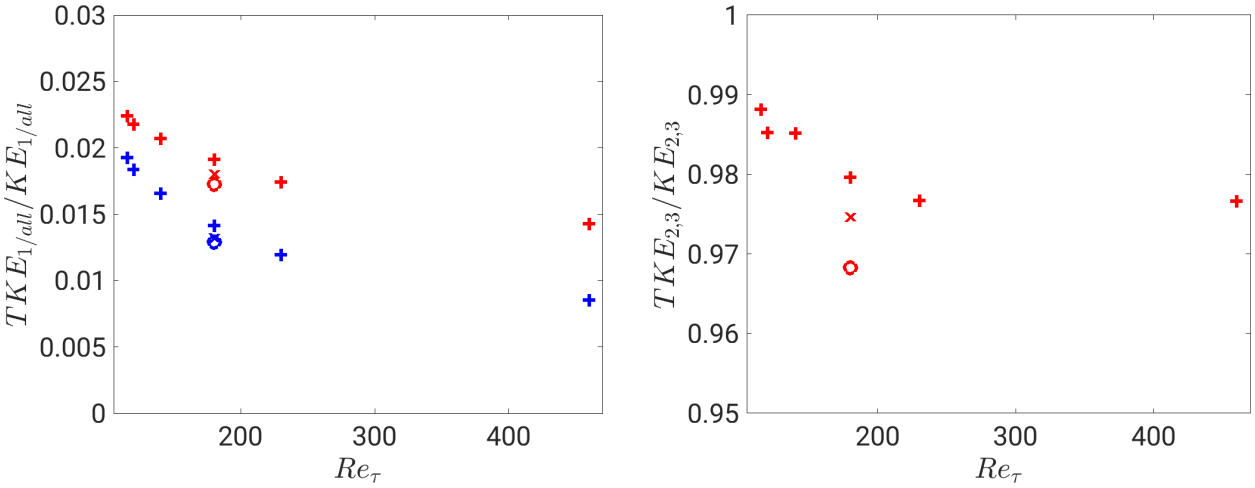

Figure 4.18: Ratio of TKE to total kinetic energy of all (red, left), only primary (blue, left) and secondary components (red, right). Pluses indicate 50% , crosses 25% and circles 75% filling ratio.

Two different possibilities are used as input for the present POD, either all three components of the velocity or – as this study focuses on secondary flow – only the cross-stream components. The identification of modes of the three-component POD is strongly dominated by the streamwise component, which is expected and of course it is important to include this fundamental part of the flow. But as reported in section 4.1.2 the secondary flow and especially its production is a key for the mean flow distribution. In order to extract the influence of the secondary flow another POD is done only with the cross-stream components. In section 4.2.1 (*Spatial Modes* $\mathbf{\Phi}$) it will be shown, that the most energy containing mode – the zeroth mode – is equal to the mean flow for all three components. This is expected as the primary MKE contains around 98% of the total kinetic energy. If only the cross-stream components serve as input for the POD, mean and fluctuating part of the flow are not sharply divided. This is also somewhat expected, as figure 4.18 (right) shows that the mean flow is responsible for only 2% of the cross-stream kinetic energy. Hence, in order to get a clear division, which is the starting point of the phenomenon of mean secondary flow, the mean flow of the secondary components is subtracted *a priori* and only the fluctuations are used as input for the second POD-approach. In the following the POD with all three components and full velocities as input gets the abbreviation *3C-POD* and the input including only fluctuations of the two in-plane components is called *2C-POD*. Please note that the most energy intense mode for 3C-POD is equal to the mean flow, see sections 4.2.1

(*Temporal Coefficients a*) and 4.2.1 (*Spatial Modes* $\mathbf{\Phi}$) and is called "zeroth" mode ($k = 0$). Hence, for both approaches, the fluctuating modes ($k > 1$) only include turbulent kinetic energy.

Energy Fractions λ

The eigenvalue problem results in temporal coefficients and the eigenvalues themselves. Each eigenvalue is equal to the kinetic energy contained in a specific mode and they are ordered from the most energy intense to the least. First of all, the normalised energy spectrum is shown for 3C-POD in figure 4.19 (left) and for 2C-POD (right). The zeroth mode of 3C-POD has a higher energy than the following modes by a factor of 1000. The following decay of the energy of the fluctuating modes gets stronger with increasing mode number. The strong energy decay, especially for the low energy modes, and the lack of energy accumulation in the low energy modes indicate that enough samples were used in order to capture the most important structures of the flow and to represent most of the energy containing modes. Moreover, both plots show that with increasing Reynolds number a larger number of modes are needed in order to achieve a satisfying degree of energy decay. However, by normalising the number of modes by $Re_b^{6/4}$ the various distributions agree well, as it would be expected for two dimensional input slices. Please note that the distribution for $Re_\tau = 460$ deviates from the others, because the resolution of the velocity fields that serve as input for the PODs is coarser by a factor of two compared to the other Reynolds numbers.

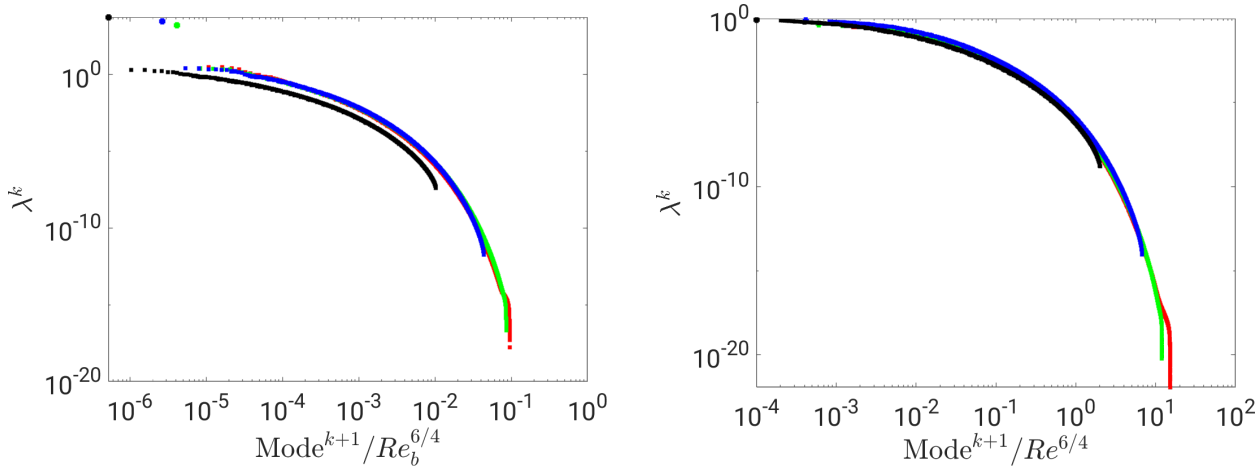

Figure 4.19: Energy spectrum of 3C-POD (left) and 2C-POD (right) of semi filled pipe flow for $Re_\tau = 115, 140, 180$ and 460 in red, green, blue and black, respectively. The number of modes are normalised by $Re_b^{6/4}$.

The partitioning of the energy among the fluctuating modes is shown for 3C-POD in figure 4.20 and for 2C-POD in figure 4.21. For both PODs either the Reynolds-dependency (left plot) or the filling ratio dependency (right plot) is shown. Generally, the energy is distributed over a greater number of modes for higher Reynolds numbers, i.e. the high energy modes contain relatively less energy. The first ten modes contain 20% ($Re_\tau = 460$) up to 50% ($Re_\tau = 115$) for 2C-POD and up to 60% for small Reynolds numbers for 3C-POD. 90% of

the energy are contained in 444 modes for 2C-POD and 618 modes for 3C-POD for semi filled pipe flow at $Re_\tau = 180$. Further details on specific numbers of modes containing a certain amount of energy can be found in table 4.2. The distribution for different FRs only deviate for the most energy containing modes. With lower FR the energy content increases for the first few modes for both input approaches. Ng *et al.* (2021) show similar results for their energy fractions. However, the magnitudes of their first modes are larger by a factor of 2-3 with a Re_b being twice as large as the highest Reynolds number of the present study and their number of snapshots is smaller by a factor of five.

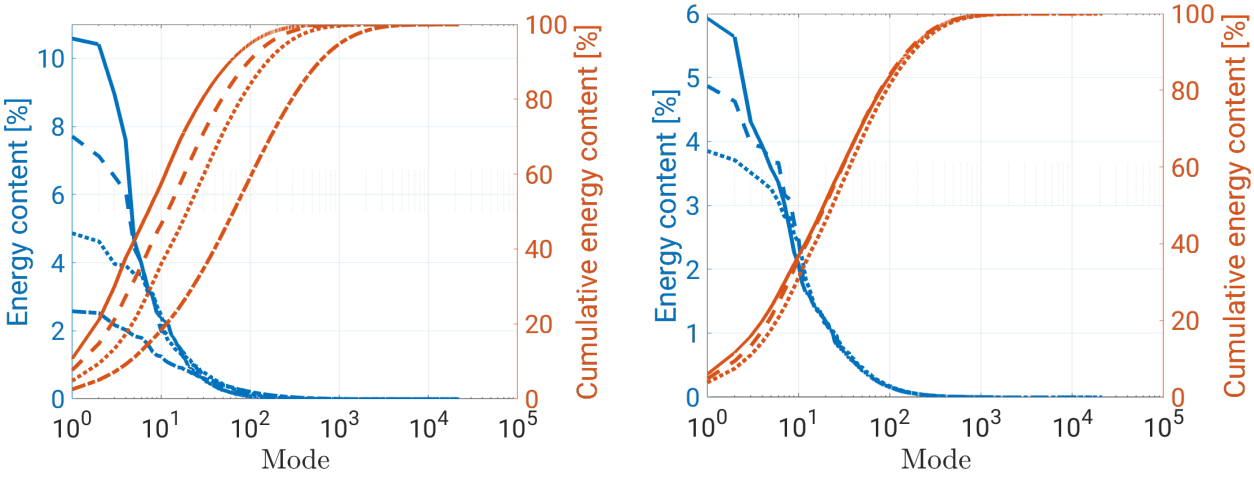

Figure 4.20: Relative (blue) and cumulative energy content (red) per mode for $Re_\tau = 115$ (solid),140 (dashed),180 (dotted),460 (dashed-dotted) (left) and different filling ratios (25%, solid; 50%, dashed; 75%, dotted) $Re_\tau = 180$ (right) for 3C-POD.

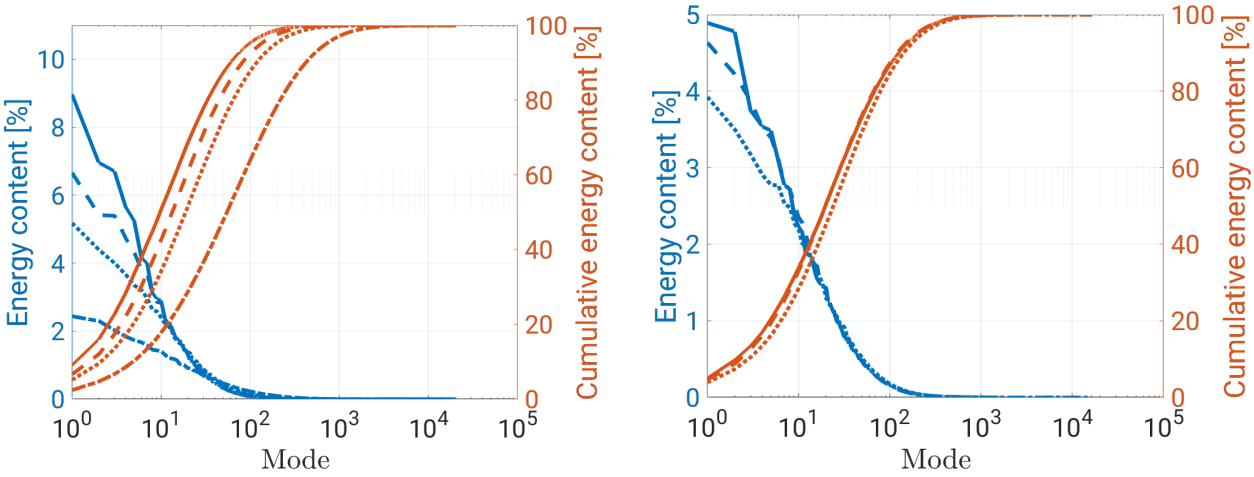

Figure 4.21: Relative (blue) and cumulative energy content (red) per mode for $Re_\tau = 115$ (solid),140 (dashed),180 (dotted),460 (dashed-dotted) (left) and different filling ratios (25%, solid; 50%, dashed; 75%, dotted) $Re_\tau = 180$ (right) for 2C-POD.

The amount of TKE contained by individual modes of the different POD approaches gives a clue how differently the two approaches distribute the fluctuating energy among the modes,

3C-POD					2C-POD				
filling ratio	Re_τ	30%	50%	90%	filling ratio	Re_τ	30%	50%	90%
50 %	115	4	8	60	50 %	115	4	9	60
50 %	140	5	12	95	50 %	140	5	13	80
50 %	180	8	20	154	50 %	180	8	18	116
50 %	230	11	29	228	50 %	230	10	25	162
50 %	460	23	65	590	50 %	460	21	54	414
25 %	180	8	20	160	25 %	180	7	18	120
75 %	180	10	24	178	75 %	180	10	23	137

Table 4.2: Number of modes needed to reconstruct more than 30%, 50% or 90% of the total energy for different Reynolds numbers and filling ratios by 3C- (left) and 2C-POD (right).

see figure 4.22. The TKE per mode was obtained by reconstructing all the flow cross-sections that served as input for the POD's per mode, using equation (4.8). Based on the instantaneous flow cross-sections the TKE was computed. It shows that for the 3C-POD the share of primary TKE decreases with increasing mode, as expected from the figures above. In contrast, the first modes of 2C-POD contain only approximately a third of TKE_1 compared to the 3C-POD modes. Moreover, the amount of primary TKE is roughly equally distributed among the first modes of 2C-POD. For higher modes the amount of TKE_1 seems to become similar for both approaches. For the modewise distribution of secondary TKE a similar partition of TKE occurs, but the 2C-POD and 3C-POD have opposite roles. The modes of the 3C-POD have an approximately constant amount of energy, whereas the energy of the first modes of the 2C-POD is larger and decreases with increasing mode. Hence, the different POD approaches decompose the flow as expected, dependent on their dominating input: the streamwise component is responsible for the partition of the 3C-POD, whereas the energy partition of the 2C-POD is driven by the secondary components.

Please note that for the 3C-POD all three velocities are used to decompose the flow, thus, all three components are available in the 3C-POD. However, despite the fact that only the cross-stream components were used for the 2C-POD to generate the temporal modes a^k and the energy fractions λ, the temporal modes can be applied not only on the cross-stream velocities to generate the spatial modes, but also on the streamwise velocity (cf. eq. (4.14)). Hence, for both approaches all three components can be analysed despite their different input. However, please further note that this procedure does not enforce orthogonality for the streamwise components of the 2C-POD.

Temporal Coefficients a

The PDF of the temporal coefficients of the most energy intense modes are very similar for both POD approaches, see figure 4.23. For both cases the distributions of the different modes are Gaussian distributed around zero. Applying the same binning range for the different approaches, the peak probabilities and the standard deviations resemble each other. Please note that the zeroth mode of 3C-POD has, in contrast to the fluctuating modes, a non-zero mean and a much smaller standard deviation than the fluctuating modes, which is not

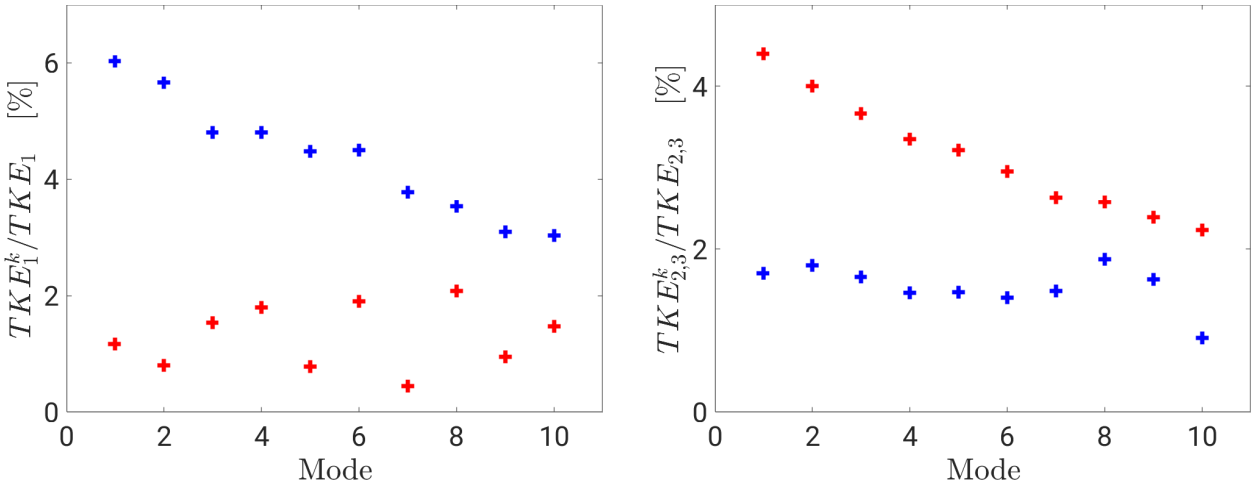

Figure 4.22: Share of primary (left) and secondary TKE (right) per mode and POD approach for semi filled pipe flow of $Re_\tau = 180$. + 3C-POD, + 2C-POD

included in the figure. Moreover, the PDF's of other fillings and other Reynolds numbers are similar for both approaches, too.

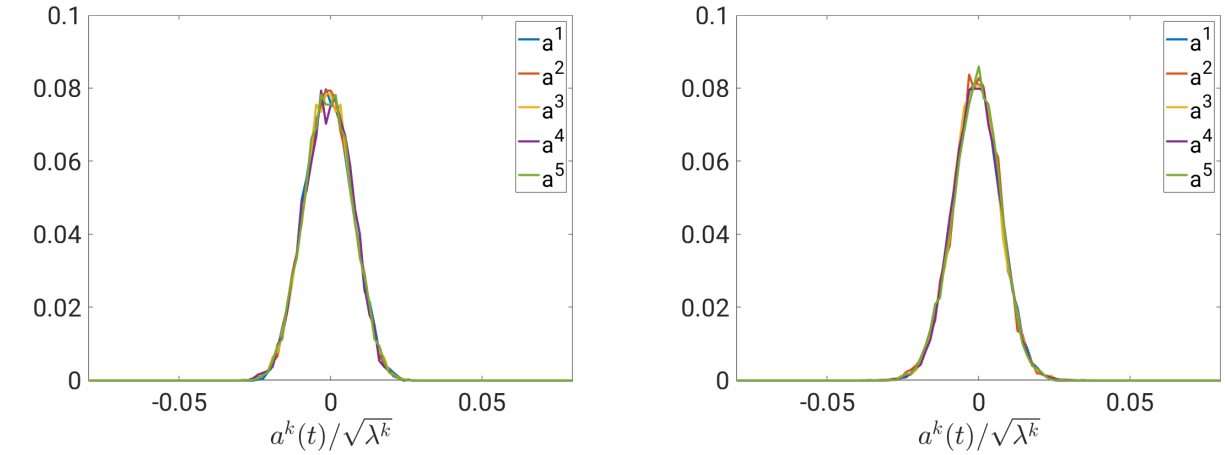

Figure 4.23: PDF of normalised modes $a^k(t)$ for 3C-POD (left) and 2C-POD (right) for $Re_\tau = 180$ with 50% filling.

Spatial Modes Φ

The spatial modes $\Phi^k(\mathbf{x})$ show a pattern of positive and negative intensities for all three velocity components over the cross-section. For the in-plane components streamlines can be computed with a distribution of intensities. However, only in combination with the temporal coefficients the flow directions can be calculated and assigned.
First, the spatial modes are shown for 3C-POD, $Re_\tau = 180$, see figures 4.24 and 4.25. The coloured contours represent the magnitude of the streamwise component. Blue and red distinguishes structures with opposite sign, but, as mentioned above, only in combination

with the temporal modes the actual direction can be stated for each time instant. The streamlines show flow paths of the cross-stream components, which can be both ways and the colour of streamlines shows the magnitude of the cross-stream velocities. Black means high intensity and white denotes low intensity. Figure 4.24 shows the zeroth mode, which is equal to the mean flow, compare figures 3.2 and 3.8. In addition to this qualitative comparison, it can be reported that the kinetic energy of the streamwise component, reconstructed from the zeroth mode, deviates from the original primary MKE only by 1.5‰. The kinetic energy of the secondary components of the zeroth mode differs by 3.1% from the original secondary MKE. Hence, the zeroth mode equals the mean flow qualitatively and quantitatively.

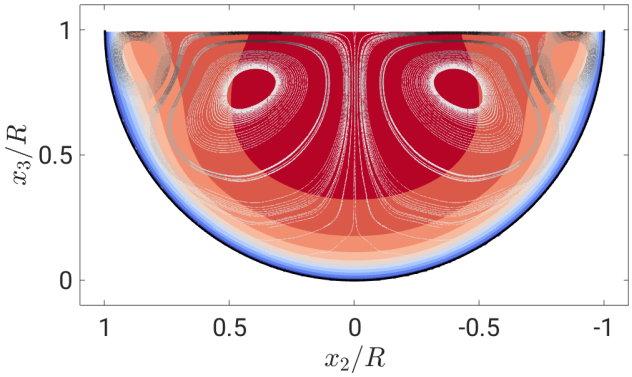

Figure 4.24: Zeroth spatial mode Φ^0 of 3C-POD for $Re_\tau = 180$ and 50% FR. Φ_1^0 is shown in blue (low) to red colour (high intensity) and the gray contours display the magnitude of the cross-stream components Φ_2^0 and Φ_3^0 (black = high intensity, white = low intensity).

The fluctuating modes of the 3C-POD show more complex patterns (fig. 4.25). The high intensities can be found along the wall, whereas the bulk region and the centre of the free surface lack high intensities. The first four modes have a pattern of negative and positive velocity streaks at the upper side wall. One positive and negative streak are connected and also include a cross-stream structure with high intensities where the streamwise component is strong, too, creating three-component structures. Especially for the first ten modes, it is visible that the modes appear in pairs – one mode is symmetric and one is anti-symmetric, which can also be seen in Matin *et al.* (2018) for a square closed-duct flow. The modes of each pair supplement each other. For example Φ^1 has two strong streamwise intensities with the same sign at the free surface. In combination with Φ^2, which has two strong streamwise intensities with opposite sign at the free surface, the intense patches of Φ^1 can either be strengthened or weakened. This depends on the combination with their temporal coefficients. For instance, if the temporal coefficients are positive for both modes, the high intensity in blue colour at the free surface in positive x_2-direction would be strengthened and the structure in negative x_2-direction would be balanced. If the temporal coefficients have opposite sign, the effect would be mirrored and if one temporal coefficient is small, the other mode dominates. Due to the possible combinations of the mode pairs, the same structures can evolve as from the modes obtained by Ng *et al.* (2021). However, because they did not include mirrored samples into the velocity correlation matrix $C(t, t')$, they obtained different modes with structures on each side only. This effect of combining mode

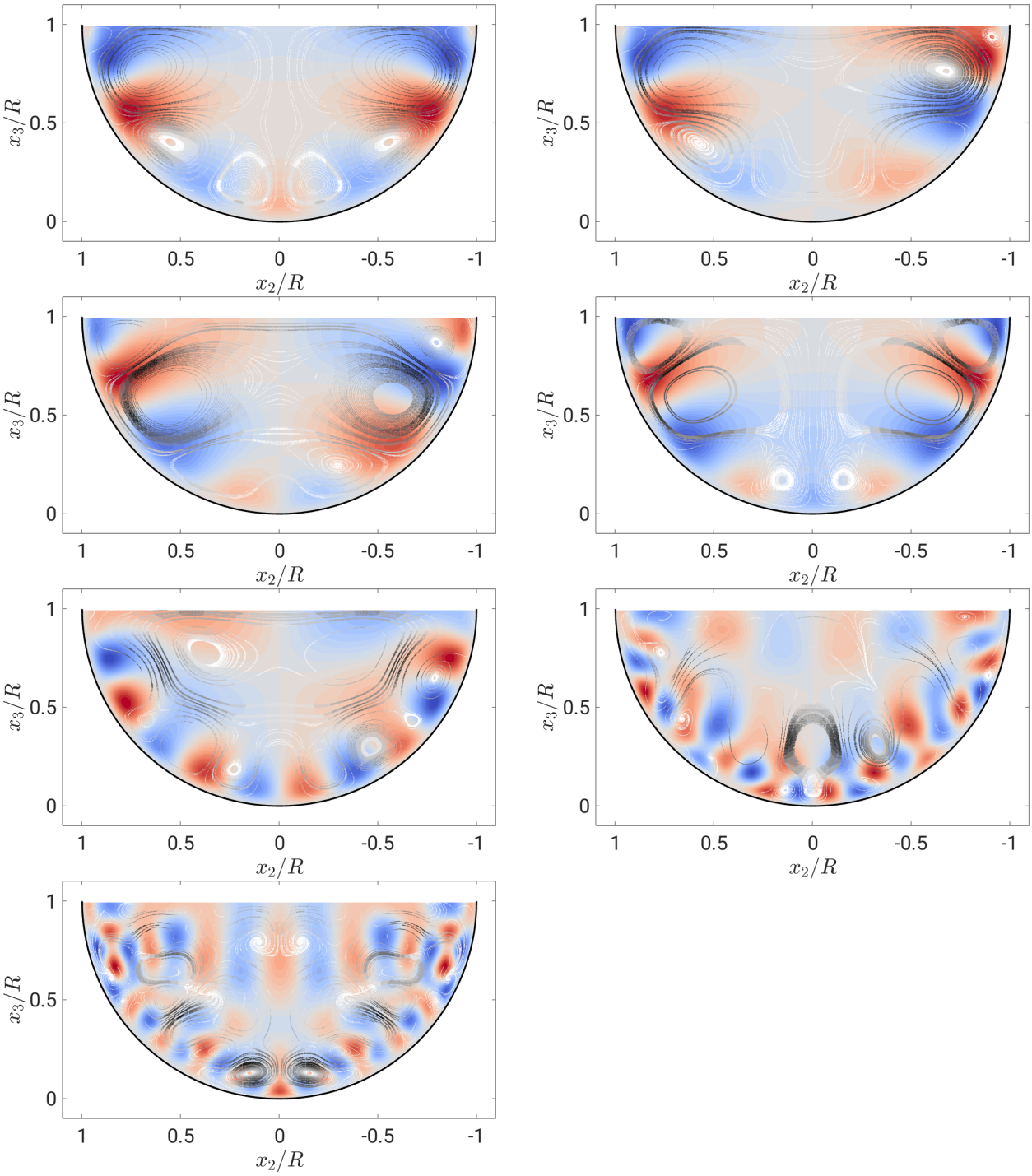

Figure 4.25: Spatial modes Φ^1, Φ^2 (top row, left and right), Φ^3, Φ^4 (second row), Φ^{11}, Φ^{80} (third row) and Φ^{146} (bottom row) for 3C-POD of $Re_\tau = 180$ and 50% FR. Φ_1^k is shown in blue to red colour and the gray contours display the magnitude of the cross-stream components Φ_2^k and Φ_3^k (black = high intensity, white = low intensity).

pairs strengthening and weakening each other also appears for the cross-stream structures of the 3C-POD. The modes Φ^1 and Φ^2 have one strong pair of streamwise intensities on

each side and one dominating cross-stream structure, resembling the outer secondary cell, whereas only a very small and weak structure is noticeable in the mixed-corner. Mode Φ^3 and Φ^4 have three intense streamwise structures in each half of the pipe and two cross-stream structures, with one structure approximately covering the inner secondary cell and another structure below, again resembling the outer secondary vortex. These first four modes contain approximately 17% of the fluctuating energy. For higher modes, see lower rows of figure 4.25, the structures get smaller and more peaks appear along the wall and several azimuthal layers of peaks appear, as known from POD in pipe flow (Hellström & Smits, 2014). In comparison to the inhomogeneous peak distribution of the high energy containing modes, the peaks of the higher modes appear along almost the complete wall, which is similar to the distribution of full pipe flow.
For 25% and 75% filling the first four spatial modes of the 3C-POD are shown in the appendix C, see figures C.1 and C.2. Generally, the modes of 75% FR are similar to the modes of 50% FR. For the 25% filled case it already became noticeable that it is different to the others, which is also present in the spatial modes. More details and a small comparison to the POD of Ng *et al.* (2021) is given in the appendix.
In figure 4.26 the spatial modes of the 2C-POD are shown. The 2C-POD modes are quite different to the 3C-POD modes, as their high peaks are not restricted to the near-wall region. The high energy modes have high magnitudes in the bulk region and at the free surface and are less attached to the wall. Similar to 3C-POD pairs of symmetric and anti-symmetric modes can be observed that supplement each other: Φ^1 and Φ^2; Φ^4 and Φ^6. Interpreting the streamwise velocity pattern as streaks, the first mode represents the flow pattern with the minimum possible number of streaks contributing to turbulent flow. For each following mode one streamwise velocity peak is added. Please note that in contrast to the pair pattern, it is also possible to interprete mode Φ^2 as a link to both modes Φ^1 and Φ^4. Nevertheless, a pair pattern can again be detected for the following modes. For higher modes, the development is similar to 3C-POD. The structures get smaller, the peaks of the structures move towards the wall and more layers of structures are possible. Please note that the appearance of the spatial modes do not differ much for different Reynolds numbers.
The first four spatial modes of the 2C-POD for 25% and 75% FR can be found in the appendix C, see figure C.3. In general, the first four modes show the same behaviour as for 50% FR, however, the structures are deformed vertically: compressed for 25% FR and stretched for 75% FR.

Reconstructed Flow Fields

The POD is often used as a tool to condensate the most important structures from the flow field, in order to make the spatio-temporal dynamics tangible. However, the temporal coefficients and spatial modes are abstract quantities and difficult to interpret. Instantaneous flow fields can be reconstructed from selected modes giving an impression about how the POD decomposes the flow. By projecting the spatial modes on the temporal coefficients, instantaneous velocity cross-sections, which were used as input for the POD, can be reconstructed.
In figure 4.27 the flow field was reconstructed using all the high energy modes, that cumulatively sum up to 30%, 50% and 90% of the fluctuating energy, i.e. for more energy a larger

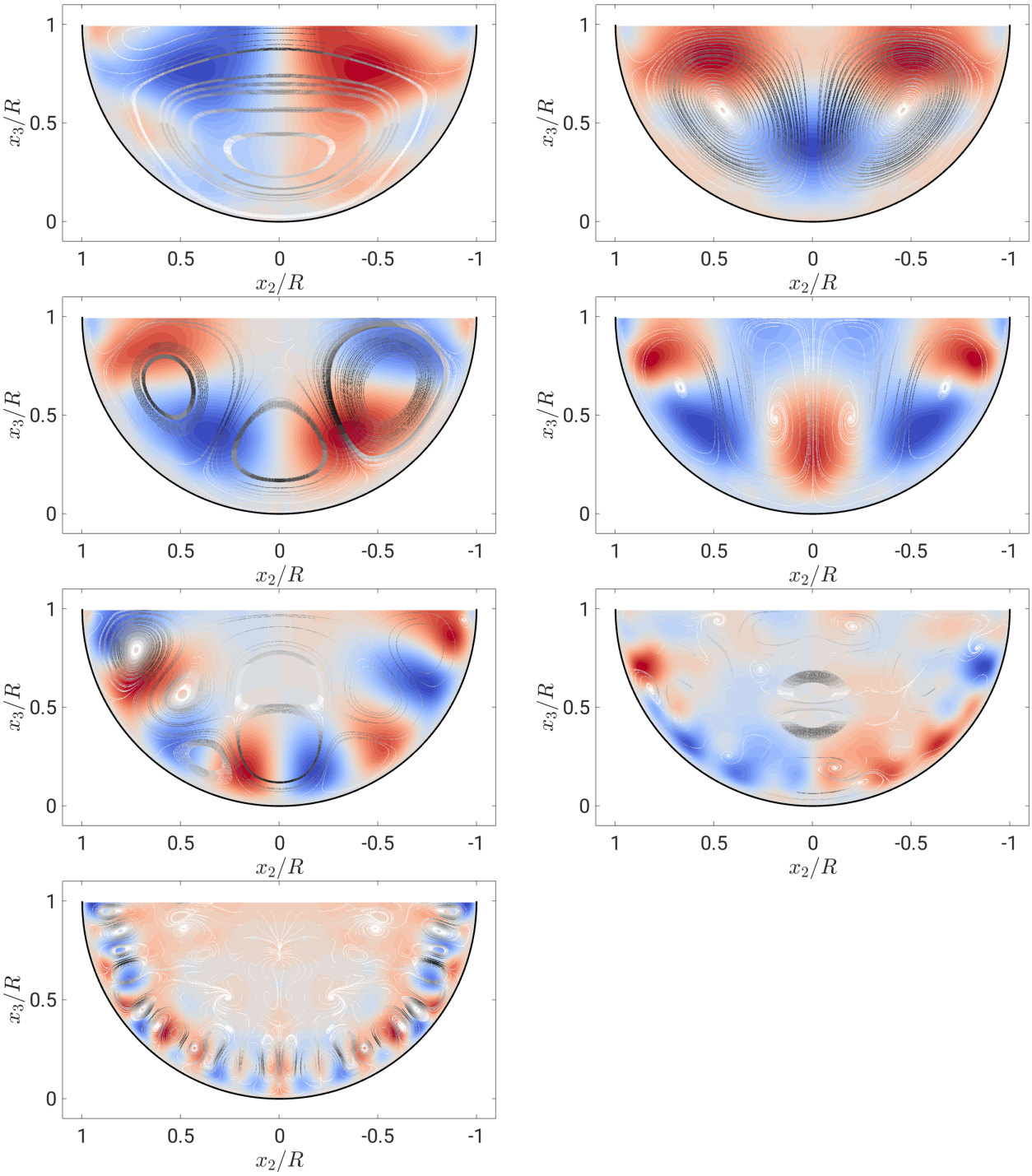

Figure 4.26: Spatial modes Φ^1, Φ^2 (top row, left and right), Φ^4, Φ^6 (second row), Φ^{11}, Φ^{80} (third row) and Φ^{146} (bottom row) for 2C-POD of $Re_\tau = 180$ and 50% FR. Φ_1^k is shown in blue to red colour and the gray contours display the magnitude of the cross-stream components Φ_2^k and Φ_3^k (black = high intensity, white = low intensity).

number of modes is used, compare table 4.2. For 30% the first eight, for 50% the first 20 and for 90% the first 154 modes are used to reconstruct the flow field. Hence, these recon-

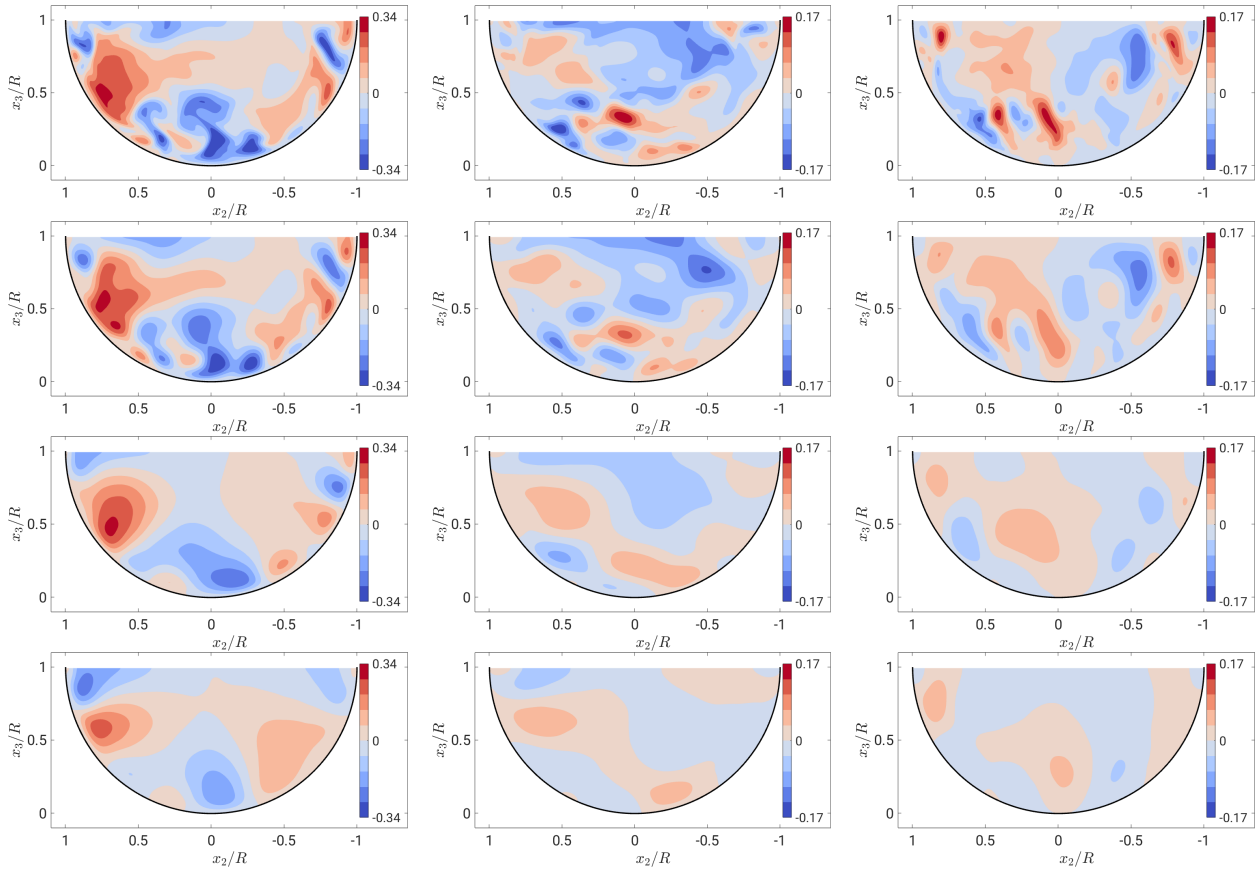

Figure 4.27: Reconstructed instantaneous and fluctuating velocities u_1'/u_b (left), u_2'/u_b (middle) and u_3'/u_b (right) from 3C-POD for $Re_\tau = 180$ and 50% FR. Using most energy containing modes representing 100%, 90%, 50% and 30% of fluctuating energy (top to bottom). The included energy corresponds to all, the first 154, 20 or 8 modes, respectively.

structed flow fields can be compared to the complete, fluctuating, instantaneous flow field of a certain time instance. Comparing the different instantaneous velocity components it can be noticed that the TKE is similarly distributed as shown in figure 4.22. On the one hand, the 50% high energy modes of the streamwise component contain approximately 63% of the complete primary TKE. On the other hand, for the cross-stream components only 21% of the complete secondary TKE is contained within the 50% high energy modes. Moreover, the reconstructed flow fields from 30% of the fluctuating energy show high intensities along the walls for all three velocity components, which is consistent with the distribution of the high energy modes.

In figure 4.28 the same velocity instance is reconstructed using the modes of the 2C-POD. The difference for 90% of the fluctuating energy is negligible, but for the lower energy fractions some interesting observations can be made. As expected from the distribution of the spatial modes, the reconstructed velocity for 30% and 50% consist of structures that are more present in the bulk region than for 3C-POD. Moreover, the amount of secondary TKE present for the 30% case is higher than for 3C-POD (approximately 50% of total secondary TKE), whereas the primary TKE is smaller, which is consistent with the observations in

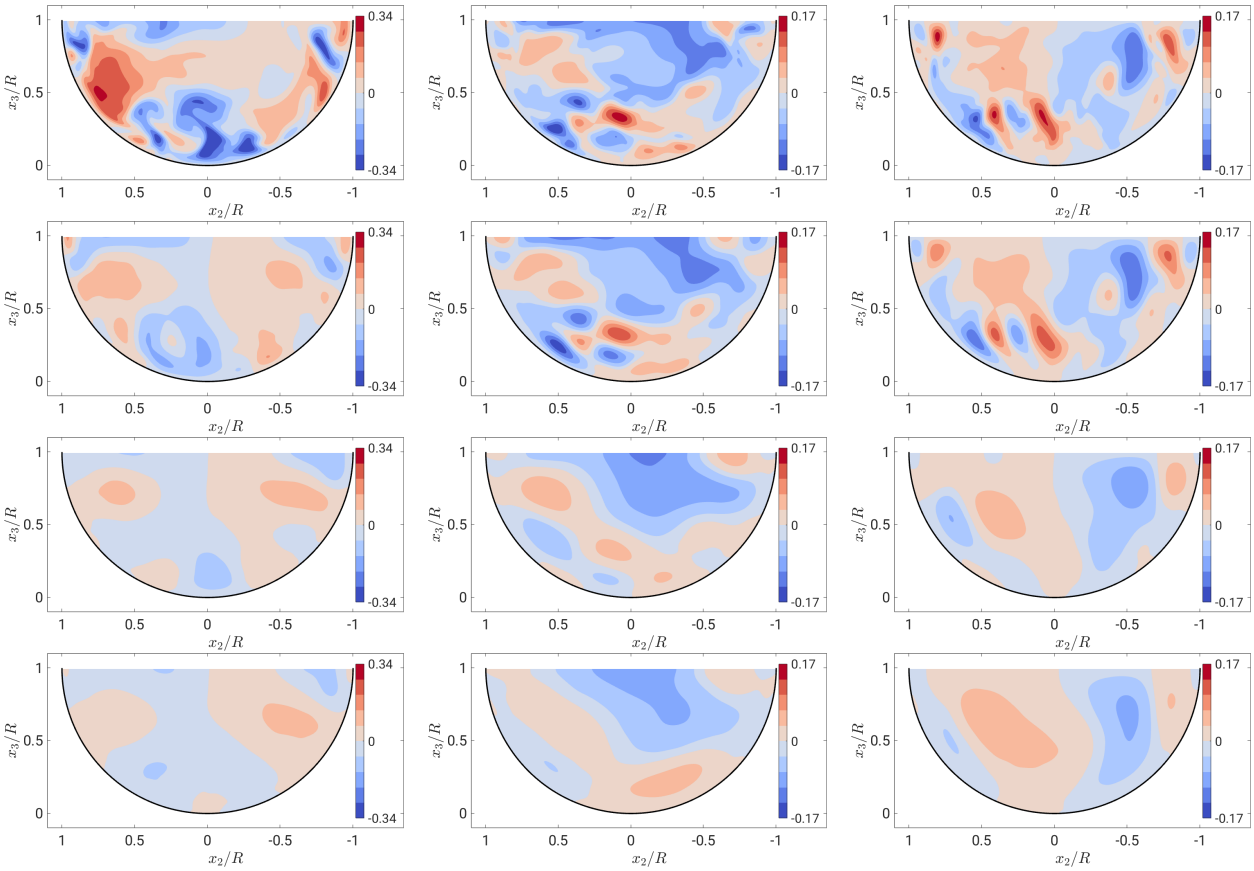

Figure 4.28: Reconstructed instantaneous and fluctuating velocities u_1'/u_b (left), u_2'/u_b (middle) and u_3'/u_b (right) from 2C-POD for $Re_\tau = 180$ and 50% FR. Using most energy containing modes representing 100%, 90%, 50% and 30% of fluctuating energy (top to bottom). The included energy corresponds to all, the first 116, 18 or 8 modes, respectively.

section 4.2.1 (*Energy Fractions* λ). Similar to the reconstructed flow field via the 3C-POD only a rough image is established by 30% of the fluctuating energy, however, some important features like the global rotational structure are already visible.

Figure 4.29 and 4.30 show the fluctuating streamwise vorticity 25 wall units below and parallel to the free surface of one snapshot in order to compare the two POD's. Please note that the vertical height of the horizontal plane was chosen, in order to cut through and, therefore, show the structures that possibly correlate to the mean secondary flow. The spatial modes were used to generate the temporal coefficients for all cross-sectional slices of a snapshot, which made it possible to reconstruct one three-dimensional snapshot from the two-dimensional POD modes. As known from chapter 3 and section 4.1 the vorticity at the mixed-corner and along the free surface are an important region for the generation of secondary flow. For both PODs, the differences for 90% of the fluctuating energy are again negligible. The vorticity magnitude and its distribution is similar for 50% and 30% for both PODs. Strong structures can be found along the side walls and in the centre mostly low magnitudes occur. However, one difference is, that 3C-POD reconstructs elongated vorticity patches and 2C-POD rather reconstructs small, alternating events. Moreover, single

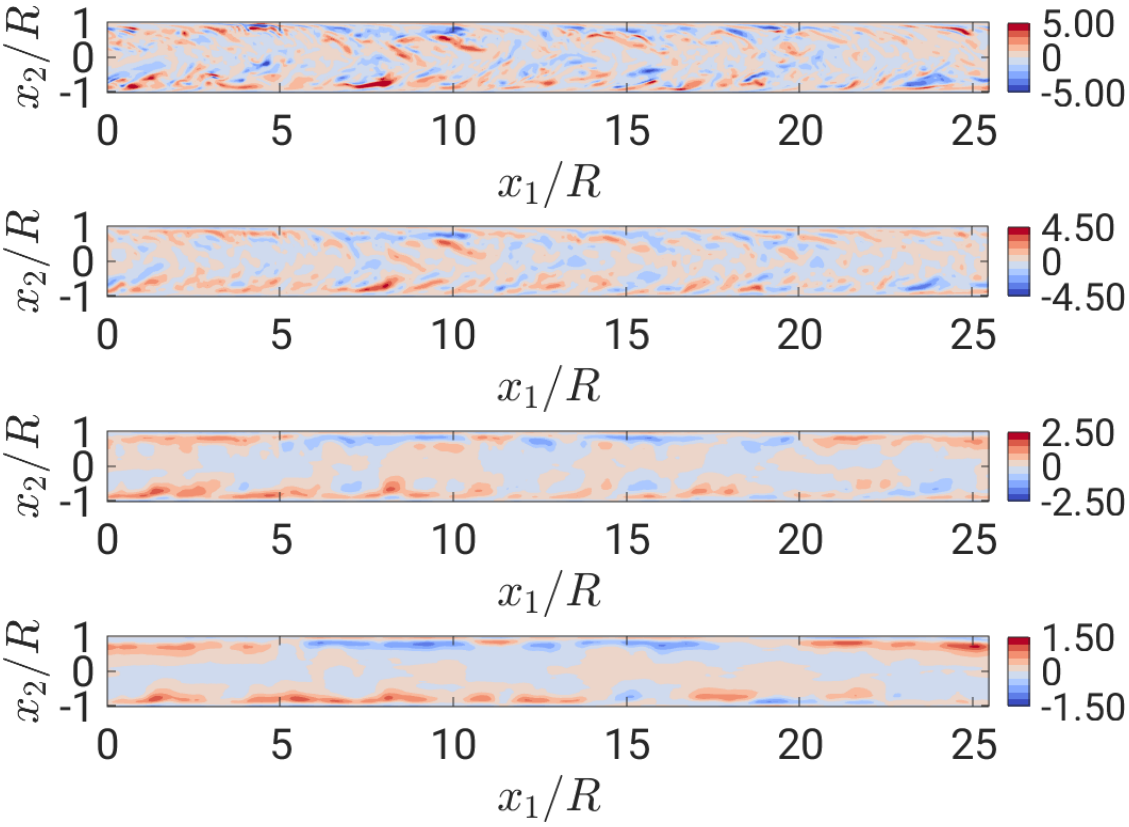

Figure 4.29: Instantaneous $\omega_1' R/u_b$ 25 wall units below and parallel to the free surface from 3C-POD for $Re_\tau = 180$ with 50% FR. Using most energy containing modes representing 100%, 90%, 50% and 30% of fluctuating energy (top to bottom).

events of strong vorticity in the complete instantaneous distribution are still assignable by the modes containing the highest 30% of the fluctuating energy by 2C-POD, whereas the 3C-POD generates mostly long structures in the vicinity of the wall, which can hardly be linked to the complete instantaneous velocity distribution.

Conclusion

To conclude the section on POD, the distribution of the full energy content of each mode does not differ too much between the 3C- and 2C-POD. However, each of the two different approaches divides the primary and secondary TKE differently, dependent on which velocity is the dominating input for each POD. For 3C-POD, the secondary TKE is equally distributed over the first 10 modes, whereas for 2C-POD the first mode contains most secondary TKE and it decreases continuously for the next modes. For the primary TKE the distributions of the individual modes show the opposite. A strong dependence for the 3C-POD and constant amount of energy for the first modes of 2C-POD can be reported for the primary TKE of the first modes. The fluctuating temporal coefficients of both PODs are Gaussian distributed around zero. The spatial modes for 3C-POD are more connected to strong streamwise velocity peaks along the wall and for 2C-POD larger structures covering more the bulk region

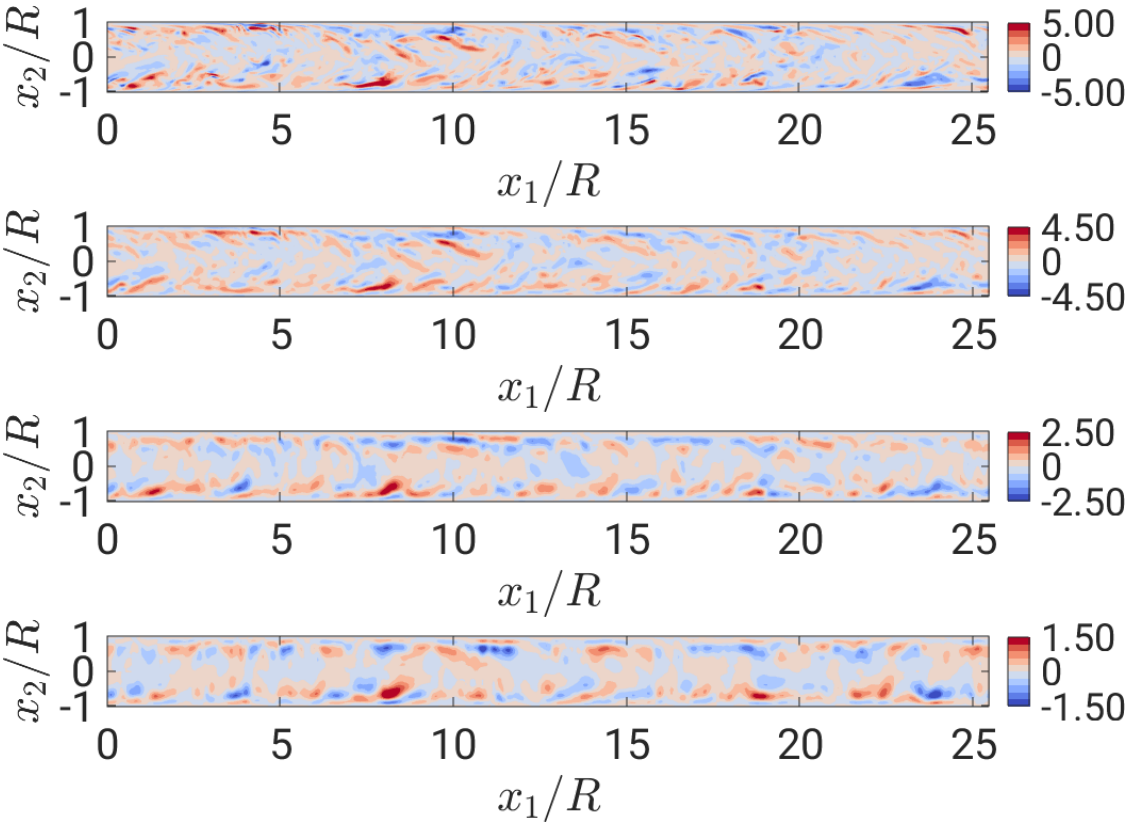

Figure 4.30: Instantaneous $\omega_1' R/u_b$ 25 wall units below and parallel to the free surface from 2C-POD for $Re_\tau = 180$ with 50% FR. Using most energy containing modes representing 100%, 90%, 50% and 30% of fluctuating energy (top to bottom).

of the flow. The spatial restriction of the high energy containing modes indicates that both POD approaches are not able to describe vortices moving over these boundaries very well. Hence, the sorting mechanism described by Sakai (2016) can hardly be reproduced by only the high energy-containing modes. The more modes are included, the more spatial dynamics are reconstructed. The differences of the spatial preferences between the two approaches are also well visible in instantaneous velocity fields being reconstructed by high energy containing modes representing 30% of the energy. On the one hand, the instantaneous streamwise vorticity along the free surface reconstructed from 2C-POD indicate that individual strong structures that resemble the instantaneous flow field are carrying a considerable amount of secondary TKE. On the other hand, elongated structures along the mixed-corner that resemble the inner secondary cell can be reported for the 3C-POD, being consistent with Ng *et al.* (2021).

Taking all the above mentioned results into account, it is difficult to judge, which POD approach is more suitable to analyse the secondary flow. On the one hand, not to take the dominating streamwise component into account seems not justifiable, because the primary and secondary flow are directly connected. On the other hand, the secondary flow is such a subtle process, whose kinetic energy is more coherently divided into modes with higher and lower energy for the 2C-POD. At first glance, it seems that the two different PODs

emphasize two different aspects of the flow – the near wall behaviour is more covered by the high energy modes of the 3C-POD and the bulk flow is more represented by the high energy modes of the 2C-POD. However, the results of section 4.1 have shown that the crucial terms of the secondary flow mechanism, the vorticity generation and secondary production, are based on secondary velocity components only. Hence, in terms of the secondary flow mechanism, the 2C-POD should be more relevant.
How the decomposed flow fields can help to further understand the secondary flow mechanism, will be investigated in the section after the next section. Before that, another tool, the Gaussian filtering, is introduced, which is also applied to study the generation mechanism of secondary flow and is compared to the approach of POD.

4.2.2. Gaussian Filtering (GF)

Considering the instantaneous flow, many detailed and small structures are visible, however, based on the knowledge of energy spectra and also by just looking at the flow fields qualitatively, larger structures do also exist. Plotting the vorticity, the most intense regions usually highlight the small scales, as the vorticity is related to terms of derivatives. In contrast, large scales are not directly available using the vorticity. One way to extract the larger structures from the flow is the POD, introduced in the last section (section 4.2.1). Another possibility is to filter the flow field with a Gaussian function, which was done for example by Lozano-Durán *et al.* (2016); Lee *et al.* (2017) and Motoori & Goto (2019). Lozano-Durán *et al.* (2016) study self-similarities of flow dynamics in the inertial range, by comparing various quantities at different scales obtained via GF. Motoori & Goto (2019) use Gaussian-filtered flow fields to investigate a hierarchy of vortices. From the filtered velocities various flow quantities can be deduced, for example, the streamwise vorticity. Of course, the vorticity is not the ideal quantity to identify coherent structures especially at the wall, where strong shear is taking place. Therefore, the swirl- and low-pressure-condition of Kida & Miura (1998) was applied and also the instantaneous wall shear stress was included. These two parameters were compared to the constructed vorticity iso-surfaces, in order to give more confidence about the extracted structures, which will be shown later on.
In contrast to the POD, which decomposes the flow into modes according to their kinetic energy, the GF can divide the flow by the size of its flow structures. As the GF is only influenced by the width of its kernel, it is a purely geometrical filter that filters the whole flow equally. Thus, all three velocity components receive the same filtering over the complete flow field, which separates the flow into small and large scales. Hence, the aim of applying GF on the flow is to understand which size of structures is involved in secondary flow and its generation mechanism. Please note that due to the relatively small Reynolds numbers, a scale separation is usually not expected to happen. However, Sakai (2016) is reporting a scale separation already for similarly small Reynolds numbers, taking place as soon as the *velocity-dip* phenomenon occurs, which is the case for the presented Reynolds number.

Theory of Gaussian Filtering

The Gaussian filter was set up, based on the approach of Lozano-Durán *et al.* (2016), who did extensive comparisons between two different implementations of the filter. The Gaussian

filter is applied on all velocity components u_i in all three directions $\mathbf{x}$, see equation (4.15), and in the same manner on the pressure.

$$\tilde{u_i}(\mathbf{x}) = \sum_{x_{3,P}} \sum_{x_{2,P}} \sum_{x_{1,P}} u_i(\mathbf{x}_P) \times C(\mathbf{x}) exp\left(-\frac{2}{\sigma^2}((x_{1,P}-x_1)^2+(x_{2,P}-x_2)^2+(x_{3,P}-x_3)^2)\right)\Delta x_1 \Delta x_2 \Delta x_3 \tag{4.15}$$

The coefficient $C(\mathbf{x})$ is adjusted in such a way, that the kernel volume is equal to one, independent of its width σ. σ describes the standard deviation of the filter kernel. Later on in the text, it will be referred to the filter width in inner units $\sigma^+ = \sigma u_\tau/\nu$. The aspect ratios of the filter widths are set homogeneously in all three directions. Different filter kernels are applied by changing σ, i.e. with a larger σ the filtered flow field represents larger structures. In figure 4.31 the one dimensional PDF and the wavenumber spectrum of the Gaussian kernel are shown. With decreasing filter width the PDF becomes more narrow but its peak magnitude increases. Please note that compared to the normal distribution the exponent in equation (4.15) is multiplied by a factor of four, which makes the present distributions more narrow. In Fourier space the filter acts like a low pass filter, hence, with increasing filter width more and more wavenumbers are cut off. However, it is not a sharp cut-off in Fourier space, but a Gaussian cut-off.

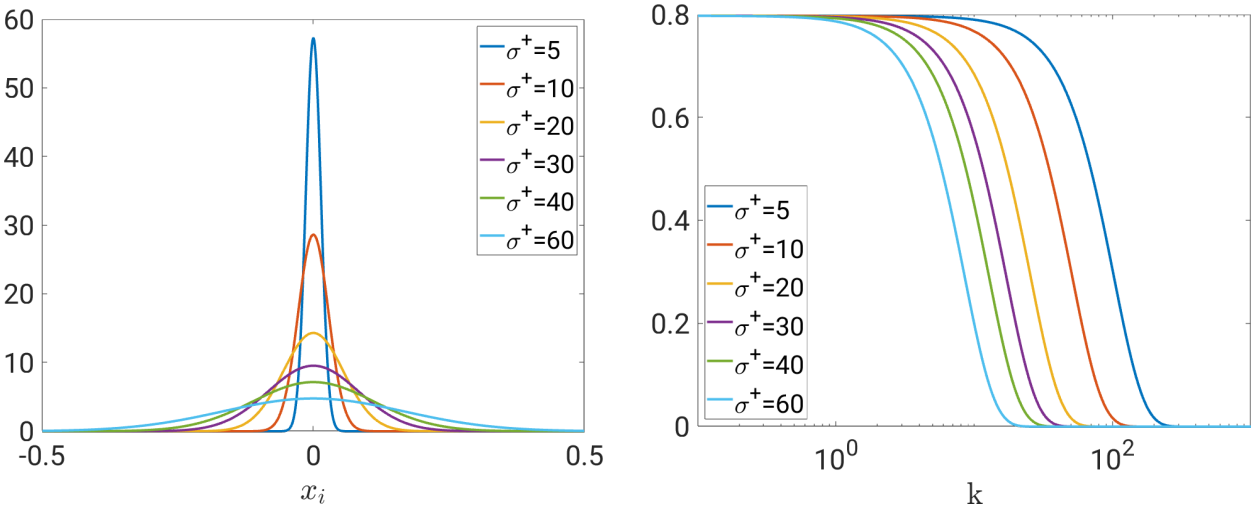

Figure 4.31: PDF (left) and wavenumber spectrum (right) of the applied Gaussian kernel for various filter widths σ^+.

As a result each velocity component and the pressure component are filtered in all three dimensions, generating instantaneous, filtered 3D-flow fields, which can be further analysed. In contrast to the channel flow of Lozano-Durán *et al.* (2016), only one homogeneous direction is present in partially filled pipe flow. Moreover, at the top boundary a free surface occurs. For the wall, Lozano-Durán *et al.* (2016) compared two different implementations of the filter, one with a mirroring of the velocities at the wall and changing the sign of the wall normal component and the other one truncates the filter kernel at the wall. The two approaches

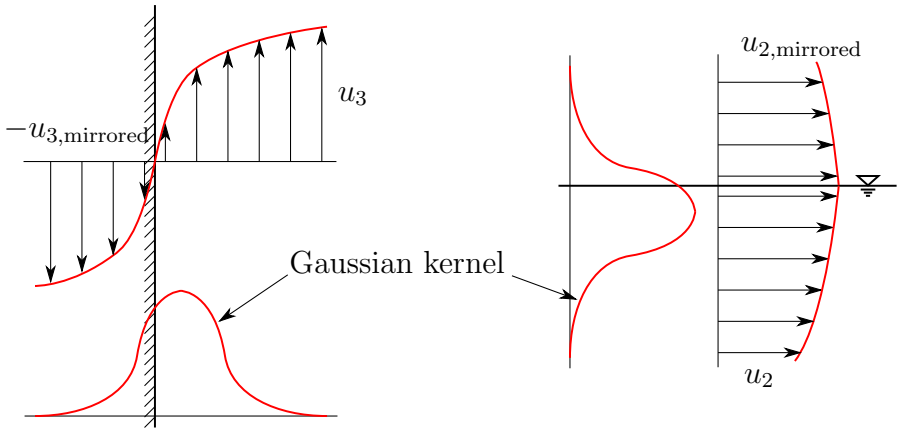

Figure 4.32: Sketch of the Gaussian kernel at the wall (left) and at the free surface (right) with the velocities u_2 and u_3 and their corresponding mirroring at the boundary.

gave similar results, however, the first generates incompressible and the second slightly compressible filtered flow fields. Because of the different boundary conditions, the approach of mirroring the velocities to the outside of the flow domain has been applied: at the wall the three velocities were mirrored with a negative sign; at the free surface, the free surface normal velocity u_3 was also mirrored with a negative sign but the free surface parallel velocities u_1 and u_2 were only mirrored without a change of sign, see figure 4.32. Hence, the filtered flow field remains incompressible. The pressure field was simply mirrored at all boundary conditions for the filtering procedure.

Filtered Flow Fields

In order to be able to compare the Gaussian filtered flow fields to the flow fields reconstructed by the POD, the amount of TKE that remains in the filtered fields is displayed, see figure 4.33. The ratio of TKE decreases continuously with increasing filter width. With increasing Reynolds numbers it decreases less strong, because the filter width becomes smaller in an absolute sense. Hence, for the model case ($Re_\tau = 180$ and FR 50%) $\sigma^+ = 5$ corresponds approximately to 90%, $\sigma^+ = 20$ to 50% and $\sigma^+ = 30$ to 30% TKE compared to the non-filtered TKE.

In order to compare the Gaussian filtered flow fields to the reconstructed flow fields of the POD, the same flow fields are shown in this subsection. Figure 4.34 shows the same instantaneous cross-section like in figures 4.27 and 4.28 for the POD's. The fluctuating velocity components $\tilde{u}_1'$, $\tilde{u}_2'$ and $\tilde{u}_3'$ are Gaussian filtered with different filter widths, which correspond approximately to the same level of TKE as shown in the POD. With increasing filter widths the velocities are more and more homogeneously distributed over the cross-section and the peaks are flattened. The streamwise component clearly shows the main velocity streaks in the vicinity of the wall. Also in the strongly filtered representation a streak pattern is visible, which is qualitatively consistent with the non-filtered flow field. Moreover, it is in good agreement with the reconstructed fluctuating velocities of the 3C-POD, see figure 4.27. With increasing filter width the in-plane components show that a large vortex can be detected rotating clockwise in the centre of the flow. In comparison to the

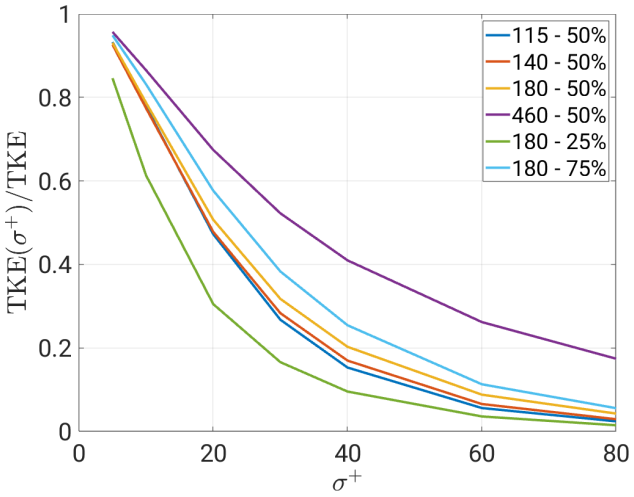

Figure 4.33: Ratio of TKE in Gaussian-filtered fields for various Reynolds numbers and FRs over the filter widths $\sigma^+ = 5, 10, 20, 30, 40, 60$ and 80.

reconstructed fluctuating velocities of the 3C-POD the represented high intensity regions of the in-plane velocities do not match for comparing 30% of the high energy modes to a filter width of $\sigma^+ = 30$. However, comparing the filtered velocities to the fluctuating velocities of the 2C-POD, a similar pattern of intensities can be noticed. Hence, the fluctuating velocity distributions of the Gaussian filtered approach indicate that they represent the near wall behaviour of the streamwise velocity, which is covered by the 3C-POD, and the characteristics of the in-plane velocity components in the bulk region, reconstructed by the 2C-POD.

In the following paragraphs the Gaussian filtered, vortical structures are investigated. Therefore, as mentioned above, GF was also applied on the pressure, which enables the usage of the structure criterion of Kida & Miura (1998). The structure criterion can be applied in a 2D-plane to detect vortex centres. For each cross-section local pressure minima are localized. At each position of the pressure minima a swirl condition is tested. The discriminant of the two-dimensional cross-stream velocity gradient tensor $D_{2,3} = 1/4(\partial u_2/\partial x_2 - \partial u_3/\partial u_3)^2 + \partial u_2/\partial x_3 \partial u_3/\partial x_2$ needs to be smaller than zero. Both conditions are applied to the Gaussian filtered fields and the identified vortex centres are compared to the Gaussian filtered vorticity distribution in figure 4.35. In the non-filtered case, most of the vortical structures represented by the vorticity are also identified by the criterion of Kida & Miura (1998). A good agreement can also be found for the filtered distributions. Not every $\tilde{\omega}_1$-peak is identified by the criterion of Kida & Miura (1998), however, it is in good accordance for the most intense $\tilde{\omega}_1$-structures. This accordance was checked for all the cross-sections of an entire snapshot for different filter widths, supporting that the vortex centres identified by the criterion of Kida & Miura (1998) match with distinct events of vorticity. Please note that the structure criterion of Kida & Miura (1998) was not applied to the structures reconstructed by POD, because the decomposed pressure was not available.

In addition the instantaneous, non-filtered wall shear stress is shown along the pipe's circumference in figure 4.35. The wall shear stress is supposed to be the foot-print of the flow on the wall. On the one hand, the comparison of the non-filtered wall shear stress with

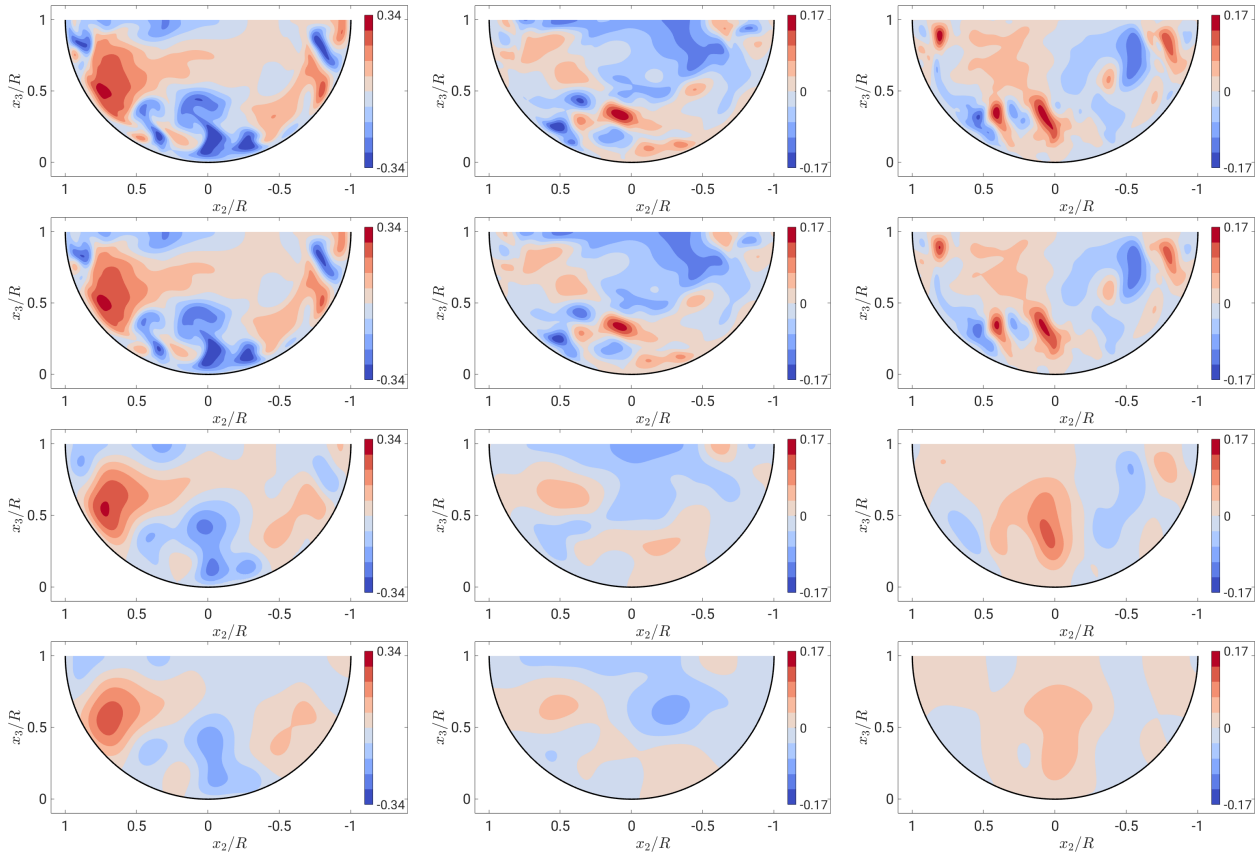

Figure 4.34: Gaussian-filtered instantaneous, fluctuating velocities $\tilde{u}_1'/u_b$ (left), $\tilde{u}_2'/u_b$ (middle) and $\tilde{u}_3'/u_b$ (right) with filter widths $\sigma^+ = 0, 5, 20, 30$ (top to bottom) for $Re_\tau = 180$ and 50% FR.

the filtered vorticity adds another possibility to check the plausibility of the visualised vortical structures. On the other hand, the question arises, which part of the flow is mostly responsible for the wall shear stress. By advancing through every cross-section of an instantaneous snapshot the spatial structure and the relations between small and large scale vortical structures and the non-filtered wall shear stress can be investigated. This is realized by a spatial sequence of cross-sectional slices displaying one non-filtered and one Gaussian filtered streamwise vorticity $\tilde{\omega}(\sigma^+ = 0; \sigma^+ = 30)$ and the non-filtered wall shear stress along the perimeter, see figure 4.36.

The small scale (non-filtered) structures are shown by red (clockwise) and blue (counter-clockwise rotation) contour lines, the large scale structures are represented by pink (clockwise rotation) and cyan (counter-clockwise rotation) filled contours and the wall shear stress is displayed along the perimeter in a colourmap from blue over green to red. The visualisation shows a highly chaotic distribution of small and large structures that strongly interact. However, certain spatial patterns are remarkable: First of all, the small and large scale structures and the wall shear stress are very consistent. Small and large scale structures are often part of the same structure, they have a large common area and overlap each other. It also occurs that a large scale structure consists of two or three small scale structures. Hence, it is difficult to detect a scale separation, which is somewhat expected, as the Reynolds number

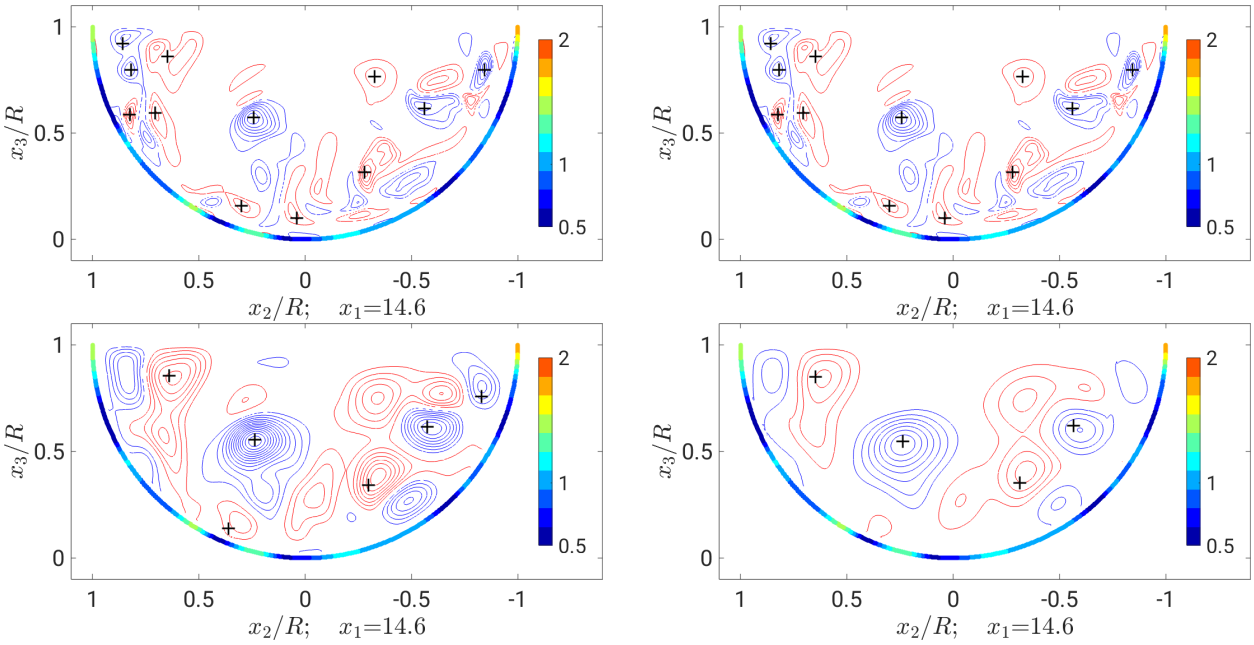

Figure 4.35: Instantaneous, Gaussian filtered $\tilde{\omega}_1 R/u_b$ for $Re_\tau = 180$ and 50% FR with a filter width of $\sigma^+ = 0$, 5 (top left and right), 20 and 30 (bottom left and right). Red contours show clockwise and blue contours show counter-clockwise rotation. + indicate vortex centres defined by the condition of Kida & Miura (1998). Outside, along the perimeter the non-filtered wall shear stress τ_w/τ_0 is plotted, with its colourmap next to the cross-section. The increments for the contourlines of $\tilde{\omega}_1 R/u_b$ are 0.83 (top) and 0.19 (bottom).

is relatively small. However, as mentioned above Sakai (2016) reports a scale separation already for similarly small Reynolds numbers. Another noticeable pattern shows a wall attached structure that consists of small and large scales, which appears in the sequence on the left side near the wall at about 45 degrees. Advancing in streamwise direction, first an increase in wall shear stress can be noticed, followed by a developing small scale structure at the wall that further grows away from the wall, where it also consists of larger scales. Usually, such structures were found to end in the buffer layer. Please note that the described, wall-attached structure agrees quite well to the concept of hairpin structure known from the near-wall turbulence (cf. section 1.2 (*Coherent Structures in a Wall-Bounded Flow*)), however, for most of the observed structures only one leg could be identified. In general, it could be observed that in addition to the large number of wall-attached structures, many structures exist that are not attached to the wall, which often have a lower intensity compared to the near-wall structures. However, there are only few structures that are further away from the wall than $0.5R$, whether they are small or large scale structures. Thus, the most active area is near the wall and in the buffer layer.

As known from section 3.2.1, the structures in the lower part of the flow balance themselves if averaged over time. Averaging over the structures in the upper part of the flow generates the mean secondary flow. The contribution of the different scales to the mean secondary flow can be investigated in figure 4.37. As in section 4.2.1, figure 4.37 shows the fluctuating streamwise

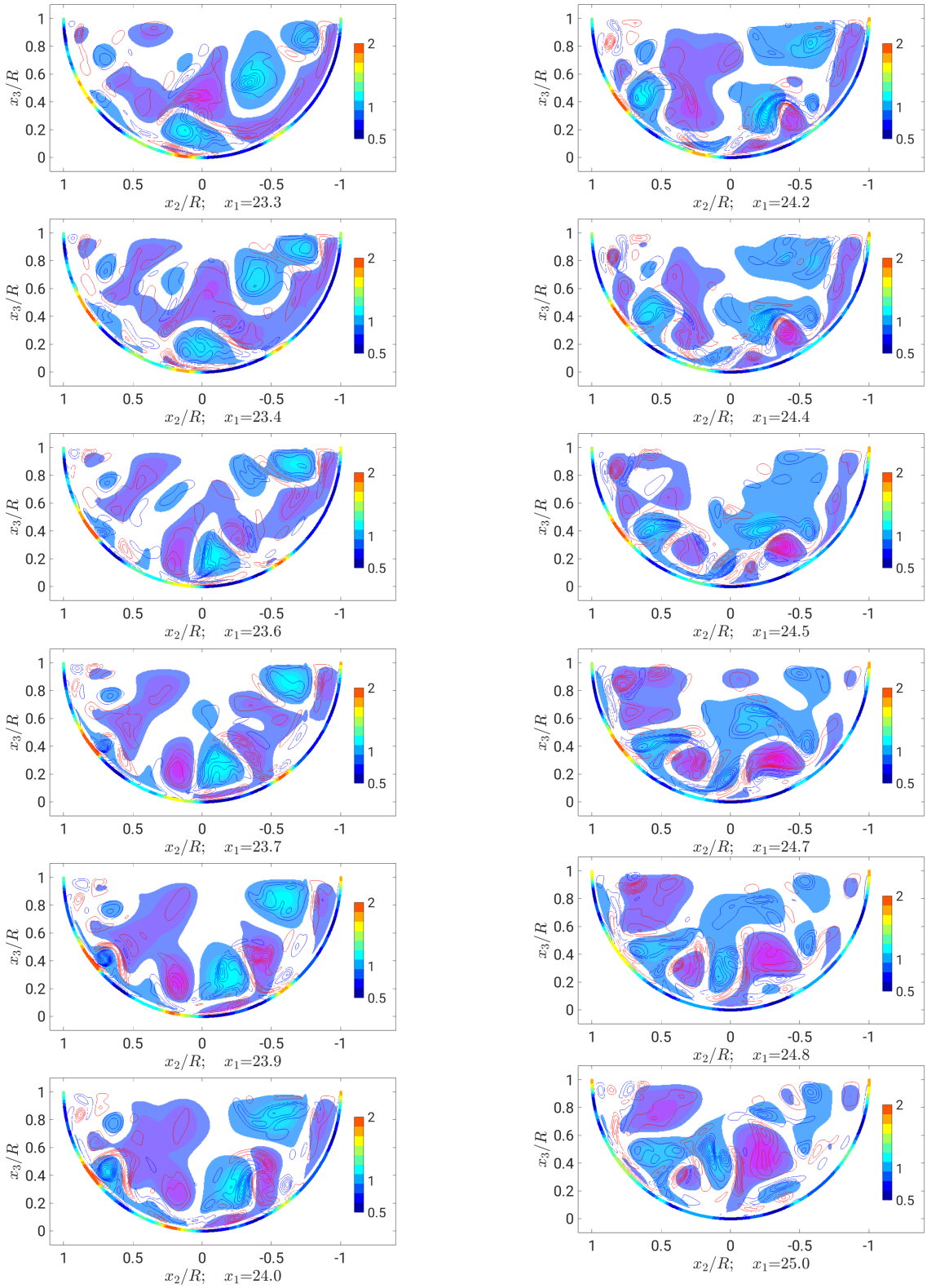

Figure 4.36: Spatial sequence of instantaneous cross-sectional slices of non-filtered $\omega_1 R/u_b$ (contour lines), Gaussian filtered $\tilde{\omega}_1 R/u_b$ (filled contours) and wall shear stress τ_w/τ_0 (colour along perimeter) of $Re_\tau = 180$ and 50% FR. The order is from top, left to bottom, right; also indicated by the streamwise coordinate x_1. The distance between each slice is approximately 29 wall units. Red and pink structures indicate clockwise and blue and cyan structures show counter-clockwise rotation. Outside, along the perimeter the non-filtered wall shear stress τ_w/τ_0 is plotted, with its colourmap next to the cross-section. The increments for the contourlines of $\omega_1 R/u_b$ are 0.3 and for the filled contour of $\tilde{\omega}_1 R/u_b$ 0.12.

vorticity in a horizontal plane parallel and 25 wall units below the free surface. From the top to the bottom σ^+ increases. In general, the vorticity distributions show their highest magnitudes mostly along the wall and hardly in the centre of the flow. With increasing filter width thin peak structures disappear, for example at $x_1/R \approx 4.5$ and $x_2/R \approx 0.9$, whereas larger structures with high intensities stay present. At the wall in negative x_2-direction many strong positive vorticity events occur directly at the wall and are often followed by a negative event. The same pattern is visible at the other mixed-corner in positive x_2-direction, however, the signs of the structures are reversed. Furthermore, it appears that for all different filter widths there are negative and positive $\tilde{\omega}_1'$- structures that reach from the mixed-corner into the centre with an angle from the wall of approximately 30°. With increasing filter width, it seems that the positive and negative structures form more pronounced pairs of counter-rotating vortices, which reach from the wall towards the centre producing an upwelling in between the vortices. In the centre of the free surface, the filtered vorticity fields also show counter-rotating vortices that create a downwelling, which is in line with the mean secondary flow. Moreover, as the filter width increases, some structures are merged forming bigger structures, nevertheless, the streamwise length of coherent structures does hardly exceed $2R$ for any filtering. Comparing the observed vortex pairs with the vortex sorting mechanism proposed by Sakai (2016), it appears difficult to apply the vortex sorting mechanism on the vortex pair. By applying Taylor's frozen turbulence hypothesis, one can argue that a temporal development of the flow can be approximated by advancing backwards in the spatial flow field. That would mean that both vortices would move towards the mixed-corner independent of their sense of rotation, which does not agree with the vortex sorting mechanism. Lastly, the instantaneous filtered fields of $\tilde{\omega}_1'$ shall be compared to filtered ω_1' obtained by the two POD's (cf. figure 4.29 and 4.30). Please keep in mind that the amount of TKE is approximately the same for the corresponding, filtered vorticity fields. Furthermore, it shall be recalled that both POD's reconstruct the vorticity in two-dimensional slices, whereas the GF acts equally in all three dimensions. The Gaussian filtered fields show a much stronger similarity to the 2C-POD, as it preserves the individual high intensities of the non-filtered field even better. Further comparing of the two approaches shows that the GF keeps the aspect ratio of the structures almost constant for different filter widths, whereas the structures generated by the 2C-POD are more round. Hence, these differences reflect the characteristics of the individual approaches.

Neither in single cross-sections (figure 4.36) nor in the horizontal plane (figure 4.37) the features of the mean secondary flow with the inner and outer secondary cell can be observed directly in the instantaneous flow. Structures that resemble the inner secondary cell appear, but they are inclined towards the flow centre and they do not span over a longer distance. A big eddy like the outer secondary cell can rarely be observed as instantaneous vortex. If such structures can be detected in single cross-sections then they soon vanish again, probably because of the interaction with other structures. Hence, the mean secondary flow does not seem to be stably present and only deviations from its mean occur, but the analysis rather suggests that the secondary flow is the result of averaging many individual events. This is consistent with the observations of the instantaneous wall shear stress distributions in section 3.2.2 and agrees with the results of the coherent structure analysis of Sakai (2016).

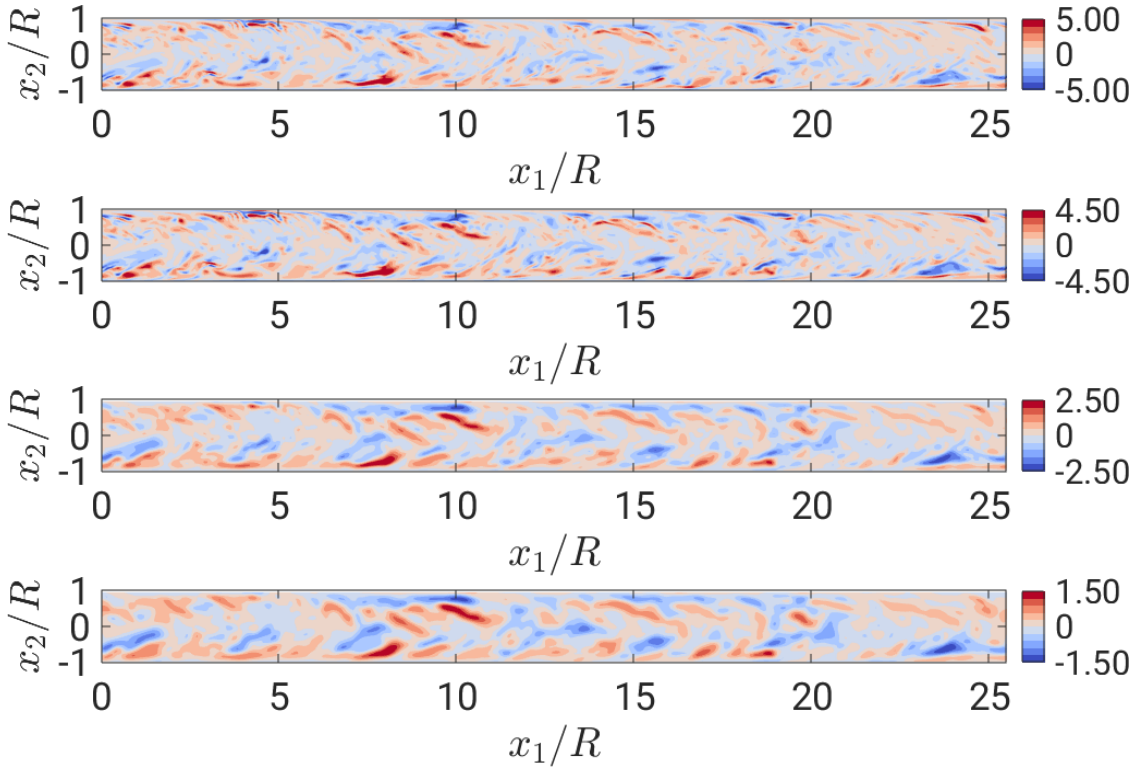

Figure 4.37: Gaussian filtered instantaneous, fluctuating streamwise vorticity $\tilde{\omega}_1' R/u_b$ 25 wall units below and parallel to the free surface of $Re_\tau = 180$ and 50% FR with a filter width scale of $\sigma^+ = 0, 5, 20, 30$ (top to bottom). Red contours show clockwise and blue contours show counter-clockwise rotation.

Conclusion

In conclusion, the GF, in contrast to the POD, is applied in all three dimensions on the complete three dimensional fields, hence, three dimensional dynamics are preserved. With enlarging the filter width, small scales are filtered and large scales become more visible, however, at the same time the kinetic energy in the filtered flow field decreases. Most of the intense small and large scale structures appear in the vicinity of the wall and the buffer layer, and occur less in the bulk region. Along the free surface a pattern of counter-rotating, streamwise vortex pairs can be detected that are inclined by approximately 30° from the wall and become more distinct with increasing filter width. Please note that the inclined vortex pairs are not consistent with the vortex sorting mechanism proposed by Sakai (2016). However, especially for larger filter widths, the overall arrangement of the vortices and their corresponding sense of rotation resemble the mean secondary flow. Most of the small and large scale structures that occur along the free surface have a streamwise length of less than $2R$ and, because of the inclined structures, an alternating pattern of positive and negative vorticity appears in streamwise direction. This indicates that the mean secondary flow is formed by averaging over a large number of different large and small scale structures, instead of a stable vortex pattern that only deviates from its mean representation.

Thus far, only the appearance of the secondary flow was investigated by the filtered flow fields. In the next section, the analysis of filtered flow fields shifts to the generation mechanism of secondary flow, especially the transfer of kinetic energy to the mean secondary flow.

4.2.3. Filtered Transfer of Kinetic Energy

In this section the approaches of the previous sections shall be combined. On the one hand, section 4.1.2 has shown, that the generation of mean secondary flow is governed by the production of secondary MKE via $P_{2,3}$. On the other hand, the flow was decomposed and filtered by means of POD and GF, see sections 4.2.1 and 4.2.2, which gave an idea about the various modes and structures that contribute to the complex instantaneous secondary flow. In combination, the above mentioned analyses provide a filtered $P_{2,3}$, which gives insights about the structures that are involved in the generation process, about which approach is more suited to extract the $P_{2,3}$-mechanism and about the relation between filtered $P_{2,3}$ and the corresponding vortical structures.

Theory of Filtered Transfer of Kinetic Energy

The idea of analysing filtered terms of the MKE- or TKE-budgets was introduced by Domaradzki *et al.* (1994), who investigated the influence of subgrid-scale processes on the energy transfer by filtering data of a DNS. They applied a spectral cut-off filter on their channel flow data to reconstruct a filtering similar to the one which occurs in a LES, because of the coarser grid compared to DNS. In addition to the subgrid-scale processes, they also investigated the energy transfer between MKE and TKE. They reported that the mean energy is mostly transferred to the large turbulent scales and the transfer takes place in the boundary layer. Bauer *et al.* (2019) extended their investigations to pipe flow for higher Reynolds numbers with a similar treatment of the data. They analyse the inter- and intrascale energy transfer with respect to the dominating streamwise component of the filtered TKE-budget with a focus on the VLSMs and how they obtain energy. The derivation of the filtered TKE-budget by Bauer *et al.* (2019) shows that, in addition to the known production term, two more terms occur that describe the subfilter-scale diffusion and the interscale flux of TKE. However, as the present study focuses on the transfer of energy between TKE and MKE only the known production term is investigated.
In the present analysis the MKE-production $\overline{u_i' u_j'}\,\partial/\partial x_j(\overline{u}_i)$ is split up into different parts. First of all, the instantaneous flow fields are split into their mean and fluctuating parts. Then one of the above introduced filters, either one of the POD's or the GF, is applied on the fluctuating flow fields. From the filtered, fluctuating flow fields $\overline{\tilde{u}_i'\tilde{u}_j'}$ can be generated, and in combination with the gradient of the mean flow the MKE-production $\overline{\tilde{u}_i'\tilde{u}_j'}\,\partial/\partial x_j(\overline{u}_i)$ is obtained. Note that filtered quantities are denoted by $\tilde{\varphi}$ and $\overline{\varphi}$ still denotes temporal averaged variables, as introduced in section 1.2. From the POD's only certain modes are selected to obtain the filtered MKE-production $\tilde{P}_{ij}$

$$\overline{\tilde{u}_i'\tilde{u}_j'}\frac{\partial \overline{u}_i}{\partial x_j} = \sum_k \overline{a_i^k(t)a_j^k(t)}\ \Phi_i^k(\mathbf{x})\Phi_j^k(\mathbf{x})\ \frac{\partial}{\partial x_j}a_i^0(t)\Phi_i^0(\mathbf{x}), \tag{4.16}$$

with a_i^k as temporal coefficients and Φ_i^k as spatial modes with the zeroth mode (k=0) as mean flow. Hence, the MKE-production term is split up into high energy and low energy containing parts. For the GF different filter widths are used to generate various filtered, fluctuating $\overline{\tilde{u}_i{}'\tilde{u}_j{}'}$, hence, in combination with the gradient of the mean flow, the filtered MKE-production $\tilde{P}_{ij}$ reads $\overline{\tilde{u}_i'\tilde{u}_j'}\,\partial/\partial x_j(\overline{u}_i)$. This filter separates the contribution of the large and the small scales. The filtered statistics for all three approaches are generated from approximately 180 snapshots. In the following subsection the filtered MKE-production is analysed with respect to the applied filter and its filtering feature. Please keep in mind that within section 4.2 the secondary MKE-production $P_{2,3}$ is defined positive, if energy is transferred from TKE to MKE. The reverse energy transfer is defined as negative.

Results of Filtered Transfer of Kinetic Energy

To begin with, the MKE-production terms of the primary component $\tilde{P}_1$ are shown in figure 4.38. Please keep in mind that for $Re_\tau = 180$ and 50% FR the filter widths of the GF correspond to a filtered ratio of TKE as follows: $\sigma^+ = 0$ to 100%, $\sigma^+ = 5$ to 90%, $\sigma^+ = 20$ to 50% and $\sigma^+ = 30$ to 30%. The distribution shows the filtered $\tilde{P}_1$ five cells below and parallel to the free surface. The different distributions of the 3C-POD resemble the non-filtered distribution quite well with a lower magnitude, especially for the near-wall peak. In contrast, for 2C-POD the 50% high energy containing modes do hardly contribute to the near-wall peak. However, in the bulk region, most of the MKE-production term is provided even by the 30% high energy containing modes. The GF seems to filter P_1 similarly as the 3C-POD. In comparison to 30% of the 3C-POD, the filter width $\sigma^+ = 30$ contains an equally high near-wall peak, whereas in the bulk region $\sigma^+ = 30$ consists of slightly higher $\tilde{P}_1$-values. Hence, near the wall P_1 rather consists of small scales and in the bulk region more of large scales.

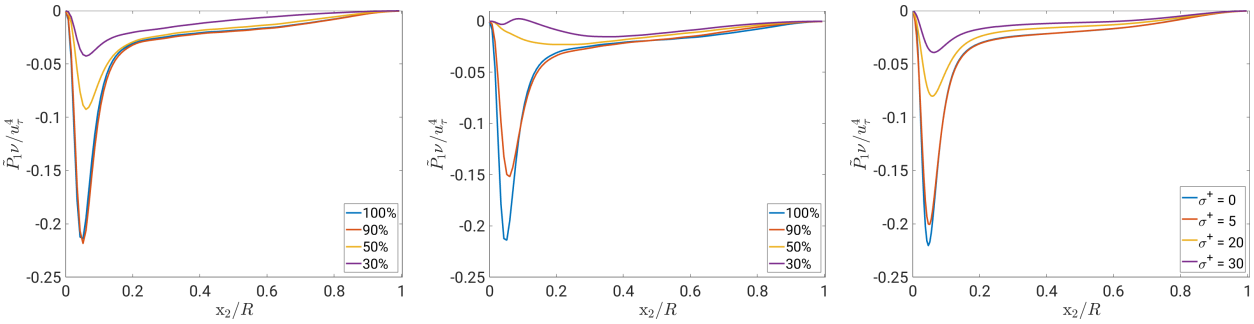

Figure 4.38: MKE-production term $\tilde{P}_1$ five cells below and parallel to the free surface in outer scaling reconstructed from 3C- (left) and 2C-POD (middle) from the first modes including various amount of the fluctuating energy and Gaussian filtered for different filter widths (right) for $Re_\tau = 180$ and 50% FR.

In the following paragraph, the key term, the filtered secondary MKE-production term $\tilde{P}_{2,3}$, is analysed. In figure 4.39, its two-dimensional distribution over the cross-section is shown, which gives a good impression of the various MKE-production peaks for the different filters. Please note that the colour map changes from top to the bottom according to the amount of TKE contained by the filtered velocity field. The POD filtered $\tilde{P}_{2,3}$ show similar

filtering effects like the instantaneous velocities reconstructed by the same POD modes (cf. figures 4.27 and 4.28). In detail, the 3C-POD shows that when only the first fluctuating modes containing 30% of the energy are used as filter, the structures of $P_{2,3}$ along the wall are predominantly conserved. Hence, the filtered MKE-production peaks at the wall and in the mixed-corner preserve higher magnitudes than the negative MKE-production in the centre of the free surface. In contrast, the 2C-POD filtering mainly conserves the features of $P_{2,3}$ at the free surface and slightly damps the peaks along the wall. However, the qualitative distribution of the peaks does hardly change, thus, the 2C-POD maps its share of the energy quite well in $\tilde{P}_{2,3}$. The magnitude of the Gaussian filtered secondary MKE-production (right column) only decreases at the wall for larger filter widths, whereas the peaks at the free surface are conserved and a little widened in the spatial sense. Hence, GF indicates that both the small and the large scales similarly contribute to the total $P_{2,3}$.

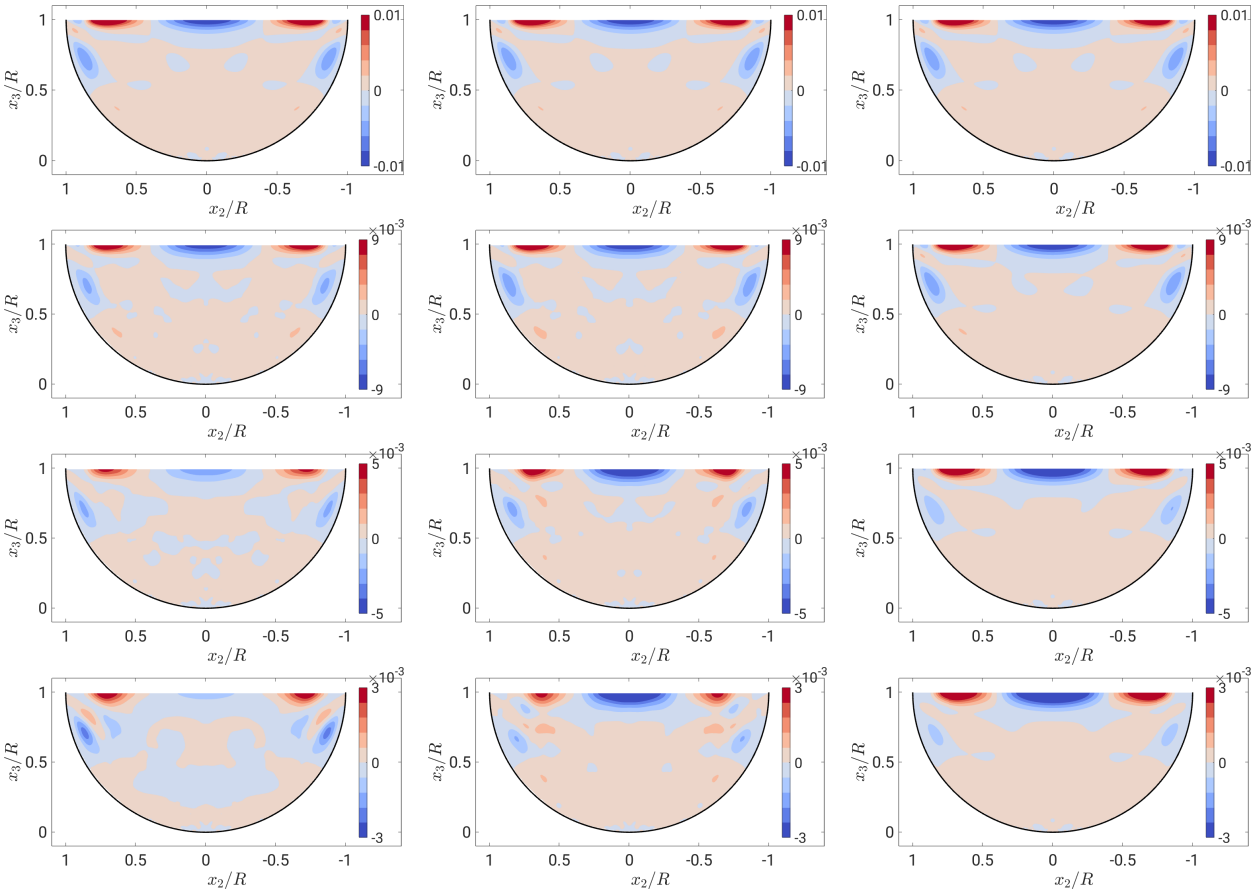

Figure 4.39: Secondary MKE-production $\tilde{P}_{2,3}$ of 3C- (left) and 2C-POD (mid), reconstructed from the first modes including 100% (first), 90% (second), 50% (third) and 30% (fourth row) of the fluctuating energy. Right: Gaussian filtered $\tilde{P}_{2,3}$ with filter widths $\sigma^+ = 0$ (first), $\sigma^+ = 5$ (second), $\sigma^+ = 20$ (third) and $\sigma^+ = 30$ (fourth row). All plots for $Re_\tau = 180$ and 50% FR.

A more quantitative comparison is possible with the line plots along the free surface, where the strongest secondary MKE-production takes place. In figure 4.40, the distributions show

that 3C-POD reconstructs a smaller share in the bulk region than the 2C-POD. The 2C-POD reconstructs a similar magnitude even in the vicinity of the wall, but the positive peak is slightly shifted away from the wall. The reproduction with 50% of the fluctuating energy by 2C-POD reconstructs a larger share throughout the distribution than the 50% distribution of 3C-POD. Moreover, the cross-sectional view shows that it also accounts similarly for the peak at the wall, which is less pronounced for 2C- than 3C-POD comparing the 30%-energy cases. It indicates that the 2C-POD is better in capturing the process of secondary MKE-production compared to 3C-POD. In contrast to the two POD approaches, the GF applies similarly well and evenly to both high peaks. Moreover, the magnitudes of the filtered peaks are equally high as the magnitudes from 2C-POD.

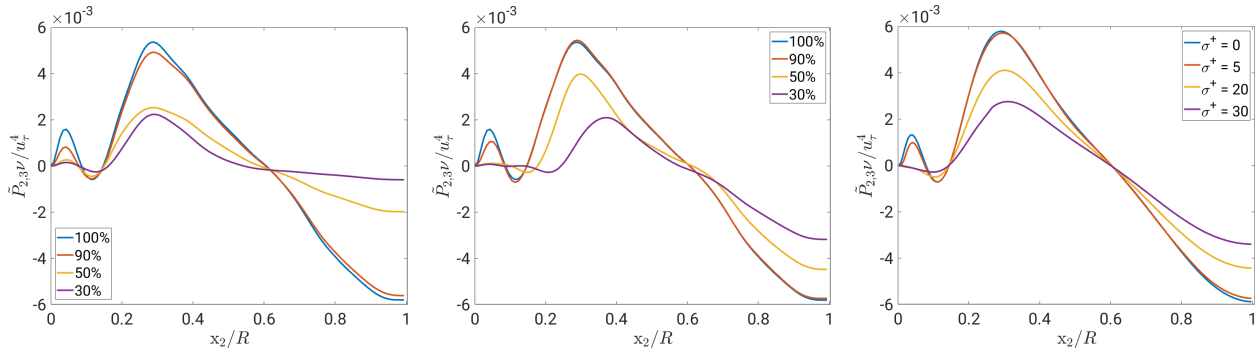

Figure 4.40: MKE-production term $\tilde{P}_{2,3}\ \nu/u_\tau^4$ five cells below and parallel to the free surface reconstructed from 3C-POD (left) and 2C-POD (middle) from the first modes including various amount of the fluctuating energy and Gaussian filtered for different filter widths (right) for $Re_\tau = 180$ and 50% FR.

In order to compare the overall MKE-production of the different Reynolds numbers and filling ratios, the positive and negative part of $\tilde{P}_{2,3}$ were separately integrated over the cross-section for the various filtering options for POD (see figure 4.41) and GF (see figure 4.42). Please note that the positive part is normalised by the non-filtered, positive part and likewise vice versa for the negative part. The amount of reconstructed $\tilde{P}_{2,3}$ can be compared to the energy included to reproduce the flow fields (30%, 50%, 90% and 99% for the POD's). The secondary MKE-production from 3C-POD contains a smaller share than the energy content introduced for the filtering, especially for the positive $\tilde{P}_{2,3}$ of 30% ($\approx 10-30\%\tilde{P}_{2,3}$) and 50% energy content ($\approx 20-55\%\tilde{P}_{2,3}$). For the 2C-POD a larger share than the energy input remains in the filtered secondary MKE-production. For an energy input of 30% approximately $30-50\%\tilde{P}_{2,3}$ is reconstructed. In most cases a larger share is reconstructed by the negative $\tilde{P}_{2,3}$ than by the positive. However, this does not mean that the absolute negative MKE-production is higher, because, as mentioned above, the normalisation is different and decouples the two variables. A Reynolds number dependency can be found for both POD-filtered cases, as for higher Reynolds numbers the share of reproduced secondary MKE-production is increased for the positive and negative part. An exceptionally high secondary MKE-production is reconstructed for 75% filled $Re_\tau = 180$ case, where more than 60% of the negative $\tilde{P}_{2,3}$ is already captured by the modes carrying only 30% of the fluctuating energy. This higher MKE-production rate is also visible for 50% of the energy.

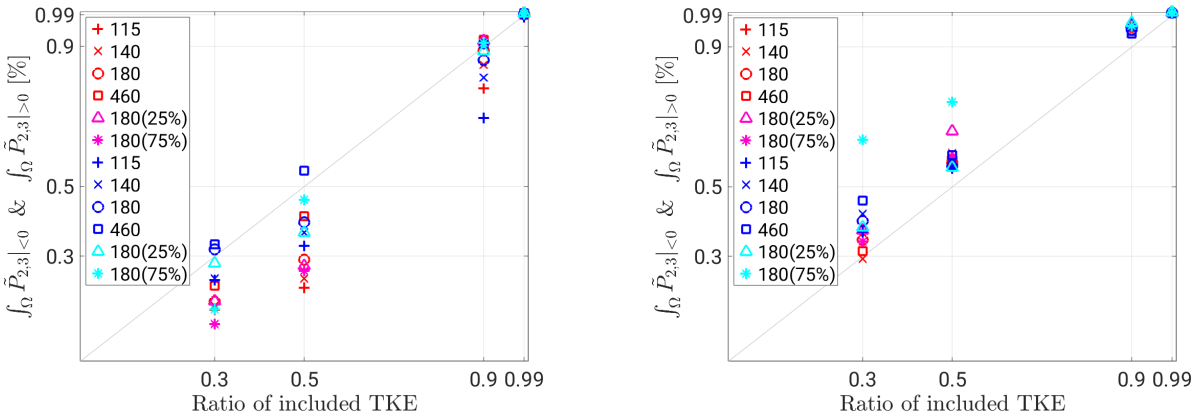

Figure 4.41: Negative and positive separately integrated secondary MKE-production $\int_\Omega \tilde{P}_{2,3} \lessgtr 0$ filtered according to their included energy to reconstruct velocities for 3C- (left) and 2C-POD (right) for various Re_τ and filling ratios. Blue: $\tilde{P}_{2,3} < 0$; red: $\tilde{P}_{2,3} > 0$. Normalised by the individual, non-filtered $\int_\Omega P_{2,3} \lessgtr 0$.

The Gaussian filtered overall MKE-production is shown in figure 4.42. Generally, most of the data points lie slightly above the diagonal, hence, in relation, the filtered flow fields contain a slightly higher amount of secondary MKE-production than corresponding TKE. In contrast to the PODs, no clear distinction can be found between positive and negative $\tilde{P}_{2,3}$. Only for 75% FR the negative value is much higher than the positive. Moreover, the same Re-dependency applies as for the PODs – with increasing Reynolds number the share of integrated MKE-production slightly increases.

In summary, the spatial distributions of $\tilde{P}_{2,3}$ and the integral analysis indicate that the small scales and the modes containing a small amount of energy, have a non-negligible contribution to the energy transfer, which is also concluded by Sakai (2016).

In order to assess the influence of single POD modes and the different Gaussian filter widths in detail, figure 4.43 gives insights about the cross-sectional averaged, complete $\tilde{P}_{2,3}$-term and its individual cross-sectional averaged terms $\tilde{P}_{22}, \tilde{P}_{33}, \tilde{P}_{23}$ and $\tilde{P}_{32}$. 3C- and 2C-POD show differences in the distribution of the single modes. As expected from the recreation of the secondary TKE (cf. figure 4.22) the high energy modes of the 2C-POD also better concentrate strong secondary MKE-production and for modes with $k > 40$ there are less deviations from zero than for the 3C-POD modes. For the GF, the cross-sectional averaged, complete $\tilde{P}_{2,3}$ shows an almost linear decrease and even negative net MKE-production occur for larger filter widths. From the spatial distributions (cf. figure 4.39) it is known, that the negative MKE-production in the centre of the free surface remains the most intense peak for stronger filtering, which results in the negative $\tilde{P}_{2,3}$. Please note an important difference between the representations is that the single values of the POD-modes can be summed up and give the total magnitude without filtering, whereas for the GF the non-filtered value is described only by $\sigma^+ = 0$. The complete secondary MKE-production can be split up into its individual terms $\tilde{P}_{22}, \tilde{P}_{33}, \tilde{P}_{23}$ and $\tilde{P}_{32}$. For all filtered and also the non-filtered field $\tilde{P}_{22}$ is the most important term, acting in the non-filtered flow mostly at the free surface. Only for the 2C-POD the negative branch is not dominated by $\tilde{P}_{22}$. The POD-filter shows that the most energy containing modes also dominate the individual MKE-production terms

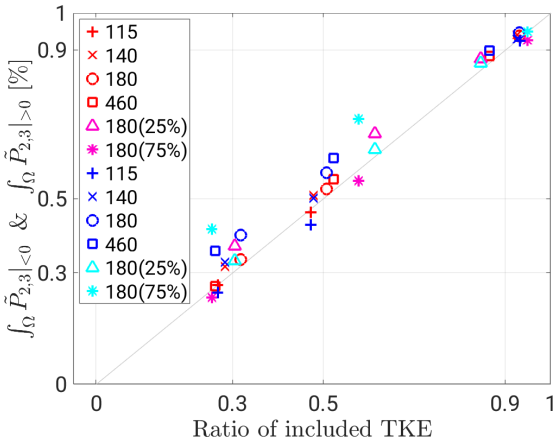

Figure 4.42: Negative and positive separately integrated secondary MKE-production $\tilde{P}_{2,3} \lessgtr 0$ filtered according to the ratio of included TKE (cf. figure 4.33; for $Re_\tau = 180$ $\sigma^+ = 5$ corresponds to 90%, $\sigma^+ = 20$ to 50% and $\sigma^+ = 30$ to 30% of TKE.) for various Re_τ and filling ratios. Blue: $\tilde{P}_{2,3} < 0$; red: $\tilde{P}_{2,3} > 0$. Normalised by the individual, non-filtered $\int_\Omega P_{2,3} \lessgtr 0$.

with a similar level of consistency as for the total $\tilde{P}_{2,3}$. The distributions of the single terms obtained by GF indicate that the terms $\tilde{P}_{22}$ and $\tilde{P}_{33}$ dominate and the shear terms are less important. Overall, the results indicate that the mean secondary MKE-production is a multi-scale process, that it is not only governed by the small or the large scales, but by all of them. Similarly, one can state that that both high and low energy modes contribute to $P_{3,2}$.

Thus far, only mean quantities were investigated for the filtered transfer of kinetic energy. In the following paragraph the instantaneous filtered secondary MKE-production $u_i' u_j' \, \partial \overline{u}_i / \partial x_j$ is studied in instantaneous snapshots in order to see, whether similar observations can be made or whether the instantaneous flow behaves differently. The visualisations of the instantaneous secondary MKE-production in figure 4.44 show the free surface plane for the same snapshot as the other instantaneous figures in the sections and chapters above. The free surface plane is the most interesting horizontal plane, because of the filtering definition $\tilde{u}_i' \tilde{u}_j' \partial \overline{u}_i / \partial x_j$. The definition determines that strong events are always located in areas, where the mean secondary flow has strong gradients, hence, in the upper third of the cross-section and especially at the free surface. The limits of the colour-map of the non-filtered case are chosen such that its strong peaks are highlighted. This colourmap is defined as 100% and for the filtered fields the limits of the colourmap are reduced to 30% as the filtered fields correspond to 30% of the fluctuating energy. Please keep in mind that in contrast to the POD filtering, which is a two dimensional filter applied on every cross-sectional slice, the GF applies on all three dimensions. Independent of the filter method, positive and negative $\tilde{P}_{2,3}$ are clearly restricted to the same areas as the average MKE-production term. Looking at the distribution of positive and negative peaks of the non-filtered and filtered fields, it does not seem that they appear in pairs or differently connected, but mostly independent from each other. For 3C-POD, some of the filtered peaks do not match to the non-filtered peaks, i.e. at $x_1/R \approx 25$ and $x_2/R \approx 0.75$. Apparently, in that case the high energy modes are more responsible for a larger share of the MKE-production event than for other peaks. In

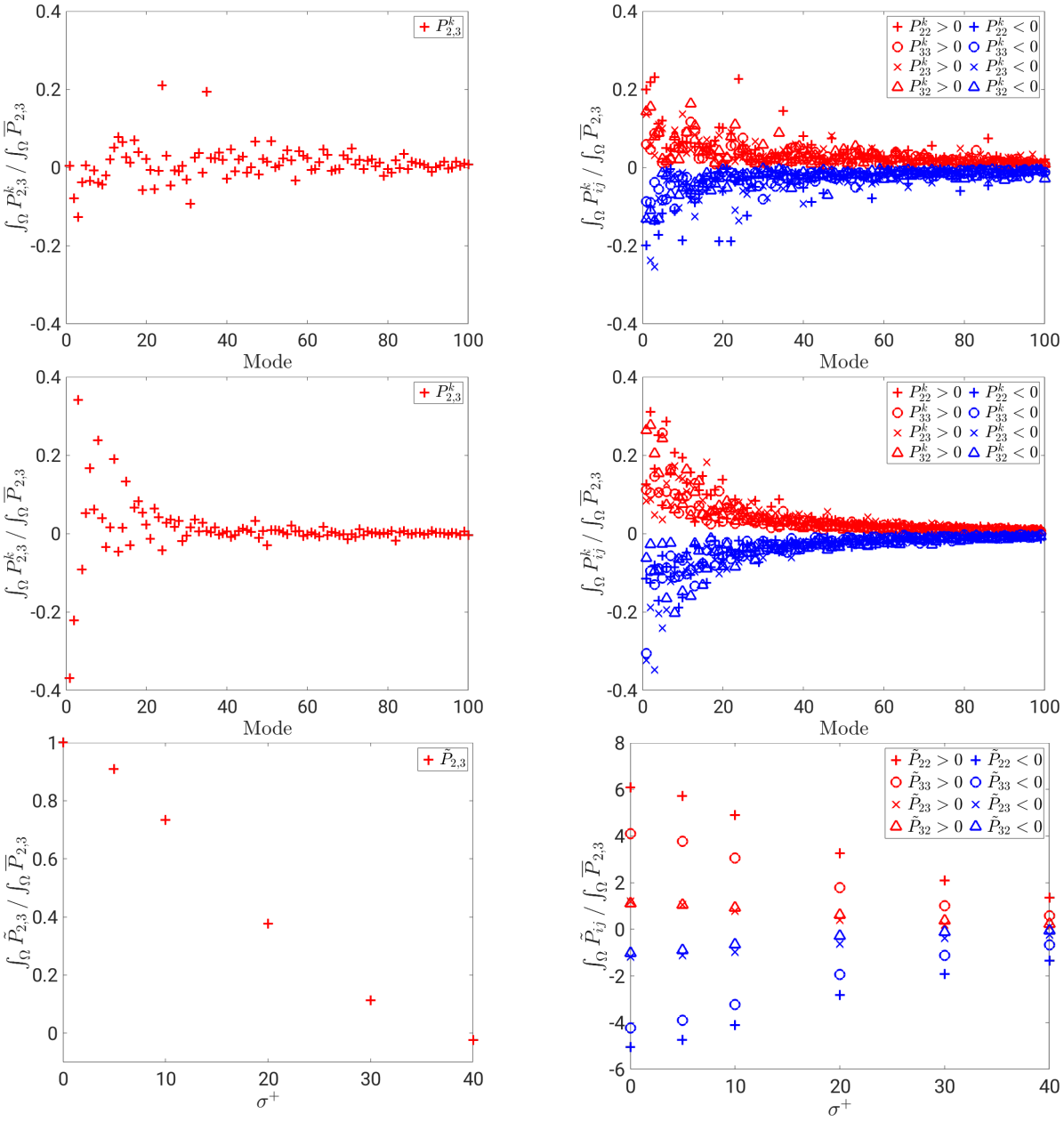

Figure 4.43: Modewise, cross-section averaged secondary MKE-production $P^k_{2,3}$ (left) and positive and negative separately integrated, individual components $P^k_{22}, P^k_{33}, P^k_{23}, P^k_{32}$ (right) of 3C- (top) and 2C-POD (middle). Bottom row: Gaussian filtered, cross-section averaged secondary MKE-production $\tilde{P}_{2,3}$ (left) and positive and negative separately integrated $\tilde{P}_{22}, \tilde{P}_{33}, \tilde{P}_{23}, \tilde{P}_{32}$ (right). All values are normalised by the cross-sectional integrated $\int_\Omega P_{2,3}$ and all plots are for $Re_\tau = 180$ and 50% FR.

contrast, the filtered $\tilde{P}_{2,3}$-peaks of the 2C-POD, and even more of the GF, are more relatable to the non-filtered peaks. Moreover, only positive peaks are noticeable for 3C-POD, whereas for 2C-POD and GF a larger amount of positive and negative peaks is visible. This is also in line with the results of the temporal averaged and filtered secondary MKE-production (cf.

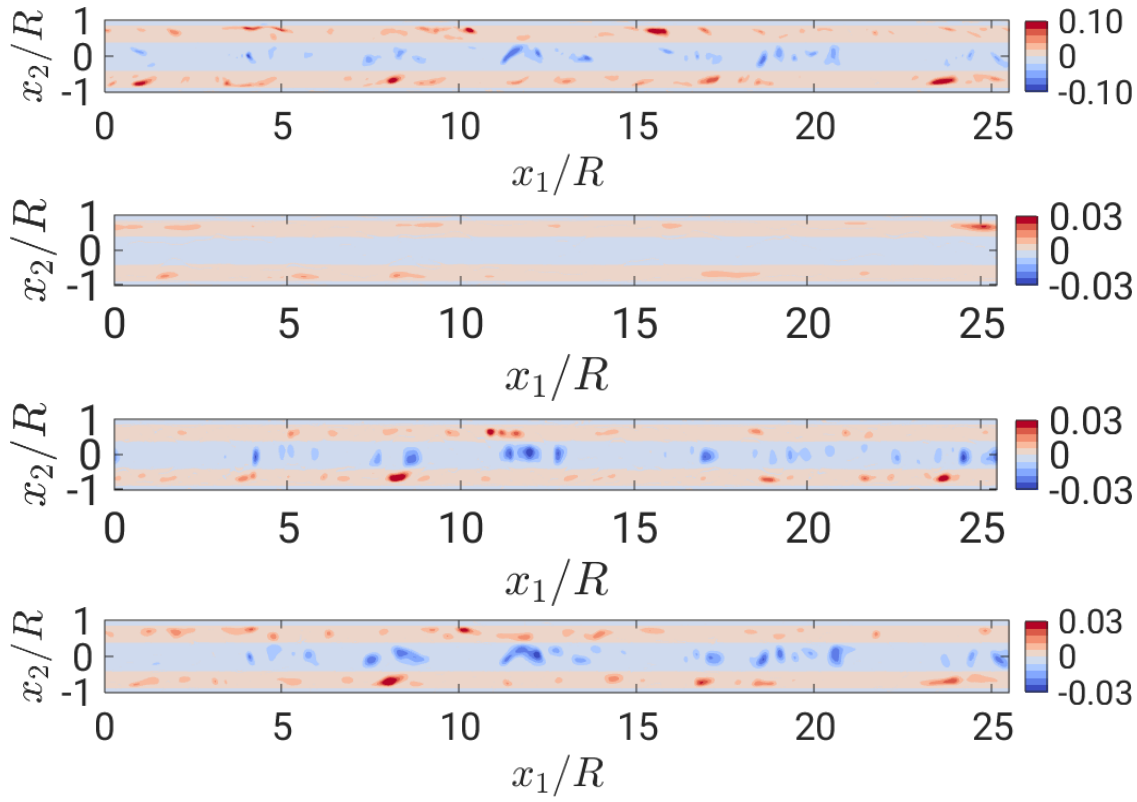

Figure 4.44: Instantaneous secondary MKE-production $\tilde{P}_{2,3}\,\nu/u_\tau^4$ along the free surface for $Re_\tau = 180$ and 50% FR. Top row: non-filtered $P_{2,3}$; second and third row: $\tilde{P}_{2,3}$ reconstructed by the first modes including 30% of the fluctuating energy from 3C-POD and 2C-POD, respectively; bottom row: Gaussian filtered $\tilde{P}_{2,3}$ with $\sigma^+ = 30$.

figure 4.39).
Lastly, the filtered $P_{2,3}$ in figure 4.44 is compared to the filtered vorticity in figures 4.29, 4.30 and 4.37. The $P_{2,3}$-peaks of 2C-POD have a rather round shape, whereas the peaks of 3C-POD and GF are more elongated being similar to the shape of the vorticity peaks of the corresponding approaches. In addition to the comparison of the shape of structures, the filtered vorticity fields and the filtered secondary MKE-production show the relation between vortical structures and $P_{2,3}$-peaks. For this investigation the focus is on the 2C-POD and the GF, because the 3C-POD hardly contains $\tilde{P}_{2,3}$-peaks along the free surface. On the one hand, the positive $\tilde{P}_{2,3}$-peaks that occur close to mixed-corner are mostly accompanied by either one or two counter-rotating vortical structures for both approaches. On the other hand, no connection can be noticed between the negative $\tilde{P}_{2,3}$-peaks in the centre and high intensities of $\tilde{\omega}_1$.

Conclusion

In conclusion, the transfer of kinetic energy between TKE and MKE is a multi-scale and multi-mode process. The 3C-POD is less suited to extract the transfer mechanism than the 2C-POD and the GF. 2C-POD and GF are able to define high energy modes and large scale

structures, respectively, which contain a slightly larger share of $P_{2,3}$ than corresponding TKE. Looking at the individual terms of the secondary MKE-production, P_{22} and P_{33} have a larger contribution compared to the shear terms. However, all applied filterings show that the low energy modes and the small scales have a non-negligible impact on the transfer mechanism, which is in agreement with the results of Sakai (2016). The instantaneous filtered and non-filtered $P_{2,3}$ indicate that strong secondary MKE-production events are often surrounded by strong vortical structures. However, a clear picture of the MKE-production between $P_{2,3}$ and ω_1 could not be detected. Therefore, a conditional averaging of strong $P_{2,3}$ events is investigated in the next section.

4.2.4. Conditional Averaging of High Secondary MKE-Production Peaks

In section 4.1.2 the path of kinetic energy towards secondary flow was reconstructed and the term of secondary MKE-production $P_{2,3}$ was found to be the link between turbulent flow and secondary flow. The modes and the scales involved in the process of secondary MKE-production were investigated in the previous sections of this chapter. In this section the tool of conditional averaging is introduced. Conditional averaging was used, for example, by Nagaosa & Handler (2003), who analysed near-wall structures and their vertical evolution. In combination with many other references, cited also in section 1.2 (*Free Surface Flows*), they conclude for open-channel flows without side walls that the structures generated near the wall move towards the free surface during strong ejection events. In this study, positive and strong $P_{2,3}$-events serve as the condition to average. The investigation of conditionally averaged flow fields shall help to get a more distinct image of positive and strong $P_{2,3}$-events, of what they have in common and what kind of structures are involved.
Please keep in mind that within this section 4.2 the secondary MKE-production term $P_{2,3}$ is defined positive, if energy is transferred from TKE to MKE. The reverse energy transfer is defined as negative.

Procedure of Conditional Averaging

In this thesis, the following procedure was applied to extract the mechanism of kinetic energy transfer between secondary MKE and TKE is as follows: In a first step, the highest positive and the lowest negative values of $P_{2,3}$ within an instantaneous cross-sectional slice are gathered and categorized as positive and negative peak ($\mathrm{ext}(P_{2,3})| > 0, < 0$). From each cross-sectional slice of over 180 snapshots the magnitude and position are collected for each peak. From the set of positive and negative peaks, the 5% of the most extreme events are selected for each case. Figure 4.45 shows the spatial distribution of the positive (red) and negative (blue) $P_{2,3}$-peaks of the 95%-quantile.
It becomes clear that many of the negative peaks occur at the side wall and most of the positive peaks at the free surface, where the mean secondary MKE-production also has its peaks (cf. figure 4.10). As the focus of this study lies on the mean secondary flow, the positive $P_{2,3}$-events that transfer energy from TKE to MKE are the most interesting events. They mostly occur along the free surface, hence, all the events which are located in the vicinity of the free surface are collected. The horizontal line delimits the peaks that appear

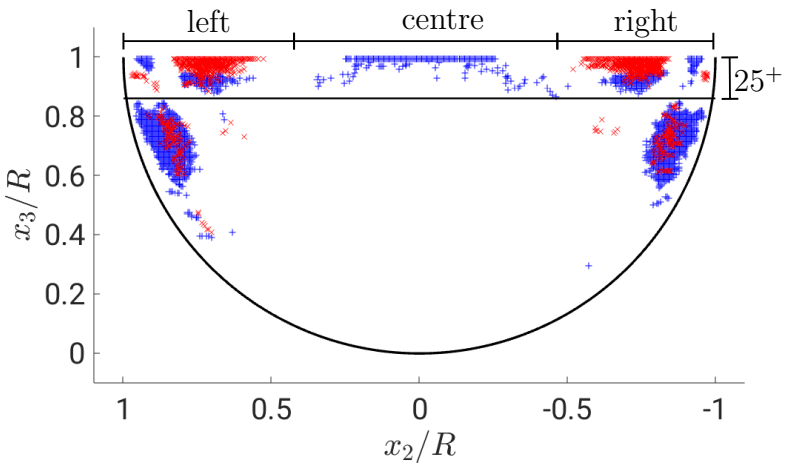

Figure 4.45: Locations of positive (×) and negative instantaneous $P_{2,3}$-peaks (+) of the 95%-quantile for $Re_\tau = 180$ and 50% FR. The black horizontal line represents the distance of 25 wall units from the free surface. At the top the horizontal categories are shown.

in the vicinity of the free surface from the peaks below. The distance of the horizontal line from the free surface is 25 wall units and defines the free surface layer, from which the peaks are collected. In a last step the collected positive and negative peaks are each categorized according to the location where they occur: in the mixed-corner in positive and negative x_2-direction or in the centre. Hence, snapshots were scanned for the following six events: minima and maxima in the free surface layer occuring in the left, centre or right section.

Quantitative Results of Conditional Averaging

Before analysing the conditionally averaged flow fields, the following paragraphs quantify how many events the procedure includes and excludes, its Reynolds- and filling-dependency and the correlation of extreme $P_{2,3}$-events to the secondary MKE-production integrated over the cross-section.

First, the PDF of instantaneous $P_{2,3}$-values over all cells is shown in figure 4.46 (left) in semi-logarithmic axes. Cell-values of 80 snapshots of the semi filled pipe flow at $Re_\tau = 180$ were used for this evaluation. The standard deviation is $\sigma = 0.0055$, which is approximately equal to the 5%- and 95%-quantiles. The distribution is right-skewed with a skewness of $S = 1.76$ and its kurtosis is $F = 134$, hence, it contains more outliers than the standard normal distribution. Around 45% of the cell values of $P_{2,3}$ are close to zero, being smaller than the standard deviation by a factor of ≈ 10. On the one hand, this reflects the fact that only very little secondary MKE-production takes place in most of the cross-section, as the gradient of mean secondary flow is strongest at the free surface and at the wall, where inner and outer secondary cell flow either towards or away from each other. On the other hand, the PDF could further indicate that $P_{2,3}$ occurs as very rare but intense events.

Let us focus on the extreme events that are part of the 95%-quantile and only occur in the free surface layer. In total 12129 extreme events were found in the free surface layer

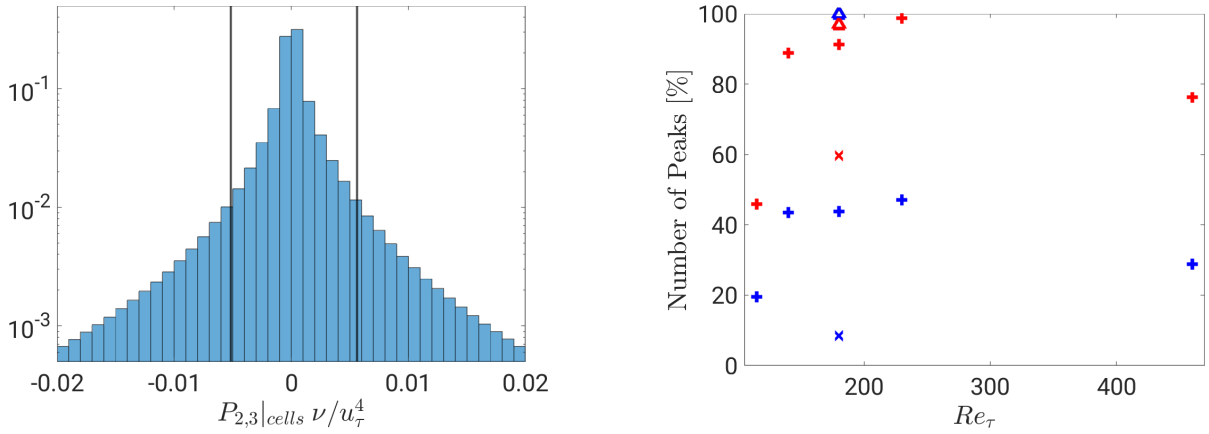

Figure 4.46: Left: PDF of all normalised instantaneous $P_{2,3}$-cell values of 80 snapshots ($Re_\tau = 180$ and 50% FR). Vertical lines: 5%- and 95%-quantile. Maximum value: 0.4441; minimum value: -0.5838. Right: Share of negative (blue) and positive (red) instantaneous $P_{2,3}$-peaks of the 95%-quantile found in the free surface layer in comparison to number of peaks of the 95%-quantile in whole cross section. + represents 50%, × 25% and △ 75% FR.

for semi filled pipe flow at $Re_\tau = 180$, which split into 7083 positive events, 2816 negative events, and 1115 events with a negative and positive peak occurring simultaneously in the free surface layer. Figure 4.46 (right) shows the ratio for positive and negative peaks from the 95%-quantile that occur in the free surface in comparison to the extreme peaks occurring in the complete cross-section. Hence, it basically shows the ratio of the number of peaks above the horizontal line to all peaks, shown in figure 4.45. This ratio was computed for five different Reynolds numbers and the different FRs. More than 80% of the positive peaks appear for intermediate Reynolds numbers in the free surface layer and approximately 40% of the negative peaks. Far less peaks occur in the free surface layer for $Re_\tau = 115$, because the distribution of $P_{2,3}$-peaks is more equally distributed over the cross-section. For $Re_\tau = 460$ almost 80% of the positive peaks take place in the free surface layer and approximately 25% of the negative peaks. Outstanding are the number of peaks for 25% and 75% filled: Only 10% of the negative and only 60% of the positive extreme events occur in the free surface layer for the small filling ratio. Whereas almost all positive and negative extreme events occur in the free surface layer for 75% filling. This is in accordance to the distribution of the mean secondary MKE-production (cf. figure 4.10). As mentioned above, please keep in mind that many negative events are excluded, because the area of negative MKE-production at the wall below the inner secondary cell is not taken into account in the free surface layer.

In figure 4.47 (left) the distribution of extreme events are shown according to their spatial categorization and in dependence of Reynolds number for semi filled pipe flows. Most of the extreme events ($70 - 80\,\%$) are maxima, hence, secondary MKE-production of mean secondary flow, in the mixed-corner, whereas minima in the mixed-corner and in the centre occur only in $8 - 20\,\%$ of the events. Maxima in the centre are negligible. The extreme events occurring in the left and right mixed-corner are evenly distributed. Overall, the separation of extreme events resembles the mean $P_{2,3}$ distribution, keeping in mind that a

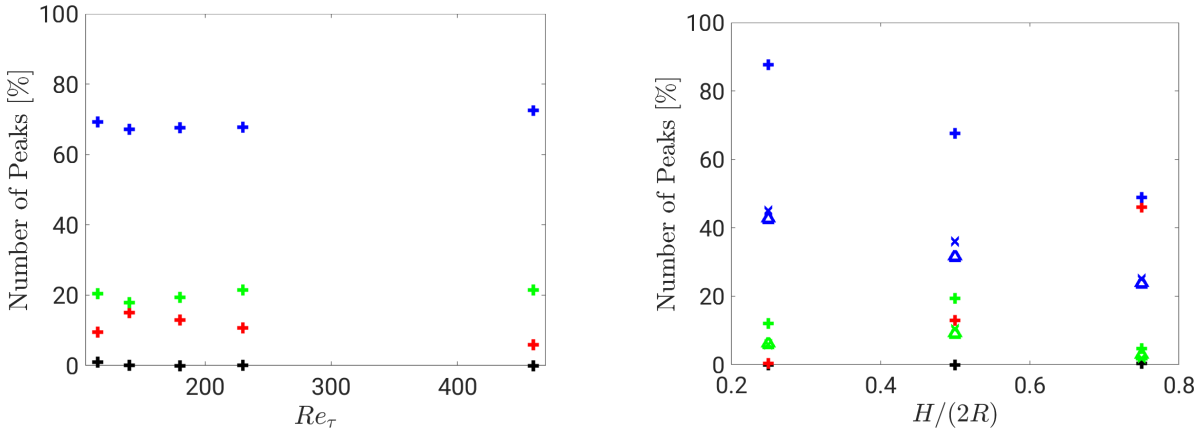

Figure 4.47: Number of peaks of $P_{2,3}$ from the 95%-quantile occurring in the free surface layer according to their categorization for $Re_\tau = 115, 140, 180, 230, 460$ for 50% FR (left) and for $Re_\tau = 180$ for 25%, 50% and 75% FR (right). + shows the share of maxima in the mixed-corner, + maxima in the centre, + the share of minima in the mixed-corner and + minima in the centre. For different filling ratios following additional symbols are introduced: × shows the share of maxima in the left mixed-corner, △ shows the share of maxima in the right mixed-corner, × the share of minima in the left mixed-corner and △ the share of minima in the right mixed-corner.

certain amount of negative events miss in this representation. For different filling rates figure 4.47 (right) provides information. With increasing filling ratio the number of minima in the centre increases, until, for 75% filling ratio, the number of minima in the centre is about 50% and equal the sum of maxima in the left and right corner. Thus, minima in the centre are more important for this filling rate. The other trend is that maxima in the mixed-corner become less with increasing filling ratio. Minima in the mixed-corner and maxima in the centre are almost negligible. Considering the results from figure 4.47 (right) that only one third of the extreme events occur in the free surface layer, it indicates that the process to generate secondary flow differs from the higher filling rates.

In order to get an impression what kind of impact a instantaneous $P_{2,3}$-peak and especially its extreme events have on the complete MKE-production over the cross-section, the relation between positive or negative $P_{2,3}$-peaks in the free surface layer ($ext(P_{2,3})|_{\leqslant 0,25^+}$) and the net MKE-production of a cross-section ($\int_\Omega P_{2,3}$) is shown in figure 4.48. The lines show the 5%-(negative) and 95%-quantile (positive) of the net MKE-production and the 95%-quantile of the negative (left plot) and positive (right plot) extreme events. Please note that both $\int_\Omega P_{2,3}$ and $ext(P_{2,3})|_{\leqslant 0,25^+}$ are normalized by the corresponding positive or negative peak of the mean secondary production $\overline{P}_{2,3}$. Negative $P_{2,3}$-peaks are multiplied with -1 to bring them to the positive scale to simplify comparisons. The negative extreme events hardly have any impact on the net MKE-production. Whereas, the positive extreme events have a more distinct correlation, which can be seen by the fact that the values above the horizontal line are mostly on the right, hence, they are linked to positive net MKE-production and only a comparably small number of extreme events are connected to negative net MKE-production.

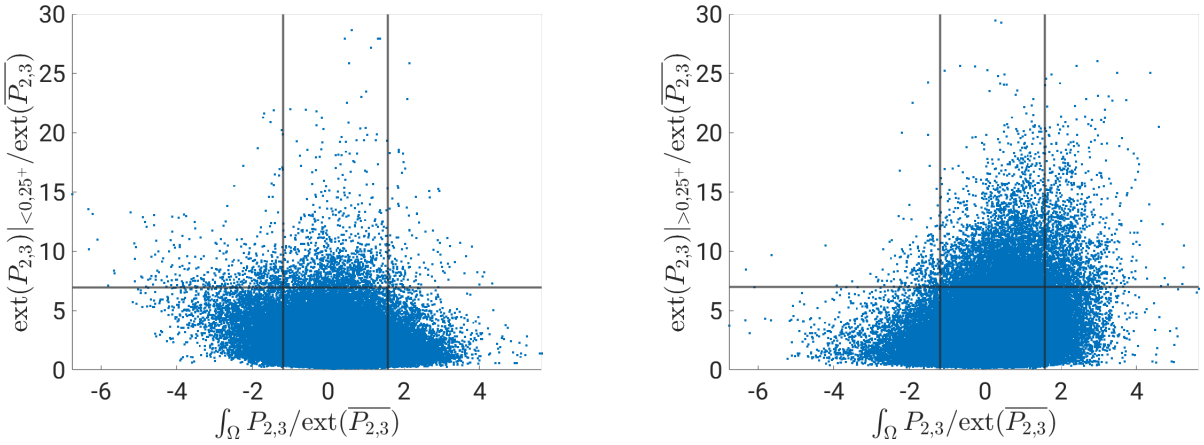

Figure 4.48: Scatter plot of cross-sectional instantaneous $P_{2,3}$-peaks occurring in the free surface layer and the corresponding secondary MKE-production integrated over the cross-section $\int_\Omega P_{2,3}$. On the left only negative $P_{2,3}|_{<0,25^+}$- and on the right only positive $P_{2,3}|_{>0,25^+}$-peaks are considered. The vertical lines indicate the 5%- and 95%-quantiles of $\int_\Omega P_{2,3}$ and the horizontal line shows 95%-quantile of the peak distribution. Both plots for $Re_\tau = 180$ and 50% FR.

Conditionally Averaged Flow Fields

After describing the procedure of gathering the conditionally averaged flow fields and quantifying the different events, the spatial distribution of the conditionally averaged flow fields are investigated by visualising the streamwise vorticity and the secondary MKE-production. Please note that the case of 25% filling is not included into the spatial analysis, because only very few events were captured in the free surface layer, hence, a different procedure to extract the extreme events of secondary MKE-production would have been necessary. Further note that the conditionally averaged flow field for a $P_{2,3}$-event in the left mixed-corner is basically symmetric to the one in the right mixed-corner and both events, right and left, occur equally often. Hence, advantage of the vertical symmetry plane was taken and the conditionally averaged field of the event in the left mixed-corner was mirrored to the right and both were averaged. This averaging increases the sample size of an event occurring in the mixed-corner by a factor of two.

In a first step, only the cross-sections where the peaks occurred, were averaged, see 4.49 for $Re_\tau = 180$ and 50% filling. The peaks for the averaged cross-sections are categorized by the location of the peak and whether it is a negative or positive peak. Please note that the increments of the contourlines are increased for this plot (negative $P_{2,3}$ peaks in the mixed-corner; top, left) by a factor of two. The negative $P_{2,3}$ peaks in the mixed-corner (top, left) show the strongest vorticity peaks compared to the other distributions. Interestingly, a pattern close to the mean vorticity pattern can be identified. The maximum events of $P_{2,3}$ in the mixed-corner (top, right) also strongly resemble the mean vorticity distribution with positive secondary MKE-production at the free surface between inner and outer secondary cell. Hence, the minima and the maxima in the mixed-corner describe a similar event, which consists of an inner and an outer secondary cell. The distribution of the minima in the centre shows only weak vorticity intensities in the centre. However, with a clear division of signs

to each side and distinct inner secondary cells. In the center of the free surface where the negative MKE-production peak is located almost no vorticity is present. In conclusion, all the different categories of extreme events at the free surface resemble the mean distribution vorticity, hence, they do not contradict each other, they rather support the same flow pattern. Note that there are no figures for maxima in the centre, because hardly any maxima occurred in the centre.

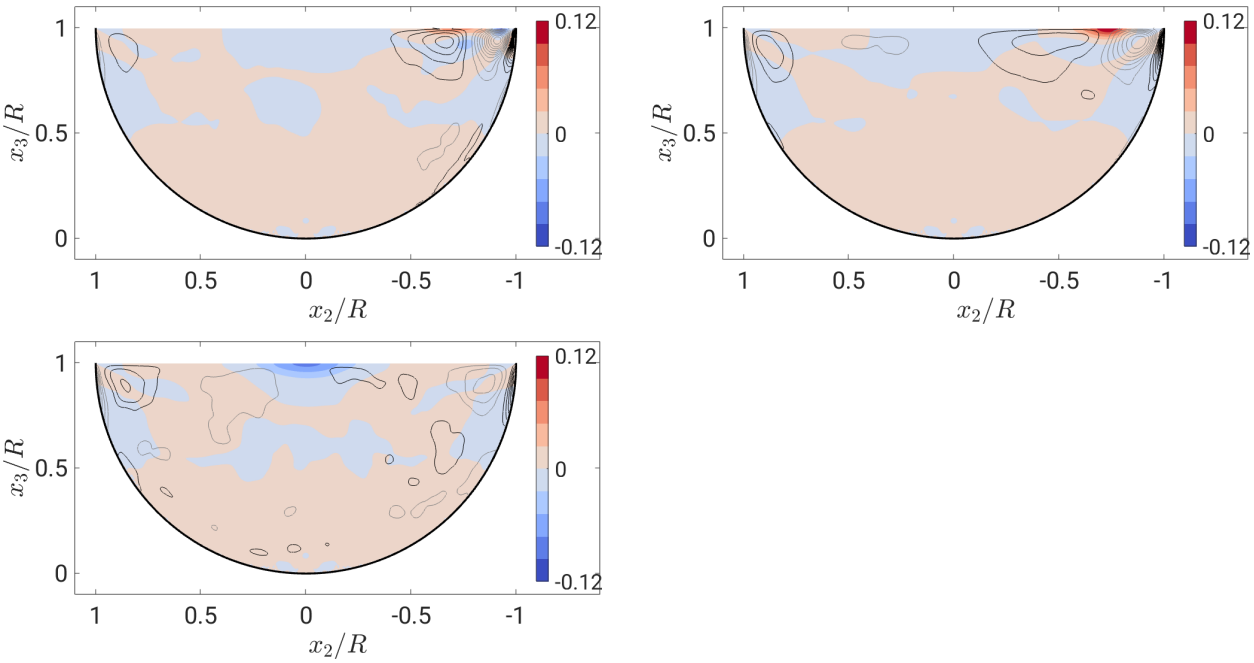

Figure 4.49: Secondary MKE-production $P_{2,3}$ normalised by ν/u_τ^4 in colour and streamwise vorticity ω_1 as gray (clockwise) and black (counterclockwise rotation) contours of $Re_\tau = 180$ and 50% FR, being conditionally averaged for minima (left) and maxima (right) secondary MKE-production peaks. Top row shows average over all corner peaks and second row shows peaks in the centre. Please note that the increments of the contourlines are increased by a factor of two for the minimum events in the mixed-corner (top, left).

For 75% filling the distributions of the streamwise vorticity (figure 4.50) are very similar at the free surface to the ones of 50% filling. This is surprising, because, in contrast, the mean secondary flow of 75% FR shows a pattern with a very small inner vortex only. This could have suggested that other dynamics take place, but apparently, the obtuse angle does not have a strong impact on the appearance of the structures of the conditionally averaged flow field. The free surface wall interactions seem to be similar, but the bottom part gets larger, where no large magnitudes occur in the conditionally averaged sense.

For the three dimensional conditionally averaged flow fields the instantaneous snapshots were averaged the following way: Each $P_{2,3}$-peak was categorised in the above mentioned manner and then the snapshot was shifted in streamwise direction such that the peak is centred within the snapshot. The velocity flow fields were centred according to the $P_{2,3}$-peak, too, and then averaged over all peak occurrences. This procedure was applied for each peak category. Moreover, as mentioned above, advantage of the vertical symmetry plane was taken, by

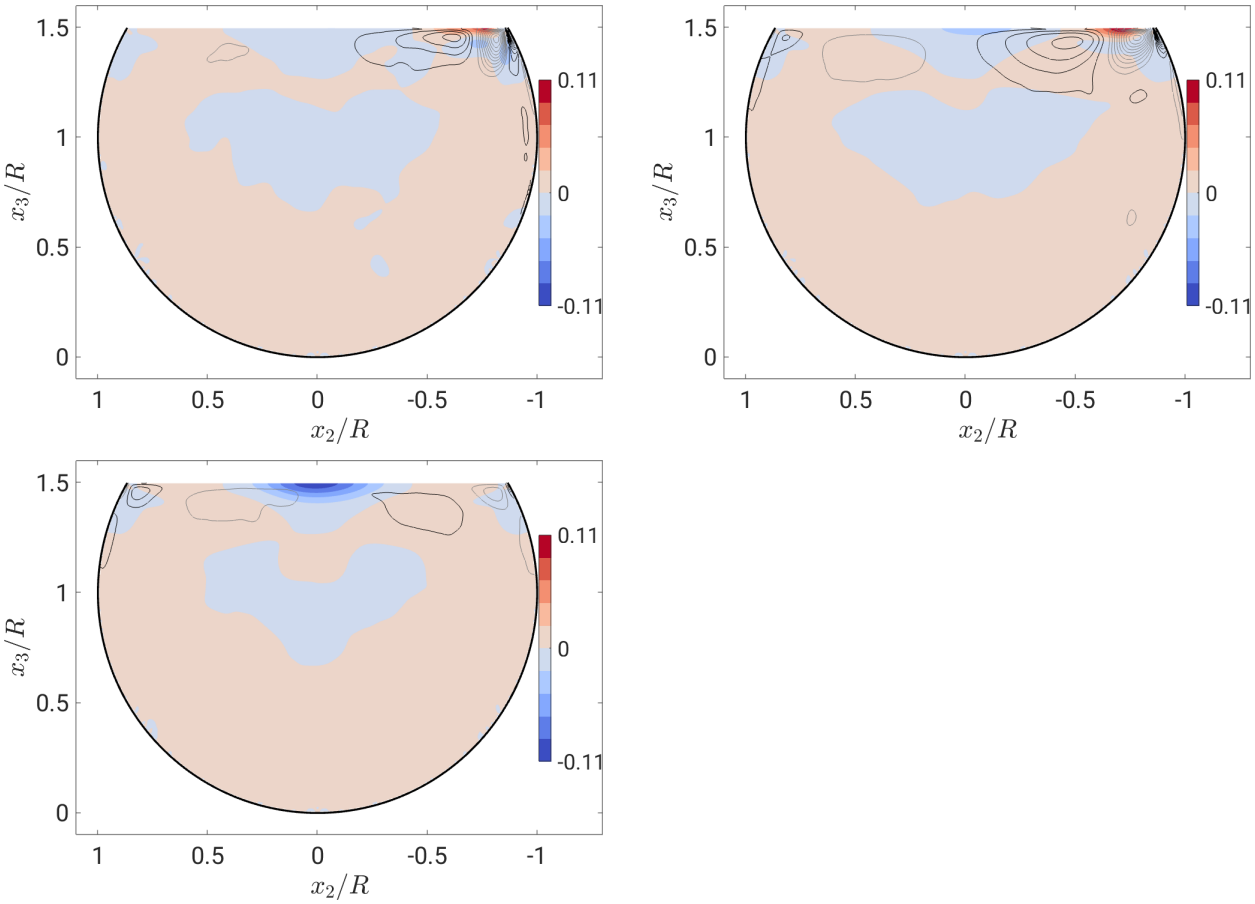

Figure 4.50: Secondary MKE-production $P_{2,3}$ normalised by ν/u_τ^4 in colour and streamwise vorticity ω_1 as gray (clockwise) and black (counterclockwise rotation) contours of $Re_\tau = 180$ and 75% FR, being conditionally averaged for minima (left) and maxima (right) secondary MKE-production peaks. Top row shows average over all corner peaks and second row shows peaks in the centre. Please note that the increments of the contourlines are increased by a factor of two for the minimum events in the mixed-corner (top, left).

mirroring the conditionally averaged field of the peak in the right mixed-corner to the left. Please note that the snapshot can be shifted in streamwise direction without limits, because of the periodic boundary condition in streamwise direction.

In 3D it is possible, instead of examining the streamwise vorticity or the contours of the stream function of the secondary flow, to calculate the Q-criterion (Hunt *et al.*, 1988). It applies to the velocity gradient tensor $J = \nabla \boldsymbol{u}$ and uses its second invariant to define structures. J can be split up into the sum of the rate-of-strain tensor $S_T = \frac{1}{2}(\nabla \boldsymbol{u} + (\nabla \boldsymbol{u})^T)$ and the vorticity tensor $\Omega_T = \frac{1}{2}(\nabla \boldsymbol{u} - (\nabla \boldsymbol{u})^T)$, being the symmetrical and anti-symmetrical part of the velocity gradient tensor, respectively. The second invariant of J can be defined as $Q = \|\Omega_T\|_2 - \|S_T\|_2$, with $\| \varphi \|_2$ being the Euclidean norm. In the case of $Q > 0$ the magnitude of vorticity is greater than the rate-of-strain magnitude, hence, vorticity is the dominating process. Please note that in the fluid mechanics community a unique definition for structures is missing and still under discussion. Nevertheless, the Q-criterion, which is used within this thesis, is widely used to define structures in 3D-space. The same analysis

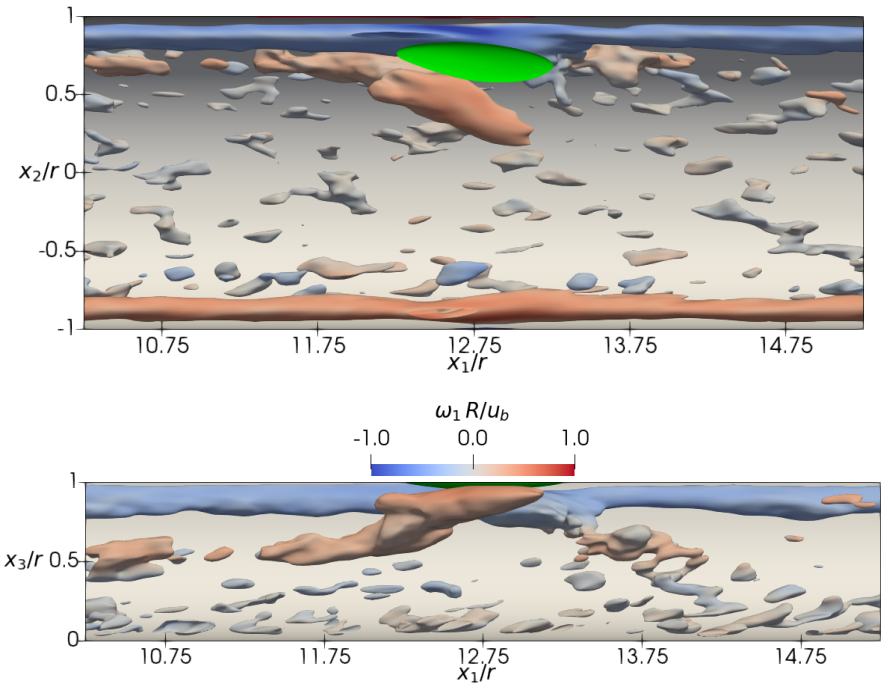

Figure 4.51: Conditionally averaged flow field of the positive extreme event of $P_{2,3}$ (green) in the mixed-corner with contour of Q-criterion ($Q\,R/u_b = 0.023$) coloured with $\omega_1\,R/u_b$ for $Re_\tau = 180$ and 50% FR. View from top (top) and view from side with a cut at $x_2 = 0$ (bottom).

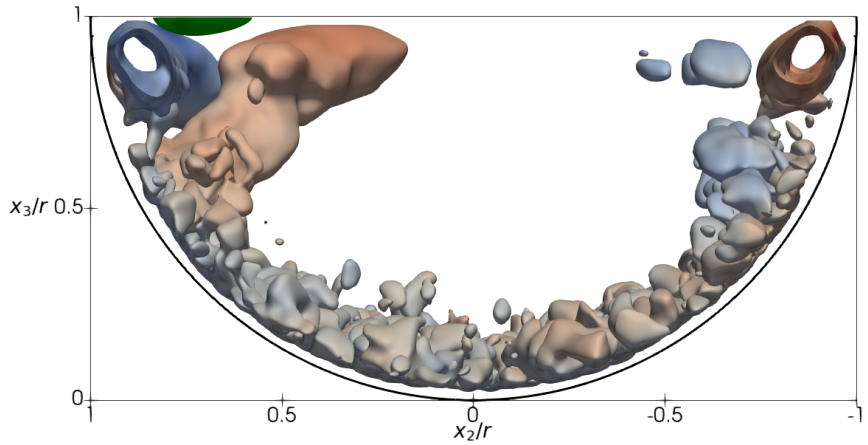

Figure 4.52: Conditionally averaged flow field of the positive extreme event of $P_{2,3}$ (green) in the mixed-corner with contour of Q-criterion ($Q\,R/u_b = 0.023$) coloured with $\omega_1\,R/u_b$ (see fig. 4.51) for $Re_\tau = 180$ and 50% FR. View in streamwise direction.

was also performed using the λ_2-criterion of Jeong & Hussain (1995), which gave almost indistinguishable results.
The most frequent event for the free surface layer in the 95%-quantile is the maximum $P_{2,3}$ in the mixed-corner for all Reynolds numbers, hence, in the following this category is investigated in detail. For $Re_\tau = 180$ and 50% FR the figures 4.51 and 4.52 show the conditionally averaged flow field of the maximum $P_{2,3}$-event in the mixed-corner. In figure 4.51 a view on the conditionally averaged structure is shown from the top (top plot) and from the side (bottom) and in figure 4.52 the domain can be seen in streamwise direction. The green patch represents the contour of the positive secondary MKE-production $P_{2,3}\,\nu/u_\tau^4 = 0.054$ and the other structures are a contour of the Q-criterion $Q\,R/u_b = 0.023$. The structures from the Q-criterion are coloured by the magnitude of the streamwise vorticity $\omega_1\,R/u_b$. Blue indicates counter- and red clockwise rotation. The inner secondary cell is present in both mixed-corners of the pipe over the whole domain with deformations, where the $P_{2,3}$-peak is located. In front of the MKE-production peak a red clockwise rotating structure is present, which reaches from the wall underneath the mixed-corner cell to the free surface. It seems the red structure is wall-attached and evolves from the wall to the free surface. In between the outer structure and the mixed-corner cell a flow towards the free surface is generated, where it is redirected, creating mean secondary flow via $P_{2,3}$. The mixed-corner vortex gets back to its shape after less than $2R$ behind the $P_{2,3}$-peak and the red structure ends again in the bulk flow. The red structure consists of two parts, one part is directly at the wall and the other is at the free surface. This configuration reminds of the mean streamwise vorticity distribution, showing two peaks, one at the wall below the inner secondary cell and one at the free surface.
As shown in figure 4.47 (right) also for 75% FR the maximum $P_{2,3}$-events are responsible for more than half of the extreme peaks in the free surface layer. As the mixed-corner has an obtuse angle, the structural connection between wall and free surface might be different for 75% filling ratio. Nevertheless, in figures 4.53 and 4.54 a very similar conditionally averaged structure is found. The basic configuration is the same for both FRs with the mixed-corner vortex and the clockwise rotating structure evolving from the side wall to the free surface. The inner secondary cell has approximately only half the size compared to the inner vortex of 50% FR. The vertical size of the outer structure is approximately $0.5R$ in both cases.
The conditionally averaged structures of different Reynolds numbers for 50% FR are shown in figure 4.55. The view on the flow fields is in flow direction. On the one hand, the mixed-corner vortex gets smaller with increasing Reynolds number, as expected from the inner scaling of the inner secondary cell of the mean flow. On the other hand, with decreasing Re the outer structure becomes more distinct and the iso-contour becomes more coherent. With the contour level of Q being approximately constant for all Reynolds numbers, it can be seen that at smaller Re less other structures are present around the peak structure in the conditionally averaged flow field, neither in front nor behind nor next to it. For the case of higher Re, many small structures that have the same rotation as the mean flow, can be observed in front and behind the $P_{2,3}$ peak at the free surface. Along the bottom small structures occur only close to the wall and seem to be randomly distributed, also according to their sign. A sensitivity study of the threshold for Q showed that the threshold seems to be sensible, because, for instance, at $Re_\tau = 460$, a higher threshold would let all

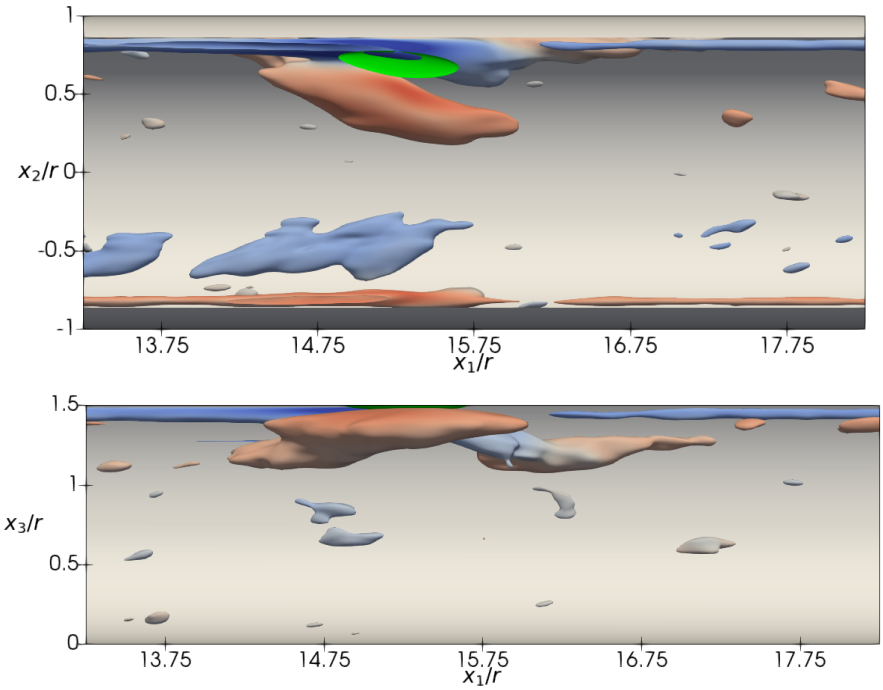

Figure 4.53: Conditionally averaged flow field of the positive extreme event of $P_{2,3}$ (green) in the mixed-corner with contour of Q-criterion ($Q\,R/u_b = 0.023$) coloured with $\omega_1\,R/u_b$ (see fig. 4.51) for $Re_\tau = 180$ and 75% FR. View from top (top) and view from side with a cut at $x_2 = 0$ (bottom).

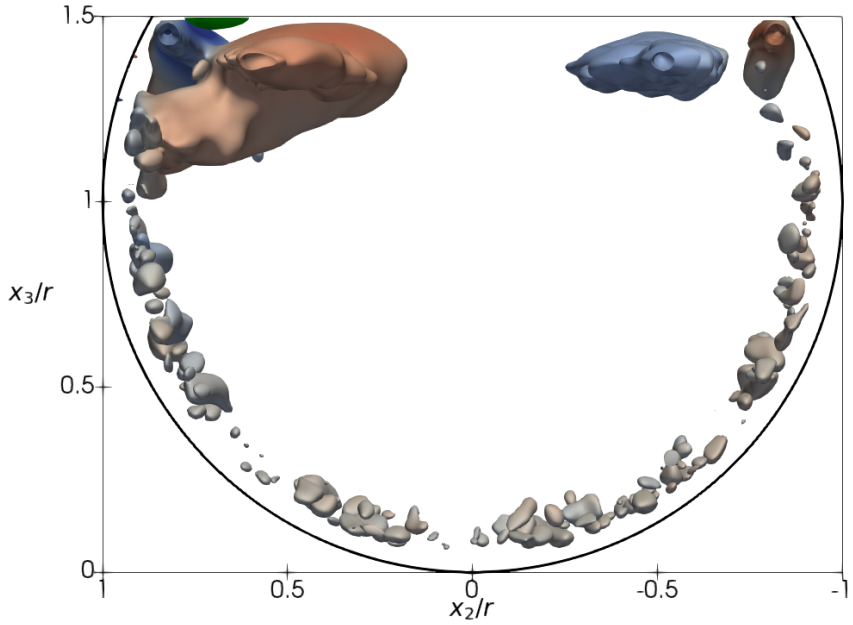

Figure 4.54: Conditionally averaged flow field of the positive extreme event of $P_{2,3}$ (green) in the mixed-corner with contour of Q-criterion ($Q\,R/u_b = 0.023$) coloured with $\omega_1\,R/u_b$ (see fig. 4.51) for $Re_\tau = 180$ and 75% FR. View in streamwise direction.

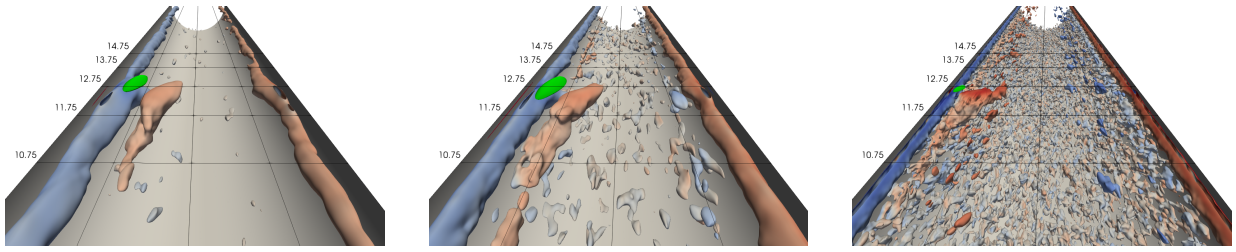

Figure 4.55: Conditionally averaged flow field of the positive extreme event of $P_{2,3}$ (green) in the mixed-corner with contour of Q-criterion coloured with $\omega_1\, R/u_b$ (see fig. 4.51). View in streamwise direction for $Re_\tau = 140$ (left), 180 (middle) and 460 (right) for 50% filling ratio. Threshold for $Q\, R/u_b$ is 0.02, 0.023 and 0.035, respectively. View in streamwise direction. Note that the figure is available in the appendix D with enlarged size.

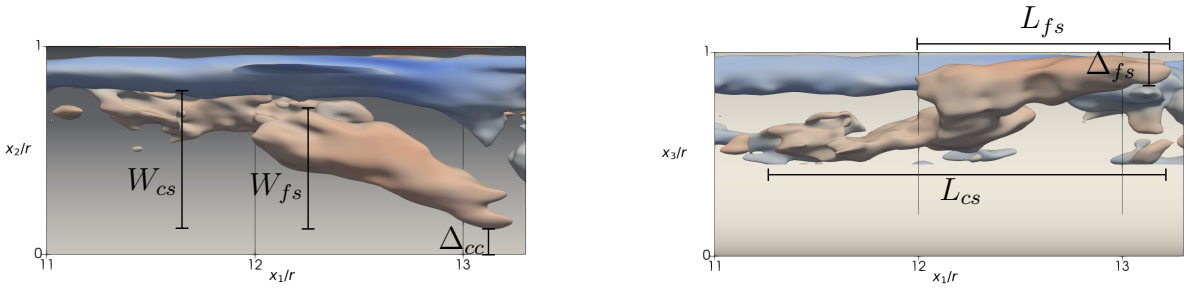

Figure 4.56: Definition of lengths of conditionally averaged structures of maximum $P_{2,3}$ events in the mixed-corner.

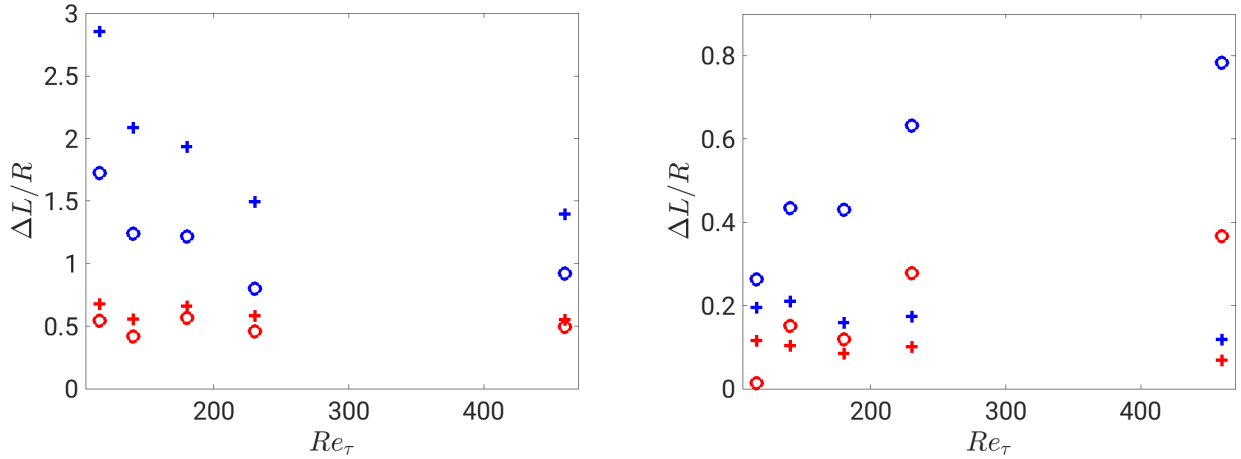

Figure 4.57: Lengths ΔL of conditionally averaged structures of maximum $P_{2,3}$ events in the mixed-corner. Left: +: transverse width complete structure W_{cs}, ∘: transverse width free surface part of structure W_{fs}, +: streamwise length complete structure L_{cs}, ∘: streamwise length free surface part of structure L_{fs}. Right: +: distance core to free surface, ∘: distance core to centre, +: distance lower contour to free surface Δ_{fs}, ∘: distance centre contour to centre Δ_{cc}.

structures disappear simultaneously and with a smaller threshold the distinction between the conditionally averaged structures and the surrounding flow field would be less clear. However, the choice of the threshold value remains subjective. Moreover, please note that the presence of randomly distributed structures along the bottom and in front and behind the peak structure indicates that the statistics are not fully converged yet. With increasing sample size these structures should disappear, however, the qualitative pattern would not change.

The dimensions of the outer structure, which are defined in figure 4.56, are compared for the different Reynolds numbers in figure 4.57. Either the dimension of the complete structure is taken, or only from its free surface part. The transverse width for the complete W_{cs} or the free surface structure W_{fs} is approximately the same for different Reynolds numbers, whereas the streamwise length gets smaller with increasing Re (fig. 4.57 left). By increasing the threshold of the Q-criterion, a core of the structure was localised in the free surface part of the structure. The right plot of figure 4.57 shows its distance to the free surface, which gets slightly less with increasing Reynolds number, whereas the distance of the core to the vertical symmetry line increases. Hence, with higher Re the outer structure moves closer to the free surface and the mixed-corner.

In a last step, the conditionally averaged structures are compared to the instantaneous extreme events, which were used for the conditional averaging. Looking at instantaneous flow fields of extreme events, a direct representation of the Q-criterion shows the smallest scales, which, mostly show a chaotic, overwhelming distribution of single structures, see figure 4.58 (top). For the bottom plot the instantaneous velocity field was Gaussian filtered with a filter width of $\sigma^+ = 20$. Then the vorticity and Q-criterion were calculated from the filtered velocity field. Surprisingly, the high MKE-production does not necessarily occur in between two counter-rotating structures. The $P_{2,3}$-event at $x_1/R \approx 10$ and $x_2/R \approx 0.8$ seems to be accompanied by two counter-rotating structures, a blue one in positive x_2-direction and a red one in negative x_2-direction. However, for the $P_{2,3}$-event at $x_1/R \approx 8$ and $x_2/R \approx -0.8$ only one red structure occurs right at its place. Hence, the structures found in the 3D-representation of the conditionally averaged flow fields, cannot be easily found in instantaneous flow fields. This underlines the mostly conceptual meaning of the conditionally averaged flow fields, as already pointed out by Jiménez & Kawahara (2012).

Conclusion

In summary, extreme events of $P_{2,3}$ were conditionally averaged for 50% and 75% FR in a 25 wall units large free surface layer. In general, the conditionally averaged flow fields resemble the mean secondary flow. Most of the extreme events that transfer TKE to MKE are occurring in the mixed-corners at the free surface. The extreme events of $P_{2,3}$ do not dominate the cross-section integrated secondary MKE-production, but they are correlated and produce a trend. Hence, the extreme events can be analysed conceptually. For 50% FR, strong secondary MKE-production occurs at the free surface between two counter-rotating vortical structures. On the one side there is a structure resembling the inner secondary cell, that is persistent over a larger distance. On the other side a bigger, wall-attached structure reaching to the central free surface occurs. Surprisingly, the same pattern of structures can be detected for 75% filled pipe flow. Although the inner secondary cell is hardly present in

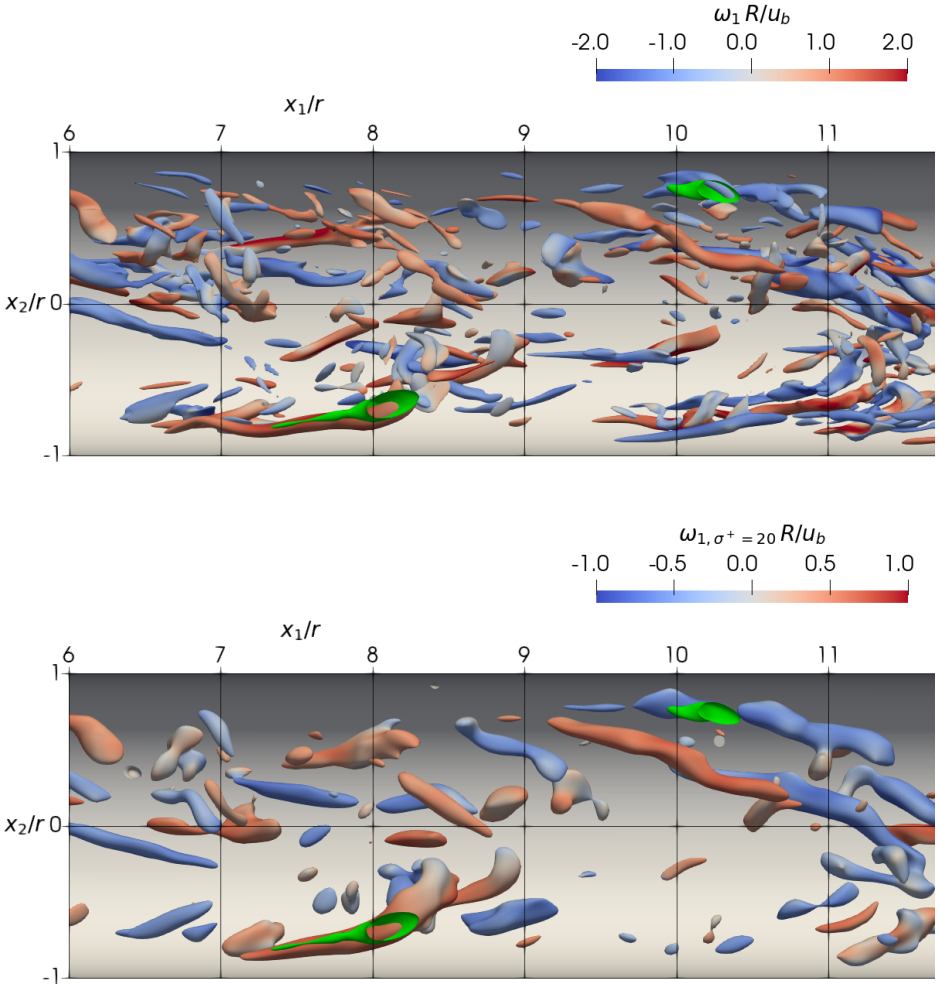

Figure 4.58: Instantaneous extreme event of $P_{2,3}$ (green) with Q-criterion coloured with $\omega_1\, R/u_b$ of complete (top) and gaussian filtered velocity field (filter width $\sigma^+ = 20$) (bottom) for $Re_\tau = 180$ and 50% FR.

the mean flow of 75% FR, similar structures are responsible for extreme events of secondary MKE-production. Hence, the impact of the obtuse angle on the extreme events of $P_{2,3}$ is small. The filling ratio 25% was not examined in detail, because most of the strong secondary MKE-production events do not occur at the free surface. Therefore, a different conditional averaging process would need to be implemented, in order to extract the extreme events for this filling ratio.

4.3. Conclusion

As mentioned in the introduction to this chapter, its aim is to show different perspectives of the secondary flow mechanism and trying to identify common and complementing features.

The classical approach of analysing the mean streamwise vorticity equation shows that the gradients of turbulence anisotropy, which are responsible for vortictiy production, have high intensities in the vicinity of the mixed-corners. Hence, in each mixed-corner, which are the only geometrical inhomogeneity in partially filled pipe flow, vorticity is generated with opposing sign being in line with the rotation of the mean secondary flow for 25% and 50% FR. As the inner secondary cell is very weak and small for 75% FR, the strong vorticity generation in the mixed-corner is not in line with the mean secondary flow.
Another perspective are the MKE- and TKE-budget, which provide a complete picture of the path of kinetic energy: the incoming energy, which only has a streamwise component, enters the MKE-budget, where it is either directly dissipated or transferred to TKE. By the intercomponent transfer energy also reaches the cross-stream components. A small share of energy is transferred back to MKE, generating secondary flow. This energy transfer is provided by the secondary production term $P_{2,3}$ and occurs in a small area around the stagnation point located at the free surface, separating the inner and the outer secondary flow cells. From this point, secondary kinetic energy is either transported along the free surface towards the pipe's centre or towards the mixed-corner. With increasing filling ratio the amount of energy directed towards the centre increases. For 75% filled pipe flow almost the entire secondary kinetic energy is directed towards the centre and the inner secondary cell almost vanishes.
Comparing the processes occurring within both kinetic energy budgets and the mean vorticity equation shows that they are compatible with each other for 25% and 50% FR. The intensity and location of vorticity generation can be connected to the location and division of secondary production and both processes are consistent with each other. However, no causality can be concluded. For 75% filled pipe flow, the location of vorticity production is in conflict with the occurring secondary flow and the results from the MKE-budget.

In addition to the mean flow analysis, which showed that the secondary production $P_{2,3}$ is a key term, coherent structures, defined by POD, GF and conditional averaging, gave insights into the turbulent dynamics of the flow and its connection to the generation process of secondary flow.
Two different two-dimensional PODs were employed, which decompose the TKE differently by taking either all three or only the cross-stream velocity components into account. On the one hand, the 3C-POD and its TKE decomposition are governed by u_1, because the streamwise component dominates the flow. On the other hand, for the 2C-POD only the cross-stream components are taken into account, thus, the most energetic modes contain the most secondary TKE. The fluctuating temporal coefficients are Gaussian distributed around zero for both PODs. The spatial modes of the 3C-POD are more connected to strong streamwise velocity peaks along the wall and for 2C-POD larger structures occur covering more the bulk region of the flow. The spatial restriction of the high energy containing modes indicates that both POD approaches are not able to describe vortices moving over these boundaries

very well. Hence, the sorting mechanism described by Sakai (2016) can hardly be reproduced by only the high energy-containing modes. The differences of the spatial preferences between the two approaches are also well visible in the instantaneous velocity and vorticity fields, reconstructed by the high energy containing modes representing 30% of the energy. On the one hand, the instantaneous streamwise vorticity along the free surface reconstructed from 2C-POD indicate that individual strong structures that resemble the instantaneous flow field carry a considerable amount of secondary TKE. On the other hand, elongated structures along the mixed-corner that resemble the inner secondary cell can be reported for the 3C-POD, being consistent with the 3C-POD of Ng *et al.* (2021).

In contrast to the POD, the GF is applied in all three dimensions on the complete three dimensional fields, hence, three dimensional dynamics are preserved. With enlarging the filter width, small scales are filtered and large scales become more visible, however, at the same time the kinetic energy in the filtered flow field decreases. Most of the intense small and large scale structures appear in the vicinity of the wall and in the buffer layer, and occur less in the bulk region. Along the free surface, a pattern of counter-rotating vortex pairs can be detected that are inclined by approximately 30° from the wall, which become more distinct with increasing filter width. Please note that the inclined vortex pairs are not consistent with the vortex sorting mechanism proposed by Sakai (2016). However, especially for larger filter widths, the overall arrangement of the vortices and their corresponding sense of rotation resemble the mean secondary flow. Most of the small and large scale structures that occur along the free surface have a streamwise length of less than $2R$ and, because of the inclined structures, an alternating pattern of positive and negative vorticity appears in streamwise direction. This indicates that the mean secondary flow is formed by averaging over a large number of different large and small scale structures, instead of a stable vortex pattern that only deviates from its mean representation. This result is consistent with Sakai (2016), whilst it does not agree with a conceptual description of the secondary flow structures by Ng *et al.* (2021). They describe an interaction between a mean outer secondary cell and instantaneous structures, however, as mentioned above, the present results do not show a temporally stable outer secondary vortex.

Applying the POD and GF on $P_{2,3}$ shows that the 3C-POD is less suited to extract the transfer mechanism than the 2C-POD and the GF. 2C-POD and GF are able to define high energy modes and large scale structures, respectively, which contain a slightly larger share of $P_{2,3}$ than corresponding TKE. However, all applied filterings show that the low energy modes and the small scales have a non-negligible impact on the transfer mechanism, which is in agreement with the results of Sakai (2016). Hence, the generation of secondary flow is a multi-scale and multi-mode process. The instantaneous filtered and non-filtered $P_{2,3}$ indicate that strong secondary MKE-production events are often surrounded by strong vortical structures.

As a further complementary approach, events of high $P_{2,3}$ magnitudes were conditionally averaged for 50% and 75% FR. In general, the conditionally averaged flow fields resemble the mean secondary flow pattern. Most of the extreme events that transfer TKE to MKE occur in the mixed-corners at the free surface. The extreme events of $P_{2,3}$ do not dominate the cross-section integrated secondary MKE-production, but they are correlated and produce a trend. For 50% FR, strong secondary MKE-production occurs at the free surface between two counter-rotating vortical structures. On the one side there is a structure resembling the

inner secondary cell, that is persistent over a larger distance. On the other side a bigger, wall-attached structure reaching to the central free surface occurs. Similar results were found by Sakai (2016), who investigated the temporal development of coherent structures in a rectangular open-channel flow. He states that the inner secondary cell consists of rather long structures, whereas the *velocity-dip* phenomenon is generated by vortices moving from the side walls to the top centre. Surprisingly, the same pattern of structures as for 50% FR can also be detected for 75% filled pipe flow. Although the inner secondary cell is hardly present in the mean flow of 75% FR, similar structures are responsible for extreme events of secondary MKE-production. Hence, the impact of the obtuse angle formed by the pipe wall and the free surface on the extreme events of $P_{2,3}$ is small.
Comparing the spatial distributions of the generation term of vorticity of the mean vorticity equation with $P_{2,3}$ and the conditionally averaged extreme events, the different perspectives do not contradict each other for the case of 50% filled pipe flow. For 75% filling ratio, the vorticity generation and conditionally averaged fields show similar distributions as for 50% FR, however, the inner secondary cell vanishes for the mean flow and the distribution of the mean secondary production does not imply a two vortex mechanism. Hence, the distributions of the generated vorticity and of the mean secondary production would contradict. But the knowledge of the conditional averaging enables to speculate that the process of generating secondary flow is similar for both filling ratios.

5. Conclusion

To the end of this thesis the main results of the present study are summarised and an outlook for future work is given.

5.1. Main Results

This thesis investigates the first results of a DNS of partially filled pipe flow for marginal to moderate Reynolds numbers. The aim of this thesis was to provide a detailed flow description and analyse the generation mechanism of the turbulence-induced secondary flow. A special focus was placed on the role of the mixed-corner, which is the only geometrical inhomogeneity in partially filled pipe flow.
The numerical methods applied in the simulations were carefully validated by a grid study. The combination of Cartesian grid and immersed boundary method was further investigated simulating a full pipe flow and comparing it to literature. Moreover, the length of the domain was assessed by analysing the streamwise two-point correlation of the velocities. For the 50% filling ratio (FR), simulations were performed from $Re_\tau = 110$, which was found to be the lowest friction Reynolds number that could sustain a turbulent flow, to $Re_\tau = 460$, which was the highest Reynolds number. In addition to the semi filled pipe flow, FRs of 25% and 75% were simulated for $Re_\tau = 180$.

Over the considered parameter range, the friction coefficient was found to agree well with Prandtl's relation for smooth full pipe flow. The present values are lower than previously published experimental results, however, Ng *et al.* (2018) reported larger uncertainties for their data. In general, a good agreement to existing experiments was obtained for the mean streamwise velocity distribution. The position of the maximum streamwise velocity is Re-dependent and seems to settle for semi filled pipe flow at $0.3 - 0.4\,R$ below the free surface for the highest simulated Reynolds number. In combination with all data available in literature on the distance between the maximum streamwise velocity and the free surface Δz, the present results indicate a linear relation between Δz and the FR ($H/2R$): $\Delta z/(2R) \approx 0.6754(H/(2R)) - 0.1642$. This relation can be used to approximate the streamwise velocity distribution applying the procedure of Guo *et al.* (2015), which provides a good estimation, however, it neglects any effect of secondary flow. In the lower half of the domain, the streamwise velocity distribution becomes closer to the standard log-law with increasing Reynolds number and, overall, it matches well with the profile measured by Ng *et al.* (2018).
The mean secondary flow has a maximum magnitude of 1-6% of u_b, which occurs at the free surface. The secondary flow pattern is organised in four vortices, which are arranged in two counter-rotating vortex pairs symmetrical to the centre plane. Thus, the existence of the so-called inner secondary cell appearing in the mixed-corner, postulated by Grega *et al.*

(2002), was confirmed for the investigated range of Reynolds numbers and the different FRs. In agreement with Sakai (2016), the present study can report that the position and size of the inner secondary cell in semi filled pipe flow scale with wall units. The fact that the inner secondary vortex becomes smaller with increasing Reynolds number could explain why it has not yet been found in experiments performed at much higher Reynolds numbers (e.g. Ng *et al.* (2018)). A larger inner secondary cell could be detected for 25% FR, whereas it almost vanishes for a high FR (75%). Hence, the outer secondary vortex becomes more dominant with increasing FR. In contrast to the inner secondary cell, the geometry and position of the outer secondary cell scale with outer units.

The wall shear stress distribution is strongly influenced by the comparably weak secondary flow. In the mixed-corner, a global wall shear stress maximum appears for all Reynolds numbers at 50% FR of up to 1.4 times the mean wall shear stress τ_0 and $1.7\,\tau_0$ for $Re_\tau = 180$ with 75% FR. The wall shear stress maximum occurs, because the inner vortex transports high-momentum fluid from the free surface towards the wall. The maximum is followed by a minimum, which creates an almost harmonic wall shear stress distribution for the lowest Reynolds numbers with a local maximum in the pipe's symmetry plane. At Reynolds numbers above $Re_\tau \approx 140$, a plateau with a magnitude of approximately $1.05\,\tau_0$ is formed in the centre of the perimeter, which becomes wider as Reynolds number increases. The region of constant wall shear stress in the centre of the perimeter enlarges also with increasing FR. Moreover, the maximum of the wall shear stress in the mixed-corner even increases for high FRs despite the less intense inner secondary cells. For 25% FR, there is an extra wall shear stress minimum directly in the mixed-corner, because of the low flow intensities generated by the narrow flow section in the mixed-corner. Instantaneous near-wall streamwise velocities are organised in a streaky pattern like in a standard full pipe flow. The increased near-wall velocities in the mixed-corner can not be seen in instantaneous distributions. However, by applying running time averages on the wall shear stress over time intervals of L/u_b, the large wall shear stress fluctuations occurring in the mixed-corner are smoothed, and the mean wall shear stress distribution becomes detectable.

The Reynolds stresses in the lower part of the pipe behave similarly to the full pipe flow and are nearly homogeneously distributed in azimuthal direction. Near the free surface this homogeneity is broken. The vertical Reynolds stress component is damped and the horizontal components are amplified. Especially at the mixed-corner local maxima or minima occur in and around the inner secondary vortex, which infers a Reynolds stress anisotropy.

Within this study different perspectives on the secondary flow mechanism were investigated to understand the mechanism and to identify common and complementing features between the perspectives.

The classical approach is the analysis of the mean streamwise vorticity equation. It shows that the gradients of the Reynolds stress anisotropy, that are responsible for vortictiy production, have high intensities in the vicinity of the mixed-corners. Hence, in each mixed-corner vorticity is generated with opposing sign being in line with the rotation of the mean secondary flow.

Another perspective are the mean kinetic energy (MKE-) and turbulent kinetic energy (TKE-) budgets, which provide a complete picture of the path of kinetic energy: the incoming energy, which only has a streamwise component, enters the MKE-budget where it

is either directly dissipated or transferred to TKE. Within the TKE-budget, the energy is also distributed to the cross-stream components. A small share of energy is transferred back to MKE, generating secondary flow. This energy transfer is provided by the secondary production term $P_{2,3}$. It occurs in a small area around the stagnation point located at the free surface, separating the inner and the outer secondary flow cells. From this point, secondary kinetic energy is either transported along the free surface towards the pipe's centre or towards the mixed-corner. With increasing FR the amount of energy directed towards the centre increases. For 75% filled pipe flow almost the entire secondary kinetic energy is directed towards the centre and the inner secondary cell almost vanishes.

Comparing the processes described by both kinetic energy budgets and the mean vorticity equation shows that they are compatible with each other for 25% and 50% FR. The intensity and location of vorticity generation can be connected to the location and division of secondary production and both processes are consistent with each other. However, no causality can be concluded. For 75% filled pipe flow, the location of vorticity production is in conflict with the occurring secondary flow and the results from the MKE-budget.

In addition to the mean flow analysis, coherent structures defined by proper orthogonal decomposition (POD), Gaussian filterting (GF) and conditional averaging, gave insights into the turbulent dynamics of the flow and its connection to the secondary flow mechanism.

Two different two-dimensional PODs were employed, which decompose the TKE differently by taking either all three or only the cross-stream velocity components into account. On the one hand, the 3C-POD and its TKE decomposition are governed by u_1, because the streamwise component dominates the flow. On the other hand, for the 2C-POD only the cross-stream components are taken into account, thus, the most energetic modes contain the most secondary TKE. The fluctuating temporal coefficients are Gaussian distributed around zero for both PODs. The spatial modes of the 3C-POD are more connected to strong streamwise velocity peaks along the wall, whereas for 2C-POD, the spatial modes represent structures that occur more in the bulk region of the flow. Interesting insights are provided by the instantaneous streamwise vorticity distribution along the free surface reconstructed from the first most energetic modes representing 30% of the TKE. ω_1 reconstructed by 2C-POD indicates that individual strong structures that resemble the instantaneous flow field carry a considerable amount of secondary TKE. In contrast, elongated structures along the mixed-corner that resemble the inner secondary cell can be reported for the 3C-POD, which is consistent with the 3C-POD by Ng *et al.* (2021).

In contrast to the POD, the GF is applied in all three dimensions on the complete three-dimensional fields, hence, three-dimensional dynamics are preserved. With enlarging the filter width, small scales are filtered and large scales become more visible, however, at the same time the kinetic energy in the filtered flow field decreases. Most of the intense small and large scale structures occur in the vicinity of the wall and the buffer layer. Along the free surface a pattern of counter-rotating vortex pairs can be detected, which are inclined by approximately 30° from the wall and become more distinct with increasing filter width. Please note that the inclined vortex pairs are not consistent with the vortex sorting mechanism proposed by Sakai (2016). The various visualisations of the filtered vorticity indicate that the mean secondary flow is formed by averaging over a large number of different large and small scale structures,

instead of a stable vortex pattern that only deviates from its mean representation. This result is consistent with Sakai (2016), whilst it does not agree with a conceptual description of the secondary flow structures by Ng *et al.* (2021).
Applying POD and GF on $P_{2,3}$ shows that the 3C-POD is less suited to extract the transfer mechanism than the 2C-POD and the GF. 2C-POD and GF are able to define high energy modes and large scale structures, respectively, which contain a slightly larger share of $P_{2,3}$ than corresponding TKE. However, all applied filterings show that the low energy modes and the small scales have a non-negligible impact on the transfer mechanism. This is in agreement with the results of Sakai (2016). Hence, the generation of secondary flow is a multi-scale and multi-mode process. Moreover, the instantaneous filtered and non-filtered $P_{2,3}$-visualisations indicate that strong secondary MKE-production events are often surrounded by strong vortical structures.
As a further complementary approach, events of high $P_{2,3}$ magnitudes were conditionally averaged for 50% and 75% FR. In general, the conditionally averaged flow fields resemble the mean secondary flow pattern. Most of the extreme events that transfer TKE to MKE occur in the mixed-corners at the free surface. However, the extreme events of $P_{2,3}$ do not dominate the cross-section integrated secondary MKE-production, but they are correlated to each other and produce a trend. For 50% FR, strong secondary MKE-production occurs at the free surface between two counter-rotating vortical structures. On the one side there is a structure resembling the inner secondary cell, that is persistent over a larger distance. On the other side a bigger, wall-attached structure reaching to the central free surface occurs. These results are compatible with the conclusions drawn by Sakai (2016). Surprisingly, the same pattern of structures as for 50% FR can be detected also for 75% filled pipe flow. Although the inner secondary cell is hardly present in the mean flow of 75% FR, similar structures are responsible for extreme events of secondary MKE-production. Hence, the impact of the obtuse angle formed by the pipe wall and the free surface on the extreme events of $P_{2,3}$ is small.
Comparing the spatial distributions of the vorticity generation term, the secondary MKE-production and the conditionally averaged extreme events, the different perspectives do not contradict each other for the case of 50% filled pipe flow. For 75% FR the vorticity generation and conditionally averaged fields show similar results as for 50% FR. However, neither does the mean flow show a distinct inner secondary cell, nor the distribution of the mean secondary production does imply a clear two vortex mechanism. Hence, the distributions of the generated vorticity and of the mean secondary production would contradict. But the knowledge of the conditional averaging enables to speculate that the generation of secondary flow is similar for both filling ratios.

5.2. Future Work

In this thesis, various fundamental questions were answered, for example, the appearance of secondary flow, how the secondary flow obtains its energy and what happens, if extreme events of secondary MKE-production occur. Nevertheless, some questions remain open whilst new questions have arisen.
First of all, the current state of art lacks confirmation of the inner secondary cell by physical experiments. This could be either done by multiple experiments of an increasing filling

ratio, starting from a quarter filled pipe, or by different angles in a trapezoidal cross-section. Another option would be to perform a low Reynolds number experiment, where the inner secondary cell becomes large enough that it should be clearly detectable.
In addition to the MKE- and TKE-budgets, Nikora & Roy (2012) suggest to also investigate the mean and turbulent enstrophy budgets which "represent a measure of the density of the kinetic energy of helical motions rather than of all motions" Nikora & Roy (2012). As the mean secondary flow is a vortical structure, it would be very interesting to investigate the coupling between the mean and turbulent vortical energy.
The present analysis of the POD lacks the dynamic interaction in streamwise direction. Hence, a next step could be to perform a three-dimensional POD generating three-dimensional modes. Moreover, the three-dimensional POD enables to analyse the interaction and exchange processes between modes, which could give insights about the exchange of kinetic energy and also of enstrophy between different modes. However, the three-dimensional POD needs a large number of three-dimensional snapshots, hence, a large eigenvalue problem has to be solved, which is computationally demanding.

The most prominent, still open question is: what is the causality within the secondary flow mechanism. Which event triggers what? At this moment only speculation is possible, however, it might be a chicken-egg problem that, when turbulence is initiated, only needs to be sustained.
Nevertheless, the self sustaining process (SSP) described by Waleffe (1997) seems to be worth to look into. High vorticity production occurs only in the mixed-corner, which indicates that this is a location where the SSP might take place and sustains the inner secondary cell. Waleffe (1997) proved the insensitivity of the SSP to both boundary conditions, slip and no-slip, which emphasizes the possible ability of the mixed-corner to accommodate the SSP. Within the SSP an instability, which can be described by Fourier-modes, occurs that triggers a non-linear feedback. The non-linear feedback is supposed to be strongest, where the vorticity generation is strongest, hence, the mixed-corner. Thus far, the idea that the mixed-corner is a location, where the SSP has higher probability to occur than elsewhere, is only speculation and needs detailed investigations. However, if it is the case, the mixed-corner vortex could be the starting point of the secondary flow mechanism.
It seems that the data of the present thesis is compatible with a SSP occurring in the mixed-corner, which enables to speculate about the secondary flow mechanism. Please note that the conditionally averaged 3D-fields show a persistent inner secondary cell not only for the extreme but also for the moderate $P_{2,3}$ events. Hence, the appearance of the inner secondary cell could be interpreted as the basic structure that is often present. In contrast, the outer vortex might be prone to occur, if the inner and a counter-rotating structure occur together by coincidence and strengthen each other. It can be speculated that the inner vortex is able to exist on its own in the mixed-corner, whereas the inner vortex is a precondition for the outer secondary vortex to be generated. However, the above mentioned thoughts are only ideas, which have to be verified by further investigations.

Bibliography

Adrian, R. J. & Westerweel, J. 2011 *Particle Image Velocimetry*. Cambridge University Press, Cambridge.

del Álamo, J. C. & Jiménez, J. 2003 Spectra of the very large anisotropic scales in turbulent channels. *Physics of Fluids* **15** (6), L41–L44.

Alfredsson, P. H., Johansson, A. V., Haritonidis, J. H. & H., Eckelmann. 1988 The fluctuating wall-shear stress and the velocity field in the viscous sublayer. *The Physics of Fluids* **31**, 1026–1033.

Anderson, W., Barros, J. M., Christensen, K. T. & Awasthi, A. 2015 Numerical and experimental study of mechanisms responsible for turbulent secondary flows in boundary layer flows over spanwise heterogeneous roughness. *Journal of Fluid Mechanics* **768**, 316–347.

Aubry, N. 1991 On the hidden beauty of the proper orthogonal decomposition. *Theoretical and Computational Fluid Dynamics* **2**, 339 – 352.

Avila, M. & Hof, B. 2013 Nature of laminar-turbulence intermittency in shear flows. *Physical Review E* **87**, 063012.

Bauer, C., von Kameke, A. & Wagner, C. 2019 Kinetic energy budget of the largest scales in turbulent pipe flow. *Physical Review Fluids* **4**, 064607.

Blanckaert, K. & De Vriend, H. J. 2004 Secondary flow in sharp open-channel bends. *Journal of Fluid Mechanics* **498**, 353–380.

Blanckaert, K., Duarte, A. & Schleiss, A. J. 2010 Influence of shallowness, bank inclination and bank roughness on the variability of flow patterns and boundary shear stress due to secondary currents in straight open-channels. *Advances in Water Resources* **33** (9), 1062–1074.

Breuer, M., Peller, N., Rapp, C. & Manhart, M. 2009 Flow over periodic hills - numerical and experimental study in a wide range of reynolds numbers. *Computers & Fluids* **38** (2), 433–457.

Broglia, R., Pascarelli, A. & Piomelli, U. 2003 Large-eddy simulations of ducts with a free surface. *Journal of Fluid Mechanics* **484**, 223–253.

Brosda, J. 2015 Theoretical and numerical investigation of secondary currents for straight, turbulent open-channel flow. Master's thesis, TU München.

Brosda, J. & Manhart, M. 2022 Numerical investigation of semifilled-pipe flow. *Journal of Fluid Mechanics* **932**, A25.

Chauvet, H., Devauchelle, O., Metivier, F., Lajeunesse, E. & Limare, A. 2014 Recirculation cells in a wide channel. *Physics of Fluids* **26** (1), 016604+.

Chiu, C. L. 1989 Velocity distribution in open channel flow. *Journal of Hydraulic Engineering* **115** (5), 576–594.

Chiu, C. L. & Said, C. A. A. 1995 Maximum and mean velocities and entropy in open-channel flow. *Journal of hydraulic engineering - ASCE* **121** (1), 26–35.

Clark, S. P. & Kehler, N. 2011 Turbulent flow characteristics in circular corrugated culverts at mild slopes. *Journal of Hydraulic Research* **49** (5), 676–684.

Demuren, A. O. & Rodi, W. 1984 Calculation of turbulence-driven secondary motion in non-circular ducts. *Journal of Fluid Mechanics* **140**, 189–222.

Domaradzki, J. A., Liu, W., Härtel, C. & Kleiser, L. 1994 Energy transfer in numerically simulated wall-bounded turbulent flows. *Physics of Fluids* **6** (4), 1583–1599.

DWA 2011 *DWA-Regelwerk / Merkblatt. 181*. Deutsche Vereinigung für Wasserwirtschaft und Abwasser.

DWA 2012 *DWA-Regelwerk / Merkblatt. 110*. Deutsche Vereinigung für Wasserwirtschaft und Abwasser.

Einstein, H. A. & Li, H. 1958 Secondary currents in straight channels. *American Geophysical Union Transactions* **39** (6), 1085–1088.

El Khoury, G. K., Schlatter, P., Noorani, A., Fischer, P. F., Brethouwer, G. & Johansson, A. V. 2013 Direct numerical simulation of turbulent pipe flow at moderately high reynolds numbers. *Flow, turbulence and combustion* **91** (3), 475–495.

Emory, M. R. & Iaccarino, G. 2014 Visualizing turbulence anisotropy in the spatial domain with componentality contours. pp. 123–138. Center for Turbulence Research, Stanford University.

Feldmann, D., Bauer, C. & Wagner, C. 2018 Computational domain length and reynolds number effects on large-scale coherent motions in turbulent pipe flow. *Journal of Turbulence* **19** (3), 274–295.

Garbrecht, G., ed. 1987 *Hydraulics and Hydraulic Research; A historical Review*. Balkema.

Garbrecht, G. 1995 *Meisterwerke antiker Hydrotechnik*. Vieweg+Teubner Verlag, Wiesbaden.

Garbrecht, G. & Netzer, E. 1991 Die Wasserversorgung des geschichtlichen Jericho und seiner königlichen Anlagen (Gut, Winterpaläste). *Mitteilungen des Leichtweiß-Instituts der TU Braunschweig* **115**.

Gavrilakis, S. 1992 Numerical simulation of low-Reynolds-number turbulent flow through a straight square duct. *Journal of Fluid Mechanics* **244**, 101–129.

Gessner, F. B. 1973 The origin of secondary flow in turbulent flow along a corner. *Journal of Fluid Mechanics* **58** (01), 1–25.

Grega, L. M., Hsu, T. Y. & Wei, T. 2002 Vorticity transport in a corner formed by a solid wall and a free surface. *Journal of Fluid Mechanics* **465**, 331–352.

Grega, L. M., Wei, T., Leighton, R. I. & Neves, J. C. 1995 Turbulent mixed-boundary flow in a corner formed by a solid wall and a free surface. *Journal of Fluid Mechanics* **294**, 17–46.

Guo, J. 2014 Modified log-wake-law for smooth rectangular open channel flow. *Journal of Hydraulic Research* **52** (1), 121–128.

Guo, J., Mohebbi, A., Zhai, Y. & Clark, S. P. 2015 Turbulent velocity distribution with dip phenomenon in conic open channels. *Journal of Hydraulic Research* **53** (1), 73–82.

Hager, W. H. 1994 *Abwasserhydraulik - Theorie und Praxis*. Springer-Verlag Berlin Heidelberg.

Haller, G. 2005 An objective definition of a vortex. *Journal of Fluid Mechanics* **525**, 1–26.

Harlow, F. H. & Welch, J. E. 1965 Numerical calculation of time-dependent viscous incompressible flow of fluid with free surface. *The Physics of Fluids* **8** (12), 2182–2189.

Hellström, L. & Smits, A. J. 2014 The energetic motions in turbulent pipe flow. *Physics of Fluids* **26** (12), 125102.

Hellström, L. H. O., Ganapathisubramani, B. & Smits, A. J. 2015 The evolution of large-scale motions in turbulent pipe flow. *Journal of Fluid Mechanics* **779**, 701–715.

Hellström, L. H. O., Marusic, I. & Smits, A. J. 2016 Self-similarity of the large-scale motions in turbulent pipe flow. *Journal of Fluid Mechanics* **792**, R1.

Hellström, L. H. O., Sinha, A. & Smits, A. J. 2011 Visualizing the very-large-scale motions in turbulent pipe flow. *Physics of Fluids* **23** (1), 011703.

Hinze, J. O. 1967 Secondary currents in wall turbulence. *Physics of Fluids (1958-1988)* **10** (9), S122–S125.

Hinze, J. O. 1973 Experimental investigation of secondary currents in the turbulent flow through a straight conduit. *Applied Science Research* **28**, 453–465.

Hsu, T. Y., Grega, L. M., Leighton, R. I. & Wei, T. 2000 Turbulent kinetic energy transport in a corner formed by a solid wall and a free surface. *Journal of Fluid Mechanics* **410**, 343–366.

Hunt, J. C. R., Wray, A. & Moin, P. 1988 Eddies, stream, and convergence zones in turbulent flows. , vol. CTR-S88, pp. 193–208. Center for Turbulence Research, Stanford University.

Jeong, J. & Hussain, F. 1995 On the identification of a vortex. *Journal of Fluid Mechanics* **285**, 69–94.

Jiménez, J. 2018 Coherent structures in wall-bounded turbulence. *Journal of Fluid Mechanics* **842**.

Jiménez, J. & Kawahara, G. 2012 *Dynamics of Wall-Bounded Turbulence*, pp. 221–268. Cambridge University Press.

Jiménez, J. & Moin, P. 1991 The minimal flow unit in near-wall turbulence. *Journal of Fluid Mechanics* **225**, 213–240.

Jiménez, J. & Pinelli, A. 1999 The autonomous cycle of near-wall turbulence. *Journal of Fluid Mechanics* **389**, 335–359.

Joung, Y. & Choi, S. U. 2009 Direct numerical simulation of low Reynolds number flows in an open-channel with sidewalls. *International Journal for Numerical Methods in Fluids* **62**, 854–874.

Kara, S., Stoesser, T. & Sturm, T. W. 2012 Turbulence statistics in compound channels with deep and shallow overbank flows. *Journal of Hydraulic Research* **50** (5), 482–493.

Kevin, K., Monty, J. & Hutchins, N. 2019 The meandering behaviour of large-scale structures in turbulent boundary layers. *Journal of Fluid Mechanics* **865**, R1.

Kida, S. & Miura, H. 1998 Swirl condition in low-pressure vortices. *Journal of the Physical Society of Japan* **67** (7), 2166–2169.

Kim, J., Moin, P. & Moser, R. 1987 Turbulence statistics in fully developed channel flow at low reynolds number. *Journal of Fluid Mechanics* **177**, 133–166.

Knight, D. W. & Sterling, M. 2000 Boundary shear in circular pipes running partially full. *Journal of Hydraulic Engineering* **126** (4), 263–275.

Kölling, C. 1994 Finite - Elemente - Simulation der Geschwindigkeitsverteilung in Kanälen und teilgefüllten Rohrleitungen. PhD thesis, Technische Universität München.

Kolmogorov, A. N., Levin, V., Hunt, J. C. R., Phillips, O. M. & Williams, D. 1991 The local structure of turbulence in incompressible viscous fluid for very large reynolds numbers. *Proceedings of the Royal Society of London. Series A: Mathematical and Physical Sciences* **434** (1890), 9–13.

Komori, S., Nagaosa, R., Murakami, Y., Chiba, S., Ishii, K. & Kuwahara, K. 1993 Direct numerical simulation of three-dimensional open-channel flow with zero-shear gas-liquid interface. *Physics of Fluids A: Fluid Dynamics* **5** (1), 115–125.

Kumar, S., Gupta, R. & Banerjee, S. 1998 An experimental investigation of the characteristics of free-surface turbulence in channel flow. *Physics of Fluids* **10** (2), 437–456.

Kundu, P. K. & Cohen, I. M. 2008 *Fluid Mechanics*. Elsevier.

Lee, J., Suh, J., Sung, H. J. & Pettersen, B. 2012 Structures of turbulent open-channel flow in the presence of an air-water interface. *Journal of Turbulence* **13**, N18+.

Lee, J., Sung, H. J. & Zaki, T. A. 2017 Signature of large-scale motions on turbulent/non-turbulent interface in boundary layers. *Journal of Fluid Mechanics* **819**, 165–187.

Liu, Y., Stoesser, T. & Fang, H. 2022 Effect of secondary currents on the flow and turbulence in partially filled pipes. *Journal of Fluid Mechanics* **938**, A16.

Lozano-Durán, A., Holzner, M. & Jiménez, J. 2016 Multiscale analysis of the topological invariants in the logarithmic region of turbulent channels at a friction reynolds number of 932. *Journal of Fluid Mechanics* **803**, 356–394.

Lozano-Durán, A. & Jiménez, J. 2014 Time-resolved evolution of coherent structures in turbulent channels: characterization of eddies and cascades. *Journal of Fluid Mechanics* **759**, 432–471.

Lumley, J.L. 1967 The structure of inhomogeneous turbulent flows. In *Atmospheric Turbulence and Radio Wave Propagation* (ed. A. M. Yaglom & V. I. Tatarski), pp. 166–178. Nauka.

Macke, E. 1982 über den feststofftransport bei niedrigen konzentrationen in teilgefüllten rohrleitungen. PhD thesis, Leichtweiß-Institut für Wasserbau.

Manhart, M. 1998 Vortex shedding from a hemisphere in a turbulent boundary layer. *Theoretical and Computational Fluid Dynamics* **12** (1), 1–28.

Manhart, M. 2004 A zonal grid algorithm for DNS of turbulent boundary layers. *Computers and Fluids* **33**, 435–461.

Manhart, M., Tremblay, F. & Friedrich, R. 2001 Mglet: a parallel code for efficient dns and les of complex geometries. In *Parallel Computational Fluid Dynamics 2000* (ed. C.B. Jenssen, H.I. Andersson, A. Ecer, N. Satofuka, T. Kvamsdal, B. Pettersen, J. Periaux & P. Fox), pp. 449 – 456. Amsterdam: North-Holland.

Matin, R., Hellström, L. H.O., Hernández-García, A., Mathiesen, J. & Smits, A. J. 2018 Coherent structures in turbulent square duct flow. *International Journal of Heat and Fluid Flow* **74**, 144–153.

Meier, G. E. A. 2000 *Ludwig Prandtl, ein Führer in der Strömungslehre, Biographische Artikel zum Werk Ludwig Prandtls*. Springer, Vieweg+Teubner.

Melhem, G. 1990 Hydraulische Berechnung teilgefüllter Rohrleitungen mit Kreisquerschnitt. *Wissenschaftliche Zeitschrift der TU Dresden* **5**, 185–189.

Mizuno, Y. & Jiménez, J. 2011 Mean velocity and length-scales in the overlap region of wall-bounded turbulent flows. *Physics of Fluids* **23** (8), 085112.

Monty, J. P., Hutchins, N., Ng, H. C. H., Marusic, I. & Chong, M. S. 2009 A comparison of turbulent pipe, channel and boundary layer flows. *Journal of Fluid Mechanics* **632**, 431–442.

Motoori, Y. & Goto, S. 2019 Generation mechanism of a hierarchy of vortices in a turbulent boundary layer. *Journal of Fluid Mechanics* **865**, 1085–1109.

Nagaosa, R. 1999 Direct numerical simulation of vortex structures and turbulent scalar transfer across a free surface in a fully developed turbulence. *Physics of Fluids* **11** (6), 1581–1595.

Nagaosa, R. & Handler, R. A. 2003 Statistical analysis of coherent vortices near a free surface in a fully developed turbulence. *Physics of Fluids* **15** (2), 375–394.

Naudascher, E. 1992 *Hydraulik der Gerinne und Gerinnebauwerke*. Springer-Verlag Wien.

Nawroth, G., Kriegseis, J., Mattern, P., Vaas, M. & Frohnapfel, B. 2015 Kohärente Sekundärströmungsstrukturen in einem offenen turbulent durchströmten Kanal. In *Lasermethoden in der Strömungsmesstechnik : 23. Fachtagung, 8. - 10. September 2015, Dresden* (ed. J. Czarske, L. Büttner, A. Fischer, B. Ruck, A. Leder & D. Dopheide), pp. 7.1–7.8. Deutsche Gesellschaft für Laser-Anemometrie, GALA, Dresden.

Nezu, I. 2005 Open-channel flow turbulence and its research prospect in the 21st century. *Journal of Hydraulic Engineering* **131** (4), 229–246.

Nezu, I. & Nakagawa, H. 1993 *Turbulence in Open-Channel Flows*. Balkema.

Nezu, I. & Rodi, W. 1986 Open-Channel Flow Measurements with a Laser Doppler Anemometer. *Journal of Hydraulic Engineering* **112** (5), 335–355.

Ng, H. C.-H., Collignon, E., Poole, R. J. & Dennis, D. J. C. 2021 Energetic motions in turbulent partially filled pipe flow. *Physics of Fluids* **33** (2), 025101.

Ng, H. C.-H., Cregan, H. L. F., Dodds, J. M., Poole, R. J. & Dennis, D. J. C. 2018 Partially filled pipes: experiments in laminar and turbulent flow. *Journal of Fluid Mechanics* **848**, 467–507.

Nikora, V. & Roy, A. G. 2012 Secondary flows in rivers: theoretical framework, recent advances and current challenges. In *Gravel bed rivers: processes, tools, environments* (ed. M. A. Church, P. Biron, A. G. Roy & P. Ashmore), pp. 3–22. Wiley-Blackwell.

Oertel, H. 2012 *Prandtl - Führer durch die Strömungslehre Grundlagen und Phänomene*. Springer Vieweg.

Orlandi, P. 1990 Vortex dipole rebound from a wall. *Physics of Fluids A: Fluid Dynamics* **2** (8), 1429–1436.

Pan, Y. & Banerjee, S. 1995 A numerical study of free-surface turbulence in channel flow. *Physics of Fluids* **7** (7), 1649–1664.

Passerat, J., Ouattara, N. K., Mouchel, J. M., Vincent, R. & Servais, P. 2011 Impact of an intense combined sewer overflow event on the microbiological water quality of the Seine River. *Water Research* **45** (2), 893–903.

Peller, N. 2010 Numerische Simulation turbulenter Strömungen mit Immersed Boundaries. PhD thesis, TU München.

Peller, N., Le Duc, A., Tremblay, F. & Manhart, M. 2006 High-order stable interpolations for immersed boundary methods. *International Journal for Numerical Methods in Fluids* **52** (11), 1175–1193.

Perot, B. & Moin, P. 1995 Shear-free turbulent boundary layers. part 1. physical insights into near-wall turbulence. *Journal of Fluid Mechanics* **295**, 199–227.

Pinelli, A., Uhlmann, M., Sekimoto, A. & Kawahara, G. 2010 Reynolds number dependence of mean flow structure in square duct turbulence. *Journal of Fluid Mechanics* **644**, 107–122.

Pirozzoli, S., Modesti, D., Orlandi, P. & Grasso, F. 2018 Turbulence and secondary motions in square duct flow. *Journal of Fluid Mechanics* **840**, 631–655.

Pope, S. B. 2000 *Turbulent Flows*. Cambridge University Press.

Prandtl, L., Oswatitsch, K. & Wieghardt, K. 1990 *Führer durch die Strömungslehre*. Springer, Vieweg+Teubner.

Replogle, I. A. & Chow, V. T. 1966 Tractive force distribution in open channels. *Journal of the hydraulics division* **92**.

Robinson, S. K. 1990 A review of vortex structures and associated coherent motions in turbulent boundary layers. In *Structure of Turbulence and Drag Reduction* (ed. A. Gyr), pp. 23–50. Berlin, Heidelberg: Springer Berlin Heidelberg.

Robinson, S. K. 1991 Coherent motions in the turbulent boundary layer. *Annual Review of Fluid Mechanics* **23** (1), 601–639.

Sakai, Y. 2016 Coherent structures and secondary motions in open duct flow. PhD thesis, Karlsruher Institut für Technologie.

Sakai, Y., Mendez, S., Strandenes, H., Ohlerich, M., Pasichnyk, I., Allalen, M. & Manhart, M. 2019 Performance optimisation of the parallel cfd code mglet across different hpc platforms. In *Proceedings of the Platform for Advanced Scientific Computing Conference*, *PASC '19* . New York, NY, USA: Association for Computing Machinery.

Sander, T. & Koch, S. 1990 Zur Geschwindigkeitsverteilung in teilgefüllten Kreisrohrleitungen im Hinblick auf neue Durchflussmeßverfahren im Abwasserbereich. *Mitteilungen des Leichtweiß-Instituts der TU Braunschweig* **108**, 427–458.

Sarpkaya, T. 1996 Vorticity, free surface, and surfactants. *Annual Review of Fluid Mechanics* **28** (1), 83–128.

Schanderl, W. & Manhart, M. 2018 Dissipation of turbulent kinetic energy in a cylinder wall junction flow. *Flow, Turbulence and Combustion* **101** (2), 499–519.

Schlichting, H. & Gersten, K. 2017 *Boundary-Layer Theory*. Springer, Berlin, Heidelberg.

Shen, L., Zhang, X., Yue, D. K. P. & Triantafyllou, G. S. 1999 The surface layer for free-surface turbulent flows. *Journal of Fluid Mechanics* **386**, 167–212.

Sillero, J. A., Jiménez, J. & Moser, R. D. 2014 Two-point statistics for turbulent boundary layers and channels at reynolds numbers up to $\delta^+ \approx 2000$. *Physics of Fluids* **26** (10), 105109.

Sirovich, L. 1987 Turbulence and the dynamics of coherent structures. i - coherent structures. ii - symmetries and transformations. iii - dynamics and scaling. *Quarterly of Applied Mathematics* **45**.

Strandenes, H., Jiang, F., Pettersen, B. & Andersson, H. I. 2019 Near-wake of an inclined 6:1 spheroid at reynolds number 4000. *AIAA Journal* **57** (4), 1364–1372.

Strauss, K. H. 1978 Geschwindigkeitsverteilung in teilgefüllten Kreisrohren. *Mitteilungen aus Hydraulik und Gewässerkunde, TU München* **24**, 81–109.

Tamburrino, A. & Gulliver, J. S. 2007 Free-surface visualization of streamwise vortices in a channel flow. *Water Resources Research* **43** (11).

Tominaga, A., Nezu, I., Ezaki, K. & Nakagawa, H. 1989 Three-dimensional turbulent structure in straight open channel flows. *Journal of Hydraulic Research* **27** (1), 149–173.

Trajkovic, B., Ivetic, M., Calomino, F. & D'Ippolito, A. 1999 Investigation of transition from free surface to pressurized flow in a circular pipe. *Water Science and Technology* **39** (9), 105–112.

Uhlmann, M., Pinelli, A., Kawahara, G. & Sekimoto, A. 2007 Marginally turbulent flow in a square duct. *Journal of Fluid Mechanics* **588**, 153–162.

Vanderwel, C., Stroh, A., Kriegseis, J., Frohnapfel, B. & Ganapathisubramani, B. 2019 The instantaneous structure of secondary flows in turbulent boundary layers. *Journal of Fluid Mechanics* **862**, 845–870.

Vinuesa, R., Schlatter, P. & Nagib, H. M. 2015 On minimum aspect ratio for duct flow facilities and the role of side walls in generating secondary flows. *Journal of Turbulence* **16** (6), 588–606.

Waleffe, F. 1997 On a self-sustaining process in shear flows. *Physics of Fluids* **9** (4), 883–900.

Weyrauch, P., Matzinger, A., Pawlowsky-Reusing, E., Plume, S., von Seggern, D., Heinzmann, B., Schroeder, K. & Rouault, P. 2010 Contribution of combined sewer overflows to trace contaminant loads in urban streams. *Water Research* **44** (15), 4451–4462.

Williamson, J.H 1980 Low-storage runge-kutta schemes. *Journal of Computational Physics* **35** (1), 48 – 56.

Yang, S. Q. 2005 Interactions of boundary shear stress, secondary currents and velocity. *Fluid Dynamics Research* pp. 121+.

Yang, S. Q. & Lim, S. Y. 1997 Mechanism of energy transportation and turbulent flow in a 3D channel. *Journal of Hydraulic Engineering* **123** (8), 684–692.

Yang, S. Q., Tan, S. K. & Lim, S. Y. 2004 Velocity Distribution and Dip-Phenomenon in Smooth Uniform Open Channel Flows. *Journal of Hydraulic Engineering* **130** (12), 1179–1186.

Yang, S. Q., Tan, S. K. & Wang, X. K. 2012 Mechanism of secondary currents in open channel flows. *Journal of Geophysical Research* **117** (F4), F04014+.

Yoon, J. I., Sung, J. & Ho Lee, M. 2012 Velocity profiles and friction coefficients in circular open channels. *Journal of Hydraulic Research* **50** (3), 304–311.

Zagarola, M. V. & Smits, A. J. 1997 Scaling of the mean velocity profile for turbulent pipe flow. *Physical Review Letters* **78**, 239–242.

Zampiron, A., Cameron, S. & Nikora, V. 2020 Secondary currents and very-large-scale motions in open-channel flow over streamwise ridges. *Journal of Fluid Mechanics* **887**, A17.

Zhong, Q., Chen, Q., Wang, H., Li, D. & Wang, X. 2016 Statistical analysis of turbulent super-streamwise vortices based on observations of streaky structures near the free surface in the smooth open channel flow. *Water Resources Research* **52** (5), 3563–3578.

Appendix

A. Transformation Scheme for Vectors and Tensors from Cartesian to Polar Coordinates

The following transformations were applied to vectors and tensors to switch from the Cartesian to the Polar coordinates (cf. section 3.2.3).

Vector transformation:

$$\begin{bmatrix} u_r \\ u_\theta \\ u_1 \end{bmatrix} = \begin{bmatrix} cos(\theta) & sin(\theta) & 0 \\ -sin(\theta) & cos(\theta) & 0 \\ 0 & 0 & 1 \end{bmatrix} \begin{bmatrix} u_2 \\ u_3 \\ u_1 \end{bmatrix} \tag{A.1}$$

Tensor transformation:

$$\begin{bmatrix} \tau_{rr} & \tau_{r\theta} & \tau_{r1} \\ \tau_{\theta r} & \tau_{\theta\theta} & \tau_{\theta 1} \\ \tau_{1r} & \tau_{1\theta} & \tau_{11} \end{bmatrix} = \begin{bmatrix} cos(\theta) & sin(\theta) & 0 \\ -sin(\theta) & cos(\theta) & 0 \\ 0 & 0 & 1 \end{bmatrix} \begin{bmatrix} \tau_{22} & \tau_{23} & \tau_{21} \\ \tau_{32} & \tau_{33} & \tau_{31} \\ \tau_{12} & \tau_{13} & \tau_{11} \end{bmatrix} \begin{bmatrix} cos(\theta) & -sin(\theta) & 0 \\ sin(\theta) & cos(\theta) & 0 \\ 0 & 0 & 1 \end{bmatrix} \tag{A.2}$$

B. Artifacts of Cartesian and Polar Coordinate System on In-Plane Components of Reynolds Normal Stresses

Figure B.1 illustrates the influence and artifacts of the Cartesian and the Polar coordinate system on the in-plane components of the Reynolds normal stresses (cf. section 3.2.3). The artifacts of the Cartesian coordinate system become visible along the wall, where the azimuthal and wall normal components are divided into the x_2- and x_3-components. The Polar coordinate system has artifacts in the pipe centre.

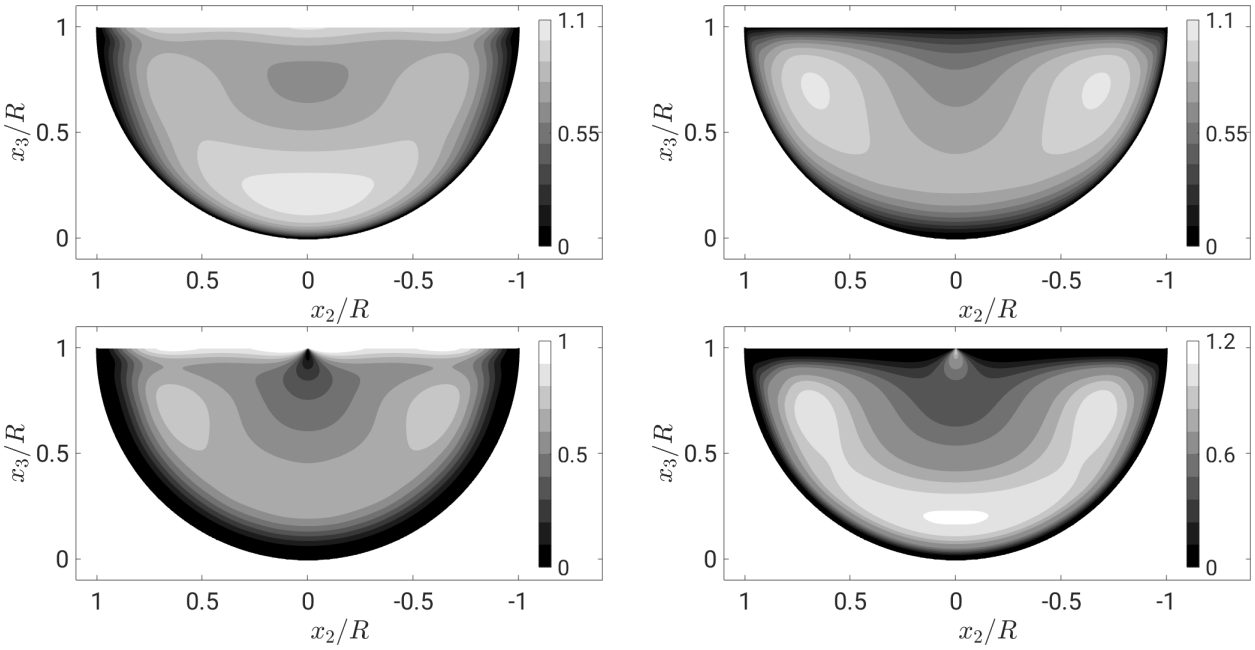

Figure B.1: Normalised root mean square of Reynolds stresses $u_{2,\mathrm{rms}}, u_{3,\mathrm{rms}}$ (top) and $u_{\mathrm{r,rms}}$, $u_{\theta,\mathrm{rms}}$ (bottom) for $Re_\tau = 180$ and 50% FR.

C. Spatial Modes of 3C- and 2C-POD for 25% and 75% FR

As additional information to section 4.2.1 (*Spatial Modes* Φ), the spatial modes Φ^k for 25% and 75% filling ratio of $Re_\tau = 180$ are shown in figures C.1 and C.2 for 3C-POD and figures C.3 for 2C-POD. The colourful contours represent the magnitude of the streamwise component. Blue and red distinguishes structures with opposite sign, but, as mentioned in section 4.2.1, only in combination with the temporal modes the actual direction can be stated for each time instance. The streamlines show flow paths of the cross-stream components, which can be both ways and the colour of streamlines shows the magnitude of the cross-stream velocities. Black means high intensity and white denotes low intensity.

For 25% and 75% filling the first four spatial modes and Φ^{11} and Φ^{80} of 3C-POD are shown in figure in figures C.1 and C.2. It already became noticeable, that the quarter filled flow case is different to the others, which is also present in the spatial modes. They cover the whole cross section with high intensities, only in a small layer at the free surface intensities are low. Unfortunately, no proper comparison to other data is possible for 25% filling, but for 75% filling Ng *et al.* (2021) provides data. They report only high intensities in the upper half of the cross-section for high energy modes, whereas figure C.1 shows high energy modes with high intensities also at the bottom. Note that this can only be stated for the six high energy modes reported by Ng *et al.* (2021). Similar to the spatial modes of 50% filling (cf. figure 4.25) the high intensities appear in small regions at the wall for the first modes. With decreasing energy content the intensities are more homogeneously distributed along the wall and also various azimuthal layers of high intensities can be identified.

The first four spatial modes of the 2C-POD for 25% and 75% FR can be found in figure C.3. In general, the first four modes show the same behaviour as for 50% FR, however, the structures are deformed vertically: compressed for 25% FR and stretched for 75% FR.

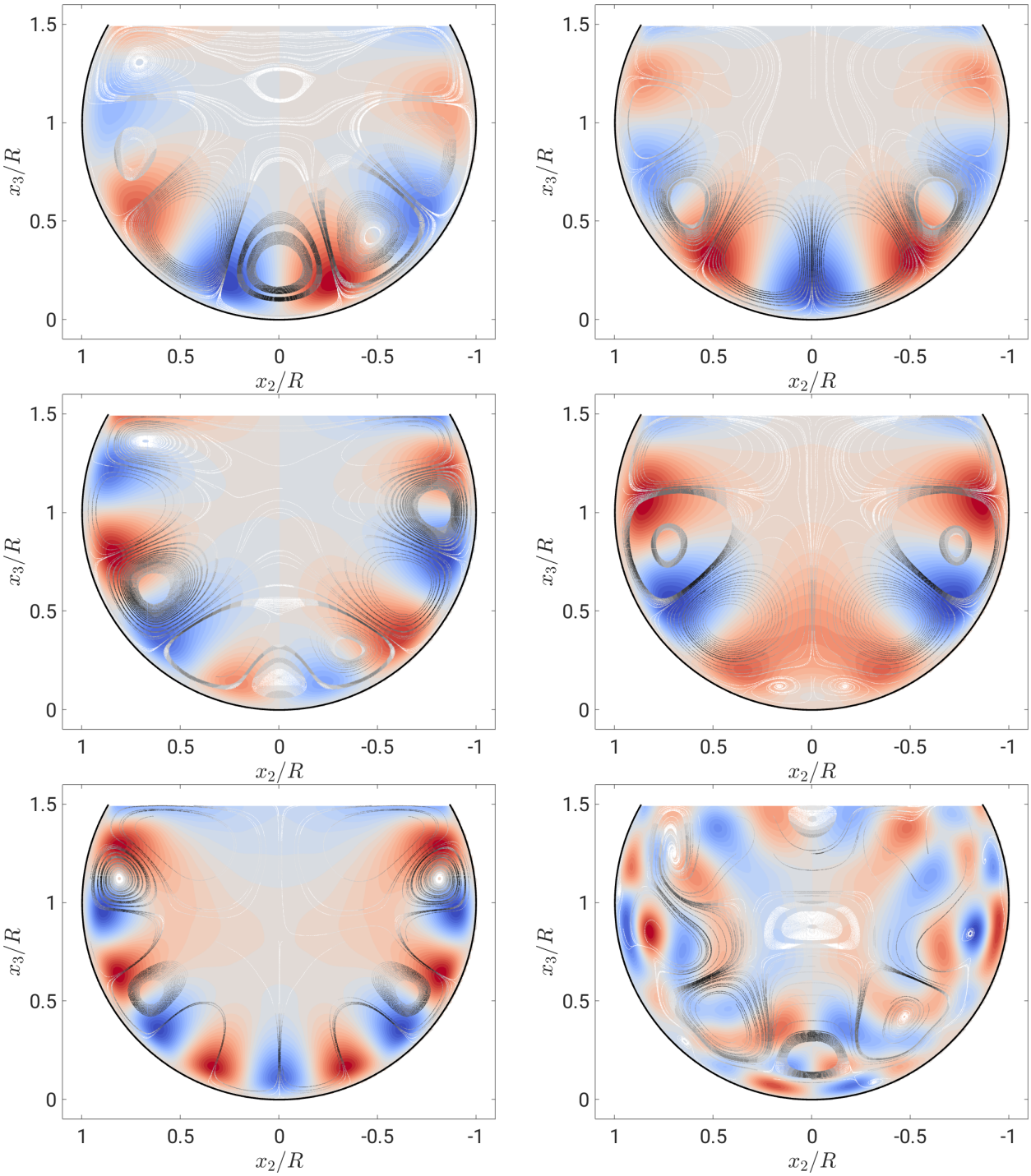

Figure C.1: Spatial modes Φ^1, Φ^2 (top row, left and right), Φ^3, Φ^4 (middle row) and Φ^{11}, Φ^{80} (bottom row) for 3C-POD of 75% FR and $Re_\tau = 180$. Φ_1^k is shown in blue to red colour and the gray contours display the magnitude of the cross-stream components Φ_2^k and Φ_3^k (black = high intensity, white = low intensity).

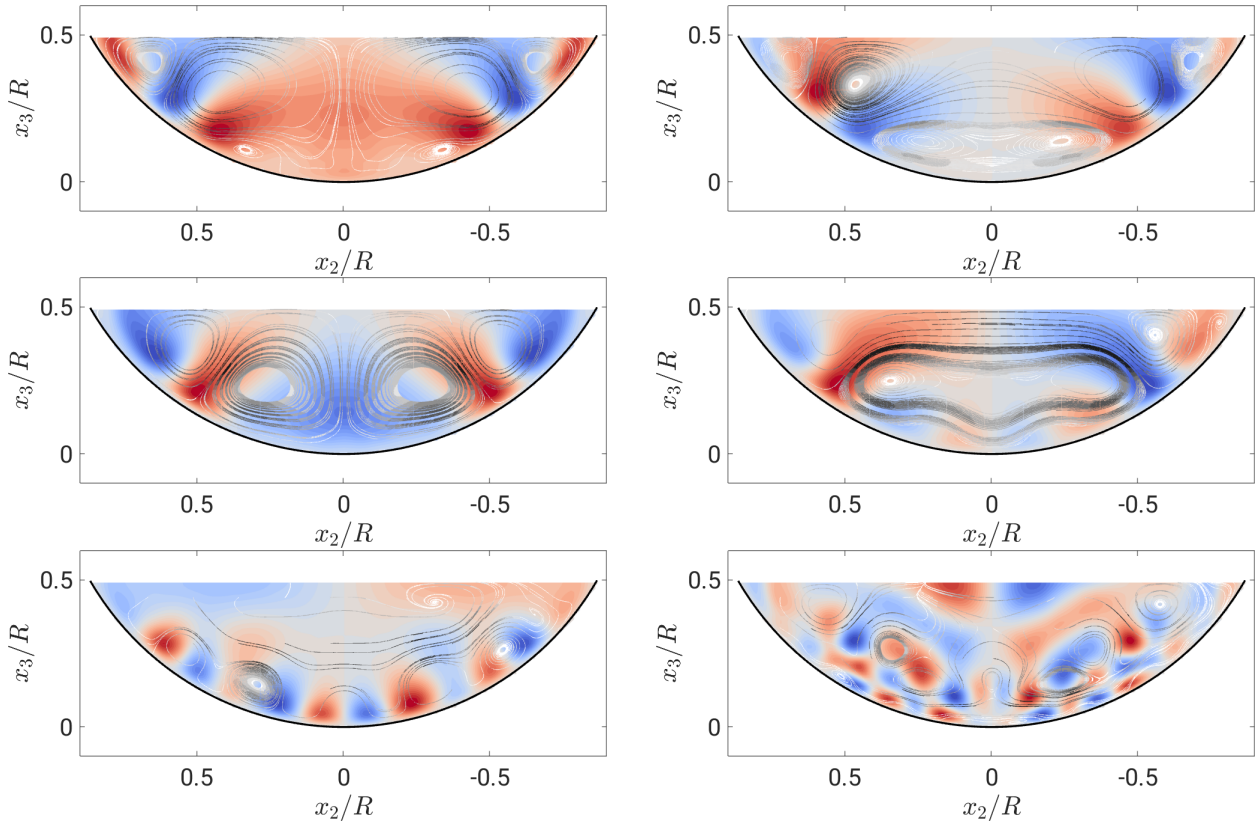

Figure C.2: Spatial modes Φ^1, Φ^2 (top row, left and right), Φ^3, Φ^4 (middle row) and Φ^{11}, Φ^{80} (bottom row) for 3C-POD of 25% FR and $Re_\tau = 180$. Φ_1^k is shown in blue to red colour and the gray contours display the magnitude of the cross-stream components Φ_2^k and Φ_3^k (black = high intensity, white = low intensity).

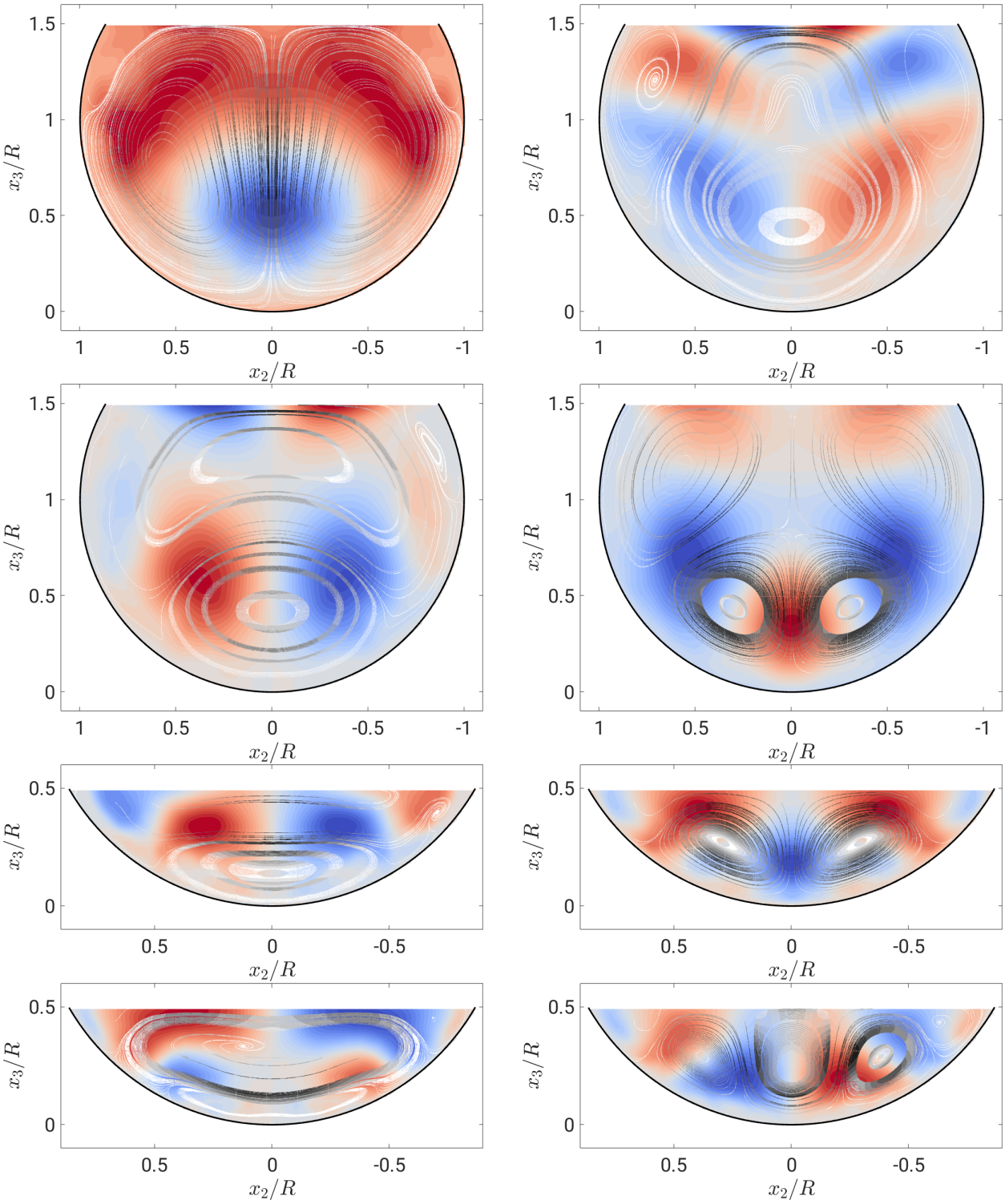

Figure C.3: Φ^1, Φ^2 (top, left and right) and Φ^3, Φ^4 (bottom) for 2C-POD of 75% FR (upper half) and 25% FR (lower half) and $Re_\tau = 180$. Φ_1^k is shown in blue to red colour and the gray contours display the magnitude of the cross-stream components Φ_2^k and Φ_3^k (black = high intensity, white = low intensity).

D. Reynolds-Dependency of Conditionally Averaged $P_{2,3}$-Event

The following figures D.1, D.2 and D.3 are already integrated in section 4.2.4 as figure 4.55. For sake of better visibility the single plots are shown again with enlarged size.

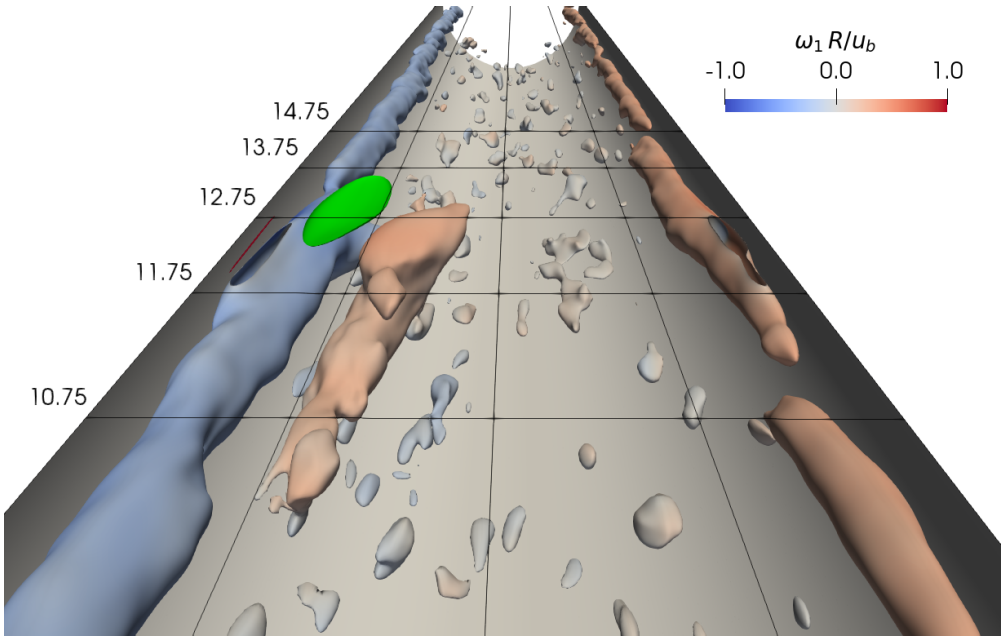

Figure D.1: Conditionally averaged flow field of the positive extreme event of $P_{2,3}$ (green) in the mixed-corner with contour of Q-criterion coloured with $\omega_1 R/u_b$. View in streamwise direction for $Re_\tau = 140$ and 50% FR. Threshold for $Q\ R/u_b$ is 0.02.

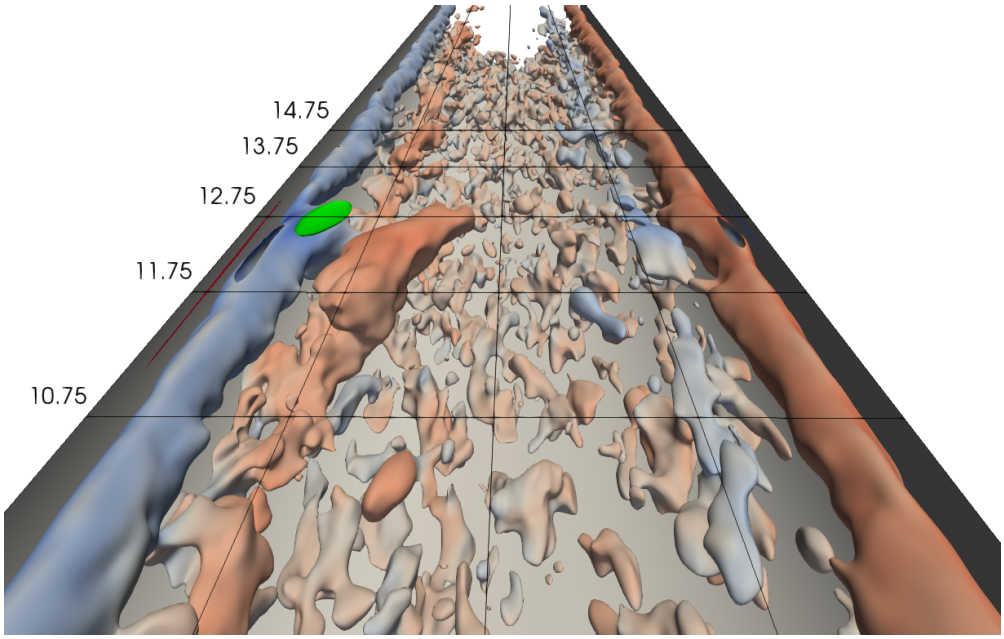

Figure D.2: Conditionally averaged flow field of the positive extreme event of $P_{2,3}$ (green) in the mixed-corner with contour of Q-criterion coloured with $\omega_1\, R/u_b$ (see fig. D.1). View in streamwise direction for $Re_\tau = 180$ and 50% FR. Threshold for $Q\ R/u_b$ is 0.023.

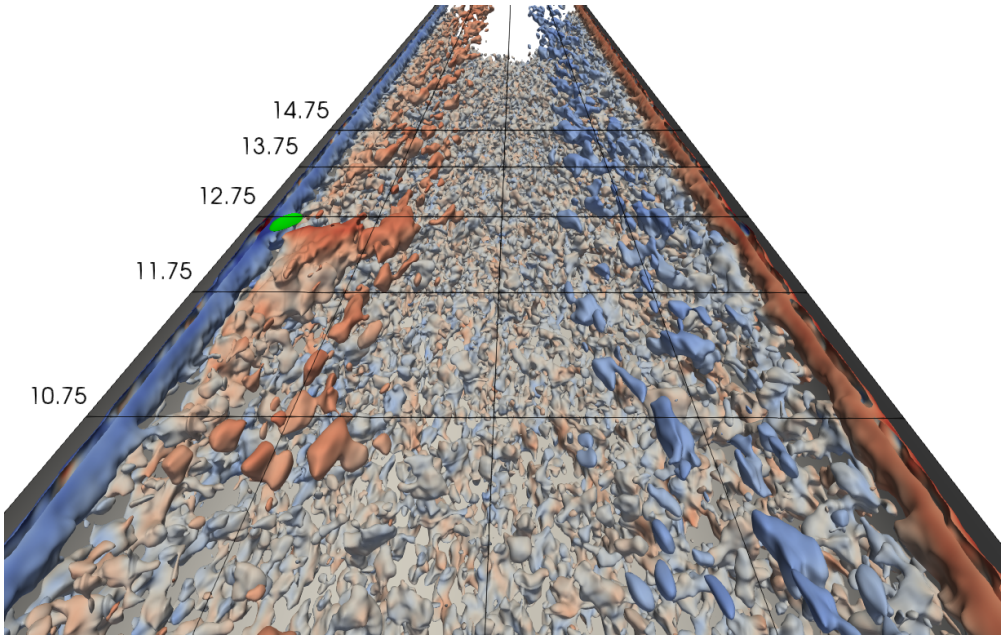

Figure D.3: Conditionally averaged flow field of the positive extreme event of $P_{2,3}$ (green) in the mixed-corner with contour of Q-criterion coloured with $\omega_1\, R/u_b$ (see fig. D.1). View in streamwise direction for $Re_\tau = 460$ and 50% FR. Threshold for $Q\ R/u_b$ is 0.035.